Multi-physics computational models of articular cartilage for estimation of its mechanical and physical properties

Arbabi, Vahid

DOI
10.4233/uuid:55b7d7ed-dba5-41ab-9796-fbe3d6659f84

Publication date
2016

Document Version
Final published version

Citation (APA)
Arbabi, V. (2016). *Multi-physics computational models of articular cartilage for estimation of its mechanical and physical properties*. [Dissertation (TU Delft), Delft University of Technology].
https://doi.org/10.4233/uuid:55b7d7ed-dba5-41ab-9796-fbe3d6659f84

MULTI-PHYSICS MODELING OF ARTICULAR CARTILAGE

FOR ESTIMATION OF ITS MECHANICAL AND PHYSICAL PROPERTIES

VAHID ARBABI

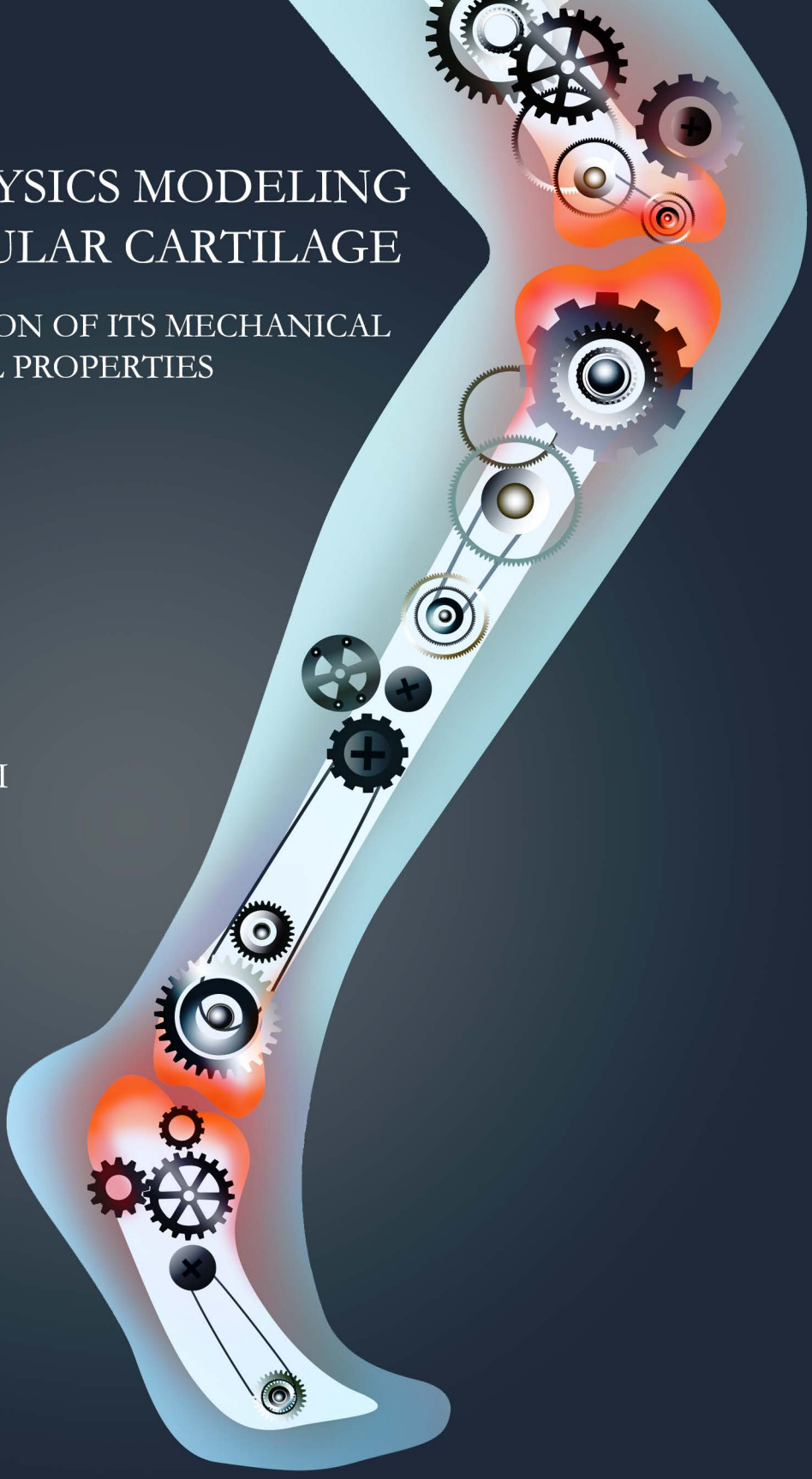

MULTI-PHYSICS COMPUTATIONAL MODELS OF ARTICULAR CARTILAGE FOR ESTIMATION OF ITS MECHANICAL AND PHYSICAL PROPERTIES

Vahid Arbabi

MULTI-PHYSICS COMPUTATIONAL MODELS OF ARTICULAR CARTILAGE FOR ESTIMATION OF ITS MECHANICAL AND PHYSICAL PROPERTIES

Proefschrift

ter verkrijging van de graad van doctor
aan de Technische Universiteit Delft,
op gezag van de Rector Magnificus prof. ir. K.C.A.M. Luyben;
voorzitter van het College voor Promoties,
in het openbaar te verdedigen op woensdag 14 september 2016 om 10:00 uur

door

Vahid ARBABI
Master of Sience in Mechanichal Engineering
Yazd University, Yazd, Iran.
geboren te Zabol, Iran

This dissertation has been approved by the
promotor: Prof. dr. ir. H. Weinans
copromotor: Dr. A.A. Zadpoor

Composition of the doctoral committee:

Rector Magnificus	Chairman
Prof. dr. ir. H. Weinans	Technical University of Delft, promotor
Dr. A.A. Zadpoor	Technical University of Delft, copromotor
Independent members	
Prof. dr. M.T. Nieminen	University of Oulu
Dr. C.C. van Donkelaar	Eindhoven University of Technology
Prof. dr. F.C.T. van der Helm	Technical University of Delft
Prof. dr. ir. C.W. Oosterlee	Technical University of Delft
Prof. dr. ir. A. van Keulen	Technical University of Delft

ISBN/EAN: 978-94-6186-713-1

v.arbabi@gmail.com

This research was carried out in *the Department* of *Biomechanical Engineering* of *Delft University of Technology*.

Keywords: multiphysics, finite element modelling, articular cartilage, osteoarthritis, poroelastic, biphasic-solute and multiphasic model, indentation, diffusion of charge and uncharged solute, fixed charge density.

Printed in the Netherlands: Gildeprint.nl
Front cover graphic: Nednapa/Shutterstock.com
Back cover graphic: Maxuser/Shutterstock.com
Published by: TU Delft Library

This PhD thesis is dedicated to my father, my mother and my wife; they have always been a constant source of support and encouragement.

TABLE OF CONTENTS

Chapter 1

Introduction

1.1. INTRODUCTION

Osteoarthritis (OA) is a multifactorial pathophysiologic condition that affects the components of articulating joints namely articular cartilage (AC), synovial fluid and subchondral bone [1-3]. Particularly, advanced OA is associated with cartilage damage, subchondral bone sclerosis, and thinning of synovial fluid that causes significant musculoskeletal morbidity (Figure 1.1) [3, 4].

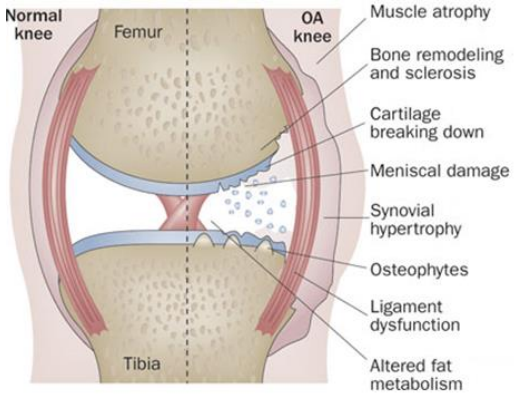

Figure 1.1. Healthy and OA joints are depicted (Adapted by permission from Macmillan publishers Ltd: Nature Reviews Rheumatology [5], Copyright 2011).

Articular cartilage comprises crucial macromolecules among which proteoglycans (PGs) and collagens are the most abundant [6]. In OA, PG loss, collagen fibril disruption, and water content alterations prevail. Those changes severely deteriorate the mechanical properties of AC including, for example, its shock absorbing properties [7]. The PGs are responsible for providing normal AC with excellent compressive mechanical properties due to the negative fixed charges associated with them that lead to considerable influx of water from the synovial fluid. To sustain electro-neutrality in AC, positively charged ions from the surroundings are therefore attracted to the AC matrix through the

water influx [8]. Consequently, the high swelling pressure generated by the PGs is restrained by the tensile properties of collagen fibrils oriented differently across cartilage thickness [9]. Non-uniform distribution of PGs and collagens, dome-shaped orientation of collagen fibrils as well as water content create significant mechanical and physical gradients across AC [10, 11]. Across healthy AC, PG concentration increases and collagen content decreases, while water content steadily decreases from 80% at the cartilage surface to 60% near the cartilage-subchondral bone interface [6]. Unlike collagens that are barely replaced by chondrocytes –the only residing cell type in AC- PGs undergo continuous turnover and are thereby repaired after being continuously cleaved by enzymes, i.e. matrix metalloproteinase [12]. The transport of solutes across AC occurs frequently via molecular diffusion and is of major metabolic importance due to cartialge avascularity (Figure 1.2) [13].

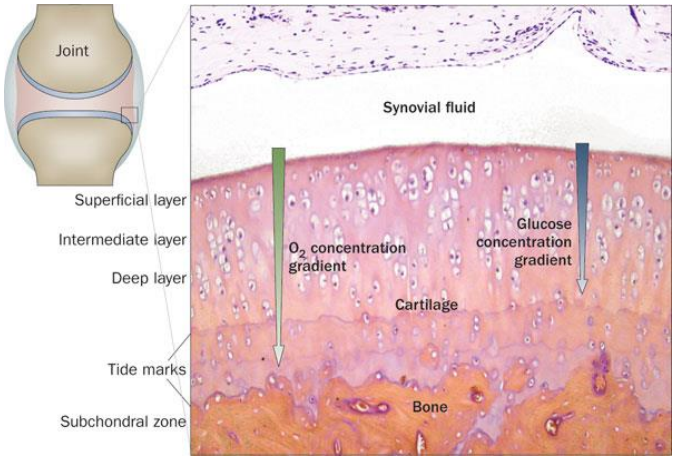

Figure 1.2. Solute transport nurtures the cartilage from the synovial fluid (Adapted by permission from Macmillan publishers Ltd: Nature Reviews Rheumatology [14], Copyright 2011).

The transport of molecules is significantly affected by the concentration of PG and collagen, orientation of collagen fibrils, water content as well as the charge and size of the molecule. PG loss and collagen fibril disruption that are considered the hallmarks of OA [13], may therefore change the transport properties of AC.

Since AC is a heterogeneous [15], multi-phasic, anisotropic, and nonlinear material, estimating its physical and mechanical properties cannot be successfully accomplished solely using analytical formulations. Therefore, the primary aim of this thesis is to develop multi-physics models that enable accurate prediction of the mechanical and physical properties of AC including the Young's modulus, permeability, Poisson's ratio, fixed charge density and the diffusivity of solutes. Since application of the developed models generally requires availability of significant computational expertise and given the fact that many labs do not have easy access to such expertise, a second goal of this thesis is to combine multi-physics models with artificial neural networks so as to make them accessible to a wider range of labs. Ease of use could significantly increase the impact of presented multi-physics models in actual practice of research on AC.

1.2. THESIS OUTLINE

The sequence of chapters in the thesis is based on a gradual trend of increasing complexity in the presented multi-physics models. Following chapter 1, which is an introductory overview of the multi-physics modeling of cartilage, the other chapters are organized as follows:

Chapter 2: A coupled finite element and artificial neural network (ANN) model to determine the mechanical and physical properties of articular cartilage as a poroelastic material using spherical

indenter was developed. The ANN was trained using noisy data to keep it robust against possible disturbances present in the input data. Since no analytical solution is available for this type of indentation and the only method is based on finite element modeling and optimization algorithm, using proposed method, one can obtain the mechanical and physical properties of cartilage robustly without any need for computational experties.

Chapter 3: A multi-zone biphasic-solute model based on contrast enhanced micro-computed tomography experiments for the transport of neutral solute across articular cartilage was developed. Using this method one can obtain diffusivity of different cartilage layers simultaneously.

Chapter 4: A coupled finite element model- artificial neural network (ANN) to determine solute diffusivity across articular cartilage in different cartilage layers based on biphasic-solute model (presented in chapter 3) was developed. The aim was to develop an algorithm to accurately obtain the diffusivity of cartilage layers without computational expertise (post-training the ANN).

Chapter 5: A contrast enhanced micro-computed tomography based on experimental setup was developed to study the isolated effects of external bath osmolality, solute concentration, and electrical charge on solute transport across articular cartilage. Quantification of solute diffusion was performed using our developed finite element models.

Chapter 6: An experimental setup was developed based on micro-computed tomography monitoring of diffusion across cartilage and subchondral plate. The goal was to confirm the diffusion of neutral solutes across osteochondral interface and to establish the relationship between microstructure of articular cartilage and

subchondral plate and the transport of molecules across articular cartilage and subchondral bone.

Chapter 7: A biphasic-solute model based on contrast enhanced micro-computed tomography experiments (chapter 6) for the transport of neutral solute across articular cartilage and subchondral plate was developed. Using this method one can obtain diffusivity of different cartilage layers as well as subchondral plate simultaneously.

Chapter 8: The effects of size and stirring of bath containing neutral solutes and stagnation layer at the bath-cartilage interface on the diffusion across cartilage were investigated by the aid of parametric biphasic-solute finite element models. The aim was to investigate the dominant parameters on diffusion and to optimize diffusion experiments.

Chapter 9: A multiphasic model based on contrast enhanced micro-computed tomography experiments (chapter 5) for the transport of charged solute across articular cartilage was developed. Using this method one can obtain fixed charge density and diffusivity at each cartilage layer simultaneously.

Chapter 10: This chapter presents and reviews the latest finite element models enabling determination of physical and mechanical properties of articular cartilage based on indentation and diffusion experiments. The emergence of artificial neural networks to reduce the reliance on the finite element modeling will be discussed and finally conclusive suggestions based on the findings of the thesis chapters will be provided.

Chapter 11: This chapter summarizes the main findings of the thesis and what we learned from multi-physics modeling of cartilage and subchondral bone that also includes some suggestions for future work.

Finally, a protocol is provided to establish experimental-computational setup to study transport of neutral and charged solutes in articular cartilage (Appendix).

1.3. REFRENCES

1. Weinans H., Siebelt M., Agricola R., Botter S.M., Piscaer T.M., Waarsing J.H., *Pathophysiology of peri-articular bone changes in osteoarthritis.* Bone, 2012. **51**(2): p. 190-6.
2. Stolz M., Gottardi R., Raiteri R., Miot S., Martin I., Imer R., Staufer U., Raducanu A., Duggelin M., Baschong W., Daniels A.U., Friederich N.F., Aszodi A., Aebi U., *Early detection of aging cartilage and osteoarthritis in mice and patient samples using atomic force microscopy.* Nature Nanonotechnology, 2009. **4**(3): p. 186-192.
3. Mathieu P., Conrozier T., Vignon E., Rozand Y., Rinaudo M., *Rheologic Behavior of Osteoarthritic Synovial Fluid after Addition of Hyaluronic Acid: A Pilot Study.* Clinical Orthopaedics and Related Research, 2009. **467**(11): p. 3002-3009.
4. Crema M.D., Cibere J., Sayre E.C., Roemer F.W., Wong H., Thorne A., Singer J., Esdaile J.M., Marra M.D., Kopec J.A., Nicolaou S., Guermazi A., *The relationship between subchondral sclerosis detected with MRI and cartilage loss in a cohort of subjects with knee pain: the knee osteoarthritis progression (KOAP) study.* Osteoarthritis and Cartilage, (0).
5. Hunter D.J., *Pharmacologic therapy for osteoarthritis the era of disease modification.* Nat Rev Rheumatol, 2011. **7**(1): p. 13-22.
6. Sophia Fox A.J., Bedi A., Rodeo S.A., *The Basic Science of Articular Cartilage: Structure, Composition, and Function.* Sports Health, 2009. **1**(6): p. 461-468.
7. Nieminen M.T., Rieppo J., Silvennoinen J., Toyras J., Hakumaki J.M., Hyttinen M.M., Helminen H.J., Jurvelin J.S., *Spatial assessment of articular cartilage proteoglycans with Gd-DTPA-enhanced T1 imaging.* Magn Reson Med, 2002. **48**(4): p. 640-8.
8. Maroudas A., *Physicochemical Properties of Cartilage in the Light of Ion Exchange Theory.* Biophysical Journal, 1968. **8**(5): p. 575-595.
9. Maroudas A., Venn M., *Chemical composition and swelling of normal and osteoarthrotic femoral head cartilage. II. Swelling.* Ann Rheum Dis, 1977. **36**(5): p. 399-406.
10. Kokkonen H.T., Jurvelin J.S., Tiitu V., Toyras J., *Detection of mechanical injury of articular cartilage using contrast enhanced computed tomography.* Osteoarthritis Cartilage, 2011. **19**(3): p. 295-301.
11. Leddy H.A., Guilak F., *Site-specific effects of compression on macromolecular diffusion in articular cartilage.* Biophys J, 2008. **95**(10): p. 4890-5.
12. Manicourt D.-H., Devogelare J.-P., Thonar E.J.M.A., *Chapter 25 - Products of Cartilage Metabolism A2 - Bilezikian, Markus J. SeibelSimon P. RobinsJohn P*, in *Dynamics of Bone and Cartilage Metabolism (Second Edition)*. 2006, Academic Press: Burlington. p. 421-449.
13. Leddy H.A., Guilak F., *Site-Specific Molecular Diffusion in Articular Cartilage Measured using Fluorescence Recovery after Photobleaching.* Annals of Biomedical Engineering, 2003. **31**(7): p. 753-760.
14. Blanco F.J., Rego I., Ruiz-Romero C., *The role of mitochondria in osteoarthritis.* Nat Rev Rheumatol, 2011. **7**(3): p. 161-169.

15. Leddy H.A., Haider M.A., Guilak F., *Diffusional anisotropy in collagenous tissues: fluorescence imaging of continuous point photobleaching.* Biophys J, 2006. **91**(1): p. 311-6.

CHAPTER 2

DETERMINATION OF THE MECHANICAL AND PHYSICAL PROPERTIES OF CARTILAGE BY COUPLING POROELASTIC-BASED FINITE ELEMENT MODELS OF INDENTATION WITH ARTIFICIAL NEURAL NETWORKS*

* This chapter is published as a scientific paper:

Arbabi V., Pouran B., Campoli G., Weinans H., Zadpoor A.A. *Determination of the mechanical and physical properties of cartilage by coupling poroelastic-based finite element models of indentation with artificial neural networks.* Journal of Biomechanics 49, 631-637, 2015.

ABSTRACT

One of the most widely used techniques to determine the mechanical properties of cartilage is based on indentation tests and interpretation of the obtained force-time or displacement-time data. In the current computational approaches, one needs to simulate the indentation test with finite element models and use an optimization algorithm to estimate the mechanical properties of cartilage. The modeling procedure is cumbersome, and the simulations need to be repeated for every new experiment. For the first time, we propose a method for fast and accurate estimation of the mechanical and physical properties of cartilage as a poroelastic material with the aid of artificial neural networks. In our study, we used finite element models to simulate the indentation for poroelastic materials with wide combinations of mechanical and physical properties. The obtained force-time curves are then divided into three parts: the first two parts of the data is used for training and validation of an artificial neural network, while the third part is used for testing the trained network. The trained neural network receives the force-time curves as the input and provides the properties of cartilage as the output. We observed that the trained network could accurately predict the properties of cartilage within the range of properties for which it was trained. The mechanical and physical properties of cartilage could therefore be estimated very fast, since no additional finite element modeling is required once the neural network is trained. The robustness of the trained artificial neural network in determining the properties of cartilage based on noisy force-time data was assessed by introducing noise to the simulated force-time data. We found that the training procedure could be optimized so as to maximize the robustness of the neural network against noisy force-time data.

2.1. INTRODUCTION

Osteoarthritis (OA) is a common chronic disease that develops as a result of the degeneration of articular cartilage (AC) which frequently leads to pain and limited mobility [1, 2]. In AC, collagen type II fibers mainly provide tensile mechanical properties while negatively charged proteoglycans macromolecules (PGs) provide shear and compressive mechanical properties of AC [3]. Changes in the mechanical and physical properties of AC such as Young's modulus and permeability as a result of PG loss and collagen fibril disintegration are the hallmarks of disease progression. Mechanical characterization of AC and its changes over time is therefore an important research line within the OA community [4-6]. Available tools to investigate the mechanical behavior of cartilage are compression tests among which the most important ones are confined compression [7-9], unconfined compression [9-11], and indentation tests [12-14].

The indentation test offers the advantage of obtaining local mechanical properties of cartilage accurately [15]. It also does not require cartilage tissue to be cut loose from the bone, and consequently sophisticated processes for preparing cartilage before the test do not cause damage to the tissue. It is therefore possible to state that the indentation test is an absolutely nondestructive test [11, 16] and consequently it can be performed *in vivo* [17, 18]. Indentation tests are shown to be capable of identifying OA and healthy cartilage at nano-scale [4] and determining the fixed charge density of cartilage tissue [19].

One way to specify cartilage's mechanical properties is to apply analytical solution to the data from the indentation test. Since no analytical solution for the indentation of poroelastic materials exists, this approach may lead to errors for the prediction of mechanical properties of cartilage [20, 21]. The other approach is to use finite element method combined with optimization

algorithm by which cartilage properties can be derived [6, 22]. This however requires cumbersome iterative processes until the best finite element model for the problem is achieved [23-26]. Moreover, the entire modeling process needs to be repeated for every new indentation test.

In this study, we first used finite element models (FEM) to simulate the indentation of cartilage as a poroelastic material in relaxation mode for a wide range of properties and their combinations i.e. Young's modulus, Poisson's ratio, permeability, and friction coefficient between the indenter and cartilage surface. Thereafter, we used force–time data obtained from FEM as inputs and properties of articular cartilage as targets to train an artificial neural network (ANN). This enabled us to extract the precise properties of articular cartilage under similar boundary conditions as were used in FEM. This approach will potentially pave the way toward predicting accurate properties of healthy and OA articular cartilage when the experimental data from indentation tests are accessible. The long-term aim of the current study is to conceive a method by which a user-friendly environment becomes available that could be used to distinguish between healthy and diseased tissue.

2.2. Methodology

2.2.1. FINITE ELEMENT MODELING

We used a finite element modeling platform i.e. Abaqus 6.11 to simulate the indentation test of a cartilage specimen introduced as a poroelastic material. The essential equations required for modelling cartilage are presented [10, 27] (Appendix A). Mechanical and physical properties as well as model assumptions were chosen based on the previous work [13, 14, 28]. The cartilage specimen was assumed to have a thickness of 3 mm and an axisymmetric radius of 20 mm to maximally eliminate the edge

effects on the fluid velocity vectors. A spherical indenter with the radius of 5 mm was used in the model (Figure 2.1). The cartilage properties are provided in Table 2.1 [14, 28-30]. The details of finite element modeling as well as the required boundary conditions are presented in Appendix B.

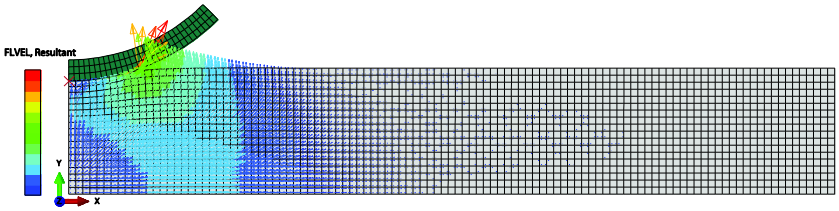

Figure 2.1. The axisymmetric model used for simulation of indentation experiments. Fluid velocity vectors are depicted in this figure for demonstration purposes.

Table 2.1. Properties of articular cartilage used in finite element simulations [14, 28-30].

Parameter	Value
Poisson's ratio, ν	0.08
Permeability, k	4.0 x 10^{-3} mm^4/N.s
Initial void ratio, e_0	4.0 (80 % interstitial fluid)
Coefficient of friction, f_f	0.02
Seepage coefficient, k_s	1 mm^3/N.s – Flow 0 mm^3/N.s – No flow
Young's modulus, E	0.54 MPa

We developed an Abaqus user subroutine to identify the contact between the cartilage and the indenter based on Pawaskar's work [14]. In this method, when contact stress on the cartilage's surface is greater than a threshold value, fluid flow is forced to stop. The developed user subroutine processed the information received from the solver in each iteration and created a common block that included all nodes with contact stress greater than the threshold (URDFILL). The common block could be accessed by another subroutine (FLOW). In the FLOW, the closest integration point to the node that has a contact stress greater than the threshold value is selected and fluid flow is stopped by setting both the seepage coefficient and sink pore pressure to zero. Otherwise, it continues to use a seepage coefficient equal to one while the sink pore pressure remains zero.

2.2.2. ARTIFICIAL NEURAL NETWORKS (ANNS) APPLICATION

In this section, we describe how we trained an ANN in MATLAB 2013 for predicting the cartilage mechanical and physical properties such as elastic modulus, Poisson's ratio, permeability, and friction coefficient using force–time data (Appendix C. How does artificial neural network function?).

The indentation test was simulated for a wide range of different mechanical and physical properties according to the previously used data from human articular cartilage [14]: elastic modulus between 0.1 and 1 MPa, Poisson's ratio between 0.01 and 0.2, permeability between 10^{-3} and 10^{-2} $mm^4/N.s$, and friction coefficient between 0 and 0.05. For every property, the variation interval was divided into 10 and finite element models were run for all possible combinations resulting in 10,000 simulations. The output of this parametric study was force-time data with 121 different time points which are originated from Abaqus resampling procedure. The input matrix for training the ANN therefore

contained 10,000×121 force–time data and the target matrix contained 10,000×4 cartilage properties. In the current sturdy we used a number of 30 hidden neurons for the noise-free data and 40 hidden neurons for noisy data. Following the training of the network, the curves by which the mechanical and physical properties can be determined were introduced into MATLAB and the results were effortlessly achieved (CPU time of 0.11 s using a computer (3.33 GHz (2 cores)).

2.2.3. Robustness assessment

In reality, noise occurs frequently during obtaining the force–time diagram using indentation tests. It is therefore crucial that the algorithm is sufficiently robust and capable of predicting the mechanical and physical properties from datasets that are associated with various levels of noise. To simulate the inaccuracies associated with noise in the force-time curve, a random Gaussian term (noise) was added to the training force-time data as follows [31, 32]:

$$F'(t) = F(t) + N(0, \sigma(t)) \tag{2.1}$$

where $N(0, \sigma(t))$ is a Gaussian distribution and standard deviation $\sigma(t) = F(t)/\lambda$. The parameter λ represents the signal to noise ratio: a smaller λ results in a noisier force-time data.

2.3. Results

2.3.1. Prediction of the cartilage's properties from noise-free force–time curves

When 10,000 samples were randomly distributed into training 90% equal to 9000 samples, validation 5% equal to 500 samples and test 5% equal to 500 samples and 30 hidden neurons were used for training the ANN [31, 33], the Pearson correlation coefficients

equalled one for training, validation, and test datasets (Figure 2.2A-C). The ANN training diagram had a small mean squared error for the training, validation and test datasets, indicating the effectiveness of the training algorithm (Figure 2.2D).

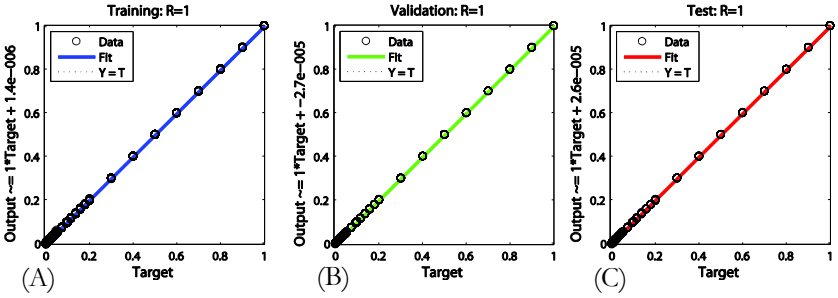

No. samples	Training	Validation	Test	No. neurons
10000	90	5%	5%	30

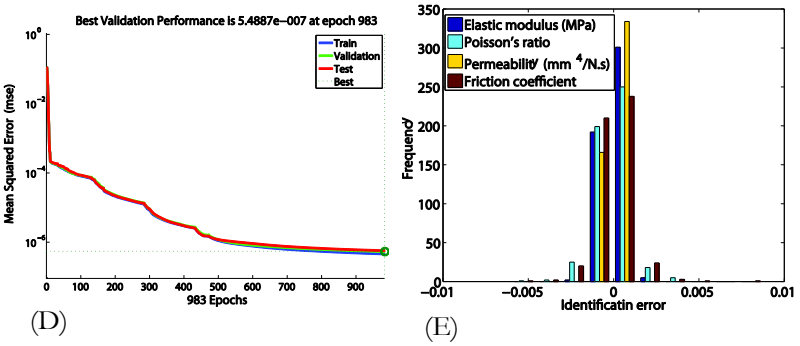

Figure 2.2. Regression diagrams for the training (A), validation (B), and test (C) datasets of the ANN trained in the absence of noise in its training and test data. ANN training diagram (D) and histogram of identification errors (e).

The improvement of the performance diagram while training the network was very similar for training, validation, and test datasets

(Figure 2.2D). The identification error – which is the value of the difference between the actual properties and ANN prediction for test data that was not used in training and validation sets – was also found to be very small (Figure 2.2E). The distribution of the identification error was similar to a normal distribution. Performing statistical analysis on test data can better show the network's performance (Figure 2.2E). In all cases, the mean identification error is of the order of -5 to -6 (Table 2.2). The small values of the mean identification error and standard deviation of identification error (Table 2.2), all confirm that the ANN can accurately identify the mechanical and physical properties of cartilage from the trained network.

Table 2.2. Mean identification error and standard deviation of identification error for the case where ANN was trained and tested with noise-free data.

	μ_{err}	σ_{err}
Elastic modulus (MPa)	-7.8e-6	5e-4
Poisson's ratio	-6.6e-5	9.4e-4
Permeability ($mm^4/N.s$)	-3.8e-6	2.3e-4
Friction coefficient	-1.2e-5	1.1e-3

Table symbols: μ_{err}: mean identification error, σ_{err}: standard deviation of identification error

2.3.2. Prediction of the cartilage's properties from noisy force–time curves

To evaluate the robustness of the trained ANN in identifying the mechanical and physical properties of cartilage in the presence of noise (section 2.3.1), we created a noisy data by adding a noise term to the simulated force-time data as described in Section 2.2.3. The signal to noise ratio parameter, λ, was between 10 and 100 for all cases considered in the current study (Figure 2.3).

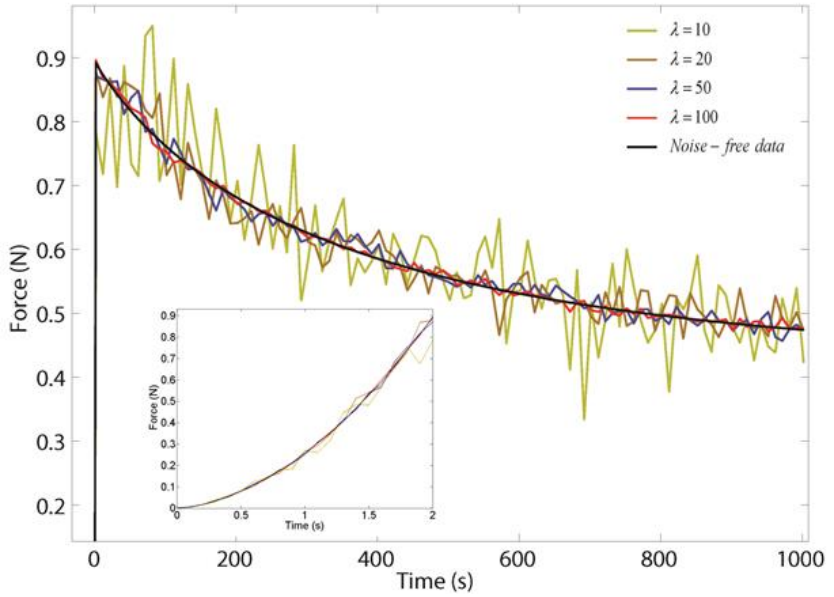

Figure 2.3. The effects of introducing noise into the force-time curve.

When the data used for training the ANN was noise-free, the slightest presence of noise in the force-time data, i.e. $\lambda = 100$, resulted in very inaccurate values of identified parameter (Appendix D1). Training the ANN with noisy dataset i.e. $\lambda = 10$-100 resulted in more accurate prediction of the mechanical and physical properties of cartilage (Figure 2.4). As expected, the accuracy of the predictions gradually decreased as the signal to noise ratio decreased (Figure 2.4). Training curves and histograms for the trained networks with noisy data are presented in Appendix D2 and D3, respectively. The small value of mean identification error and standard deviation of identification error for noisy data ($\lambda = 20$ i.e. 5% noise) indicates that ANN trained with noisy data performs efficiently (Table 2.3). The mean identification error was of the order of -3 to -4 (Table 2.3) that is slightly more than the case of noise-free ANN (Table 2.2).

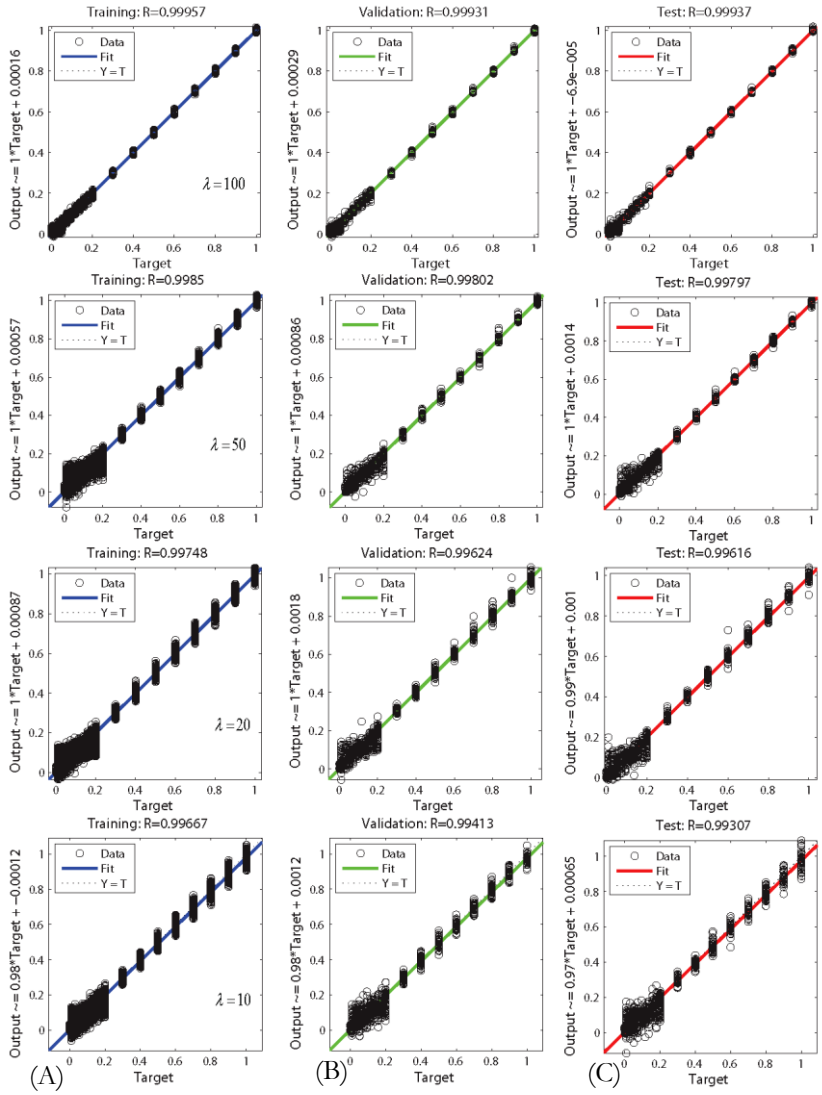

No. samples	Training	Validation	Test	No. neurons
10000	90%	5%	5%	40

Figure 2.4. Regression diagrams for training (A), validation (B) and test (C) datasets when neural networks were trained with noisy datasets with different signal to noise ratios.

A MATLAB code for generating noisy data, training an ANN and extracting the results is available in Appendix E.

Table 2.3. Mean identification error and standard deviation of identification error for the case where ANN was trained and tested with noisy data.

	μ_{err}	σ_{err}
Elastic modulus (MPa)	-6.9e-4	1.8e-2
Poisson's ratio	1.7e-3	3.9e-2
Permeability ($mm^4/N.s$)	1.5e-4	1.6e-3
Friction coefficient	-1.8e-4	1.5e-2

Table symbols: μ_{err}: mean identification error, σ_{err}: standard deviation of identification error.

2.4. Discussion

In this study, we used ANNs to predict the mechanical and physical properties of articular cartilage from the force–time curve of simulated cartilage indentation. The advantage of validation of the ANN based on simulated experimental data and not based on the actual experiments is that the mechanical and physical properties are already known, thereby, comparisons between simulated data and ANN output can be more easily made. The results of the noise-free ANN prove that the ANN is capable of predicting the parameters of the poroelastic model from the force-time data. However, the ANN failed to predict the properties of cartilage when a small level of noise was present in the force-time data. This might be due to the fact that training the ANN with noise-free force-time data obtained using finite element models results in over-fitting of the ANN to the simulation data. As a safeguard against errors, a Gaussian noise term was added to contaminate the training dataset. The ANN is therefore trained such that it is most sensitive to the general trends and ignores small deviations from the finite element solution either caused by uncertainties present in actual experiments or by other factors. The

results of this study show that such a strategy drastically improves the robustness of the ANN.

So far the most widely used option for interpretation of indentation data has been the use of analytical relationships. However, application of analytical relationships is often associated with many simplifying assumptions as they are not available for all practical indentation experiments. In particular, no analytical relationships are available for indentation of poroelastic/biphasic materials particularly when specific types of indenters are used or when anisotropic properties of cartilage are taken into account. Oyen [21] developed an analytical model for poroelastic creep response of hydrated bone for impermeable spherical indenter which is based on an analytical theory for creep response of viscoelastic materials. The behavior of solid part is assumed to be linear elastic and isotropic while Poisson's ratio equals 0.5. The latter might impose critical errors while estimating the mechanical properties of cartilage since the range of Poisson's ratio has been proven to be wide [34]. Therefore, recent studies have focused on finite element modeling of poroelastic indentation [23, 35-37]. The availability of a pre-trained ANN means that labs and researchers not equipped with the computational expertise could quickly analyze the results of their indentation experiments using the ANN and achieve the same level of accuracy that are normally only achieved using computational models.

The proposed methodology might also be used for analyzing indentation data from other musculoskeletal biological tissues and biomaterials, possibly in combination with viscoelastic and fiber-reinforced models [37-39]. It is worth to mention that the ultimate accuracy of the proposed approach in this study is only as good as the accuracy of the finite element model underneath. But that is also the case for all alternative approaches that could be used for estimation of the mechanical properties of biological tissues using indentation data.

By training the ANN for wide intervals of mechanical and physical properties with enough datasets in different scales and indentation protocols, we can have a powerful tool that is capable of determining material properties of articular cartilage regardless of scale and species from which the tissue is originating. This allows to potentially identifying the progress of osteoarthritis using indentation tests at the nano- and the micro-scale [4, 22, 40]. Our proposed approach can potentially be used in designing articular cartilage tissue engineered constructs and examining mechanical functionality of repaired articular cartilage post-surgery by simultaneously comparing their stiffness, permeability and Poisson's ratio with those of the native tissue.

The current study has several limitations. Most importantly, anisotropic properties of cartilage were not taken into account when creating the finite element models of cartilage indentation [41, 42]. However, taking the anisotropy into account will require estimation of even more parameters based on the indentation data that might not be feasible given the already large number of the involved parameters of the poroelastic model.

To our best of knowledge, we are the first to report the feasibility of cartilage properties determination by combining ANN and biphasic finite element models. In all inverse problems such as in our study, one needs to note that the validity of the determined quantities is linked to the validity of the formulated inverse problem. The cartilage properties determined in the current study are therefore limited to the conditions where the assumptions of the poroelastic/biphasic theory hold.

In summary, we established that artificial neural networks are capable of estimating cartilage mechanical properties by using force-time data obtained using indentation. We investigated the effects of noise on the network performance, and the results showed that training the artificial neural network with noisy data could make the system more robust against uncertainties and

errors that could be present in experimental/clinical data. In conclusion, the trained artificial neural network could be used for determining the material properties of cartilage without the need for computational modeling expertise.

2.5. REFERENCES

1. Lories R.J., Luyten F.P., *Osteoarthritis, a disease bridging development and regeneration.* Bonekey Rep, 2012. **1**(Article number: 136).
2. Liu A., Kendzerska T., Stanaitis I., Hawker G., *The relationship between knee pain characteristics and symptom state acceptability in people with knee osteoarthritis.* Osteoarthritis and Cartilage, 2014. **22**(2): p. 178-183.
3. Sophia Fox A.J., Bedi A., Rodeo S.A., *The Basic Science of Articular Cartilage: Structure, Composition, and Function.* Sports Health, 2009. **1**(6): p. 461-468.
4. Stolz M., Gottardi R., Raiteri R., Miot S., Martin I., Imer R., Staufer U., Raducanu A., Duggelin M., Baschong W., Daniels A.U., Friederich N.F., Aszodi A., Aebi U., *Early detection of aging cartilage and osteoarthritis in mice and patient samples using atomic force microscopy.* Nature Nanonotechnology, 2009. **4**(3): p. 186-192.
5. Wilusz R.E., Zauscher S., Guilak F., *Micromechanical mapping of early osteoarthritic changes in the pericellular matrix of human articular cartilage.* Osteoarthritis and Cartilage, 2013. **21**(12): p. 1895-1903.
6. Wang L., Kalu D.N., Banu J., Thomas J.B., Gabriel N., Athanasiou K., *Effects of ageing on the biomechanical properties of rat articular cartilage.* Proc Inst Mech Eng H, 2006. **220**(4): p. 573-8.
7. Boschetti F., Pennati G., Gervaso F., Peretti G.M., Dubini G., *Biomechanical properties of human articular cartilage under compressive loads.* Biorheology, 2004. **41**(3-4): p. 159-66.
8. DiSilvestro M.R., Suh J.-K.F., *A cross-validation of the biphasic poroviscoelastic model of articular cartilage in unconfined compression, indentation, and confined compression.* Journal of Biomechanics, 2001. **34**(4): p. 519-525.
9. Wilson W., van Donkelaar C.C., van Rietbergen B., Huiskes R., *A fibril-reinforced poroviscoelastic swelling model for articular cartilage.* Journal of Biomechanics, 2005. **38**(6): p. 1195-1204.
10. Mow V.C., Kuei S.C., Lai W.M., Armstrong C.G., *Biphasic Creep and Stress Relaxation of Articular Cartilage in Compression: Theory and Experiments.* Journal of Biomechanical Engineering, 1980. **102**(1): p. 73-84.
11. Lu X.L., Mow V.C., *Biomechanics of articular cartilage and determination of material properties.* Med Sci Sports Exerc, 2008. **40**(2): p. 193-9.
12. Korhonen R.K., Laasanen M.S., Töyräs J., Rieppo J., Hirvonen J., Helminen H.J., Jurvelin J.S., *Comparison of the equilibrium response of articular cartilage in unconfined compression, confined compression and indentation.* Journal of Biomechanics, 2002. **35**(7): p. 903-909.
13. Warner M.D., Taylor W.R., Clift S.E., *Finite element biphasic indentation of cartilage: A comparison of experimental indenter and physiological contact geometries.* Proceedings of the Institution of Mechanical Engineers, Part H: Journal of Engineering in Medicine, 2001. **215**(5): p. 487-496.

14. Pawaskar S.S., Fisher J., Jin Z., *Robust and general method for determining surface fluid flow boundary conditions in articular cartilage contact mechanics modeling.* J Biomech Eng, 2010. **132**(3): p. 031001.
15. Rettler E., Hoeppener S., Sigusch B.W., Schubert U.S., *Mapping the mechanical properties of biomaterials on different length scales: depth-sensing indentation and AFM based nanoindentation.* Journal of Materials Chemistry B, 2013. **1**(22): p. 2789-2806.
16. Franz T., Hasler E.M., Hagg R., Weiler C., Jakob R.P., Mainil-Varlet P., *In situ compressive stiffness, biochemical composition, and structural integrity of articular cartilage of the human knee joint.* Osteoarthritis and Cartilage, 2001. **9**(6): p. 582-592.
17. Knecht S., Vanwanseele B., Stüssi E., *A review on the mechanical quality of articular cartilage – Implications for the diagnosis of osteoarthritis.* Clinical Biomechanics, 2006. **21**(10): p. 999-1012.
18. Sim S., Chevrier A., Garon M., Quenneville E., Yaroshinsky A., Hoemann C.D., Buschmann M.D., *Non-destructive electromechanical assessment (Arthro-BST) of human articular cartilage correlates with histological scores and biomechanical properties.* Osteoarthritis Cartilage, 2014. **22**(11): p. 1926-35.
19. Le N.-A.T., Fleming B.C., *Measuring fixed charge density of goat articular cartilage using indentation methods and biochemical analysis.* Journal of Biomechanics, 2008. **41**(3): p. 715-720.
20. Rauker J., Moshtagh P.R., Weinans H., Zadpoor A.A., *Analytical Relationships for Nanoindentation-Based Estimation of Mechanical Properties of Biomaterials.* Journal of Mechanics in Medicine and Biology, 2014. **14**(03): p. 1430004.
21. Oyen M.L., *Poroelastic nanoindentation responses of hydrated bone.* Journal of Materials Research, 2011. **23**(05): p. 1307-1314.
22. Cao L., Youn I., Guilak F., Setton L.A., *Compressive properties of mouse articular cartilage determined in a novel micro-indentation test method and biphasic finite element model.* J Biomech Eng, 2006. **128**(5): p. 766-71.
23. Gupta S., Lin J., Ashby P., Pruitt L., *A fiber reinforced poroelastic model of nanoindentation of porcine costal cartilage: A combined experimental and finite element approach.* Journal of the Mechanical Behavior of Biomedical Materials, 2009. **2**(4): p. 326-338.
24. Miller G.J., Morgan E.F., *Use of microindentation to characterize the mechanical properties of articular cartilage: comparison of biphasic material properties across length scales.* Osteoarthritis and Cartilage, 2010. **18**(8): p. 1051-1057.
25. Richard F., Villars M., Thibaud S., *Viscoelastic modeling and quantitative experimental characterization of normal and osteoarthritic human articular cartilage using indentation.* Journal of the Mechanical Behavior of Biomedical Materials, 2013. **24**(0): p. 41-52.
26. Seifzadeh A., Oguamanam D.C.D., Trutiak N., Hurtig M., Papini M., *Determination of nonlinear fibre-reinforced biphasic poroviscoelastic constitutive parameters of articular cartilage using stress relaxation indentation testing and an*

optimizing finite element analysis. Computer Methods and Programs in Biomedicine, 2012. **107**(2): p. 315-326.
27. Manda K., *Finite Element Simulations of Biphasic Articular Cartilages With Localized Metal Implants*. Technical Reports from Royal Institute of Technology Department of Mechanics SE - 100 44 Stockholm, Sweden, December 2010.
28. Spilker R.L., Suh, J. K., and Mow, V. C, *A finite element analysis of the indentation stress-relaxation response of linear biphasic articular-cartilage*. Journal of Biomechanical Engineering-Transactions of the ASME, 1992. **114**(2): p. 191-201.
29. Warner M.D., *Finite Element Biphasic Modeling of Articular Cartilage: An investigation into Crystal induced Damaged*. PhD Thesis, University of Bath, Bath, UK, 2000.
30. Goldsmith A.A.J., Hayes, A., and Clift, S. E, *Modelling the response of biomaterials and soft, hydrated biological tissues using soils consolidation theory*. ABAQUS User's Conference. Paris, France, 1995: p. 305-319.
31. Zadpoor A.A., Campoli G., Weinans H., *Neural network prediction of load from the morphology of trabecular bone*. Applied Mathematical Modelling, 2012. **37**(7): p. 5260-5276.
32. Campoli G., Weinans H., Zadpoor A.A., *Computational load estimation of the femur*. J Mech Behav Biomed Mater, 2012. **10**: p. 108-19.
33. Zadpoor A.A., Sinke J., Benedictus R., *Formability prediction of high strength aluminum sheets*. International Journal of Plasticity, 2009. **25**(12): p. 2269-2297.
34. Jurvelin J.S., Buschmann M.D., Hunziker E.B., *Mechanical anisotropy of the human knee articular cartilage in compression*. Proc Inst Mech Eng H, 2003. **217**(3): p. 215-9.
35. Hu Y., Zhao X., Vlassak J.J., Suo Z., *Using indentation to characterize the poroelasticity of gels*. Applied Physics Letters, 2010. **96**(12): p. 121904.
36. Chan E.P., Hu Y., Johnson P.M., Suo Z., Stafford C.M., *Spherical indentation testing of poroelastic relaxations in thin hydrogel layers*. Soft Matter, 2012. **8**(5): p. 1492.
37. Taffetani M., Griebel M., Gastaldi D., Klisch S.M., Vena P., *Poroviscoelastic finite element model including continuous fiber distribution for the simulation of nanoindentation tests on articular cartilage*. Journal of the Mechanical Behavior of Biomedical Materials, 2014. **32**(0): p. 17-30.
38. Taffetani M., Griebel M., Gastaldi D., Klisch S.M., Vena P., *Poroviscoelastic finite element model including continuous fiber distribution for the simulation of nanoindentation tests on articular cartilage*. Journal of the Mechanical Behavior of Biomedical Materials, 2013(0).
39. Lei F., Szeri A.Z., *Inverse analysis of constitutive models: Biological soft tissues*. Journal of Biomechanics, 2007. **40**(4): p. 936-940.
40. Wang M., Peng Z., Price J., Ketheesan N., *Study of the nano-mechanical properties of human knee cartilage in different wear conditions*. Wear, 2013. **301**(1-2): p. 188-191.

41. Mow V.C., Guo X.E., *Mechano-electrochemical properties of articular cartilage: their inhomogeneities and anisotropies*. Annual Review of Biomedical Engineering, 2002. **4**(1): p. 175-209.
42. Arbabi V., Pouran B., Weinans H., Zadpoor A.A., *Transport of Neutral Solute Across Articular Cartilage: The Role of Zonal Diffusivities*. Journal of Biomechanical Engineering, 2015. **137**(7): p. 071001-071001.

APPENDIX A. GOVERNING EQUATIONS FOR A POROELASTIC MATERIAL

The essential equations required for modelling cartilage consist of conservation of mass and conservation of momentum [1, 2]. A poroelastic material virtually contains two separate phases i.e. solid and fluid. Assuming the entire volume of mixture as V, volume fractions (n_i) of the solid and fluid can be expressed as:

$$n_i = dV_i/dV \qquad i = s, f \tag{A.1}$$

where s and f represent solid and fluid phases, respectively. This will require the following relationship to be satisfied:

$$n_s + n_f = 1 \tag{A.2}$$

The overall stress ($\sigma_{Overall}$) acting at each point within the tissue is produced by the summation of the hydrostatic stress tensor in the fluid phase ($-p\,\mathrm{I}$) and the effective stress tensor in the solid phase (σ_E):

$$\sigma_{Overall} = \sigma_E - p\,\mathrm{I} \tag{A.3}$$

where I is the unit tensor. The effective stress tensor in a linear isotropic material can be expressed as follows:

$$\sigma_E = \lambda e_s\,\mathrm{I} + 2\mu\varepsilon \tag{A.4}$$

where e_s is the cubic dilatation, ε is the strain tensor, and λ and μ are the first and second Lame' constants, respectively. The aggregate modulus of the solid matrix (H_A) in the poroelastic model is related to the Young's modulus (E) and Poisson ratio (ν) as [2]:

$$H_A = \lambda + 2\mu, \quad E = \frac{\mu(3\lambda + 2\mu)}{\lambda + \mu}, \quad \nu = \frac{\lambda}{2(\lambda + \mu)} \tag{A.5}$$

The conservation of mass necessitates that the total mass change equals the fluid flow flux through the surface of the tissue. In the case where fluid phase saturates the solid phase completely and

solid phase can be assumed as an incompressible material, the continuity equation for the mixture can be written as:

$$\nabla.(n_s\overrightarrow{v_s} + n_f\overrightarrow{v_f}) = 0 \tag{A.6}$$

where $\overrightarrow{v_s}$ and $\overrightarrow{v_f}$ are the velocities of the solid and fluid phases, respectively. Darcy's law states that the fluid flux is related to the hydrostatic fluid pressure as follows:

$$n_f(\overrightarrow{v_f} - \overrightarrow{v_s}) = -k\nabla p \tag{A.7}$$

where k is hydraulic permeability.

Inserting equation (A.7) into equation (A.6) yields:

$$\nabla.\overrightarrow{v_s} + \nabla.(k\nabla p) = 0 \tag{A.8}$$

Permeability of cartilage (k) is strain-dependent and can be described as [3]:

$$k = k_0\left(\frac{e}{e_0}\right)^{\kappa}\exp\left\{\frac{M}{2}\left(\frac{1+e}{1+e_0}\right)^2 - 1\right\} \tag{A.9}$$

where k_0 is initial permeability, κ and M are material parameters, and e and e_0 are current and initial void ratios.

APPENDIX B. FINITE ELEMENT MODELING

The finite element model was discretized with four-node bilinear displacement and pore pressure elements (CAX4P). Mesh sensitivity analysis was performed for the force–time diagram in the indenter reference point (RP) with regard to changes in the peak of contact pressure and pore pressure data. The average difference, R_v, between force-time curves, Var and Var', was defined to study the difference between two force-time curves:

$$R_v = \frac{1}{n}\sum_{i=1}^{n}\left(\frac{|Var\text{-}Var'|}{Var}\right) \quad \text{(A.10)}$$

Concerning the boundary conditions, the bottom surface nodes were constrained in horizontal and vertical directions, which is in agreement with physiologic ratio of subchondral bone's elastic modulus to cartilage's elastic modulus [4]. The nodes on the axisymmetric boundary were constrained in the horizontal direction. To have an unlimited fluid flow, the pore pressure i.e. total pore pressure in the porous medium, on the nodes of the external edges was set to zero. Fluid flow was prevented in the bottom and in the axisymmetric surfaces. The reference point on the indenter was constrained in the horizontal direction (Figure 2.1). Stress–relaxation step was kept linear for 2 seconds with 0.3 mm displacement toward the negative Y-axis (step deformation). It then remained constant until 1000 seconds (step consolidation).

APPENDIX C. HOW DOES ARTIFICIAL NEURAL NETWORK FUNCTION?

Artificial neural networks (ANNs) consist of artificial neurons that its building blocks are placed in different layers (Figure A1).

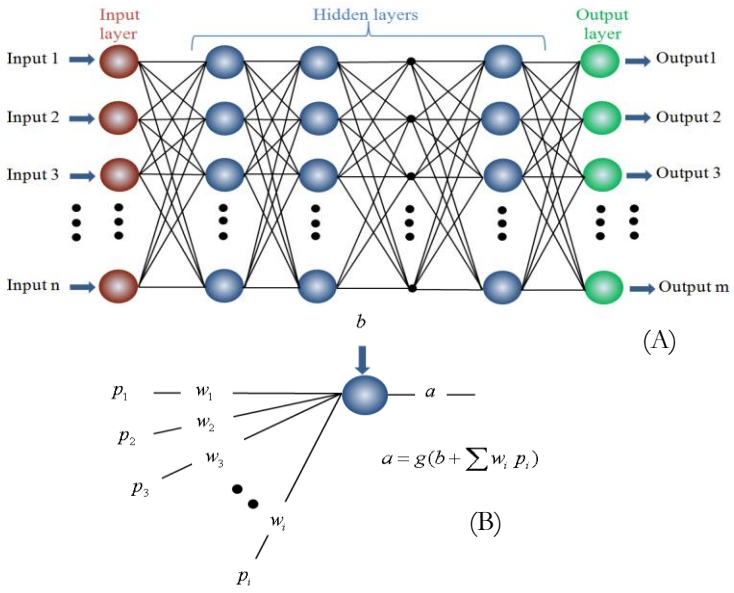

Figure A1. A typical artificial neural network (A) and a single neuron (B).

The main function of the ANN is to map the space of the inputs to the outputs using the multiple layers in between of them (hidden layers) where each layer consists of several artificial neurons (called hidden neurons). Each hidden layer is capable of containing as many hidden neurons as needed. The received signal by each neuron is processed using a so-called activation function, g, such as the tang-sigmoid function. The neurons assign weights (w_i) to each transmitted signal (p_i) and the product is summed and biased (summed with b) before being introduced to the activation function (Figure A1). The scalar output of the function will be transferred throughout the connections within the network.

The parameters of the neural network (weights and biases) are required to be tuned such that the product will be as close as possible to the desired output (training). Therefore, a training dataset has to be introduced to the network that consists of a number of inputs and target outputs [5, 6].

APPENDIX D. ARTIFICIAL NEURAL NETWORK (EFFECT OF NOISE)

APPENDIX D1.

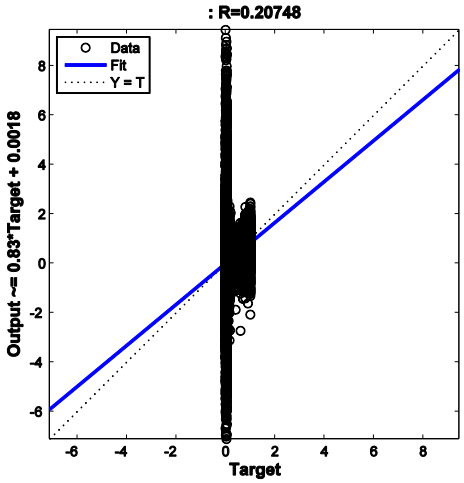

Figure A2. Regression diagrams for a neural network trained using noise-free data and tested using noisy force-time data $(\lambda = 100)$.

APPENDIX D2.

Training curves of different ANNs trained with different levels of signal to noise ratio were quite healthy with similar training curves for the training, validation, and tests datasets (Figure A3).

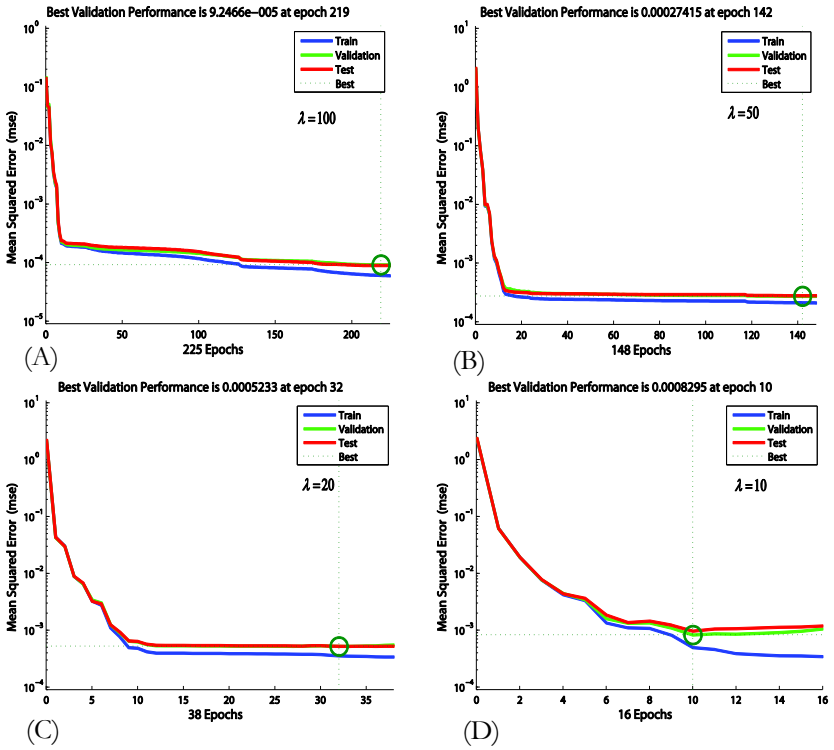

Figure A3. The training curves of the ANN trained using noisy dataset with different signal to noise ratios**.**

APPENDIX D3.

The number of hidden neurons was 40 and the histograms of identification errors were quite close to normal distributions for all cases, regardless of how small the signal to noise ratio was (Figure A4).

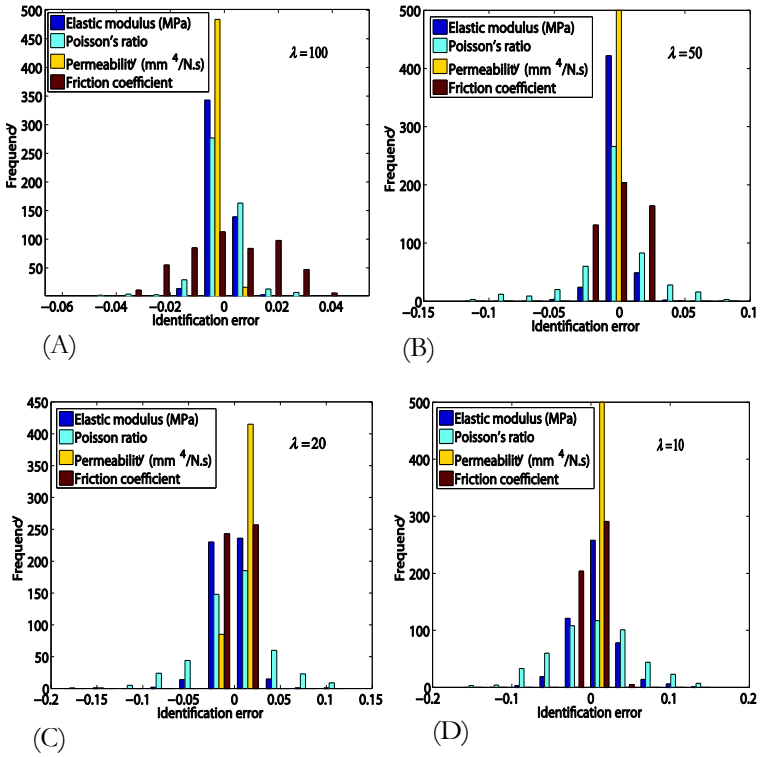

Figure A4. The distribution of identification errors for the test dataset presented for different values of the signal to noise ratio (λ).

APPENDIX E. MATLAB CODE

MATLAB script

This MATLAB code is developed to create noisy indentation data (reaction force: finite element model in ABAQUS) with different levels of noise as the input. The artificial neural network is trained using then input and mechanical and physical properties as the target. Then the mechanical and physical properties of a poroelastic material can be determined using the trained artificial neural network.

Mechanical and physical properties: elastic modulus (MPa), Poisson's ratio, Permeability (mm4/N.s), friction coefficient

```
load input.txt % A matrix (10000*121) consisting of reaction force
data (FEM) at 121 time points
load target.txt% A matrix (10000*4) consisting of mechanical and
physical properties

%%%%%%%%%%%%%%%%%%%%%%%%%%%%%%%
%%%%%%%
% Contamination of data with noise

% By tuning lambda different levels of noise can be produced
lambda=100; % Please insert a value for lambda
for k=1:10000
    for l=1:121
        input_lambda(k,l)=input(k,l)+normrnd(0,input(k,l)/lambda);
    end
end
save input_lambda.txt input_lambda -ASCII
```

```
%%%%%%%%%%%%%%%%%%%%%%%%%%%%%%%
%%%%%%%%%

%%%%%%%%%%%%%%%%%%%%%%%%%%%%%%%
%%%%%%%%%
% Training, validation and test of the artificial neural network

% This script assumes these variables are defined:
%   input_lambda - input data.
%   target - target data.

x = input_lambda';
t = target';

% Create a Fitting Network
hiddenLayerSize = 40;
net = fitnet(hiddenLayerSize);

% Choose Input and Output Pre/Post-Processing Functions
% For a list of all processing functions type: help nnprocess
net.input.processFcns = {'removeconstantrows','mapminmax'};
net.output.processFcns = {'removeconstantrows','mapminmax'};


% Setup Division of Data for Training, Validation, Testing
% For a list of all data division functions type: help nndivide
net.divideFcn = 'dividerand';  % Divide data randomly
net.divideMode = 'sample';  % Divide up every sample
net.divideParam.trainRatio = 90/100;
net.divideParam.valRatio = 5/100;
net.divideParam.testRatio = 5/100;

% For help on training function 'trainlm' type: help trainlm
```

```
% For a list of all training functions type: help nntrain
net.trainFcn = 'trainlm';  % Levenberg-Marquardt

% Choose a Performance Function
% For a list of all performance functions type: help
nnperformance
net.performFcn = 'mse';  % Mean squared error

% Choose Plot Functions
% For a list of all plot functions type: help nnplot
net.plotFcns = {'plotperform','plottrainstate','ploterrhist', ...
  'plotregression', 'plotfit'};


% Train the Network
[net,tr] = train(net,x,t);

% Test the Network
y = net(x);
e = gsubtract(t,y);
performance = perform(net,t,y)

% Recalculate Training, Validation and Test Performance
trainTargets = t .* tr.trainMask{1};
valTargets = t  .* tr.valMask{1};
testTargets = t  .* tr.testMask{1};
trainPerformance = perform(net,trainTargets,y)
valPerformance = perform(net,valTargets,y)
testPerformance = perform(net,testTargets,y)

% View the Network
view(net)
```

```
% Plots
% Uncomment these lines to enable various plots.
%figure, plotperform(tr)
%figure, plottrainstate(tr)
%figure, plotfit(net,x,t)
%figure, plotregression(t,y)
%figure, ploterrhist(e)

% Deployment
% Change the (false) values to (true) to enable the following code blocks.
if (false)
  % Generate MATLAB function for neural network for application deployment
  % in MATLAB scripts or with MATLAB Compiler and Builder tools, or simply
  % to examine the calculations your trained neural network performs.
  genFunction(net,'myNeuralNetworkFunction');
  y = myNeuralNetworkFunction(x);
end
if (false)
  % Generate a matrix-only MATLAB function for neural network code
  % generation with MATLAB Coder tools.
  genFunction(net,'myNeuralNetworkFunction','MatrixOnly','yes');
  y = myNeuralNetworkFunction(x);
end
if (false)
  % Generate a Simulink diagram for simulation or deployment with.
  % Simulink Coder tools.
  gensim(net);
```

```
end
save
%%%%%%%%%%%%%%%%%%%%%%%%%%%%%%%
%%%%%%%%%

%%%%%%%%%%%%%%%%%%%%%%%%%%%%%%%
%%%%%%%%%
% Obtaining mechanical and physical properties using noisy
reaction force data

load reaction_force.txt % A matrix (1*121) consisting of reaction
force at 121 time points
output_lambda=sim(net,reaction_force)
%%%%%%%%%%%%%%%%%%%%%%%%%%%%%%%
%%%%%%%%%
```

REFERENCES

1. Manda K., *Finite Element Simulations of Biphasic Articular Cartilages With Localized Metal Implants*. Technical Reports from Royal Institute of Technology Department of Mechanics SE - 100 44 Stockholm, Sweden, December 2010.
2. Mow V.C., Kuei S.C., Lai W.M., Armstrong C.G., *Biphasic Creep and Stress Relaxation of Articular Cartilage in Compression: Theory and Experiments*. Journal of Biomechanical Engineering, 1980. **102**(1): p. 73-84.
3. Pawaskar S.S., Fisher J., Jin Z., *Robust and general method for determining surface fluid flow boundary conditions in articular cartilage contact mechanics modeling*. J Biomech Eng, 2010. **132**(3): p. 031001.
4. Choi K., Kuhn J.L., Ciarelli M.J., Goldstein S.A., *The elastic moduli of human subchondral, trabecular, and cortical bone tissue and the size-dependency of cortical bone modulus*. Journal of Biomechanics, 1990. **23**(11): p. 1103-1113.
5. Zadpoor A.A., Campoli G., Weinans H., *Neural network prediction of load from the morphology of trabecular bone*. Applied Mathematical Modelling, 2012. **37**(7): p. 5260-5276.
6. Zadpoor A.A., Sinke J., Benedictus R., *Formability prediction of high strength aluminum sheets*. International Journal of Plasticity, 2009. **25**(12): p. 2269-2297.

CHAPTER 3

TRANSPORT OF NEUTRAL SOLUTE ACROSS ARTICULAR CARTILAGE: THE ROLE OF ZONAL DIFFUSIVITIES*

* This chapter is published as a scientific paper:

Arbabi V., Pouran B., Weinans H., Zadpoor A.A. *Transport of Neutral Solute Across Articular Cartilage: The Role of Zonal Diffusivities*. Journal of Biomechanical Engineering, 2015. 137(7): p. 071001-071001.

ABSTRACT

Transport of solutes through diffusion is an important metabolic mechanism for the avascular cartilage tissue. Three types of inter-connected physical phenomena, namely mechanical, electrical, and chemical, are all involved in the physics of transport in cartilage. In this study, we use a carefully designed experimental-computational setup to separate the effects of mechanical and chemical factors from those of electrical charges. Axial diffusion of a neutral solute (iodixanol) into cartilage was monitored using calibrated micro-CT images for up to 48 hours. A biphasic-solute computational model was fitted to the experimental data to determine the diffusion coefficients of cartilage. Cartilage was modeled either using one single diffusion coefficient (single-zone model) or using three diffusion coefficients corresponding to superficial, middle, and deep cartilage zones (multi-zone model). It was observed that the single-zone model cannot capture the entire concentration-time curve and under-predicts the near-equilibrium concentration values, whereas the multi-zone model could very well match the experimental data. The diffusion coefficient of the superficial zone was found to be at least one order of magnitude larger than that of the middle zone. Since neutral solutes were used, GAG content cannot be the primary reason behind such large differences between the diffusion coefficients of the different cartilage zones. It is therefore concluded that other features of the different cartilage zones such as water content and the organization (orientation) of collagen fibers may be enough to cause large differences in diffusion coefficients through the cartilage thickness.

3.1. INTRODUCTION

Articular cartilage is a multiphasic, porous, and avascular tissue that primarily relies on diffusion for transport of crucial signaling molecules, oxygen, and nutrients that help maintain its proper metabolic function [1-5]. Osteoarthritis is recognized as a debilitating disease that mainly affects articular cartilage and subchondral bone, and is characterized by abnormal loss of glycosaminoglycans (GAGs) molecules, subsequent collagen damage, and increased subchondral bone remodeling [6-11]. Reduced GAG concentration and disrupted collagen fibers can directly affect the interactions between the solutes and the cartilage's matrix. Solute-matrix interaction plays an integral role in the diffusion of various molecules ranging from therapeutics and fragments of GAGs and collagen II to the contrast agents [12, 13]. Effective early diagnosis of cartilage degeneration most importantly using computed tomography (CT) and magnetic resonance imaging (MRI) therefore requires in-depth knowledge of solute diffusion and partitioning within articular cartilage [11, 14-17]. That is why several previous studies have used imaging modalities such as CT, MRI, and fluorescent-based diagnostic techniques to study the diffusion of contrast agents and fluorescent labeled molecules across articular cartilage and to obtain the diffusion coefficient of articular cartilage, e.g. [1, 3, 18-22].

The above-mentioned studies contributed towards better understanding of diffusion across articular cartilage. However, there are certain limitations associated with their methodology. In particular, large baths of contrast agent are often used in diffusion experiments to I) facilitate the use of analytical relationships or computational models that have been developed for infinite bath conditions and II) simultaneously perform diffusion experiments for several specimens [6, 7, 23, 24]. This type of experimental

setup introduces certain inaccuracies in the measurements. Most importantly, large baths of concentrated solutions of contrast agents could cause substantial beam hardening artifacts in CT measurements as a result of preferential absorption of low-energy photons [25, 26]. Moreover, excessive amount of solutions has to be used to establish a successful diffusion setup. Finally, testing multiple specimens at the same time requires the use of a larger field of view in CT scanners [7], thereby reducing the maximum achievable resolution [27, 28].

As previously mentioned, the infinite bath assumption was applied to keep a relatively easy mathematical operation [24]. However, the use of those simplified analytical or computational models may be associated with some limitations of their own. Firstly, these models often overlook the effects of limited solute diffusivity within the bath itself [6, 7, 24, 27-29]. Those effects are particularly important for non-stirred viscous baths, because a thin layer forms at the interface of bath and cartilage that has high solute concentration values and results in additional transport resistance that is not captured by simple analytical and computational models. Ultimately, in the vast majority of previous studies, only one diffusion coefficient is used for the entire cartilage [6, 7, 22, 24, 28, 29]. That assumption neglects the potentially large differences between the diffusion coefficients of the superficial, middle, and deep cartilage zones [1, 30], in particular since the collagen orientation and likely the preferred diffusion direction as well, varies considerably in the different zones.

This research aims to study the transport of neutral solutes across articular cartilage using a combination of an experimental setup and a computational model that represents the involved physics as faithfully as possible. Regarding the experimental setup, finite baths were used to minimize beam hardening. Different concentrations of contrast agent and osmolality of the solution

were used to study the effects of those on diffusion. On the computational front, we used a finite-bath biphasic-solute computational model that properly captures the transport of neutral solutes across articular cartilage in the experimental setup. In addition, the computational model takes the diffusion of solute in the bath into account. We then determine the diffusion coefficient of cartilage by directly fitting the computational model to experimental readings. The diffusion of solute is studied both using single-zone and multi-zone computational models to see how zonal difference in diffusion coefficient could influence the transport of neutral solutes across articular cartilage.

3.2. METHODOLOGY

3.2.1. EXPERIMENTS

3.2.1.1. BATH AND SAMPLE PREPARATION

Visipaque solutions that contained iodixanol solutes (1550.191 g/mol, charge=0) were prepared in different concentrations and osmolalities (Table 3.1).

Table 3.1. Experimental conditions (A-C) for diffusion from a finite bath of iodixanol with different concentrations and osmolalities.

Condition	Concentration [mM]	Osmolality [mOsm/kg H_2O]
A	420	290
B	420	600
C	210	290

Solution A was directly taken from the original vial of Visipaque (*GE Healthcare, The Netherlands*) resulting in an osmolality of 290 mOsm/kg H_2O and a concentration of 420 mM (Table 3.1). In order to assess the effect of bath osmolality on the transport of

iodixanol, we elevated the osmolality of solution A using NaCl to make condition B (600 mOsm/kg H_2O and 420 mM) (Table 3.1). Finally, condition C was prepared by two-fold dilution of solution A, while maintaining the final osmolality the same as in condition A (Table 3.1). A freezing point osmometer (*Advanced® Model 3320 Micro-Osmometer, The Netherlands*) was used to measure osmolalities.

Osteochondral plugs (n=3, cartilage thickness= 2.8 mm, and diameter= 8.5 mm) were drilled out of two fresh equine femora using custom-made drill tips. During drilling, phosphate buffer serum (PBS) was constantly sprayed on the site of sample extraction to prevent thermal damage to the cartilage. The samples were kept in PBS solution enriched with protease inhibitor and ethylenediaminetetraacetic acid (EDTA) at -20 ^{o}C before proceeding to diffusion experiments. Upon thawing, samples were wrapped laterally using impermeable shrinking tube (*CTFC Series, pro-POWER, UK*) to prevent leakage and to ensure axial diffusion through the cartilage surface. During our pilot studies, we measured the grey values of the shrinking tube and found no evidence of the diffusion of iodixanol into the material. Moreover, the osteochondral plugs were placed firmly on a plastic support. A schematic drawing of the sample is presented in Figure 3.1.

3.2.1.2. IMAGE ACQUISITION

We used a micro-CT scanner (*Quantum FX, Perkin Elmer, USA*) to measure the transport of iodixanol across cartilage. The samples were placed on a holder during scans to minimize possible movement artifacts. The fluid baths contained 650 µL (equal to 14 mm bath height) of solutions A, B & C and were positioned on top of the cartilage specimens. Images were acquired before adding the solution and up to 48 hours after adding the solution (17 times points). The scanning parameters were: 180 µA tube current, 90 kV tube voltage, 2 min scan time, 40×40×40 μm^3 voxel size and

3600 projections. After completion of each experiment, the diffused molecules within each sample were fully washed out using serial desorption baths (PBS+ protease inhibitor + EDTA at 4 °C, 48 hours) before performing diffusion experiments using the next solution.

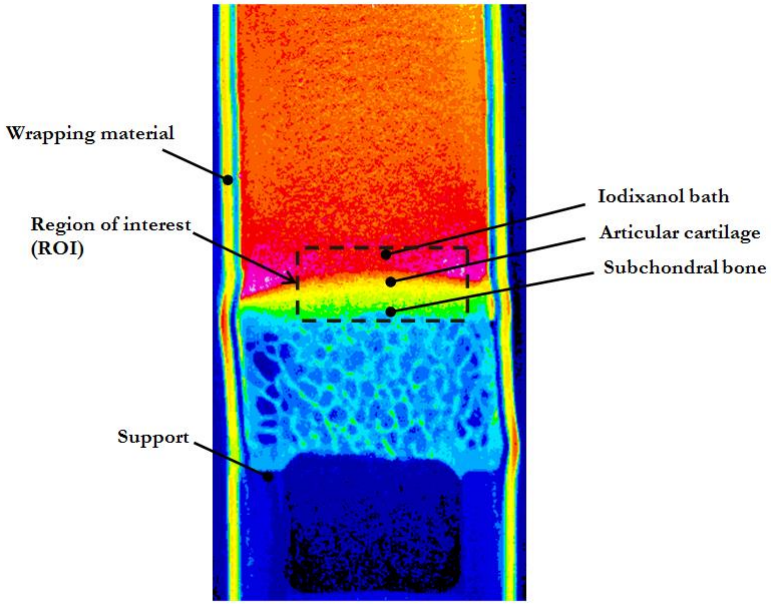

Figure 3.1. The specimen used in the diffusion experiments.

3.2.1.3. IMAGE PROCESSING

The 3D reconstructed images were converted to 2D slices (TIFF format) using in-built software of the micro-CT machine (*Analyze 11.0*). We used a Gaussian filter to enhance the signal to noise ratio. Thereafter, we used *ImageJ 1.47v* to select the mid sagittal slice of each stack and assigned a rectangular region of interest (ROI) that contained the cartilage, the subchondral bone, and a small part of the bath (Figure 3.1). The images within the

prescribed ROI were then thresholded globally for each experimental time point to isolate cartilage from subchondral bone and the contrast agent solution. The outline of the cartilage mask at different time points (Figure 3.2) was then laid over the original cartilage image to calculate the average grey value.

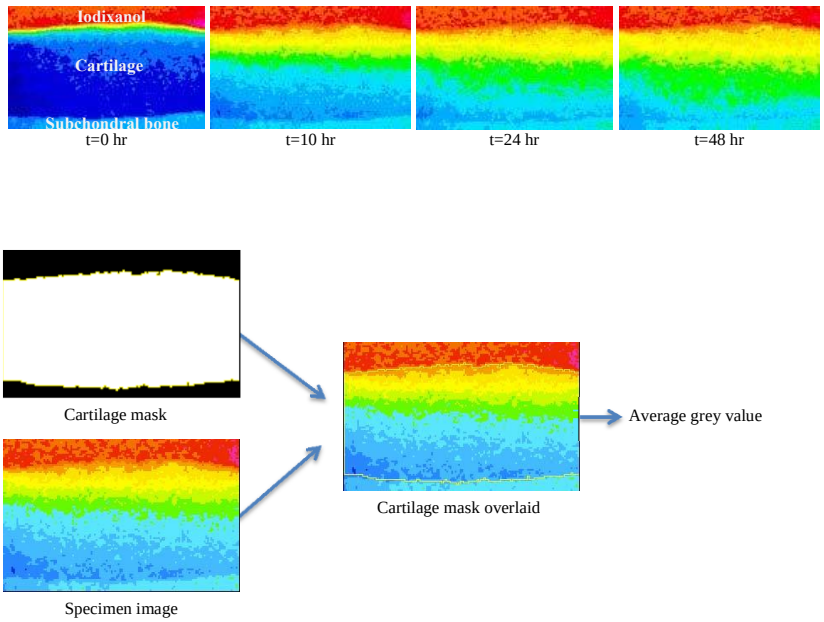

Figure 3.2. The sequence of images for one sample specimen and the different image processing steps used for calculating the average gray values.

No diffusion at $t=0$ and known concentration of the contrast agent solution at $t=0$ were then used to establish a linear relationship that could convert the average grey values to iodixanol concentration. The average grey values were calculated using *ImageJ 1.47v* based on the following equation:

$$\text{Average gray value} = \frac{\sum P_i X_i}{\sum X_i} \tag{3.1}$$

where Pi and Xi are pixel intensity and pixel frequency, respectively.

3.2.2. COMPUTATIONAL MODEL

Biphasic-solute mixture models are capable of capturing the diffusion of neutral solutes across cartilage [31]. Three governing equations need to be solved for such mixture models including the conservation of linear momentum for the mixture, conservation of mass for the mixture, and the conservation of mass for the solute [31-33]. Conservation of linear momentum for the mixture can be expressed as:

$$div\,\mathbf{T} = 0 \tag{3.2}$$

where $\mathbf{T}$ is the Cauchy stress for the mixture. Conservation of mass for the mixture is given as:

$$div\left(\mathbf{v}^s + \mathbf{w}\right) = 0 \tag{3.3}$$

where $\mathbf{v}^s$ is the solid matrix velocity and $\mathbf{w}$ is the volume flux of solvent relative to the solid. Finally, the overall amount of solute in the bath and tissue remains constant:

$$\frac{1}{J}\frac{D^s(J\varphi^w\tilde{\kappa}\tilde{C})}{Dt} + div\,\mathbf{j} = 0 \tag{3.4}$$

where $J = \det\mathbf{F}$, $\mathbf{F}$ is the deformation gradient of the solid matrix, D^s/Dt is the material time derivative in the spatial frame, and $\mathbf{j}$ is the molar flux of solute relative to the solid. In Equation (3.4), φ^w is volume fraction of the solvent, $\tilde{\kappa}$ is the effective solubility, and C is the solute concentration. Since effective solute concentration $(\tilde{C} = C/\tilde{\kappa})$ is continuous across boundaries and contact surfaces, it has been used in the computational model

instead of C [32, 34, 35]. The volume flux of solvent relative to the solid, $\mathbf{w}$, and the relative molar solute flux, $\mathbf{j}$, are given as [32, 36, 37]:

$$\mathbf{w} = -\tilde{\mathbf{k}}.\text{grad}\, p \tag{3.5}$$

$$\mathbf{j} = \tilde{\kappa} d.\left(-\varphi^w \mathbf{grad}\, \tilde{c} + \frac{\tilde{c}}{d_0}\mathbf{w} \right) \tag{3.6}$$

where

$$\tilde{\mathbf{k}} = \left[\mathbf{k}^{-1} + \frac{R\theta}{\varphi^w}\frac{\tilde{\kappa}\tilde{c}}{d_0}\left(\mathbf{I} - \frac{\mathbf{d}}{d_0} \right) \right]^{-1} \tag{3.7}$$

$$\varphi^w = 1 - \frac{\varphi_r^s}{J} \tag{3.8}$$

where p is the fluid pressure, $\tilde{\mathbf{k}}$ is the hydraulic permeability tensor for the flow of the solution, i.e., solvent plus solute through the solid matrix, $\mathbf{k}$ is the hydraulic permeability tensor for the flow of pure solvent, through the solid matrix, $\mathbf{d}$ is the solute diffusivity tensor in the mixture, d_0 is the solute diffusivity in absence of the solid phase, R is the universal gas constant, θ is the absolute temperature, and φ_r^s is the volume fraction of the solid phase in the reference configuration [32, 36, 37].

The virtual work principle was used to solve the conservation equations according to the previous studies [33, 38]. The dedicated open-source finite element modeling platform FEBio 2.0.1 was used for solving the governing equations of the biphasic-solute model.

3.2.2.1. GEOMETRY

The diffusion of solutes was assumed to happen primarily in the axial direction [6, 7]. The computational model consisted of cartilage and an overlaying bath. Two types of computational models were used to analyze the diffusion of neutral solutes across cartilage, namely single-zone and multi-zone models. In the single zone approach, we considered the cartilage specimen as a single phase with spatially homogenized properties in the axial direction (Figure 3.3A) including one single diffusion coefficient. A mesh was generated using an 8-node trilinear hexahedral element, which was more refined close to the cartilage-bath interface to ensure high computational accuracy (Figure 3.3A).

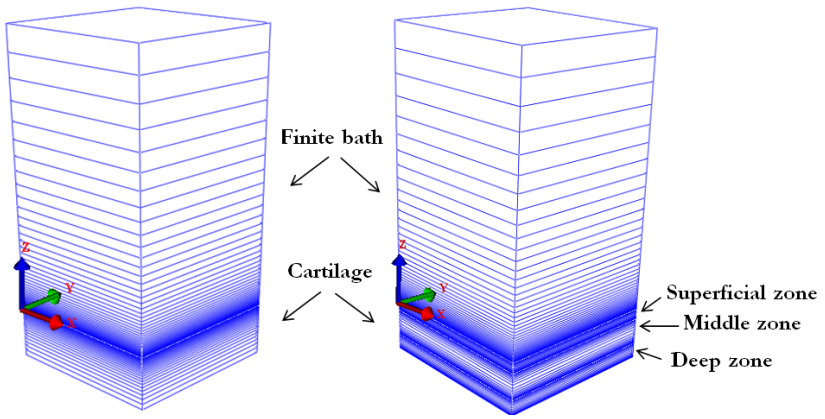

Figure 3.3. Schematic drawings of the single-zone (A) and multi-zone (B) for computational models.

In the multi-zone approach, cartilage was assumed to be composed of three zones with three different sets of properties including three different diffusivities. The multi-zone approach

may better capture the inhomogeneous structure of cartilage caused by uneven distribution of Glycoaminoglycans (GAGs) and different density and orientation of collagen (type II) fibers. This results in location-dependency of mechanical and physical properties of cartilage. The first zone considered in the model was the superficial zone that formed 20% of the cartilage thickness, while the second and third zones were the middle and deep zones respectively representing 50% and 30% of the cartilage thickness [39]. In this approach, the mesh is refined also at the boundary of the different zones (Figure 3.3B).

3.2.2.2. MECHANICAL AND PHYSICAL PROPERTIES OF CARTILAGE AND BATH

Similar to previous studies [32, 33], cartilage was modeled as a neo-Hookean material with a Young's modulus (E) of 10 MPa and a Poisson's ratio (ν) of 0. The hydraulic permeability of the cartilage to the solvent (k) and the effective solubility ($\tilde{\kappa}$) were set to 10^{-3} mm^4/Ns and 1, respectively [33, 36]. The diffusivity tensor was considered isotropic. The iodixanol diffusivity within the bath was set according to a previous study [40]. In the cases where the well-stirred condition in the bath was to be simulated, the solute diffusivity in the bath was set much higher than the diffusivity of the solute in cartilage. The cartilage water content was assumed to be 0.8 in the single-zone approach [32, 33].

In the multi-zone approach, we introduced three different values of water content for each cartilage zone: 0.8 for the superficial zone, 0.7 for the middle zone, and 0.6 for the deep zone [1, 14, 39].

3.2.2.3. INITIAL AND BOUNDARY CONDITIONS

Solute concentration in the bath (C) was prescribed as an initial condition for the bath. The concentrations presented in Table 3.1 were used to simulate the diffusion of the solutes under conditions A, B, and C. Continuity of effective pressure ($p_{effective}$) across boundaries is ensured [32, 33] through:

$$p_{effective} = p - R\theta C\phi, \tag{3.9}$$

where $R = 8.314\times10\text{-}6$ mJ/nmol·K and ϕ is the osmotic coefficient that was assumed to be 1 for all simulations. The ambient fluid pressure and absolute temperature were considered $p = 101$ kPa and $\theta = 298$ K, respectively.

A prescribed displacement equal to 0.001 mm was applied to maintain a stable contact between the finite bath and cartilage [33]. All faces except for the cartilage-bath interface (Figure 3A-B) were assigned the no-flux boundary condition.

3.2.2.4. FITTING METHOD

In the single-zone approach, the diffusivity value in cartilage was determined by minimizing the difference between the computationally predicted curve and experimental data points based on the root mean squared error (RMSE) value of their difference. A similar approach was used in the multi-zone approach to determine the diffusion coefficients of the superficial ($D_{Superficial}$), middle (D_{Middle}), and deep (D_{Deep}) zones. Direct scanning of the parameter space was used for minimizing the RMSE values. This approach ensures all possible solutions are found within the tolerance of the scanning resolution.

3.2.3. ANALYTICAL MODEL

To verify the computational model for a finite bath, we used an analytical model. The analytical solution for axial diffusion from a well-stirred finite bath to cartilage can be obtained by solving the Fick's 2nd law using the Laplace transformation [41]:

$$\frac{C(z,t)}{C_\infty} = \left\{ 1 + \sum_{n=1}^{\infty} \frac{2(1+\alpha)\exp\left(-\gamma^2 t\right)}{\left(1+\alpha+\alpha^2 q_n^2\right)} \frac{cos\left(\frac{q_n z}{l}\right)}{cosq_n} \right\} \tag{3.10}$$

where $\gamma = \frac{\sqrt{D}q_n}{l}$ and q_n s are the none-zero roots of $\tan(q_n) = -\alpha q_n$ with $\alpha = \frac{a}{l}$. D is the solute diffusivity across cartilage, $C(z,t)$ is the solute concentration profile within the cartilage as a function of time (t) and spatial dimension (z), C_∞ is the equilibrium solute concentrations in the cartilage and a and l are the length of the solution and length of the cartilage specimen, respectively.

Assuming a final solute uptake equal to 30% within cartilage, we calculated the bath height as 2.33 mm with a given cartilage thickness of 1 mm using the following mass conservation equation ($K = 1$) [41]:

$$\frac{aC_\infty}{K} + lC_\infty = aC_0, \tag{3.11}$$

where K is the partition coefficient equal to the ratio of the equilibrium solute concentration in cartilage and in the bath and C_0 is the initial solute concentration in the bath, respectively [41].

We set the operating conditions and mechanical properties of cartilage according to a previous study by Ateshian et. al [33]. The cartilage is modeled as a neo-Hookean material with E=10 MPa, ν=0 and fluid volume fraction of 0.8. The other parameters were assumed to be: k=10^{-3} mm^4/Ns, C=1 mM, θ=298 K, p=0 kPa, ϕ=1, $\tilde{\kappa}=1$ and D=5×10-4 mm^2/s. Equation (3.10) was used to validate the results of the computational model in different locations across cartilage, i.e. z=-0.15, -0.29, -0.5, and -0.94 mm for the well-stirred condition. We also simulated the same diffusion process in FEBio and plotted the solute concentration vs. $\eta=\sqrt{Dt}/l$.

3.3. RESULTS

3.3.1. VERIFICATION OF THE COMPUTATIONAL MODEL

To assess the robustness of the computational model for predicting diffusion from a well-stirred finite bath, we plotted the ratio of normalized concentration (C/C_∞) at several locations versus time (Figure 3.4). The computational results perfectly matched the analytical solution for all considered cases (Figure 3.4). The concentration rate decreased by both time lapse and distance from the surface of the cartilage specimen (Figure 3.4). The larger the distance from the cartilage surface, the more time was required for equilibrium (Figure 3.4). All layers of cartilage could finally reach the equilibrium concentration (C_∞) (Figure 3.4). Moreover, the finite element model could predict the transient solute diffusion for a well-stirred finite bath model for all η values (Figure 3.4).

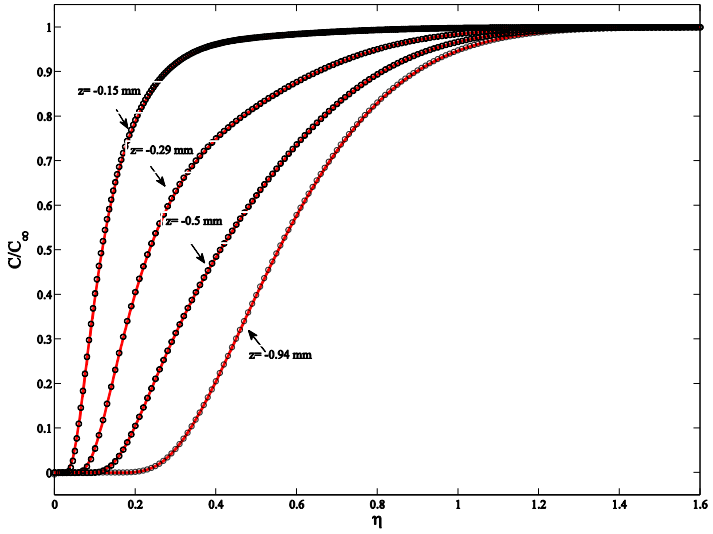

Figure 3.4. Analytical (symbols) and finite element model (solid lines) solutions for finite well-stirred bath: normalized concentration (C / C_{∞}) is plotted versus $\eta = \sqrt{Dt} / l$ for different locations within cartilage.

3.3.2. EXPERIMENTS

For all conditions (A-C), the highest diffusion rate was observed for the early-time points (Figure 3.5). The near equilibrium state could be observed 24 hours after the start of the experiments (Figure 3.5). The normalized near-equilibrium iodixanol concentrations (%initial bath concentration) were 27.8±4.6% (mean ± SD) for condition A, 28.8±8.8% for condition B, and 30.9±7.1% for condition C.

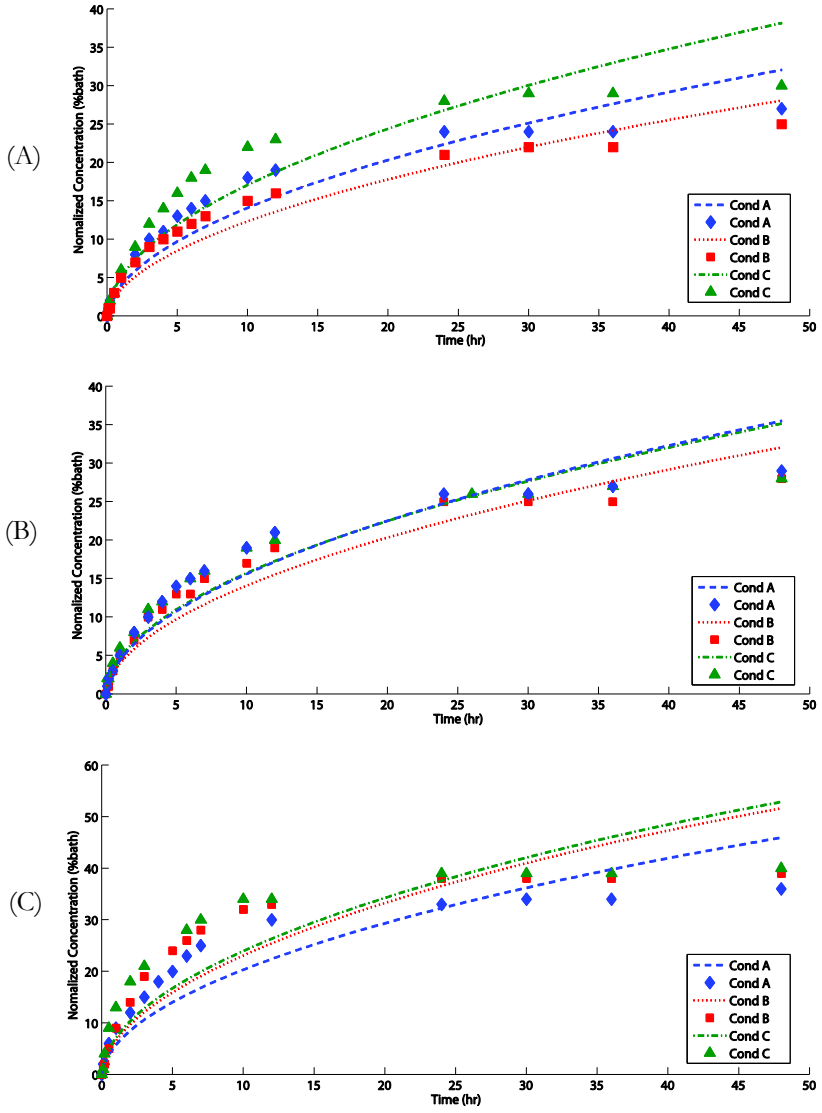

Figure 3.5. Experimental (symbols) and simulated (dashed-lines) concentration vs. time for conditions A-C and samples 1(A) to 3 (C). Computational models (single-zone) were fitted to all experimental data points.

3.3.3. COMPUTATIONAL MODEL

3.3.3.1. SINGLE-ZONE MODEL

When the single-zone model was fitted to all experimental data points of the concentration-time curves, the coefficient of determination (R^2) was ranging between 0.85 and 0.96 for conditions A-C (Table 3.2). Moreover, the computational model did not follow the experimental data points and substantially over-predicted the near-equilibrium concentration values for all conditions (A-C) (Figure 3.5). Once the single-zone computational model was only fitted to the early-time points, the coefficient of determination increased to values ranging between 0.97 and 1.00 (Table 3.2) for conditions A-C, indicating that the computational model could very well capture the early-time diffusion behavior of cartilage (Figure 3.6). As expected, when the computational model was fitted only to early-time diffusion data, there was a poor agreement between the near-equilibrium concentration values predicted by the model and the measured concentrations (Figure 3.6).

Table 3.2. RMSE and R^2 to compare the experimental and simulation solute concentration vs. time for the single-zone computational model.

	Condition	A		B		C	
	Fitting data	Total	Early-time	Total	Early-time	Total	Early-time
Sample 1	R^2	0.94	1	0.96	0.99	0.91	0.99
	RMSE	0.0266	0.0040	0.0201	0.0056	0.0355	0.0082
Sample 2	R^2	0.95	0.99	0.95	0.99	0.94	1
	RMSE	0.0286	0.0052	0.0234	0.0054	0.0259	0.0046
Sample 3	R^2	0.88	0.99	0.86	0.99	0.85	0.97
	RMSE	0.0518	0.0085	0.0634	0.0144	0.0710	0.0232

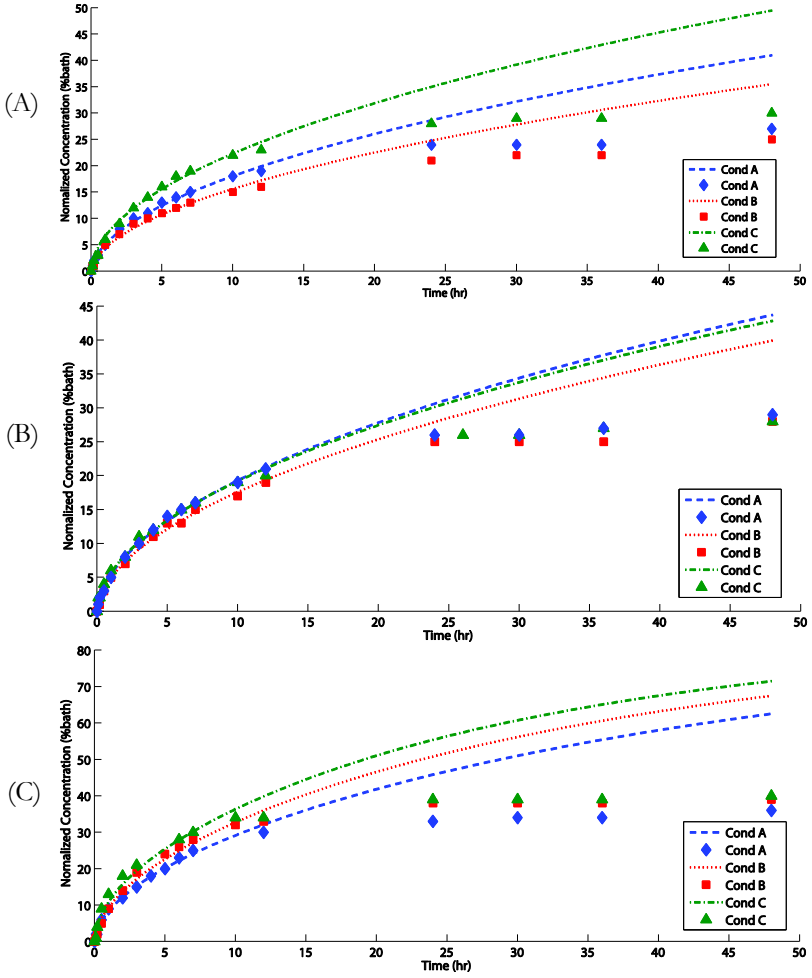

Figure 3.6. Experimental (symbols) and simulated (dashed-lines) concentration vs. time for conditions A-C and samples 1(A) to 3 (C). Computational models (single-zone) were fitted only to early-time experimental data points.

In all conditions and for all specimens, the diffusion coefficients determined using the early-time diffusion data were larger than the ones determined using all data points (Table 3.3). The diffusivities determined for sample 3 were larger than those of both other samples (Table 3.3).

Table 3.3. Diffusion coefficients obtained from the single-zone computational model based on fitting of the model to both early-time data points and all data points.

	Fitting data	Condition A	Condition B	Condition C
Sample 1	Total	4	3	6
	Early-time	6.9	5	11
Sample 2	Total	5	4	5
	Early-time	8	6.5	7.8
Sample 3	Total	9	12	13
	Early-time	20.8	27.5	36

3.3.3.2 MULTI-ZONE MODEL

The multi-zone computational model could very well capture the diffusion behavior of neutral solutes in articular cartilage both for the early and late time points (Figure 3.7). The coefficients of determination were between 0.99 and 1.00 for samples 1 and 2 (Table 3.4) regardless of condition (A-C). The coefficients of determination were slightly lower for sample 3, i.e. between 0.94 and 0.97 (Table 3.4). For this last sample, the multi-zone model could not fully capture the concentration curve. In agreement with the above-mentioned coefficients of determination, the computational model could follow the experimental data points very well and could predict not only the early-time concentration values but also the near-equilibrium concentration values particularly for samples 1 and 2 (Figure 3.7).

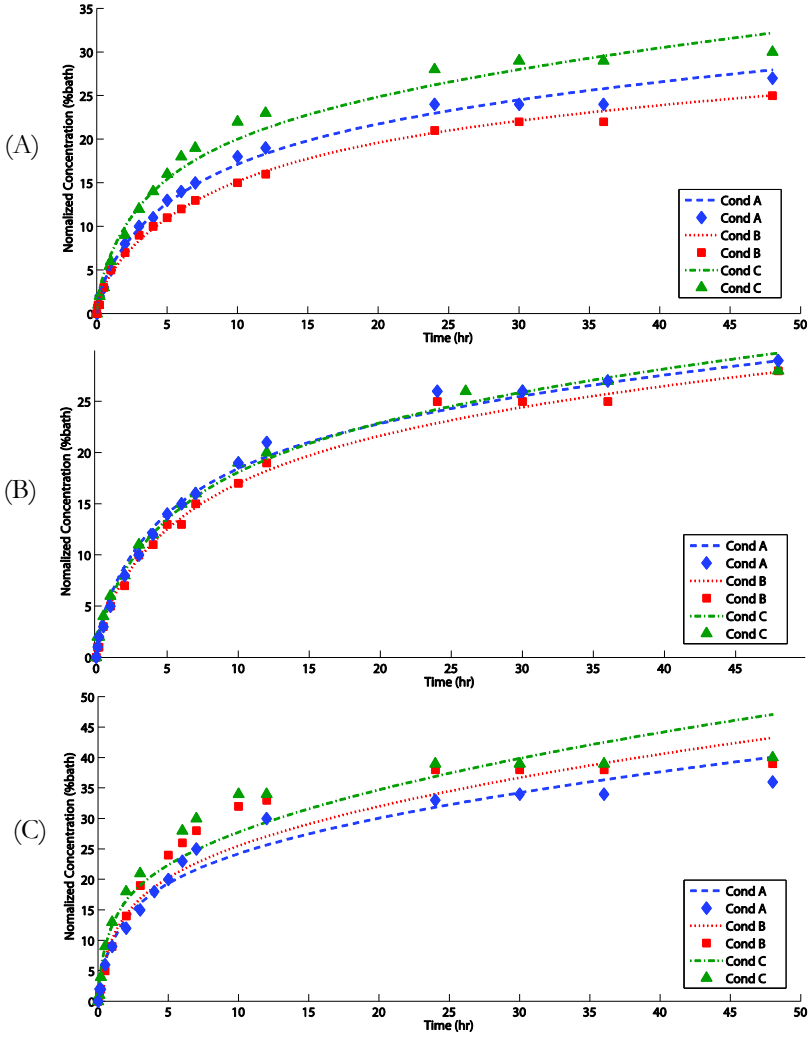

Figure 3.7. Experimental (symbols) and simulated (dashed-lines) concentration vs. time for conditions A-C and samples 1(A) to 3 (C). Computational models (multi-zone) were fitted to all experimental data points.

Table 3.4. RMSE and R^2 to compare the experimental and simulation solute concentration vs. time for the multi-zone computational model.

	Condition	A	B	C
Sample 1	R^2	0.99	1	0.99
	RMSE	0.0068	0.0044	0.0122
Sample 2	R^2	1	0.99	0.99
	RMSE	0.0058	0.0074	0.0079
Sample 3	R^2	0.97	0.95	0.94
	RMSE	0.0207	0.0348	0.0349

A parametric study indicated that the diffusivities of the superficial and middle zones played key roles in contrast to that of the deep zone, which had minimal impact on the predicted diffusion behavior of cartilage. Therefore, only the diffusivities of the superficial and middle zones are reported (Table 3.5). Similar to the single-zone model, the diffusion coefficients determined for sample 3 were larger than those of samples 1 and 2 (Table 3.5). However, the ratio of the diffusion coefficient of the superficial zone to that of the middle zone ($D_{Superficial} / D_{Middle}$) was consistent between all samples and for all conditions (Table 3.6): 14.53±1.88 for condition A, 14.23±3.1 for condition B, and 13.25±1.64 for condition C.

Table 3.5. Diffusion coefficients obtained from the multi-zone computational model based on fitting of the model to all experimental data points.

	Diffusion coefficient ($\mu m^2/s$)								
	Condition A			Condition B			Condition C		
	$D_{Superficial}$	D_{Middle}	D_{Deep}	$D_{Superficial}$	D_{Middle}	D_{Deep}	$D_{Superficial}$	D_{Middle}	D_{Deep}
Sample 1	7.5	0.55	*Insensitive**	5.5	0.3	*Insensitive*	13	1	*Insensitive*
Sample 2	10	0.6	*Insensitive*	7.3	0.55	*Insensitive*	8.8	0.74	*Insensitive*
Sample 3	30	2.25	*Insensitive*	35	3	*Insensitive*	60	4	*Insensitive*

*The average concentration values were not sensitive enough to the diffusion coefficient of the deep cartilage zone to enable us determine the diffusion coefficient of the deep cartilage zone.

Table 3.6. The ratio of diffusion coefficient of superficial zone to middle zone ($D_{Superficial} / D_{Middle}$).

Condition	A	B	C
Diffusion coefficient ratio	$D_{Superficial}/D_{Middle}$	$D_{Superficial}/D_{Middle}$	$D_{Superficial}/D_{Middle}$
Sample 1	13.6	17.7	13
Sample 2	16.7	13.3	11.7
Sample 3	13.3	11.7	15

3.4. DISCUSSION

Due to the importance of diffusion for nutrition and oxygenation of cells in the avascular cartilage tissue, transport of solutes in cartilage has been studied in several previous studies. There are three main categories of inter-connected physical phenomena, namely mechanical, chemical, and electrical that occur simultaneously and complicate understanding the diffusion of solutes across cartilage. Those physical complexities particularly the role of fixed electrical charges and mechanical stresses/strain were not respected in many previous studies where purely Fickean diffusion models were used to describe the transport of charged particles across cartilage. In this study, we used neutral solutes to separate the effects of electrical charges from those of mechanics, i.e. stresses and deformations, and concentration gradients as much as possible. To make sure the role of both mechanical forces and concentration gradients are taken into account, a biphasic-solute model was used to describe the transport of neutral solutes across articular cartilage. Moreover, the effects of variation in the diffusion coefficients of the various cartilage zones, i.e. superficial, middle, and deep zones, on the transport of neutral solutes were

studied using both single-zone and multi-zone computational models. The fact that the presented computational model perfectly matches the analytical solution in the case of finite well-stirred bath (one of the closest cases for which an analytical solution is available) increases our confidence in the accuracy of the presented computational model.

3.4.1. EFFECTS OF CARTILAGE ZONES ON DIFFUSION

Perhaps the most important conclusion of the current study is that a single diffusion coefficient is not sufficient to describe the transport of solutes across articular cartilage. The biphasic-solute model is incapable of following the experimental concentration-time curve when the entire cartilage is considered to be one tissue with one single diffusion coefficient. It is well known that the different cartilage layers are different both in terms of GAG content and the arrangement of collagen fibers. The use of neutral solutes means that electrical charges are not playing a major role in this observation, suggesting that variation in the organization of collagen fibers may be sufficient to cause large variations in the diffusion coefficients of the different cartilage zones.

One needs to note that only the averaged concentration values were used in the current study to describe the diffusion of neutral solutes. Two diffusion coefficients may be sufficient to describe these averaged concentration values because the concentration values of the deep cartilage zone do not significantly influence the average concentration value that is calculated for the entire cartilage. The concentration values of the deep cartilage zone are expected to play more important roles when the spatial distribution of concentration is taken into account. However, two diffusion coefficients may not be enough for capturing the spatial variation of solute concentration values through the cartilage thickness. We therefore need detailed experimental data regarding

the spatial distribution of concentration values throughout cartilage in order to be able to determine the diffusion coefficient of the deep cartilage zone.

Throughout the course of diffusion experiments under large osmolality differences, cartilage is likely to experience large thickness variations due to swelling/shrinkage. This causes serious complexities when trying to determine the concentration values through the cartilage thickness. Major improvements in experimental and image processing techniques are therefore needed before one could determine the number of zones required for accurately capturing the spatial distribution of concentration values through the cartilage thickness. The mechanical property gradient across the cartilage's zones due to altered collagen fiber orientation, concentration and thickness as well as water content might also play a role in the diffusion. However, we observed only a negligible shift in the diffusion curves when the hydraulic permeability and Poisson's ratio were varied within the expected range of the cartilage mechanical properties. Young's modulus was chosen so that it was always significantly greater than the effective pressure generated within the cartilage to prevent large deformations, which was in accordance with the experimental observations. On the contrary, water content gradient presents a strong effect on the diffusion behavior. The near-equilibrium condition was reached after 24 hr in experiments. However, even after 48 hr the concentration curve still had the tendency to slightly rise. As for computational results, the single-zone model highly overestimated the increase of the concentration after 24 hr. It is much less so for the multi-zone computational model. The concentration curves obtained by both multi-zone computational model and experiments show slight increase after 24 hr. For the first two samples, the level of the increase in the concentration curves is similar in the multi-zone computational model and

experiments. For sample 3, however, there is increased discrepancy between the concentration curve of the multi-zone computational model and the experimentally determined concentration curve.

3.4.2. DIFFUSION COEFFICIENTS

The diffusion coefficients are comparable in conditions A-C, despite large differences in the concentration values. This shows the Fickian nature of diffusion in the case of neutral solutes: there is a more or less linear relationship between the concentration gradient and diffusion flux.

As for the different zones, the diffusion coefficient of the middle zone is at least one order of magnitude lower than that of the superficial zone. This is consistently observed within the three samples used in the current study and implies that the structure of the superficial zone is specialized for facilitating the diffusion of solutes into cartilage. As previously mentioned, this observation may not be primarily attributed to the fixed charge density of the superficial zone (i.e. its GAG content), as the solutes used in the current study are not electrically charged. The arrangement of collagen fibers including their orientation, density, and the steric hindrance may, however, play important roles in this regard. Since nutrition and oxygenation of cells inside cartilage should occur through diffusion and given that the superficial zone is responsible for most of that diffusion, it is natural to expect the superficial zone to be specialized in facilitating the process of solute transport across cartilage.

Interestingly, the diffusion coefficients calculated for sample 3 are much higher than those of both other samples. A relatively wide range of diffusion coefficients is therefore observed in the current study. This is consistent with the previous studies that report wide ranges of diffusion coefficients [30, 42]. Despite these relatively

large differences in the absolute values of the diffusion coefficients, the ratio of the diffusion coefficients of different zones is very consistent between samples, highlighting the observation that the diffusion coefficient of the superficial zone is much higher than of the middle zone regardless of the absolute values of the diffusion coefficients.

3.4.3. LIMITATIONS AND RECOMMENDATIONS FOR FUTURE RESEARCH

As mentioned several times so far, we tried to minimize the effects of fixed charge density on our study through the use of neutral solutes and a biphasic-solute computational model. It should be, however, noted that the assumed water content could significantly influence the diffusion of neutral solutes across cartilage. In this study, we used realistic water contents decreasing from 80% at the superficial zone to 60% for the deep layer [1, 14, 39]. This assumption helps us obtain realistic results in terms of diffusion, but also indirectly introduces the effects of fixed charge density (i.e. GAG content). That is because water content is, among other factors, a function of the fixed charge density [12]. It is therefore not possible to entirely exclude the indirect effects of GAG content on diffusion, even in this carefully designed set of experiments and computational models.

Similar to many recent studies [6, 7, 24], only through-the-thickness (i.e. axial) diffusion of contrast agent was considered in the current study. The diffusion tensor is, however, known to be anisotropic [13] and this could cause specific patterns of radial diffusion that cannot be captured using axial models. The specific patterns of radial diffusion are, however, outside the scope of the current study.

Finally, the biphasic-solute model presented here could be replaced by a multi-phasic model to study the diffusion of charged molecules into cartilage. The experiments need to be performed using both neutral and charged molecules to enable separation of the effects of electrical charges from those of other effects. These topics will be addressed in a future study.

In this study, we tried to take advantage of a clinically used radiopaque molecule, i.e. iodixanol, to facilitating the use of CT technology for monitoring the diffusion process. In reality, wide ranges of molecules with significantly different sizes are transported in and out of cartilage through diffusion. Some of the molecules important for cartilage metabolism such as collagen fragments generated during enzymatic activity and some therapeutics are small enough to be comparable to our solute [43, 44]. But many other relevant molecules are much larger than iodixanol. Since the size of relevant molecules could be very different and given that diffusion coefficients change with molecule size, no single molecule could represent the entire range of all relevant molecules. However, this study shows the difference between the diffusion coefficients of the different zones within cartilage. Even though the absolute diffusivity values might be different for different molecules, the main conclusion of the current study, i.e. significantly different diffusion coefficients through the cartilage thickness, is expected to hold regardless of the molecule size.

3.5. CONCLUSIONS

The diffusion of neutral solutes across cartilage was studied using both experiments and computational models. It was found that one single diffusion coefficient is not sufficient to describe the

diffusion of solutes across cartilage even when the solutes are uncharged and, thus, not influenced by GAG content. Computational models with three separate zones corresponding to superficial, middle, and deep cartilage zones could very well describe the diffusion of neutral solutes. The diffusion coefficient of the superficial zone was in all three tested samples at least one order of magnitude larger than that of the middle zone.

3.6. REFERENCES

1. Leddy H.A., Guilak F., *Site-Specific Molecular Diffusion in Articular Cartilage Measured using Fluorescence Recovery after Photobleaching.* Annals of Biomedical Engineering, 2003. **31**(7): p. 753-760.
2. Torzilli P.A., Adams T.C., Mis R.J., *Transient solute diffusion in articular cartilage.* Journal of Biomechanics, 1987. **20**(2): p. 203-214.
3. Williams R.M., Zipfel W.R., Tinsley M.L., Farnum C.E., *Solute transport in growth plate cartilage: in vitro and in vivo.* Biophys J, 2007. **93**(3): p. 1039-50.
4. Abazari A., Elliott J.A.W., McGann L.E., Thompson R.B., *MR spectroscopy measurement of the diffusion of dimethyl sulfoxide in articular cartilage and comparison to theoretical predictions.* Osteoarthritis and Cartilage, 2012. **20**(9): p. 1004-1010.
5. Abazari A., Thompson R.B., Elliott J.A., McGann L.E., *Transport phenomena in articular cartilage cryopreservation as predicted by the modified triphasic model and the effect of natural inhomogeneities.* Biophys J, 2012. **102**(6): p. 1284-93.
6. Kokkonen H.T., Mäkelä J., Kulmala K.A.M., Rieppo L., Jurvelin J.S., Tiitu V., Karjalainen H.M., Korhonen R.K., Kovanen V., Töyräs J., *Computed tomography detects changes in contrast agent diffusion after collagen cross-linking typical to natural aging of articular cartilage.* Osteoarthritis and Cartilage, 2011. **19**(10): p. 1190-1198.
7. Kulmala K.A.M., Korhonen R.K., Julkunen P., Jurvelin J.S., Quinn T.M., Kröger H., Töyräs J., *Diffusion coefficients of articular cartilage for different CT and MRI contrast agents.* Medical Engineering & Physics, 2010. **32**(8): p. 878-882.
8. Siebelt M., Groen H.C., Koelewijn S.J., de Blois E., Sandker M., Waarsing J.H., Muller C., van Osch G.J., de Jong M., Weinans H., *Increased physical activity severely induces osteoarthritic changes in knee joints with papain induced sulphate-glycosaminoglycan depleted cartilage.* Arthritis Res Ther, 2014. **16**(1): p. R32.
9. Siebelt M., van der Windt A.E., Groen H.C., Sandker M., Waarsing J.H., Müller C., de Jong M., Jahr H., Weinans H., *FK506 protects against articular cartilage collagenous extra-cellular matrix degradation.* Osteoarthritis and Cartilage, 2014. **22**(4): p. 591-600.
10. Piscaer T.M., Sandker M., van der Jagt O.P., Verhaar J.A., de Jong M., Weinans H., *Real-time assessment of bone metabolism in small animal models for osteoarthritis using multi pinhole-SPECT/CT.* Osteoarthritis Cartilage, 2013. **21**(6): p. 882-8.
11. Weinans H., Siebelt M., Agricola R., Botter S.M., Piscaer T.M., Waarsing J.H., *Pathophysiology of peri-articular bone changes in osteoarthritis.* Bone, 2012. **51**(2): p. 190-6.
12. Ko Lok S., Quinn Thomas M., *Matrix Fixed Charge Density Modulates Exudate Concentration during Cartilage Compression.* Biophysical Journal, 2013. **104**(4): p. 943-950.

13. Leddy H.A., Guilak F., *Site-Specific Effects of Compression on Macromolecular Diffusion in Articular Cartilage.* Biophysical Journal, 2008. **95**(10): p. 4890-4895.
14. Salo E.N., Nissi M.J., Kulmala K.A.M., Tiitu V., Töyräs J., Nieminen M.T., *Diffusion of Gd-DTPA2− into articular cartilage.* Osteoarthritis and Cartilage, 2012. **20**(2): p. 117-126.
15. van Tiel J., Siebelt M., Waarsing J.H., Piscaer T.M., van Straten M., Booij R., Dijkshoorn M.L., Kleinrensink G.J., Verhaar J.A., Krestin G.P., Weinans H., Oei E.H., *CT arthrography of the human knee to measure cartilage quality with low radiation dose.* Osteoarthritis Cartilage, 2012. **20**(7): p. 678-85.
16. Siebelt M., Waarsing J.H., Kops N., Piscaer T.M., Verhaar J.A., Oei E.H., Weinans H., *Quantifying osteoarthritic cartilage changes accurately using in vivo microCT arthrography in three etiologically distinct rat models.* J Orthop Res, 2011. **29**(11): p. 1788-94.
17. Siebelt M., Waarsing J.H., Groen H.C., Muller C., Koelewijn S.J., de Blois E., Verhaar J.A., de Jong M., Weinans H., *Inhibited osteoclastic bone resorption through alendronate treatment in rats reduces severe osteoarthritis progression.* Bone, 2014. **66**: p. 163-70.
18. Leddy H.A., Awad H.A., Guilak F., *Molecular diffusion in tissue-engineered cartilage constructs: effects of scaffold material, time, and culture conditions.* J Biomed Mater Res B Appl Biomater, 2004. **70**(2): p. 397-406.
19. Greene G.W., Zappone B., Zhao B., Söderman O., Topgaard D., Rata G., Israelachvili J.N., *Changes in pore morphology and fluid transport in compressed articular cartilage and the implications for joint lubrication.* Biomaterials, 2008. **29**(33): p. 4455-4462.
20. Bansal P.N., Joshi N.S., Entezari V., Grinstaff M.W., Snyder B.D., *Contrast Enhanced Computed Tomography can predict the glycosaminoglycan content and biomechanical properties of articular cartilage.* Osteoarthritis and Cartilage, 2010. **18**(2): p. 184-191.
21. Chin H.C., Moeini M., Quinn T.M., *Solute transport across the articular surface of injured cartilage.* Arch Biochem Biophys, 2013. **535**(2): p. 241-7.
22. Decker Sarah G.A., Moeini M., Chin Hooi C., Rosenzweig Derek H., Quinn Thomas M., *Adsorption and Distribution of Fluorescent Solutes near the Articular Surface of Mechanically Injured Cartilage.* Biophysical Journal, 2013. **105**(10): p. 2427-2436.
23. Huttunen J.M.J., Kokkonen H.T., Jurvelin J.S., Töyräs J., Kaipio J.P., *Estimation of fixed charge density and diffusivity profiles in cartilage using contrast enhanced computer tomography.* International Journal for Numerical Methods in Engineering, 2014. **98**(5): p. 371-390.
24. Kokkonen H.T., Jurvelin J.S., Tiitu V., Toyras J., *Detection of mechanical injury of articular cartilage using contrast enhanced computed tomography.* Osteoarthritis Cartilage, 2011. **19**(3): p. 295-301.
25. Meganck J.A., Kozloff K.M., Thornton M.M., Broski S.M., Goldstein S.A., *Beam hardening artifacts in micro-computed tomography scanning can be reduced by X-ray beam filtration and the resulting images can be used to accurately measure BMD.* Bone, 2009. **45**(6): p. 1104-16.

26. Bansal P.N., Stewart R.C., Entezari V., Snyder B.D., Grinstaff M.W., *Contrast agent electrostatic attraction rather than repulsion to glycosaminoglycans affords a greater contrast uptake ratio and improved quantitative CT imaging in cartilage.* Osteoarthritis Cartilage, 2011. **19**(8): p. 970-6.
27. Aula A.S., Jurvelin J.S., Töyräs J., *Simultaneous computed tomography of articular cartilage and subchondral bone.* Osteoarthritis and Cartilage, 2009. **17**(12): p. 1583-1588.
28. Tuomo S. Silvast J.S.J., Virpi Tiitu, Thomas M. Quinn and Juha Töyräs, *Bath Concentration of Anionic Contrast Agents Does Not Affect Their Diffusion and Distribution in Articular cartilage In Vitro.* Cartilage, 2013. **4**(1): p. 42-51.
29. Silvast T.S., Jurvelin J.S., Lammi M.J., Töyräs J., *pQCT study on diffusion and equilibrium distribution of iodinated anionic contrast agent in human articular cartilage – associations to matrix composition and integrity.* Osteoarthritis and Cartilage, 2009. **17**(1): p. 26-32.
30. Pan J., Zhou X., Li W., Novotny J.E., Doty S.B., Wang L., *In situ measurement of transport between subchondral bone and articular cartilage.* J Orthop Res, 2009. **27**(10): p. 1347-52.
31. Mauck R.L., Hung C.T., Ateshian G.A., *Modeling of Neutral Solute Transport in a Dynamically Loaded Porous Permeable Gel: Implications for Articular Cartilage Biosynthesis and Tissue Engineering.* Journal of biomechanical engineering, 2003. **125**(5): p. 602-614.
32. Ateshian G.A., Albro M.B., Maas S., Weiss J.A., *Finite element implementation of mechanochemical phenomena in neutral deformable porous media under finite deformation.* J Biomech Eng, 2011. **133**(8): p. 081005.
33. Ateshian G.A., Maas S., Weiss J.A., *Solute transport across a contact interface in deformable porous media.* Journal of Biomechanics, 2012. **45**(6): p. 1023-1027.
34. Ateshian G.A., *On the Theory of Reactive Mixtures for Modeling Biological Growth.* Biomechanics and modeling in mechanobiology, 2007. **6**(6): p. 10.1007/s10237-006-0070-x.
35. Sun D.N., Gu W.Y., Guo X.E., Lai W.M., Mow V.C., *A mixed finite element formulation of triphasic mechano-electrochemical theory for charged, hydrated biological soft tissues.* International Journal for Numerical Methods in Engineering, 1999. **45**(10): p. 1375-1402.
36. Ateshian G.A., Weiss J.A., *Finite Element Modeling of Solutes in Hydrated Deformable Biological Tissues.* 2013: p. 231-249.
37. Ateshian G.A., Maas S., Weiss J.A., *Finite element algorithm for frictionless contact of porous permeable media under finite deformation and sliding.* J Biomech Eng, 2010. **132**(6): p. 061006.
38. Bonet J., Wood, R.D., *Nonlinear Continuum Mechanics for Finite Element Analysis.* Cambridge University Press, Cambridge, NewYork, NY, 1997.
39. Sophia Fox A.J., Bedi A., Rodeo S.A., *The Basic Science of Articular Cartilage: Structure, Composition, and Function.* Sports Health, 2009. **1**(6): p. 461-468.

40. Nair N., Kim W.J., Braatz R.D., Strano M.S., *Dynamics of surfactant-suspended single-walled carbon nanotubes in a centrifugal field.* Langmuir, 2008. **24**(5): p. 1790-5.
41. Crank J., *The mathematics of diffusion.* Clarendon Press:, Oxford, Eng:, 1979.
42. Jackson A., Gu W., *Transport Properties of Cartilaginous Tissues.* Curr Rheumatol Rev, 2009. **5**(1): p. 40.
43. Schadow S., Siebert H.C., Lochnit G., Kordelle J., Rickert M., Steinmeyer J., *Collagen metabolism of human osteoarthritic articular cartilage as modulated by bovine collagen hydrolysates.* PLoS One, 2013. **8**(1): p. e53955.
44. Ameye L.G., Chee W.S., *Osteoarthritis and nutrition. From nutraceuticals to functional foods: a systematic review of the scientific evidence.* Arthritis Res Ther, 2006. **8**(4): p. R127.

CHAPTER 4

COMBINED INVERSE-FORWARD ARTIFICIAL NEURAL NETWORKS FOR FAST AND ACCURATE ESTIMATION OF THE DIFFUSION COEFFICIENTS OF CARTILAGE BASED ON MULTI-PHYSICS MODELS*

* This chapter is published as a scientific paper:

Arbabi V., Pouran B., Weinans H., Zadpoor A.A. *Combined inverse-forward artificial neural networks for fast and accurate estimation of the diffusion coefficients of cartilage based on multi-physics models.* Journal of Biomechanics, 2016. 49: p.631–637.

ABSTRACT

Analytical and numerical methods have been used to extract essential engineering parameters such as elastic modulus, Poisson's ratio, permeability and diffusion coefficient from experimental data in various types of biological tissues. The major limitation associated with analytical techniques is that they are often only applicable to problems with simplified assumptions. Numerical multi-physics methods, on the other hand, enable minimizing the simplified assumptions but require substantial computational expertise, which is not always available. In this work, we propose a novel approach that combines inverse and forward artificial neural networks (ANNs) which enables fast and accurate estimation of the diffusion coefficient of cartilage without any need for computational modeling. In this approach, an inverse ANN is trained using our multi-zone biphasic-solute finite-bath computational model of diffusion in cartilage to estimate the diffusion coefficient of the various zones of cartilage given the concentration-time curves. Robust estimation of the diffusion coefficients, however, requires introducing certain levels of stochastic variations during the training process. Determining the required level of stochastic variation is performed by coupling the inverse ANN with a forward ANN that receives the diffusion coefficient as input and returns the concentration-time curve as output. Combined together, forward-inverse ANNs enable computationally inexperienced users to obtain accurate and fast estimation of the diffusion coefficients of cartilage zones. The diffusion coefficients estimated using the proposed approach are compared with those determined using direct scanning of the parameter space as the optimization approach. It has been shown that both approaches yield comparable results.

4.1. INTRODUCTION

Transport of molecules in articular cartilage depends on factors such as orientation and concentration of collagen fibrils, proteoglycans, and water content, which vary significantly across cartilage thickness [1]. The rate of transport can be affected by the progression of the most common disease of diarthrodial joints, i.e. osteoarthritis (OA), which is due to changes in molecular structure of cartilage [2-6]. Molecular transport (diffusion) plays a key role in monitoring OA progression, delivery of therapeutics and nutrients as well as in the exchange of signaling molecules between cartilage and its surrounding tissues of subchondral bone and synovial fluid [7-9]. Previous studies used analytical solutions, mathematical fits, and computational models to derive the diffusion coefficients of solutes in cartilage [2-4, 10-12]. The available analytical solutions can only be applied to problems where either simple geometries are used or simplified assumptions are made [13]. Occasionally mathematical fits have been used when analytical solutions were not available, however, since mathematical formulae involving diffusion coefficients are fitted to the experimental data, the physical importance of certain phenomena might be neglected [4]. Computational models have been used to obtain the diffusion coefficient of neutral and charged solutes in complex geometries [2, 11]. Nevertheless, computational models are often associated with optimization algorithms which require advanced computational expertise while being cumbersome and lacking the capacity to recognize pattern of the experimental data.

Artificial neural networks (ANNs) are considered as intelligent tools which can be trained using input data and output target to efficiently fulfill pattern recognition [14]. In biomechanics, ANNs have been applied to problems such as bone remodeling, indentation tests as well as sport/gait mechanics [15-19].

Previously, we described a finite-bath finite element model and derived the diffusion coefficients of a neutral solute across cartilage zones using direct scanning of the parameter space as the optimization algorithm (chapter 3) [2]. We aim to create a package that can obtain the diffusion coefficients of a neutral solute in cartilage zones using series of micro-computed tomography (micro-CT) data even in labs where no computational expertise is available. From our previous study, we know that ANNs are extremely sensitive to deviations from their underlying model (chapter 2) [14]. To improve the robustness of ANN the training data has to be contaminated with some level of stochastic variation i.e. noise (chapter 2). Since the required level of noise is generally unknown, we have proposed, for the first time, to use a second ANN that could be used to estimate the required level of noise. The combination of both ANNs (after training) enables estimating the diffusion coefficients of a neutral solute across different zones of cartilage without any computational modeling.

4.2. METHODOLOGY

4.2.1. EXPERIMENTS

The descriptive details of the experiments consisting of sample preparation, image acquisition, and image processing are presented elsewhere (chapters 3 and 5) [2, 6]. Osteochondral plugs (n=3, cartilage thickness= 2.8 mm, and diameter= 8.5 mm) were extracted from two fresh equine femora using custom-made drill bits while the site of extraction was constantly sprayed using phosphate buffer solution (PBS) to prevent overheating. Iodixanol solutions (finite bath of 650 µL, 1550.2 g/mol, charge=0, condition A: 420 mM, 290 mOsm/kg H_2O, condition B: 420 mM, 600 mOsm/kg H_2O, condition C: 210 mM, 290 mOsm/kg H_2O, GE Healthcare, *The Netherlands*) were prepared and the diffusion of

iodixonal from each condition was restricted to occur only from the articular surface of cartilage (Figure 4.1A). A micro-CT scanner (40 μm spatial resolution, *Quantum FX, Perkin Elmer, USA*) allowed monitoring the transport of iodixonal through cartilage at room temperature. After each experiment, samples underwent desorption process using a large bath of PBS and protease inhibitor (*cOmplete*, *Roche, The Netherlands*). Using the in-built software of micro-CT (*Analyze 11.0*), 2D slices with TIFF format were generated. The mid-sagittal slice was then isolated and processed to render the concentration-time curves for 17 different time points until 48 hours (Figure 4.2).

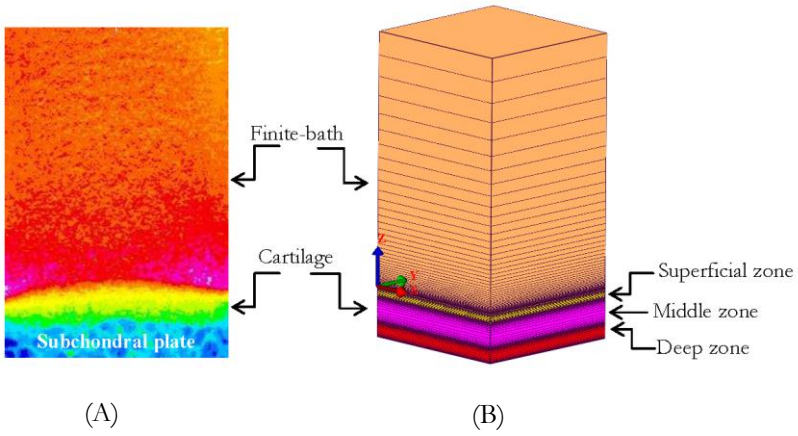

Figure 4.1. Experimental (A) versus computational (B) models: Iodixonal finite bath is placed on the surface of the articular cartilage to study its axial diffusion across various zones of articular cartilage i.e. superficial zone (20% of cartilage thickness), middle zone (50% of cartilage thickness) and deep zone (30% of cartilage thickness).

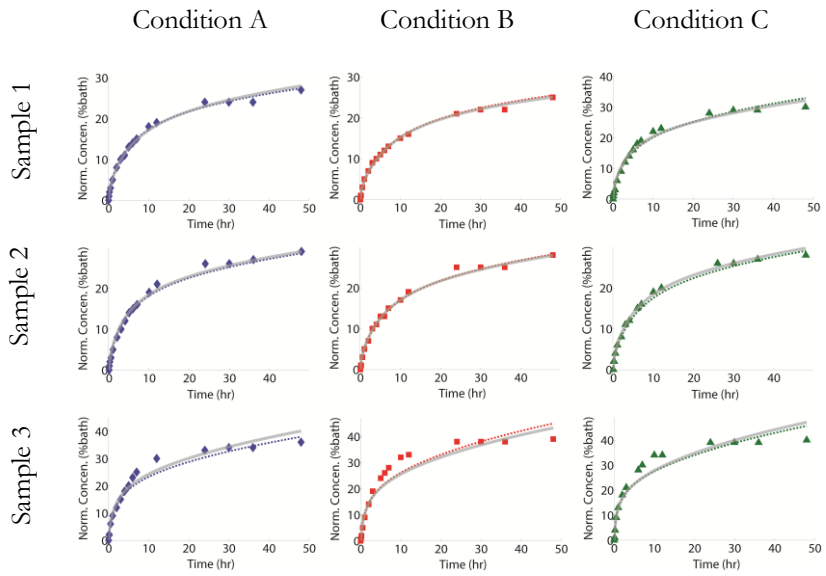

Figure 4.2. Normalized concentration of iodixonal versus time for samples 1-3 and conditions A-C: points represent the experimental data, solid line is the inverse-forward ANNs result and dashed line is the optimization algorithm result.

4.2.2. COMPUTATIONAL MODEL

The required equations to describe the transport of iodixanol across cartilage are conservation of linear momentum for the mixture, conservation of the mass for the mixture, and conservation of mass for solute, which were described in our previous work (chapter 3) [2]. We assigned a neo-Hookean material model for cartilage with a Young's modulus of 10 MPa, Poisson's ratio of 0, hydraulic permeability of 10^{-3} mm^4/Ns, and effective solubility of 1. Diffusion coefficient of iodixanol was set to 0.00025 mm^2/s [21] and the diffusion tensor was assumed isotropic. Since cartilage is a heterogeneous material, we used a previously proposed multi-zone model (chapter 3) where water

content varied from 0.8 in the superficial zone (20% of the cartilage thickness) to 0.7 in the middle zone (50% of the cartilage thickness) and 0.6 in the deep zone (30% of the cartilage thickness) [22](Figure 4.1B). The required initial and boundary conditions to solve the problem have been presented earlier [2].

4.2.3. INVERSE-FORWARD ARTIFICIAL NEURAL NETWORKS

A conventional feed-forward ANN consists of artificial neurons that is trained using a set of input data and a set of target data. The trained ANN processes the data in the hidden layer and generates the result as the output signal (Figure 4.3).

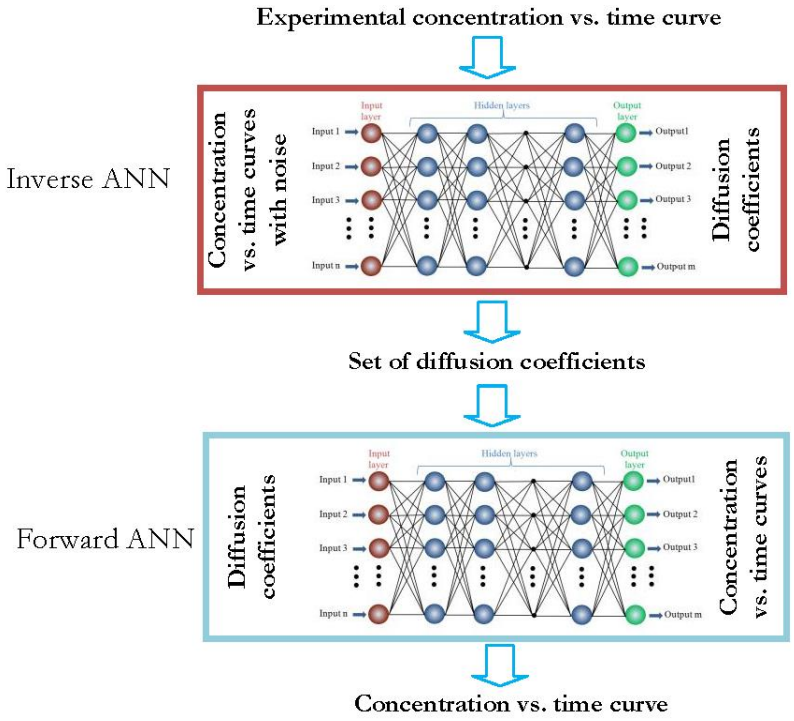

Figure 4.3. Anatomy of the inverse-forward ANNs.

Each artificial neuron in the hidden layer has a so-called signal activation function such as tang-sigmoid function which processes the signal transmitted by the other artificial neurons, gives a weight to it, and biases it to generate the output signal (chapter 2) [14]. The biphasic-solute multi-zone finite element modeling was performed in FEBio for a wide range of diffusion coefficients in the superficial (0.1-99.1 $\mu m^2/s$ with interval 1 $\mu m^2/s$) and middle zones (0.1-10 $\mu m^2/s$ with interval 0.1 $\mu m^2/s$) resulting in 10,000 models, based on the findings of our previous study (chapter 3) [2]. Using a FEBio-MATLAB interfacing program developed in-house, concentration-time curves (10,000×17 time points) were obtained from the biphasic-solute multi-zone finite element model and constituted the input matrix of the so-called inverse ANN while diffusion coefficients of superficial and middle zones (10,000×2 diffusion coefficients) served as the target matrix of the same ANN. Since the diffusion within the deep zone is not high enough to enable accurate determination of diffusion coefficient in the deep zone, we did not report the diffusion coefficients of the deep cartilage zone (chapter 3) [2]. Our previous study (chapter 2) showed that ANNs are very sensitive to any deviations from the underlying computational model that is used for their training [14]. To alleviate this problem, the training data of ANNs can be contaminated with some level of noise [14, 23, 24] to increase the robustness of ANN. Therefore, we trained the ANN using the input concentration vs. time curves contaminated with different levels of Gaussian noise, i.e. 1-20%. The contaminated concentration function ($c'(t)$) is produced as follows:

$$c'(t) = c(t) + N(0, \sigma(t)) \tag{4.1}$$

where $N(0, \sigma(t))$ is a Gaussian distribution function with the standard deviation $\sigma(t) = c(t)/\lambda$, and $c(t)$ is the concentration data obtained from finite element modeling. The parameter λ

represents the signal to noise ratio, which varies between 100 and 5 with step-size of 5 corresponding to noise levels 1-20%. We used 90% of the input data for the training, 5% for the validation, and 5% for the test of the ANN (30 neurons in the hidden layer).

Next, we introduce the experimental concentration vs. time curves to the trained inverse ANNs to obtain diffusion coefficients of superficial ($D_{Superficial}$) and middle (D_{Middle}) zones corresponding to each noise level as the outputs. The only remaining question to answer is "what level of noise should be used for contaminating the training data of the inverse ANN". This question cannot be answered in the general case without performing the actual finite element simulation to see which noise level produces diffusion coefficients that result in concentration-time curves that are as close as possible to the experimental values of the concentration-time curve. To circumvent this problem and avoid performing direct finite element simulations, we propose a novel approach that is based on using a forward ANN. This second ANN receives the diffusion coefficients as input and returns the concentration-time curve associated with those values of diffusion coefficients. To maximize the fidelity of the forward ANN to the actual finite element simulations, fully clean training data is used for its training. Similar to inverse ANN, we used 90% of the input data for training, 5% for validation, and 5% for testing the forward ANN (30 neurons in the hidden layer). The diffusion coefficients estimated by the inverse ANN were then fed back to the forward ANN to estimate the concentration-time curve. The noise level was optimized to minimize the root mean square error (RMSE) between the experimental concentration-time curve and the concentration-time curve estimated by the forward ANN (Figure 4.4). A MATLAB code for generating noisy data and training inverse-forward artificial networks is available in the Appendix.

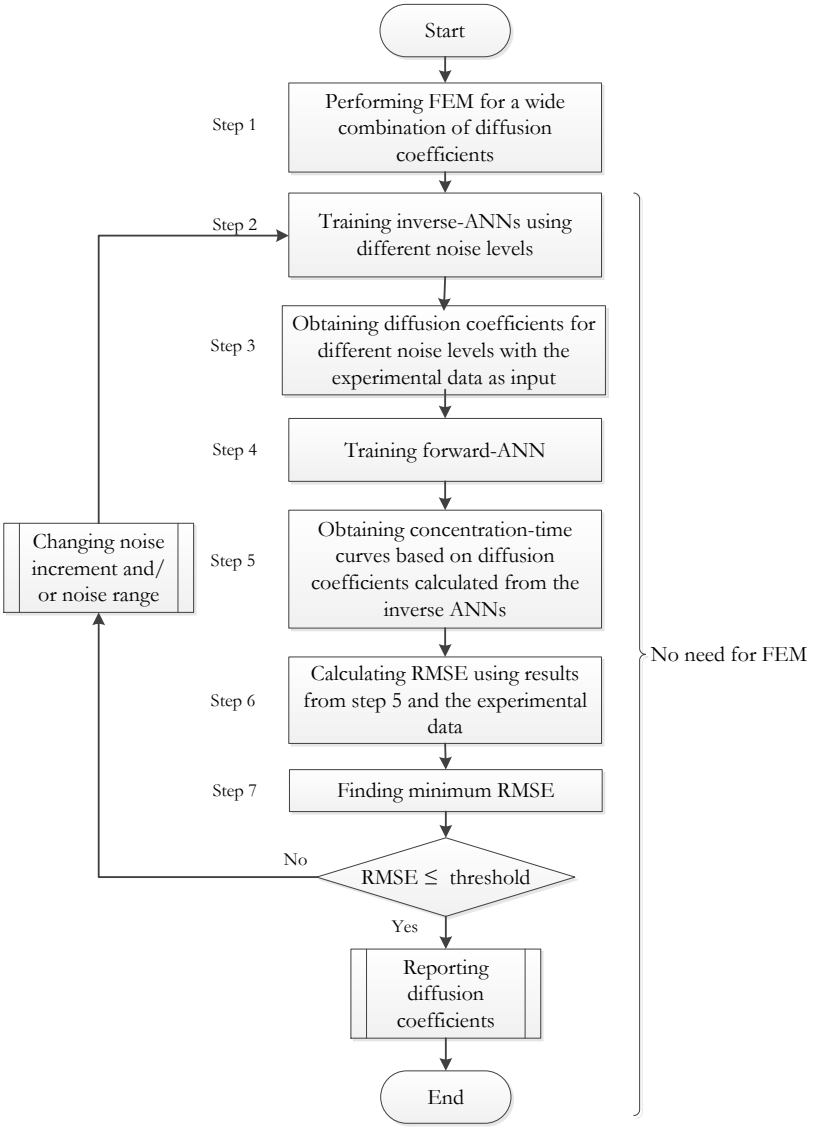

Figure 4.4 Flowchart of inverse-forward ANNs to obtain diffusion coefficients.

4.3. RESULTS

The high values of the Pearson correlation coefficients (R) clearly showed robustness of the inverse ANN when trained under different levels of noise (e.g. Figure 4.5A-C). The mean squared error drops to very low values for the training, validation, and test datasets, thereby confirming the efficacy of the training process (Figure 4.5D). All training, validation, and test datasets showed similar improvement as the training iterations progressed (Figure 4.5D). The identification error, i.e. the difference between the actual set of diffusion coefficients and those predicted by inverse ANN, for the test dataset that was not used in training process, was reminiscence of a normal distribution and was quite small (e.g. Figure 4.5E). Similar results were obtained for all levels of noise and the same observations held true (data not shown).

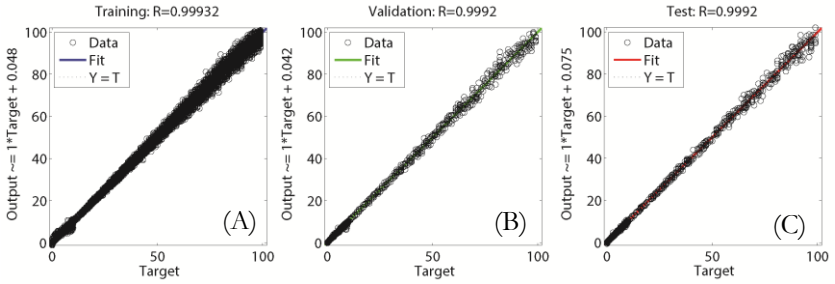

No. samples	Training	Validation	Test	No. neurons
10000	90%	5%	5%	30

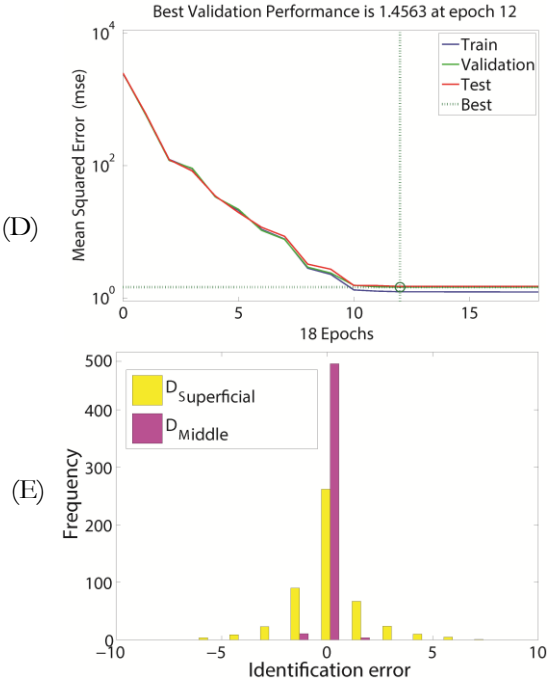

Figure 4.5. Regression diagrams for the training (A), validation (B), and test (C) datasets of the inverse ANN trained when it was trained with signal to noise ratio of 50 (2% noise level). ANN training diagram (D) and histogram of identification errors (E).

The Pearson correlation coefficients for the forward ANN for all training, validation, and test datasets was equal to one (Figure 4.6A-C), which suggests perfect capability of the forward ANN in replacing the actual finite element model for the purpose of predicting the concentration-time curve given the diffusion coefficient. Similar to inverse ANN, the training diagram of the inverse ANN reveals a very small mean squared error for the training, validation, and test datasets, which further confirms the efficacy of the training process (Figure 4.6D).

The combined forward-inverse ANN approach proposed here and the direct scanning of the parameter space as the optimization approach resulted in similar values of diffusion coefficients (Table 4.1B) and similar concentration-time curves for all the cartilage samples for which experimental data were available from our previous experimental study (Figure 4.2). The coefficient of determination (R^2) and RMSE between were similar for the combined forward-inverse ANN approach and the optimization approach (Table 4.1A). Except for sample 3 and condition C where the required noise level in the training phase was around 7%, the other samples and conditions resulted in required noise levels below 2.5% (Table 4.1B).

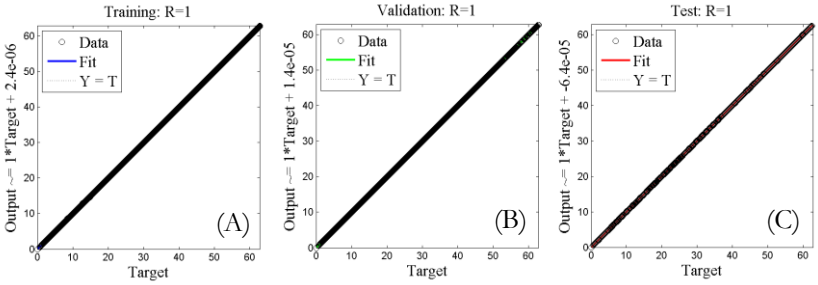

No. samples	Training	Validation	Test	No. neurons
10000	90%	5%	5%	30

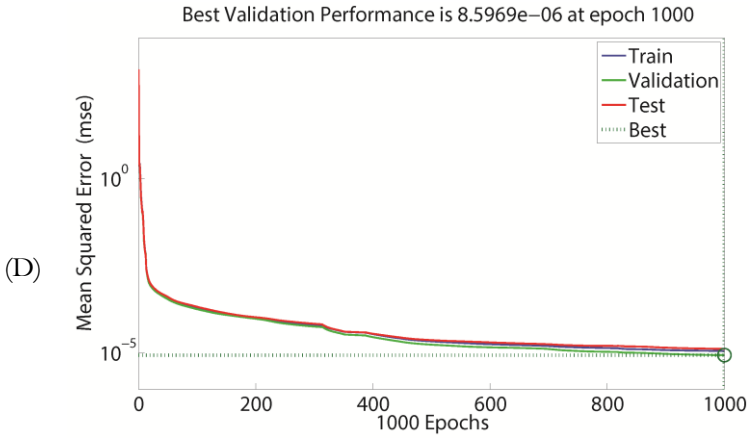

Figure 4.6. Regression diagrams for the training (A), validation (B), and test (C) datasets of the forward-ANN (noise-free). ANN training diagram (D).

Table 4.1. R^2 and RMSE for samples 1-3 and conditions A-C for inverse-forward ANNs and optimization algorithm (A), Diffusion coefficients in the superficial ($D_{Superficial}$) and middle (D_{Middle}) zones obtained using inverse-forward ANNs and optimization algorithm (B).

Condition		A		B		C	
(A)		ANN	Optimization	ANN	Optimization	ANN	Optimization
Sample 1	R^2	1.00	0.99	1.00	1.00	0.99	0.99
	RMSE	0.0059	0.0068	0.0052	0.0044	0.0131	0.0122
Sample 2	R^2	0.99	1.00	0.99	0.99	0.99	0.99
	RMSE	0.0081	0.0058	0.0068	0.0074	0.01	0.0079
Sample 3	R^2	0.97	0.97	0.95	0.95	0.95	0.94
	RMSE	0.0230	0.0207	0.0330	0.0348	0.0320	0.0349

	Condition	Diffusion coefficient (μm²/s)					
		A		B		C	
(B)		$D_{Superficial}$	D_{Middle}	$D_{Superficial}$	D_{Middle}	$D_{Superficial}$	D_{Middle}
Sample 1	ANN	8.00	0.48	5.28	0.35	11.5	1.20
	Optimization	7.50	0.55	5.30	0.30	13.00	1.00
Sample 2	ANN	9.34	0.59	8.00	0.65	7.40	0.72
	Optimization	10.00	0.60	7.30	0.55	8.80	0.75
Sample 3	ANN	26.00	1.85	35.20	3.50	60.40	3.50
	Optimization	30.00	2.25	35.00	3.00	60.00	4.00

4.4. Discussion

Interpretation of experimental data in tissue biomechanics often requires the use of complex material models such as multiphasic, biphasic-solute, as well as complex boundary conditions and/or geometries. Analytical and computational solutions have been developed to interpret experimental data while capturing the real multi-physics phenomena to the maximum possible extent [2, 11, 12]. Computational models such as FEM can remarkably boost the solution for more complex problems when complicated material models, boundary conditions, and geometries are concerned [25]. The major drawback of computational models is that they are time-consuming to develop and require considerable computational modeling and mathematical physics expertise.

Recently, we developed a multi-zone multi-physics model (chapter 3) to study the transport of neutral solutes across articular cartilage which enabled us estimate the diffusion coefficients of different cartilage layers [2]. In spite of being a powerful approach for accurate estimation of diffusion coefficients, computational models similar to the one proposed in our previous study require considerable computational expertise that is not universally available. Based on the proposed method regarding the trained ANNs with noise (chapter 2) [14] in the present study we aimed to obtain the diffusion coefficients of different cartilage layers using experimental data collected during diffusion experiments. In the current work we proposed to combines inverse and forward artificial neural networks (ANNs) to provide a fast and accurate estimation of the diffusion coefficient of cartilage without any need for computational modeling to simulate the diffusion. Determining the required level of stochastic variation was performed by coupling the inverse ANN with the forward ANN,

which receives the concentration-time curve and returns the diffusion coefficient.

This approach presented in this study is not only capable of cancelling the noise, but also eliminates the need for FEM knowledge. The first element of the inverse-forward ANNs is the inverse ANN which is trained with noisy data and is responsible to filter the noise, while the second element is the forward ANN which eliminates the necessity of FEM. Training with noise-free FEM data of the inverse ANN would result in overfitting and its subsequent failure [14, 24]. The inverse ANN trained with noisy data (Gaussian random noise) is most sensitive to the general trend of the experimental data without being influenced by small deviations from FEM caused by uncertainties involved in the experimental data.

The pattern recognition feature of ANN has been previously stressed and our findings also underscored this feature [14, 26]. The difference between RMSE and R^2 from optimization algorithm and ANN predictions although not large (Table 4.1A), might be due to differences in interval step sizes by which ANN was trained and optimization algorithm was processed.

By training the ANN using sufficiently wide range of diffusion coefficients for different thicknesses of cartilage, different bath sizes and concentrations, non-FEM specialists can easily benefit from the application of the inverse-forward ANNs proposed in this work. Besides, since ANN has been shown to be applicable for both indentation of poroelastic materials (chapter 2) [14] and our diffusion experiments, one can take advantage of it in other areas of tissue biomechanics where complex multi-physics computational models are needed to estimate specific properties of tissues.

More complex computational models particularly nonlinear (i.e. hyperplastic) models may be needed for estimation of the diffusion coefficients of cartilage under different (loading) conditions. For example, there is some evidence that loading may influence the process of solute transport in cartilage [27, 28]. Experiments that investigate the effect of mechanical loading on the diffusion process may therefore be associated with relatively high levels of strain in cartilage, thereby necessitating the use of hyperplastic models for describing the elastic part of the cartilage mechanical behavior. The presence of large deformations and the use of hyperplastic models introduce strong nonlinearities in the involved equations one of the consequences of which may be non-uniqueness of the solutions to the problem of identifying the physical properties of cartilage. It is important to assess the capability of ANN in estimating the diffusion coefficient in the cases where, similar to the case of large deformations, strong nonlinearity is present. Handling non-uniqueness is one of the challenging tasks for ANNs because non-uniqueness in the training data may confuse the training process of ANN and make it difficult for the ANN to find even one of the (non-unique) solutions of the problem.

The present study has several limitations. First, cartilage was modeled as a laterally isotropic material, although it is intrinsically an anisotropic material mainly due to spatial differences in terms of collagen fiber distribution/orientation. The molecular size has been shown to influence the diffusion, however, its effect could not be considered by the software used in this study. These limitations are, however, the intrinsic limitations of the full computational model which is used for training the forward and inverse ANNs. Should these limitations be remedied in the full computational model, it is expected that their correction can be

reflected in the proposed approach simply by using training data that are generated using the improved finite element model.

In summary, a novel algorithm combining inverse and forward ANNs was proposed to estimate the diffusion coefficient of the various zones of cartilage based on multi-physics model. The diffusion coefficients obtained using the proposed approach were found to be similar to the ones obtained using the conventional approach of combining full multi-physics computational models and optimization algorithms. This approach, however, has an important advantage as compared to the conventional approaches: researchers and labs without computational modeling expertise can use it effortlessly, although it should be noted that the methodology of this work urges for initial FEM expertise but once established for a specific tissue type e.g. equine cartilage with similar morphology, no further computational skill will be required. The proposed algorithm comprising of inverse-forward ANNs which could cancel out the input data noise (inverse-ANN) and eliminate the need for FEM expertise (forward-ANN) as much as possible could be used for similar biomechanical applications.

4.5. REFERENCES

1. Leddy H.A., Guilak F., *Site-specific effects of compression on macromolecular diffusion in articular cartilage.* Biophys J, 2008. **95**(10): p. 4890-5.
2. Arbabi V., Pouran B., Weinans H., Zadpoor A.A., *Transport of Neutral Solute Across Articular Cartilage: The Role of Zonal Diffusivities.* Journal of Biomechanical Engineering, 2015. **137**(7): p. 071001-071001.
3. Huttunen J.M.J., Kokkonen H.T., Jurvelin J.S., Töyräs J., Kaipio J.P., *Estimation of fixed charge density and diffusivity profiles in cartilage using contrast enhanced computer tomography.* International Journal for Numerical Methods in Engineering, 2014. **98**(5): p. 371-390.
4. Kokkonen H.T., Jurvelin J.S., Tiitu V., Toyras J., *Detection of mechanical injury of articular cartilage using contrast enhanced computed tomography.* Osteoarthritis Cartilage, 2011. **19**(3): p. 295-301.
5. Ko Lok S., Quinn Thomas M., *Matrix Fixed Charge Density Modulates Exudate Concentration during Cartilage Compression.* Biophysical Journal, 2013. **104**(4): p. 943-950.
6. Pouran B., Arbabi V., Zadpoor A.A., Weinans H., *Isolated effects of external bath osmolality, solute concentration, and electrical charge on solute transport across articular cartilage.* (Under review), 2016.
7. Jackson A., Gu W., *Transport Properties of Cartilaginous Tissues.* Curr Rheumatol Rev, 2009. **5**(1): p. 40.
8. Pan J., Wang B., Li W., Zhou X., Scherr T., Yang Y., Price C., Wang L., *Elevated cross-talk between subchondral bone and cartilage in osteoarthritic joints.* Bone, 2012. **51**(2): p. 212-7.
9. Pan J., Zhou X., Li W., Novotny J.E., Doty S.B., Wang L., *In situ measurement of transport between subchondral bone and articular cartilage.* J Orthop Res, 2009. **27**(10): p. 1347-52.
10. Kokkonen H.T., Mäkelä J., Kulmala K.A.M., Rieppo L., Jurvelin J.S., Tiitu V., Karjalainen H.M., Korhonen R.K., Kovanen V., Töyräs J., *Computed tomography detects changes in contrast agent diffusion after collagen cross-linking typical to natural aging of articular cartilage.* Osteoarthritis and Cartilage, 2011. **19**(10): p. 1190-1198.
11. Ateshian G.A., Albro M.B., Maas S., Weiss J.A., *Finite element implementation of mechanochemical phenomena in neutral deformable porous media under finite deformation.* J Biomech Eng, 2011. **133**(8): p. 081005.
12. Ateshian G.A., Maas S., Weiss J.A., *Solute transport across a contact interface in deformable porous media.* Journal of Biomechanics, 2012. **45**(6): p. 1023-1027.
13. Crank J., *The mathematics of diffusion.* Clarendon Press:, Oxford, Eng:, 1979.
14. Arbabi V., Pouran B., Campoli G., Weinans H., Zadpoor A.A., *Determination of the mechanical and physical properties of cartilage by coupling poroelastic-based finite element models of indentation with artificial neural networks.* Journal of Biomechanics, 2016. **49**(5): p. 631-637.
15. Campoli G., Weinans H., Zadpoor A.A., *Computational load estimation of the femur.* J Mech Behav Biomed Mater, 2012. **10**: p. 108-19.

16. Zadpoor A.A., Campoli G., Weinans H., *Neural network prediction of load from the morphology of trabecular bone.* Applied Mathematical Modelling, 2012. **37**(7): p. 5260-5276.
17. Oh S.E., Choi A., Mun J.H., *Prediction of ground reaction forces during gait based on kinematics and a neural network model.* Journal of Biomechanics, 2013. **46**(14): p. 2372-2380.
18. Hahn M.E., Farley A.M., Lin V., Chou L.-S., *Neural network estimation of balance control during locomotion.* Journal of Biomechanics, 2005. **38**(4): p. 717-724.
19. Darling E.M., Guilak F., *A neural network model for cell classification based on single-cell biomechanical properties.* Tissue Eng Part A, 2008. **14**(9): p. 1507-15.
20. Arbabi V., Pouran B., Campoli G., Weinans H., Zadpoor A.A., *Determination of the mechanical and physical properties of cartilage by coupling poroelastic-based finite element models of indentation with artificial neural networks.* Journal of biomechanics, 2015.
21. Nair N., Kim W.J., Braatz R.D., Strano M.S., *Dynamics of surfactant-suspended single-walled carbon nanotubes in a centrifugal field.* Langmuir, 2008. **24**(5): p. 1790-5.
22. Sophia Fox A.J., Bedi A., Rodeo S.A., *The Basic Science of Articular Cartilage: Structure, Composition, and Function.* Sports Health, 2009. **1**(6): p. 461-468.
23. Derks E.P.P.A., Pauly B.A., Jonkers J., Timmermans E.A.H., Buydens L.M.C., *Adaptive noise cancellation on inductively coupled plasma spectroscopy.* Chemometrics and Intelligent Laboratory Systems, 1997. **39**(2): p. 143-159.
24. Zur R.M., Jiang Y., Pesce L.L., Drukker K., *Noise injection for training artificial neural networks: a comparison with weight decay and early stopping.* Med Phys, 2009. **36**(10): p. 4810-8.
25. Ateshian G.A., Maas S., Weiss J.A., *Multiphasic Finite Element Framework for Modeling Hydrated Mixtures With Multiple Neutral and Charged Solutes.* Journal of Biomechanical Engineering, 2013. **135**(11): p. 111001-111001.
26. C. M. Bishop, *Neural Networks for Pattern Recognition.* Oxford University Press, New York, 1995.
27. Mauck R.L., Hung C.T., Ateshian G.A., *Modeling of Neutral Solute Transport in a Dynamically Loaded Porous Permeable Gel: Implications for Articular Cartilage Biosynthesis and Tissue Engineering.* Journal of biomechanical engineering, 2003. **125**(5): p. 602-614.
28. Entezari V., Bansal P.N., Stewart R.C., Lakin B.A., Grinstaff M.W., Snyder B.D., *Effect of mechanical convection on the partitioning of an anionic iodinated contrast agent in intact patellar cartilage.* J Orthop Res, 2014. **32**(10): p. 1333-40.

Appendix

MATLAB script

This MATLAB code is developed to create noisy indentation data (reaction force: finite element model in ABAQUS) with different levels of noise as the input. The artificial neural network is trained using then input and mechanical and physical properties as the target. Then the mechanical and physical properties of a poroelastic material can be determined using the trained artificial neural network.

Mechanical and physical properties: elastic modulus (MPa), Poisson's ratio, Permeability (mm4/N.s), friction coefficient

```
load input.txt % A matrix (10000*121) consisting of reaction force data (FEM)
at 121 time points
load target.txt% A matrix (10000*4) consisting of mechanical and physical
properties

%%%%%%%%%%%%%%%%%%%%%%%%%%%%%%%%%%%%%
%
% Contamination of data with noise

% By tuning lambda different levels of noise can be produced
lambda=100; % Please insert a value for lambda
for k=1:10000
    for l=1:121
        input_lambda(k,l)=input(k,l)+normrnd(0,input(k,l)/lambda);
    end
end
save input_lambda.txt input_lambda -ASCII
%%%%%%%%%%%%%%%%%%%%%%%%%%%%%%%%%%%%%
%%%

%%%%%%%%%%%%%%%%%%%%%%%%%%%%%%%%%%%%%
%%%
% Training, validation and test of the artificial neural network
```

```
% This script assumes these variables are defined:
%   input_lambda - input data.
%   target - target data.

x = input_lambda';
t = target';

% Create a Fitting Network
hiddenLayerSize = 40;
net = fitnet(hiddenLayerSize);

% Choose Input and Output Pre/Post-Processing Functions
% For a list of all processing functions type: help nnprocess
net.input.processFcns = {'removeconstantrows','mapminmax'};
net.output.processFcns = {'removeconstantrows','mapminmax'};



% Setup Division of Data for Training, Validation, Testing
% For a list of all data division functions type: help nndivide
net.divideFcn = 'dividerand';  % Divide data randomly
net.divideMode = 'sample';  % Divide up every sample
net.divideParam.trainRatio = 90/100;
net.divideParam.valRatio = 5/100;
net.divideParam.testRatio = 5/100;

% For help on training function 'trainlm' type: help trainlm
% For a list of all training functions type: help nntrain
net.trainFcn = 'trainlm';  % Levenberg-Marquardt

% Choose a Performance Function
% For a list of all performance functions type: help nnperformance
net.performFcn = 'mse';  % Mean squared error

% Choose Plot Functions
% For a list of all plot functions type: help nnplot
net.plotFcns = {'plotperform','plottrainstate','ploterrhist', ...
  'plotregression', 'plotfit'};
```

```
% Train the Network
[net,tr] = train(net,x,t);

% Test the Network
y = net(x);
e = gsubtract(t,y);
performance = perform(net,t,y)

% Recalculate Training, Validation and Test Performance
trainTargets = t .* tr.trainMask{1};
valTargets = t  .* tr.valMask{1};
testTargets = t  .* tr.testMask{1};
trainPerformance = perform(net,trainTargets,y)
valPerformance = perform(net,valTargets,y)
testPerformance = perform(net,testTargets,y)

% View the Network
view(net)

% Plots
% Uncomment these lines to enable various plots.
%figure, plotperform(tr)
%figure, plottrainstate(tr)
%figure, plotfit(net,x,t)
%figure, plotregression(t,y)
%figure, ploterrhist(e)

% Deployment
% Change the (false) values to (true) to enable the following code blocks.
if (false)
  % Generate MATLAB function for neural network for application deployment
  % in MATLAB scripts or with MATLAB Compiler and Builder tools, or
simply
  % to examine the calculations your trained neural network performs.
  genFunction(net,'myNeuralNetworkFunction');
  y = myNeuralNetworkFunction(x);
end
```

```
if (false)
  % Generate a matrix-only MATLAB function for neural network code
  % generation with MATLAB Coder tools.
  genFunction(net,'myNeuralNetworkFunction','MatrixOnly','yes');
  y = myNeuralNetworkFunction(x);
end
if (false)
  % Generate a Simulink diagram for simulation or deployment with.
  % Simulink Coder tools.
  gensim(net);
end
save
%%%%%%%%%%%%%%%%%%%%%%%%%%%%%%%%%%%%%
%%%

%%%%%%%%%%%%%%%%%%%%%%%%%%%%%%%%%%%%%
%%%
% Obtaining mechanical and physical properties using noisy reaction force data

load reaction_force.txt % A matrix (1*121) consisting of reaction force at 121
time points
output_lambda=sim(net,reaction_force)
%%%%%%%%%%%%%%%%%%%%%%%%%%%%%%%%%%%%%
%%%
```

CHAPTER 5

ISOLATED EFFECTS OF EXTERNAL BATH OSMOLALITY, SOLUTE CONCENTRATION, AND ELECTRICAL CHARGE ON SOLUTE TRANSPORT ACROSS ARTICULAR CARTILAGE*

*This chapter is submitted as a scientific paper:

Pouran B., Arbabi V., Zadpoor A.A., Weinans H. *Isolated effects of external bath osmolality, solute concentration, and electrical charge on solute transport across articular cartilage.* 2016 (under review).

ABSTRACT

The metabolic function of cartilage primarily depends on transport of solutes through diffusion mechanism. In the current study, we use contrast enhanced micro-computed tomography to determine equilibrium concentration of solutes through different cartilage zones and solute flux in the cartilage, using osteochondral plugs from equine femoral condyles. Diffusion experiments were performed with two solutes of different charge and approximately equal molecular weight, namely iodixanol (neutral) and ioxaglate (charge = -1) in order to isolate the effects of solute charge on diffusion. Furthermore, solute concentrations as well as bath osmolality were changed to isolate the effects of steric hindrance on diffusion. Bath concentration and bath osmolality only had minor effects on the diffusion of the neutral solute through cartilage at the surface, middle and deep zones, indicating that the diffusion of the neutral solute was mainly Fickian. The charged solute diffused considerably slower through cartilage than the neutral solute, indicating a large non-Fickian contribution in the diffusion of charged molecules. The numerical models determined maximum solute flux in the superficial zone up to a factor of 2.5 lower for the negatively charged solutes (charge= -1) as compared to the neutral solutes confirming the importance of charge-matrix interaction in diffusion of molecules across cartilage.

5.1. INTRODUCTION

Articular cartilage is an avascular tissue with highly inhomogeneous organization that lines the end of long bones and enables low-friction joint mobility [1, 2]. The avascular nature of articular cartilage means that it has to rely mainly on diffusion for transport of vital signaling molecules, nutrients and oxygen. Cyclic loading and the associated fluid flow augment the transport of large molecules through an additional transport mechanism, namely convection [3-5]. Transport of small solutes such as ions, however, cannot be significantly amplified via convection [5]. Extracellular matrix (ECM) of cartilage consists mostly of collagen type II, proteoglycans (PGs) and water. Fragments of PG and collagen type II are continuously transported within ECM as a result of enzymatic digestion and remodeling. Collagen type II and PGs account for the major components of cartilage that provide the ECM with its shear and tensile properties as well as with resilience [2, 6]. Articular cartilage is characterized by a zonal architecture where water content, as the major parameter influencing solute diffusion, varies from 80% in the superficial layer to 60% in the deep layer [7-10]. The orientation, thickness, and concentration of collagen type II fibrils together with uneven distribution of PGs in various zones of articular cartilage play significant roles in the solute diffusion across the tissue [1, 11]. Solute diffusion depends predominantly on the nature of the interaction that can vary as a consequence of different density and morphology of the tissue at the molecular level (steric hindrance) and ion-ion interactions. The latter is believed to take place when the solute is charged and thereby repulsion/attraction interaction with the negatively fixed charges of the glycosaminoglycans chains (GAGs) is dominant [12-14]. The combined effects of electric phenomena with the steric hindrance make the diffusion process across the articular cartilage extremely complicated.

To better understand the above-mentioned complexities in the transport of solutes across cartilage, the current study aims to separate the various physical mechanisms as much as possible by using a carefully designed set of diffusion experiments and associated finite element modeling.

First, we address the question whether the solute transport in cartilage has a Fickian nature. This would be the case if the concentration-time curves remain unchanged for different levels of osmolality and different levels of solute concentration in case the solute molecules are non-charged. Osmolality difference between bath and cartilage deforms the cartilage and consequently alters the molecular morphology and thus the interaction between the solute and the extracellular matrix that causes deviation from Fickian diffusion. For instance, it has been shown that Fickian models could poorly predict the diffusion of cryoprotective agent (CPA) through articular cartilage primarily due to local osmolality variation within the extracellular matrix [15].

Second, we address the contribution of electrical charges to the transport of solutes across cartilage. In the majority of previous studies, the charged solute's diffusion attributes have been obtained by adopting Fickian-based models [16-18]. Answering the second research question allows us to quantify the effect of this simplification on the accuracy of determined solute fluxes and the described diffusion behavior. We therefore not only isolate the effects of external bath osmolality, concentration and charge from each other but also quantify those effects using equilibrium curves and zonal concentration curves as well as solute fluxes. The present study features a unique experimental approach through which the aforementioned effects could be separated. Moreover, biphasic-solute and multiphasic models [9, 19] that we had previously developed have been used to determine solute fluxes.

5.2. MATERIALS AND METHODS

5.2.1. SAMPLE HARVEST AND CONDITIONING

Equine knees for this study were obtained from the Equine Clinic in Utrecht University (approved by *Animal Experiments Committee in Utrecht University*). Using a custom-made hollow drill bit, four osteochondral plugs (8.5 mm diameter, cartilage thickness = 2.57±0.27 mm) were harvested from the medial femoral condyle of two 6-year old equine femurs (samples 1 and 2 from one donor and samples 3 and 4 from the other). To prevent sample overheating and to keep the drilling site moist during drilling, we continuously sprayed phosphate buffer saline (*PBS, 290 mOsmol/kg H_2O, pH=7.4, Life technologies*) on the drilling site. We stored the osteochondral plugs in a large bath of a solution comprising PBS, protease inhibitors (*cOmplete tablets, EDTA free, Roche, Netherlands*) and 5 mM Ethylenediaminetetraacetic acid (EDTA) at -20 °C before the diffusion experiments. Upon thawing, the samples were tightly wrapped laterally using heat-shrinking sleeves to prevent lateral contrast agent leakage (Figure 5.1). The sample was protected from heat during heat-shrinking process by optimizing the heat source distance from the sample, constantly spraying cold PBS on the sample surface, and mounting small wet cotton pieces on the boundaries.

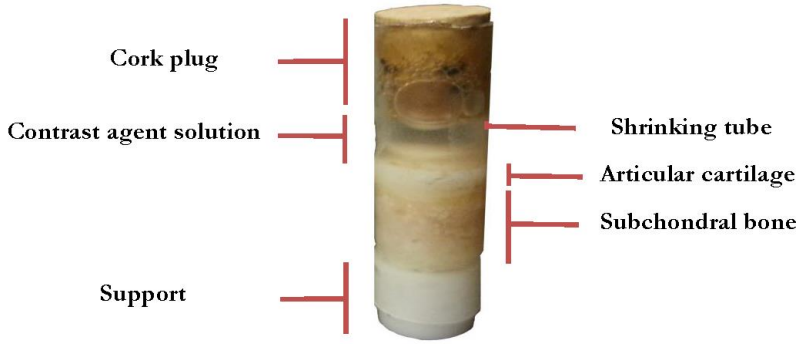

Figure 5.1. The sample consists of an osteochondtal plug, a cork plug, a shrinking tube, contrast agent solution and a support.

5.2.2. CONTRAST AGENT SOLUTIONS

The transport of two clinical contrast agents with similar molecular weights was investigated: iodixanol (*Visipaque, 1550 g/mol, charge=0, GE Healthcare, Netherlands*) and ioxaglate (*Hexabrix, 1269 g/mol, charge=-1, GE Healthcare, Netherlands*). In order to study the effects of bath concentration, osmolality, and electrical charge on solute transport, we prepared four different contrast agent baths (Table 5.1). We adjusted the osmolality of each solution at the required level by adding sodium chloride. Enzymatic digestion was prevented during the diffusion experiments through the addition of protease inhibitors (*cOmplete, Roche, Netherlands*) and EDTA to the baths. A freezing point osmometer (*Advanced® Model 3320 Micro-Osmometer, Netherlands*) was used to measure osmolalities.

5.2.3. CECT IMAGING

We placed the wrapped samples on a custom-made holder and fixed the holder inside micro-CT (*Quantum FX, Perkin Elmer, USA*). In each condition, we loaded approximately 650 µL from

Table 5.1. Specification of the baths used in the diffusion experiments: Four different bath conditions were used to investigate the effects of concentration (*Iodix 320,290* vs. *Iodix 160,290*), external bath osmolality (*Iodix 320,290* vs. *Iodix 320,600*) and solute's charge (*Iodix 320,600* vs. *Ioxag 320,600*) on the diffusion in cartilage.

Bath	Solute	Charge	Concentration (mgI/ml)	Osmolality ($mOsm/kg\ H_2O$)
*Iodix 320,290**	Iodixanol	0	320	290
*Iodix 320,600**	Iodixanol	0	320	600
*Iodix 160,290**	Iodixanol	0	160	290
*Ioxag 320,600**	Ioxaglate	-1	320	600

* The conditions are described by their abbreviated solute name (iodixanol (*Iodix*) and ioxaglate (*Ioxag*)), solute concentration in the bath and bath's osmolality.

the baths onto the cartilage surface. A cork plug and proper micro-CT chamber humidification were used to minimize solution evaporation during micro-CT scans (Figure 5.1). We scanned the samples at room temperature using micro-CT under a tube current of 180 μA and a tube voltage of 90 kV, resulting in a scan time of 2 min and a voxel size of 40×40×40 μm^3. The resolution was chosen such that the field of view included the cartilage specimen, the contrast agent bath, and the subchondral bone. We acquired images during diffusion process at time points t_{-1} (before adding the bath), $t_{\_0}$ (bath injection), t= 5, 10, 30 min and t= 1, 2, 3, 4, 5, 7, 10, 12, 24 and 48 hours. When the experiment on every specimen was finished using one bath and before starting a new experiments with another bath (Figure 5.2), we washed the osteochondral plugs in series of large desorption baths [20] (*PBS+protease inhibitor+EDTA* (5mM) for 48 hours (4 °C) which proved to be effective (less than 5% difference between the gray values). The average grey values for each sample and each condition were recorded at $t_{\_0}$ to make sure of the efficacy of the

contrast agent washout process. The equilibrium concentration of ioxaglate (inversely related to GAG content [21]) did not vary after performing the aforementioned experiments during our pilot studies suggesting no cartilage degeneration (data not shown). Furthermore, the remaining of each bath was tested after each experiment to search for any clues of GAG leakage using Dimethylmethylene Blue assay (DMMB), which proved no visual sign of GAG loss.

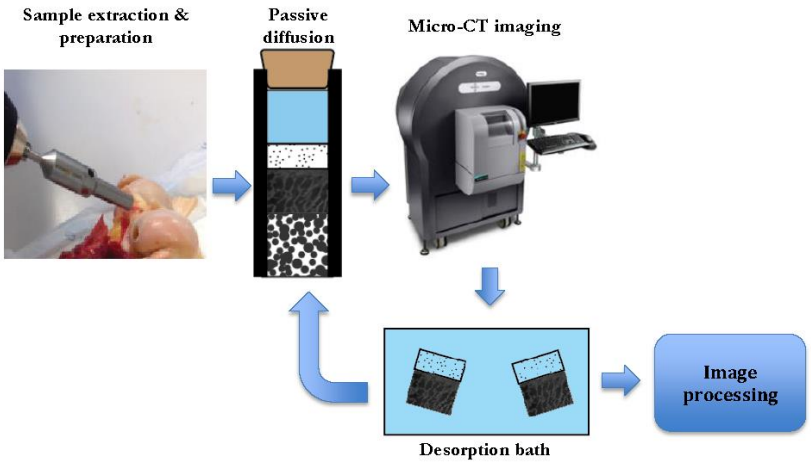

Figure 5.2. Flowchart of the experimental setup: Osteochondral plugs from the fresh equine femoral condyles were extracted. The osteochondral plugs were mounted on a support while being wrapped using a shrinking tube. Passive diffusion experiments were conducted in a micro-CT chamber. Immediately after each experiment the samples underwent serial desorption process within large baths before start of the next experiment.

5.2.4. IMAGE ACQUISITION AND PRE-PROCESSING

Image acquisition included 3D image reconstruction that was undertaken automatically using the built-in micro-CT software. The 3D files were transferred to Anlayze 11.0 (*Perkin elmer, USA*)

to convert them to a sequence of 2D images (*TIFF* format). The images underwent noise removal using 3D Gaussian filter (*ImageJ, 1.47v*).

5.2.5. EQUILIBRIUM CURVES

We then exported the 2D image sequences to ImageJ (*ImageJ, 1.47v*) to process the images. The mid-sagittal slice that included cartilage, contrast agent, and subchondral bone was chosen as the representative image to study the transport of contrast agent molecules across cartilage. Our earlier calculations suggest that mid-sagittal slice can act as a representative slice and therefore we restricted our analyses to a single mid-sagittal slice. We applied a rectangular region of interest (ROI) (width = 5.6 mm) to all mid-sagittal images at every time point. The cartilage was segmented from the contrast agent bath and subchondral bone by global thresholding. This allowed for generation of cartilage masks that could be used to create another ROI that precisely outlined the cartilage. We overlaid this ROI onto the corresponding original images to evaluate the average grey values (Q). The average grey values were then calculated using the following formula:

$$\mathrm{Q} = \frac{\sum P_i X_i}{\sum X_i} \tag{1}$$

where P_i and X_i are the pixel intensity and frequency, respectively.

We used an experimentally confirmed linear relationship between the grey value of the cartilage at $t = 0$ and that of the contrast agent bath and their corresponding concentrations to obtain the actual solute concentration within cartilage:

$$C = \alpha Q + \beta \tag{2}$$

where C is the solute concentration, Q is the average grey value and α and β are constants.

5.2.6. IMAGE REGISTRATION

To obtain the zonal diffusion curves, we performed elastic (i.e. deformable) image registration, which accounted for small elastic deformations in the cartilage as observed in our experiments (8±2.55 % of the total cartilage thickness) and spatial movements during the diffusion process. We registered the images using the *Elastix* package (*University Medical Center Utrecht, Netherlands*) [22, 23]. Two images were required to perform the registration process, a moving image and a fixed image. Images at t = 0 minutes for each bath condition (Table 5.1) were selected as the fixed images while images at t = 1, 6, 12, 24, 30 and 48 hours were selected as the moving images to which the ROIs for the zonal equilibrium curves will be assigned. Registration is mathematically formulated as an optimization problem where the cost function has to be minimized with respect to T to achieve the optimal transformation [22]. T is the image transformation matrix which is given as:

$$T(x) = x + u(x) \tag{3}$$

where $u(x)$ is the translation vector.

Elastix software limits the amount of possible transformations by introducing a parameterization of the transformation. Eventually, we examined the accuracy of the registration process through checking the location of a few fixed points on the cartilage-bath and cartilage-subchondral bone interfaces using MeVisLab (*MeVis Medical Solutions AG, Bremen, Germany*) (Figure 5.3).

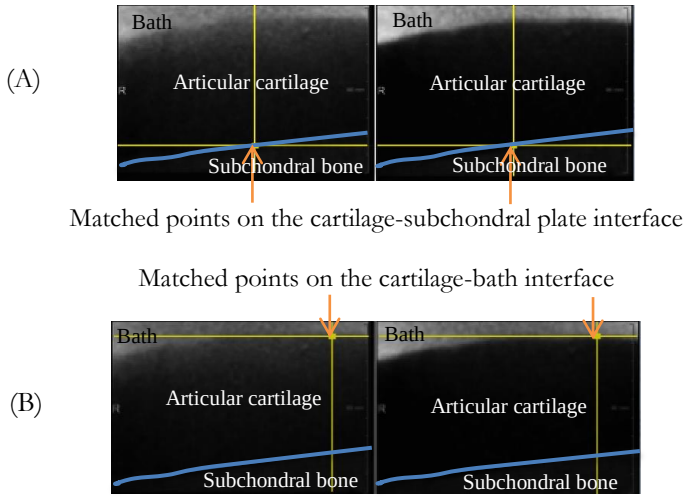

Figure 5.3. Visual inspection of the registration outcome using *MeVisLab*. Random points on the (A) cartilage-subchondral bone interface (blue line) and (B) cartilage-bath interface were selected to visually inspect whether the points in the fixed and the registered image matched.

5.2.7. ZONAL DIFFUSION CURVES

Articular cartilage can be considered to comprise three major zones, i.e. superficial, middle, and deep zones [7, 24-26]. Zonal diffusion curves can therefore be obtained to provide a more detailed description of diffusion and equilibrium concentration in each individual zone. Zonal diffusion curves were generated based on the previously registered images at 0, 1, 6, 12, 24 and 48 hours. The first step was to determine the thickness of cartilage at $t = 0$ for each sample using *BoneJ* (plugin of *imageJ*). Then, for each image, cartilage was divided into three different zones: superficial (20% of cartilage thickness), middle (50% of cartilage thickness), and deep zone (30% of cartilage thickness) [7]. Thereafter, *ImageJ* was used to cover the superficial, middle, and deep zones separately, thereby generating three new ROIs corresponding to

each zone. Those ROIs were applied to the registered images at 0, 1, 6, 12, 24 and 48 hours to obtain the average grey values. The average grey values were converted to concentration values using a similar approach as described in equilibrium curves. The normalized concentrations were then obtained by dividing the concentration values by the initial bath concentration.

Since solute flux is the rate of solute transport per unit area, we used multi-zone biphasic-solute and multiphasic models to curve-fit the concentration-time data followed by plotting the solute flux versus time in the middle of the superficial zone (20% of cartilage thickness) in each sample to compare the transport of neutral (*Iodix 320,600*) and charged (*Ioxag 320,600*) solutes in cartilage. The models [9, 27, 28] included the solid phase, the fluid phase, and the solutes and could describe the interactions of the solid matrix and the fluid and solute phases. Physical phenomena such as water exodus and return, cartilage swelling, electric interactions (ioxaglate) and the deformations of the solid phase caused by osmolality shocks and water transport were therefore taken into account [9, 27]. The model consisted of a finite bath (≈14 mm) and a cartilage that resembled the experimental setup. The diffusion was restricted to occur only through the surface of the cartilage (axial diffusion) while the cartilage-subchondral bone interface was prescribed as a no-flux boundary condition. The initial concentration of the solute in the cartilage was set to zero. The model was fitted to the equilibrium curves and the solute flux curves were subsequently plotted.

5.2.8. Statistical Analysis

Two-factor ANOVA statistical analysis was used to determine the statistical significance of the normalized concentrations at 48 hours in the equilibrium curves as well as in the zonal diffusion curves. A significance threshold of $p < 0.05$ was used. It should be noted

though that the aim of this chapter is to address the effects of external bath osmolality, solute concentration as well as solute's charge on the transport within each sample, thereby those effects should be studied in each sample separately.

5.3. RESULTS

Changes in bath concentration and osmolality may cause local deformation in cartilage matrix and mass transfer resistance at the bath-cartilage interface, which consequently alter solute-matrix interactions through steric hindrance mechanism. On the other hand, strong solute charge-matrix charge interactions affect the diffusion and make it deviate from Fickian behavior. Here we study these interactions with the aid of equilibrium curves, zonal diffusion curves and solute flux curves.

5.3.1. EQUILIBRIUM CURVES

The near-equilibrium state was reached approximately 24 hours after the start of the experiments (Figure 5.4). The effect of bath solute concentration on diffusion was assessed by comparing the equilibrium curves of bath *Iodix 320,290* and *Iodix 160,290* that represent the diffusion of iodixanol at different solute concentrations but with the same osmolality. The normalized concentrations (% initial bath concentration) for both baths *Iodix 320,290* and *Iodix 160,290* were very close to each other (Table 5.2A). For the early time points, *Iodix 160,290* showed a steeper slope compared to *Iodix 320,290* indicating a faster diffusion rate (Figure 5.4).

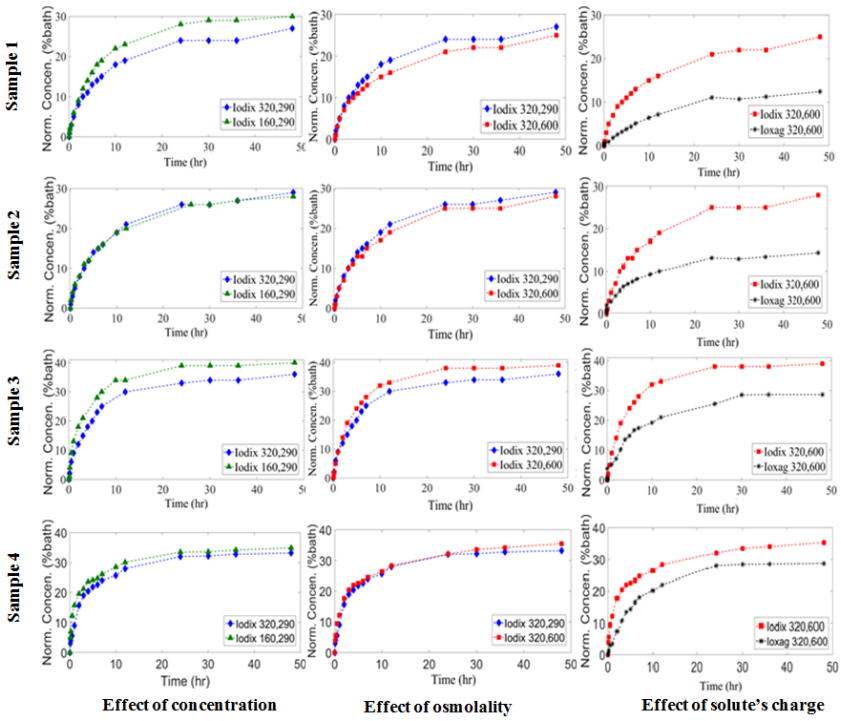

Figure 5.4. Plot of normalized concentration (% initial bath concentration) vs. time for the full thickness of the cartilage for samples 1-4. Slight difference for the effect of bath concentration (*Iodix 320,290 & Iodix 160,290*) and bath osmolality (*Iodix 320,290 & Iodix 320,600*) can be observed whereas effect of solute's charge is more pronounced (*Iodix 320,600 & Ioxag 320, 600*).

Table 5.2. Solute's equilibrium concentrations. Effect of bath concentration on the solute transport was investigated by comparing normalized final concentration value in finite baths *Iodix 320,290* and *Iodix 160,290*. Effect of bath osmolality on the solute transport was investigated by comparing normalized final concentration value in finite baths *Iodix 320,290* and *Iodix 320,600*. Effect of solute's charge on the solute transport was investigated by comparing normalized final concentration value in finite baths *Iodix 320,600* and *Ioxag 320,600* (A). Final normalized concentrations in the superficial, middle and deep zones (B).

(A)

Condition	*Iodix 320,290**	*Iodix 160,290**	*p-value*	*Iodix 320,290**	*Iodix 320,600**	*p-value*	*Iodix 320,600**	*Ioxag 320,600**
Concentration (*mgI/ml*)	33.7±5.9	33±6.1	0.082	33.7±5.9	30.7±7.4	0.133	30.7±7.4	18.3±9.3

(B)

	Condition		*p*-value	Condition		*p*-value	Condition		*p*-value
	*Iodix 320,290**	*Iodix 160,290**		*Iodix 320,290**	*Iodix 320,600**		*Iodix 320,600**	*Ioxag 320,600**	
Superficial concen. (*mgI/ml*)	57.58±1.37	54.25±4.98	0.374	57.58±1.37	61.4±6.98	0.422	61.4±6.98	52.18±6.75	0.00008
Middle concen. (*mgI/ml*)	30.55±5.31	32.44±5.21	0.435	30.55±5.31	31.57±5.99	0.987	31.57±5.99	25.37±4.61	0.00838
Deep concen. (*mgI/ml*)	16.62±2.78	19.48±3.20	0.051	16.62±2.78	17.17±5.25	0.099	17.17±5.25	11.80±3.42	0.02731

*The conditions are described by their abbreviated solute name (iodixanol (*Iodix*) and ioxaglate (*Ioxag*)), solute's concentration in the bath and bath's osmolality.

The effect of osmolality on diffusion was assessed by comparing the equilibrium curves of *Iodix 320,290* and *Iodix 320,600* that represent the diffusion of iodixanol at different osmolalities but with the same concentration. In this experiment, the different osmolalities (hypo- and hyper-osmolal) will lead to differences in expansion and as a consequence the diffusion can deviate from Fickian through potential effects of steric hindrance. Fickian diffusion would require identical diffusion curves for the two conditions. For both conditions, the near-equilibrium state was reached at 24 hours (Figure 5.4). On average, the difference between these two conditions was very small.

We further investigated the effects of charge and consequently non-Fickian solute diffusion across articular cartilage by comparing the normalized concentration curves between *Iodix 320,600* and *Ioxag 320,600*. These conditions represented the same contrast agent concentration and osmolality, but different solute charges. Similar to the previous situations, for both conditions, the near-equilibrium state was reached at 24 hours (Figure 5.4). The diffusion rate in *Iodix 320,600* was considerably higher than that of *Ioxag 320,600* particularly in the very early time points (Figure 5.4). Moreover, the equilibrium normalized concentrations in *Iodix 320,600* were markedly higher than those in *Ioxag 320,600* (*p-value=0.006*, Table 5.2A), which indicate a fairly large non-Fickian aspect in the diffusion.

5.3.2. ZONAL DIFFUSION CURVES

The superficial zone represents the highest values of normalized concentrations (Figure 5.5A). Solute transport rate was found to be the highest in the superficial layer for all conditions. However, it approached the near-equilibrium state shortly after the onset of the experiments (Figure 5.5A).

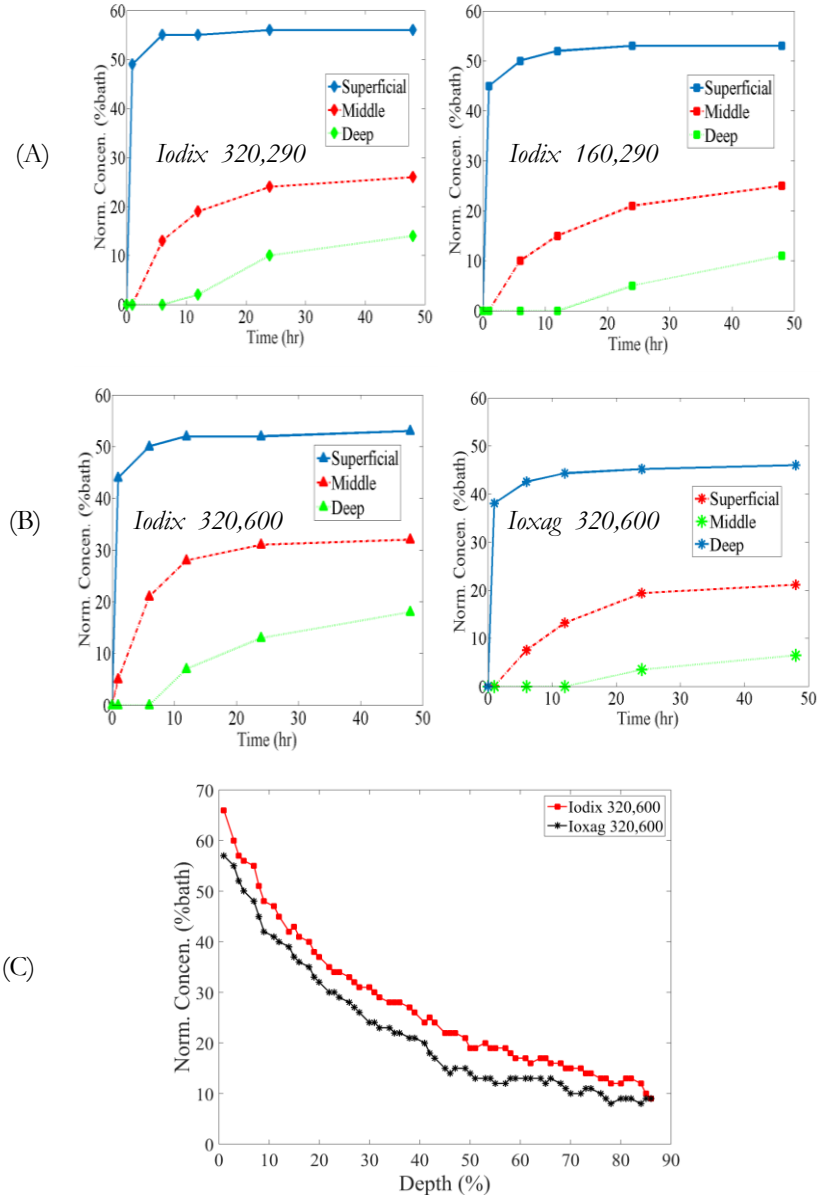

Figure 5.5. (A) Plot of normalized concentration vs. time in the superficial, middle and deep zones (example, sample 1). For all different conditions the concentration values are lower in the deep zones. In all zones effect of charge on the transport is tangible. (B) Plot of concentration vs. cartilage depth for *Iodix 320,600* and *Ioxag 320,600* to highlight the effect of charge on solute transfer (example, sample 1).

To address the effect of concentration on diffusion, resulting curves for *Iodix 320,290* and *Iodix 160,290* were compared. The diffusion rate was similar between *Iodix 320,290* and *Iodix 160,290* but the deep layer showed a larger difference (Figure 5.5A). In the superficial zone, the near-equilibrium state is reached for *Iodix 320,290* and *Iodix 160,290* after 6 hours (Figure 5.5A). Regardless of bath conditions, the equilibrium state is not reached for the middle or deep zones since the diffusion curves keep rising (Figure 5.5A). The equilibrium concentration was not significantly higher in *Iodix 160,290* within the deep zone compared to that in *Iodix 320,290* (*p-value>0.05*, Table 5.2B).

Effect of osmolality on diffusion was addressed by comparing resulting curves for *Iodix 320,290* and *Iodix 320,600*. Both *Iodix 320,290* and *Iodix 320,600* reached the near-equilibrium concentrations at 12 hours in the superficial zone (Figure 5.5A). The equilibrium concentrations in the superficial, middle and deep zones between *Iodix 320,290* and *Iodix 320,600* were not significantly different (*p-value>0.05*, Table 5.2B).

The effect of solute's charge on diffusion was studied by comparing *Iodix 320,600* and *Ioxag 320,600*. In all zones, the normalized concentration curve for *Ioxag 320,600* depicts significantly lower concentrations compared to those of *Iodix 320,600* (Figure 5.5, $p < 0.05$, Table 5.2B). However, the time point where each condition reaches near-equilibrium state was almost similar and was 12 hours (Figure 5.5A). The typical concentration versus cartilage depth curves at 48 hours showed also higher concentration of iodixanol (*Iodix 320,600*) compared to ioxaglate (*Ioxag 320,600*) (Figure 5.5B).

The solute flux for *Iodix 320,600* showed higher peak than that of *Ioxag 320,600* and the peak occurred in the early time points (Figure 5.6). The maximum flux of iodixanol was 0.0084 ± 0.0061

mmol/m^2.s, while that of ioxaglate was 0.0047±0.0031 mmol/m^2.s (p-value=0.185).

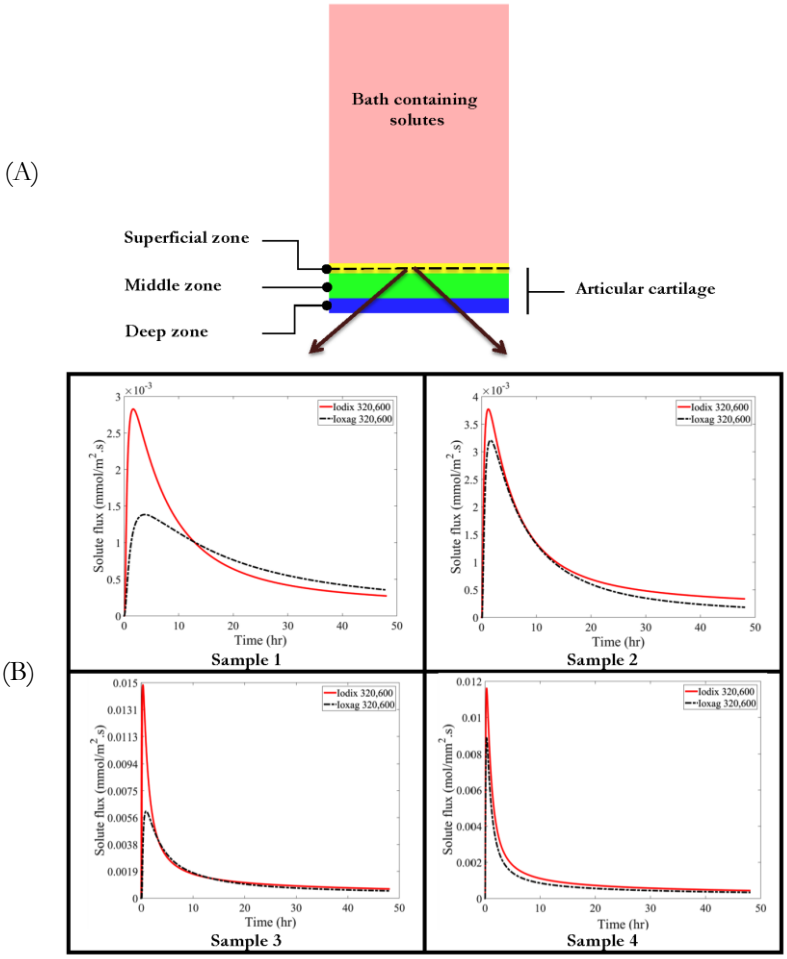

Figure 5.6. (A) Computational model representing bath containing either iodixanol or ioxaglate and articular cartilage comprising of superficial, middle and deep zones. (B) Plot of solute flux vs. time in the middle of superficial zone for both Iodixanol (*Iodix 320,600*) and Ioxaglate (*Ioxag 320,600*) for samples 1-4 to investigate the effect of charge on solute transport.

5.4. DISCUSSION

Multiple factors contribute simultaneously to the diffusion of solutes across cartilage. In this study, we strived to use a carefully designed set of experiments to separate the effects of three of those factors, namely bath concentration, bath osmolality and solute's charge, from each other. Exact Fickian diffusion should lead to exactly the same diffusion patterns for all experiments and deviation from this can be observed by comparing the various experiments. We used equilibrium and zonal diffusion curves as well as finite element models to study the effects of those factors.

5.4.1. EFFECT OF CONCENTRATION

Normalized concentration values as well as diffusion rates at early time points within cartilage were slightly higher in the bath with lower concentration (*Iodix 160,290*) compared to the more concentrated bath (*Iodix 320,290*) (Figure 5.4). Nevertheless, the final normalized values were largely similar regardless of concentration (Table 5.2A). Previous study showed insignificant effect of concentration on the diffusion mechanism using charged, i.e. anionic solutes [18].

Somewhat different behaviors in *Iodix 320,290* and *Iodix 160,290* are observed when the superficial, middle and deep zones are concerned (Figure 5.5A). That is associated with some mild differences between the final normalized concentration values of *Iodix 320,290* and *Iodix 160,290* in those zones (Table 5.2B). However, the final normalized concentration in all zones is not significantly different between *Iodix 160,290* and *Iodix 320,290* (Table 5.2B). It can be therefore concluded that while the main diffusion mechanism for neutral solutes is Fickian, some zonal deviations from the Fickian assumption can be pinpointed. The final normalized concentration values for the superficial zone were

observed to be higher compared to middle and deep zones for both *Iodix 320,290* and *Iodix 160,290* that refers to highly inhomogeneous nature of the articular cartilage. The major reason that leads to enhancement of diffusion rate in the superficial zone might be the sparse distribution of GAGs, high water content, and fine collagen fibers [1, 14, 29, 30]. A previous study, however, showed that collagen does not considerably affect the transport of small solutes because collagen fibrils are widely spaced in comparison to proteoglycans [31]. Relevant research also addressed the importance of various cartilage zones when determining the diffusion coefficient of cartilage. Indeed, up to 100 times higher diffusion coefficients were found in the superficial zone as compared to the deep cartilage zone [9, 24, 32]. The effects of concentration can also be viewed from the standpoint of more facilitated transport in low concentrated solutions due to lower mass transfer resistance in the cartilage-bath interface [33]. Furthermore, lower concentration might lead to lower solution viscosity that in turn enhances the transport rate within the bath and also in the cartilage-bath interface [34]. This underscores the fact that the solute diffusivity within the bath may need to be considered as a separate parameter to improve on the accuracy of previously conducted research [14, 16-18].

5.4.2. EFFECT OF OSMOLALITY

Equilibrium curves showed a subtle difference between *Iodix 320,290* and *Iodix 320,600* indicating that the effect of osmolality on the transport of neutral solutes is insignificant (Figure 5.4, Table 5.2A) and the diffusion therefore can be considered Fickian. The zonal differences between *Iodix 320,290* and *Iodix 320,600* were present but generally small (Figure 5.5 and Table 5.2B). Since we used a hyper-osmolal bath, cartilage shrank 8±2.55 % of its total thickness in the early time points due to water loss.

Thereafter, cartilage recovered to its original thickness, since increased ionic concentration in cartilage after initial water loss caused reversal of the water exodus. This could lead to a more compact structure of the ECM giving rise to increased solute-ECM friction and therefore hindered diffusion. However, water exodus stopped after a few hours and water gain started to maintain the equilibrium between the cartilage and the bath. This counteracts the previous hindrance phenomenon and can potentially nullify the reduced diffusion rate within the ECM. In spite of little effect of osmolality on diffusion of small molecules observed in this study, larger tissue deformation and its consequent local re-orientation of collagen fibrils as well as alterations of proteoglycans concentration is anticipated to change the cartilage diffusive attributes [1].

5.4.3. EFFECT OF CHARGE

Negatively charged fixed macromolecules, i.e. keratin sulfate and chondroitin sulfate, are the major components that give cartilage its excellent physical and mechanical features [35]. These highly charged molecules interact with the diffusing charged solutes, thereby introducing an additional mechanism that, together with steric hindrance, cause the diffusion process to deviate from the Fickian model. The last aim of this work was to study the effects of solute charge on the diffusion of solutes across articular cartilage. Equilibrium curves for *Iodix 320,600* showed considerably higher diffusion rate as well as higher final normalized concentration values as compared to *Ioxag 320,600* (Figure 5.4, Table 5.2A). Zonal diffusion curves also confirm the trends seen in the equilibrium curves (Figure 5.5A, Table 5.2B). Ioxaglate, as a negatively charged contrast agent, had the highest final normalized concentration in the superficial zone as compared to two other zones chiefly due to higher water content, less concentrated GAGs, and less interaction with the ECM in the

superficial zone. Moreover, the concentration versus cartilage depth at equilibrium for ioxaglate lied below that of iodixanol (Figure 5.5B) underscoring the effect of repulsion between two negatively charged molecules (PGs and ioxaglate) on the diffusion. The effect of proteoglycans on the diffusion of solutes even neutral ones rather than collagen has been confirmed due to their compact structure [36]. It is worth mentioning that the negatively charged ioxaglate solute has considerably slower diffusion rate and lower final normalized concentration, as compared to the neutral iodixanol solute (Figure 5.6 and Table 5.2). The two contrast agents used in this study had very similar molecular weights i.e. hydrodynamic radii and therefore it allowed studying the effect of charge while neglecting the effect of solute size on diffusion across cartilage.

Based on the prescribed experimental boundary conditions solute diffusion occurred primarily along the vertical axis of the cylindrical specimens and therefore the radial component of diffusion equations has been neglected in our models. Lower ioxaglate flux peak compared to that of iodixanol (Figure 5.6) indicates the restrictive effect of electric interactions between the negatively charged solute (ioxaglate) and negative fixed charges of articular cartilage. Furthermore, samples 3 and 4, which demonstrated lower GAG content compared to samples 1 and 2 (higher ioxaglate equilibrium penetration) showed higher maximum solute flux (Figure 5.4 and Figure 5.6). The findings of this study highlight the importance of electrical charge and show that the effects of electrical charge by far exceed those of other factors considered in the current study including solute concentration and external bath osmolality.

5.4.4. LIMITATIONS

This study introduces a few limitations associated with the experiments. Since the aim of this study was to investigate the

isolated effects of physical parameters on the diffusive transport in articular cartilage, four samples were randomly extracted from two different same-age equine femoral condyles, which enables drawing general conclusion regardless of the donor's joint. The sample size could be increased to enhance the power of the study; nevertheless, the aim was to create an experimental setup by which conclusions could be made while comparing conditions within each individual sample without further need to increase sample size. The time frame of the experiments was chosen to be 48 hours to ensure reaching the equilibrium state although this might slightly affect the GAG concentration within the tissue. To support that, our previous experiments using DMMB assay of the bath confirmed minimal GAG loss. The study of the effects of ionic strength and concentration of charged solutes in the bath on the diffusion process are proposed for the future studies. In this study, we used osteochondral plugs to ensure minimal damage to the cartilage constituents particularly collagen fibrils and proteoglycans. This allowed maintaining physiologic diffusion condition as faithfully as possible. In our computational model, we used a no-flux boundary condition at the cartilage-bone interface, which stayed valid within the timeframe of the experiments.

5.5. CONCLUSIONS

We investigated the isolated effects of solute concentration, external bath osmolality, and solute charge on the diffusion of solutes across articular cartilage. The main novelties of the study are in using the experiments that separate the effects of different factors from each other to the maximum possible extent and using zonal diffusion curves and computational models to study the diffusion behavior of the various cartilage zone, namely superficial, middle, and deep zones. It was observed that the concentration

and external bath osmolality do not significantly change the diffusion behavior of cartilage as a whole and the various cartilage zones. The diffusion mechanism of neutral solutes was therefore found to be Fickian in general with some zonal deviations from the Fickian model, thereby justifying the use of terms such as near-Fickian for describing the diffusion mechanism of neutral solutes across cartilage. Comparing the solute fluxes and the diffusion behavior of solutes with similar sizes but different charges (neutral versus negatively charged) showed that the maximum solute fluxes are significantly smaller for negatively charged solutes, indicating the profound effect of electrical charge on the diffusion behavior. The effects of electrical charge on the diffusion behavior were the same regardless of the cartilage zone under consideration.

5.6. ACKNOWLEDGMENT

This work was supported by a grant from Dutch Arthritis Foundation (13-3-406).

5.7. REFERENCES

1. Leddy H.A., Guilak F., *Site-Specific Molecular Diffusion in Articular Cartilage Measured using Fluorescence Recovery after Photobleaching.* Annals of Biomedical Engineering, 2003. **31**(7): p. 753-760.
2. Decker Sarah G.A., Moeini M., Chin Hooi C., Rosenzweig Derek H., Quinn Thomas M., *Adsorption and Distribution of Fluorescent Solutes near the Articular Surface of Mechanically Injured Cartilage.* Biophysical Journal, 2013. **105**(10): p. 2427-2436.
3. Ohara B.P., Urban J.P.G., Maroudas A., *Influence of Cyclic Loading on the Nutrition of Articular-Cartilage.* Annals of the Rheumatic Diseases, 1990. **49**(7): p. 536-539.
4. Evans R.C., Quinn T.M., *Dynamic compression augments interstitial transport of a glucose-like solute in articular cartilage.* Biophys J, 2006. **91**(4): p. 1541-7.
5. Jackson A., Gu W., *Transport Properties of Cartilaginous Tissues.* Curr Rheumatol Rev, 2009. **5**(1): p. 40.
6. Allhands R.V., Torzilli P.A., Kallfelz F.A., *Measurement of diffusion of uncharged molecules in articular cartilage.* Cornell Vet, 1984. **74**(2): p. 111-23.
7. Sophia Fox A.J., Bedi A., Rodeo S.A., *The Basic Science of Articular Cartilage: Structure, Composition, and Function.* Sports Health, 2009. **1**(6): p. 461-468.
8. Arkill K.P., Winlove C.P., *Solute transport in the deep and calcified zones of articular cartilage.* Osteoarthritis Cartilage, 2008. **16**(6): p. 708-14.
9. Arbabi V., Pouran B., Weinans H., Zadpoor A.A., *Transport of Neutral Solute Across Articular Cartilage: The Role of Zonal Diffusivities.* Journal of Biomechanical Engineering, 2015. **137**(7): p. 071001-071001.
10. Kock L., van Donkelaar C., Ito K., *Tissue engineering of functional articular cartilage: the current status.* Cell and Tissue Research, 2012. **347**(3): p. 613-627.
11. Leddy H.A., Awad H.A., Guilak F., *Molecular diffusion in tissue-engineered cartilage constructs: effects of scaffold material, time, and culture conditions.* J Biomed Mater Res B Appl Biomater, 2004. **70**(2): p. 397-406.
12. Bansal P.N., Joshi N.S., Entezari V., Malone B.C., Stewart R.C., Snyder B.D., Grinstaff M.W., *Cationic contrast agents improve quantification of glycosaminoglycan (GAG) content by contrast enhanced CT imaging of cartilage.* Journal of Orthopaedic Research, 2011. **29**(5): p. 704-709.
13. Stewart R.C., Bansal P.N., Entezari V., Lusic H., Nazarian R.M., Snyder B.D., Grinstaff M.W., *Contrast-enhanced CT with a high-affinity cationic contrast agent for imaging ex vivo bovine, intact ex vivo rabbit, and in vivo rabbit cartilage.* Radiology, 2013. **266**(1): p. 141-50.
14. Kokkonen H.T., Mäkelä J., Kulmala K.A.M., Rieppo L., Jurvelin J.S., Tiitu V., Karjalainen H.M., Korhonen R.K., Kovanen V., Töyräs J., *Computed tomography detects changes in contrast agent diffusion after collagen cross-linking typical to natural aging of articular cartilage.* Osteoarthritis and Cartilage, 2011. **19**(10): p. 1190-1198.
15. Abazari A., Thompson R.B., Elliott J.A., McGann L.E., *Transport phenomena in articular cartilage cryopreservation as predicted by the modified*

triphasic model and the effect of natural inhomogeneities. Biophys J, 2012. **102**(6): p. 1284-93.
16. Kokkonen H.T., Jurvelin J.S., Tiitu V., Toyras J., *Detection of mechanical injury of articular cartilage using contrast enhanced computed tomography*. Osteoarthritis Cartilage, 2011. **19**(3): p. 295-301.
17. Kulmala K.A.M., Korhonen R.K., Julkunen P., Jurvelin J.S., Quinn T.M., Kröger H., Töyräs J., *Diffusion coefficients of articular cartilage for different CT and MRI contrast agents*. Medical Engineering & Physics, 2010. **32**(8): p. 878-882.
18. Tuomo S. Silvast J.S.J., Virpi Tiitu, Thomas M. Quinn and Juha Töyräs, *Bath Concentration of Anionic Contrast Agents Does Not Affect Their Diffusion and Distribution in Articular cartilage In Vitro*. Cartilage, 2013. **4**(1): p. 42-51.
19. Arbabi V., Pouran B., Weinans H., Zadpoor A.A., *Multiphasic modeling of charged solute transport across articular cartilage: Application of multi-zone finite-bath model*. J Biomech, 2016. **49**(9): p. 1510-7.
20. Entezari V., Bansal P.N., Stewart R.C., Lakin B.A., Grinstaff M.W., Snyder B.D., *Effect of mechanical convection on the partitioning of an anionic iodinated contrast agent in intact patellar cartilage*. J Orthop Res, 2014. **32**(10): p. 1333-40.
21. van Tiel J., Siebelt M., Waarsing J.H., Piscaer T.M., van Straten M., Booij R., Dijkshoorn M.L., Kleinrensink G.J., Verhaar J.A., Krestin G.P., Weinans H., Oei E.H., *CT arthrography of the human knee to measure cartilage quality with low radiation dose*. Osteoarthritis Cartilage, 2012. **20**(7): p. 678-85.
22. Klein S., Staring M., Murphy K., Viergever M.A., Pluim J.P., *elastix: a toolbox for intensity-based medical image registration*. IEEE Trans Med Imaging, 2010. **29**(1): p. 196-205.
23. Bron E.E., van Tiel J., Smit H., Poot D.H., Niessen W.J., Krestin G.P., Weinans H., Oei E.H., Kotek G., Klein S., *Image registration improves human knee cartilage T1 mapping with delayed gadolinium-enhanced MRI of cartilage (dGEMRIC)*. Eur Radiol, 2013. **23**(1): p. 246-52.
24. Huttunen J.M.J., Kokkonen H.T., Jurvelin J.S., Töyräs J., Kaipio J.P., *Estimation of fixed charge density and diffusivity profiles in cartilage using contrast enhanced computer tomography*. International Journal for Numerical Methods in Engineering, 2014. **98**(5): p. 371-390.
25. Pouran B., Kock L., Gawlitta D., Zadpoor A.A., Weinans H., *Zone-dependent diffusion of contrast agent molecules in healthy articular cartilage*. Osteoarthritis and Cartilage, 2014. **22**: p. S105-S106.
26. Pouran B., Arbabi V., Villamar J.A., Zadpoor A.A., Weinans H., *Contrast Agent's Transport Across Healthy Articular Cartilage Under Various Bath Conditions*. ORS 2015 Annual Meeting, Las Vegas, Nevada, 2015.
27. Arbabi V., B. Pouran, H. Weinans and A. A. Zadpoor, *Multiphasic modeling of charged solute transport across articular cartilage: application of finite-bath model*. Journal of Biomechanics (under review), 2015.
28. Ateshian G.A., Maas S., Weiss J.A., *Multiphasic Finite Element Framework for Modeling Hydrated Mixtures With Multiple Neutral and Charged Solutes*.

Journal of Biomechanical Engineering, 2013. **135**(11): p. 111001-111001.
29. Han J., Herzfeld J., *Macromolecular diffusion in crowded solutions.* Biophys J, 1993. **65**(3): p. 1155-61.
30. Pluen A., Netti P.A., Jain R.K., Berk D.A., *Diffusion of Macromolecules in Agarose Gels: Comparison of Linear and Globular Configurations.* Biophysical Journal, 1999. **77**(1): p. 542-552.
31. Maroudas A., *Biophysical chemistry of cartilaginous tissues with special reference to solute and fluid transport.* Biorheology, 1975. **12**(3-4): p. 233-48.
32. Pan J., Zhou X., Li W., Novotny J.E., Doty S.B., Wang L., *In situ measurement of transport between subchondral bone and articular cartilage.* J Orthop Res, 2009. **27**(10): p. 1347-52.
33. Maroudas A B.P., Swanson SA, Freeman MA, *The permeability of articular cartilage.* J Bone Joint Surg [Br], 1968. **50**: p. 166–177.
34. Pyun C.W., Fixman M., *Frictional Coefficient of Polymer Molecules in Solution.* Journal of Chemical Physics, 1964. **41**(4): p. 937-&.
35. Mow V.C., Ateshian G.A., Lai W.M., Gu W.Y., *Effects of fixed charges on the stress–relaxation behavior of hydrated soft tissues in a confined compression problem.* International Journal of Solids and Structures, 1998. **35**(34–35): p. 4945-4962.
36. Leddy H.A., Guilak F., *Site-specific effects of compression on macromolecular diffusion in articular cartilage.* Biophys J, 2008. **95**(10): p. 4890-5.

CHAPTER 6

SOLUTE TRANSPORT AT THE INTERFACE OF CARTILAGE AND SUBCHONDRAL BONE PLATE: EFFECT OF MICRO-ARCHITECTURE*

* This chapter is submitted as a scientific paper:

Pouran B., Arbabi V., Bleys R.L., van Weeren P.R., Zadpoor A.A., Weinans H. *Solute transport at the interface of cartilage and subchondral bone plate: effect of micro-architecture.* 2016 (under review).

ABSTRACT

Cross-talk of subchondral bone and articular cartilage could be an important aspect in the etiology of osteoarthritis. Previous research has provided some evidence of transport of small molecules (~370 Da) through the calcified cartilage and subchondral bone plate in murine osteoarthritis models. The current study, for the first time, employs a diffusing computed tomography (CT) contrast agent (iodixanol, neutral, ~1550 Da) to study the permeability of the osteochondral interface in equine and human samples. Sequential monitoring of diffusion after injecting a finite amount of contrast agent solution onto the cartilage surface using a micro-CT showed penetration of the contrast molecules across the cartilage-bone interface. Moreover, diffusion through the cartilage-bone interface was affected by thickness and porosity of the subchondral bone as well as the cartilage thickness in both human and equine samples. Our results revealed that in healthy equine samples, porosity of the subchondral plate contributed more strongly to the diffusion across osteochondral interface compared to other morphological parameters. However, in slightly osteoarthritic human samples, thickness of the subchondral plate contributed more strongly to the diffusion compared to porosity of the subchondral plate.

6.1. INTRODUCTION

Etiology of osteoarthritis (OA) implies deterioration of subchondral bone plate quality such as early thinning, sclerosis and porosity alterations beside the damage of articular cartilage [1, 2]. The severity and type of those changes depend primarily on the OA stage [3-6]. According to some theories that go against conventional theories [7, 8], OA initiates from the subchondral bone, over-time progressing to the overlying articular cartilage [9, 10]. Regardless of whether one subscribes to the conventional or alternative theories associated with the etiology of OA, it is clear that morphological changes in the subchondral bone and articular cartilage create a driving force for transfer of putative harmful molecules [1]. Enhanced activity of osteoclasts and subsequent increased subchondral bone perforations and thinning augment the diffusion of cytokines and enzymes as well as cross-talk between cartilage and subchondral bone [2, 5, 11, 12]. These mechanisms highlight the fact that diffusion likely plays a key role in molecular signaling across the osteochondral interface. Some earlier studies on OA models of rabbits and rats reported the diffusion at the osteochondral interface [1]. The diffusion of small molecules (<400 Da) was confirmed between the uncalcified and calcified cartilage in the metacarpophalangeal joints of healthy mature horses [13]. Diffusion of small molecules across the osteochondral interface in a murine model using sodium fluorescein (376 Da) was correlated with OA progression and diffusion of Gd-DTPA^{2-} (MRI contrast agent, 547 Da) in the clinic was observed [2, 11, 14]. The presence of non-mineralized patches (~100 nm) within the calcified cartilage as well as invasion of uncalcified cartilage through the calcified cartilage might explain the molecular transport [11, 15]. Unlike articular cartilage, consensus exists regarding the diffusion of molecules between the intervertebral disk (IVD) and the vertebral body through the

endplate. Diffusion is known to dramatically influence the health of the spine, because insufficient nutrition of the IVD is suggested to accelerate its degeneration [16]. However, it was shown that load-dependent convection facilitates the transport in the IVD as well as across the endplate-IVD interface in both healthy and degenerated disks [17, 18]. A previous study using advanced micro-computed tomography (micro-CT) showed increased perforations in the subchondral endplate when the IVD degenerates [19]. All the previous evidence therefore supports the theory that direct diffusion between cartilaginous tissues and underlying bone plays a key role in the normal physiology of articulating joints as well as the spine.

In the present study, we aim to investigate solute transport between articular cartilage and subchondral bone of equine and human samples using multi-resolution micro-CT by applying a neutral solute. Using the neutral solute enables to exclude the mechano-electrical phenomena arising when an external charged solute is transferred through the highly charged articular cartilage. The effects of the micro-architecture (i.e. porosity and thickness) of the calcified cartilage/subchondral bone plate complex and thickness of uncalcified cartilage on diffusion will be determined.

6.2. METHODOLOGY

6.2.1. EXPERIMENTS

6.2.1.1. BATH AND SAMPLE PREPARATION

Cylindrical osteochondral plugs from four cadaveric fresh-frozen human medial femoral condyles with slight OA (approved by university medical center Utrecht, age=67-85, n=4, cartilage thickness=2.53±0.31, diameter=8.5 mm) and one healthy cadaveric equine medial femoral condyle (approved by Utrecht university, age=7, n=6, cartilage thickness=1.25±0.52 mm, diameter=8.5 mm) were drilled using custom-made drill bits

(Figure 6.1). For the human samples, care was taken to extract them from a location that was visually intact. The site of drilling was constantly sprayed using phosphate buffer serum (PBS) to ensure minimal dehydration and damage to the cartilage.

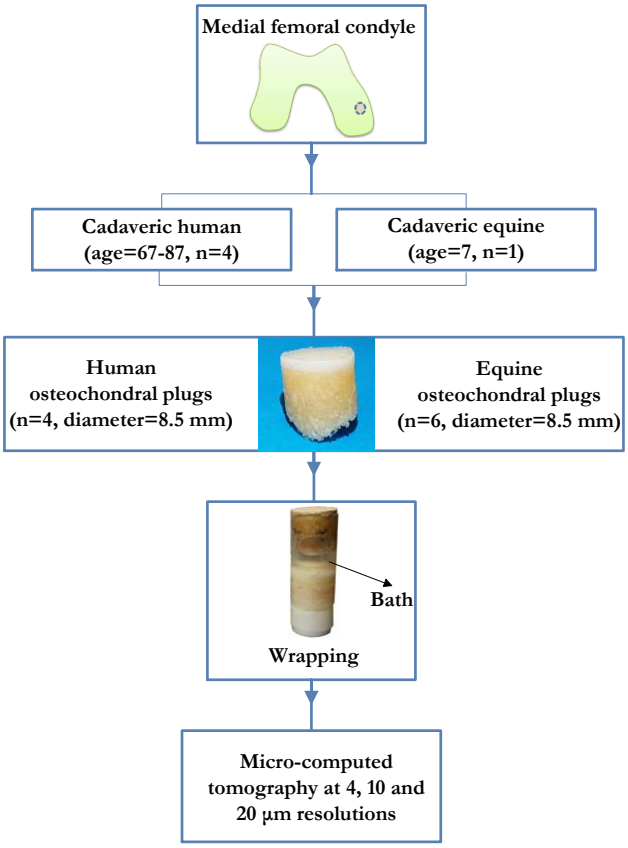

Figure 6.1. Preparing samples for the micro-CT scanning: osteochondral plugs were extracted from four cadaveric human medial femoral condyles and one cadaveric equine medial femoral condyle. A shrinking sleeve was used to wrap the samples before injecting the contrast agent onto the cartilage surface. Then the samples underwent multi-resolution micro-computed tomography.

We prepared iodixanol solutions (molecular weight (MW)=1.55 kDa, concentration=420 mM, charge=0, osmolality=300

mOsm/kgH_2O, volume≃600 µL, *GE Healthcare*, *Netherlands*) enriched with protease inhibitors (5mM) to study the axial diffusion through cartilage and the cartilage-bone interface. Since iodixanol is a neutral contrast agent, the effect of cartilage charge on molecular transport was eliminated. Immediately post-harvest, the osteochondral plugs were wrapped using plastic shrinking sleeves to prevent lateral diffusion (Figure 6.1).

6.2.1.2. QUANTITATIVE MICRO-CT

To study the transport of iodixanol across cartilage and the cartilage-bone interface, we used a micro-CT scanner (*Quantum FX*, *Perkin Elmer, USA*, spatial resolution of 20 μm^3 voxel size, scan time= 2 min, tube voltage= 90 kV and tube current=180 µA, number of projections=3600) and captured images at t_{-1} (before injection of iodixanol solution), t_0 (point of injection of iodixanol solution), t= 12, 24, 48 and 72 hours within the field of views consisting of bath, cartilage, and subchondral bone (Figure 6.2A).

The projected images were transformed automatically to 3D reconstructed files using in-built software of the micro-CT machine (*Quantum FX*). After rigid image registration based on the t_0 images, the 3D reconstructed files were converted to a series of 2D images for further analyses (*Analyze 11.0*). We used Gaussian blurring 3D filter (radius=3) to minimize the noise and then selected 20 middle slices of the 2D stack and created rectangular regions of interest (ROI) in *FIJI* (*free software for image analyses*), which comprised the bath, cartilage, and subchondral plate. The t_{-1} images were locally thresholded (*Bernsen*) using *BoneJ* (plugin of *FIJI*) to calculate the thickness and porosity of the subchondral plate/calcified cartilage as well as the thickness of uncalcified cartilage (Figure 6.2B and Table 6.1). The subchondral plate/calcified cartilage zone was defined as the region lying above the region where the trabecular structure could be easily

pinpointed. The mean of the average grey values of the subchondral plate/calcified cartilage at t_0 in 20 selected slices was subtracted from the mean average grey values at the later time points to measure the diffusion. The relationship between the diffusion at 72 hours with the micro-architecture of subchondral plate/calcified cartilage, i.e. porosity and thickness, was also investigated.

6.2.1.3. QUALITATIVE MICRO-CT

To qualitatively visualize the diffusion at the cartilage-bone interface we also performed micro-CT scan using the previously mentioned micro-CT parameters but with higher spatial resolution of 10 μm^3. To visualize the cartilage-bone interface with ultra-high resolution *phoenix nanotom* micro-CT was used (GE, USA, tube voltage= 70 kV tube current=110 μA, 4 μm^3 voxel size, scan time= 2 hours, field of view: 4 mm).

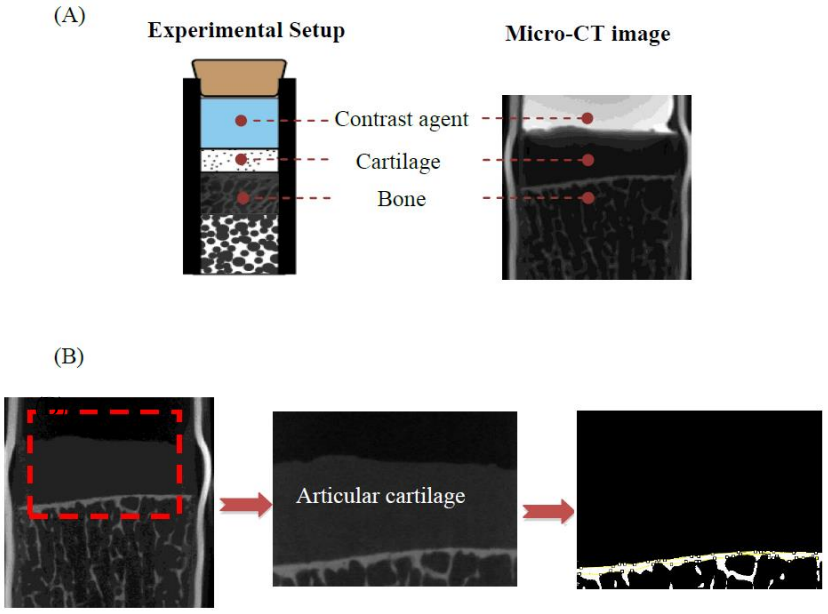

Figure 6.2. Micro-computed tomography image with spatial resolution of 20 μm^3 (A). Local thresholding was employed before injection of contrast agent to calculate the thickness and porosity of the subchondral bone plate/calcified cartilage (B).

Table 6.1. Cartilage thickness, subchondral plate/calcified cartilage thickness and porosity for human samples and for equine samples.

Sample		Cartilage thickness (μm)	Subchondral/calcified cartilage thickness (μm)	Subchondral/calcified cartilage porosity (%)
Human	1	2500	175	4.8
	2	2700	115	6.4
	3	2100	186	4.0
	4	2800	147	8.1
Equine	1	700	178	12.1
	2	1100	468	7.6
	3	830	117	17.2
	4	1320	193	5.1
	5	1190	175	3.5
	6	2100	332	1.5

6.3. RESULTS

The thickness of cartilage for human and equine samples was 2525±310 μm and 1207±494 μm, respectively. For human samples the thickness and porosity of the subchondral plate were 155.7±31.3 μm and 5.8±1.8 % and for equine samples the thickness and porosity of the subchondral plate were 243.7±131.0 μm and 7.8±5.9 % (Table 6.1).

Diffusion of iodixanol from uncalcified cartilage to the subchondral bone via the calcified cartilage layer for both the human and equine samples was confirmed (Figure 6.3 and 6.4).

Low cartilage thickness, high subchondral plate/calcified cartilage porosity and low subchondral plate/calcified cartilage thickness are factors contributing to diffusion (Table 6.1, Figure 6.5A and 6.5B). In the human samples, we observed the steepest rise in the diffusion within the subchondral plate/calcified cartilage until t=24 h (Figure 6.5A). After 24 hours, the diffusion curves tended to reach near-equilibrium, achieving the highest average grey value at 72 hours. For all time points, the average grey values were the highest in sample 2 (human), which has the lowest thickness of the subchondral plate/calcified cartilage (Figure 6.5A and Table 6.1). Samples 1 and 3 (human) showed diffusion patterns that were very similar to each other (Figure 6.5A), as well as similar morphological characteristics (Table 6.1). Like the observations regarding human samples, the diffusion curves in the equine samples reach near-equilibrium at 72 hours (Figure 6.5B).

Plots of near-equilibrium increase in average grey values versus morphological features (porosity and thickness) of the subchondral plate/calcified cartilage for both equine and human samples suggested a link between diffusion behavior of the neutral solute and the micro-architecture of the subchondral plate/calcified cartilage (Figure 6.6). To investigate the effect of cartilage thickness and subchondral plate/calcified thickness and porosity on diffusion we performed multi-regression analysis. This analysis was not possible to perform on human samples due to relatively low sample number. Multi-regression on equine samples showed significance of cartilage thickness (p-value=0.019) as well as porosity (p-value=0.0011) and thickness (p-value=0.003) of subchondral plate/calcified cartilage on diffusion. Diffusion in human samples did not correlate with porosity as compared to equine samples (Figure 6.6A, R^2= 0.24 vs. R^2= 0.91). Nevertheless, diffusion in the human samples had a stronger correlation with the

thickness of subchondral plate/calcified cartilage compared to equine samples (Figure 6.6B, R^2 = 0.92 vs. R^2= 0.43).

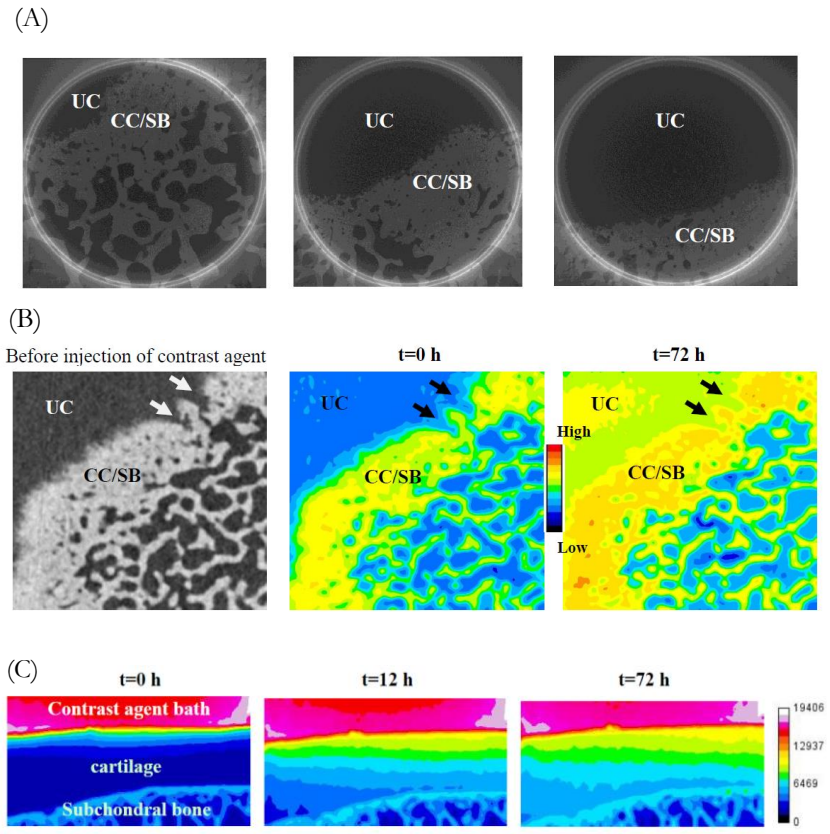

Figure 6.3. Ultra-high micro-CT (4 μm³ spatial resolution) was used to highlight the interface of cartilage and subchondral bone plate in three representative slices in a human osteochondral plug. The diffusion at the interface of uncalcified cartilage (UC) and subchondral bone plate (SB)/calcified cartilage (CC) is depicted (A). The protrusion of uncalcified cartilage into the calcified cartilage and mineralized region (arrows) facilitates the diffusion (10 μm³ spatial resolution) (B). The progress of the diffusion front wave is shown at different time points (20 μm³ spatial resolution) (C).

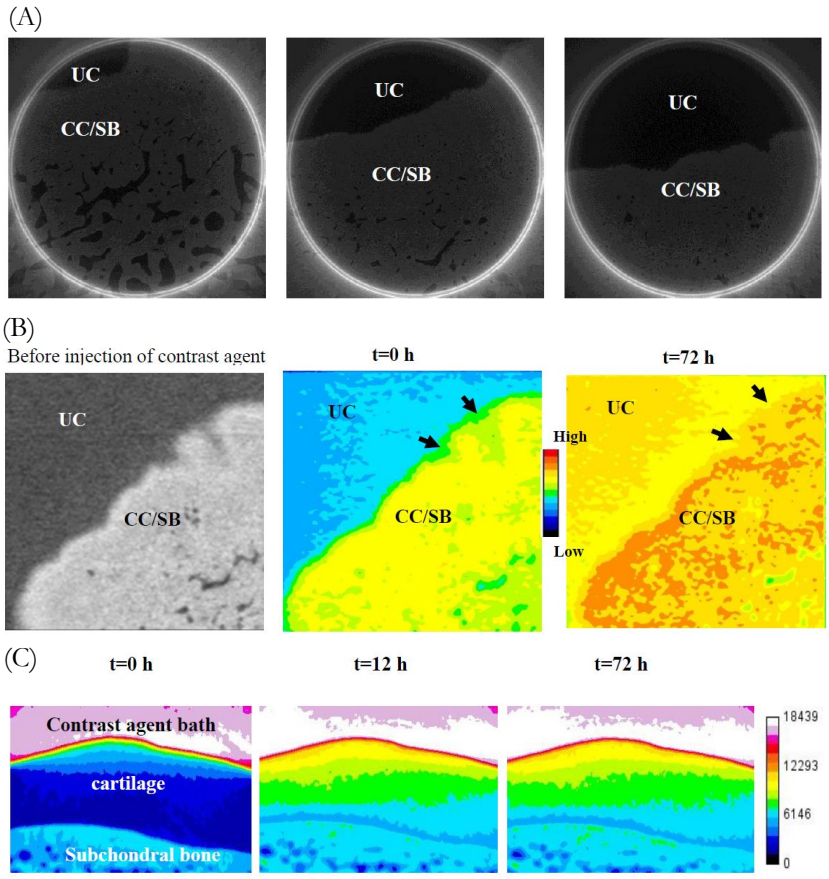

Figure 6.4. Ultra-high micro-CT (4 μm³ spatial resolution) was used to highlight the interface of cartilage and subchondral bone plate in three representative slices in an equine osteochondral plug. The diffusion at the interface of uncalcified cartilage (UC) and subchondral bone plate (SB)/calcified cartilage (CC) is depicted (A). The protrusion of uncalcified cartilage into the calcified cartilage and mineralized region (arrows) facilitates the diffusion (10 μm³ spatial resolution) (B). The progress of the diffusion front wave is shown at different time points (20 μm³ spatial resolution) (C).

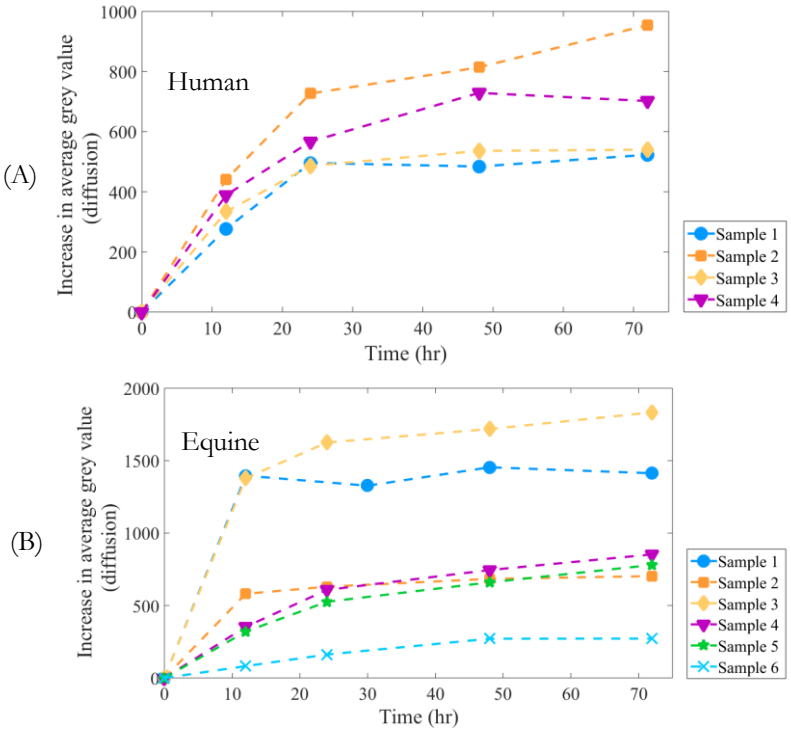

Figure 6.5. Average grey values (diffusion) in the subchondral plate/calcified cartilage over time for human (A) and equine samples (B).

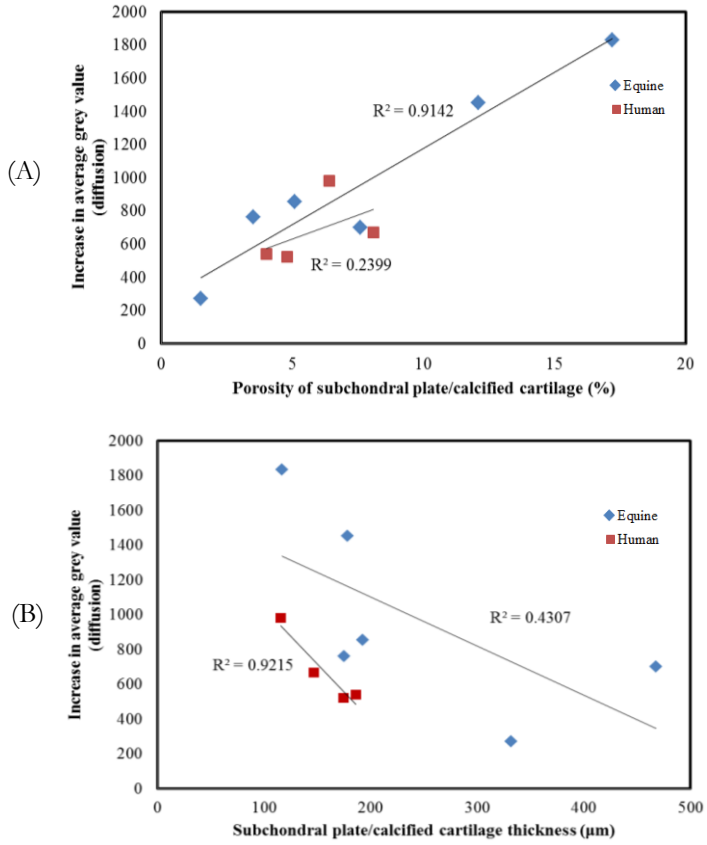

Figure 6.6. Plot of average grey values (diffusion) at 72 hours in the subchondral plate/calcified cartilage versus subchondral plate/calcified cartilage porosity (A) and subchondral plate/calcified cartilage thickness (B).

6.4. Discussion

In this study, we have observed the direct diffusion between articular cartilage and subchondral bone plate/calcified cartilage in human as well as equine osteochondral plugs when a finite volume of bath containing a neutral solute was inserted at the cartilage

surface. Furthermore, we confirmed that the molecular transport to the subchondral bone plate depends on the morphological parameters of both uncalcified cartilage and subchondral bone plate. We identified cartilage thickness and porosity and thickness of subchondral bone plate as the factors influencing the transport. Porosity and thickness of the subchondral plate in horse samples were found to have more effect on the diffusion across osteochondral interface compared to cartilage thickness. Although in human samples small variation in subchondral plate porosity was observed, the effect of subchondral plate on diffusion was more tangible.

The electrically neutral molecules (MW=1.55 kDa) used in our study allowed excluding the effects of fixed charges entrapped in the articular cartilage and the resulting electro-mechanically induced transport. Therefore, in the current study molecular friction between the diffusing solute and the extracellular matrix of the cartilage, i.e. water content, collagen fibrils and proteoglycans as well as the morphology of subchondral plate (porosity and thickness) are the only limiting factors for neutral molecular transport between cartilage and underlying bone. This implies that the diffusion mechanism in our study can be described as a Fickean diffusion process. In human samples with similar thickness of the articular cartilage, we observed higher near-equilibrium increase in average grey value (diffusion, 72 hours) (Figure 6.5A), which is likely due to the thinner subchondral plate/calcified cartilage (28% difference, Table 6.1). Similar diffusion behavior in human samples before 12 hours (Figure 6.5A) may be linked to the fact that similar cartilage thicknesses could lead to similar frictional loss in driving force eventually causing similar diffusion behavior in the subchondral plate/calcified cartilage (Table 6.1).

The structural changes such as thinning of the subchondral plate in early OA [3, 5] and subchondral bone sclerosis observed in advanced OA may alter the transport rate causing interruptions in trans-signaling between cartilage and subchondral bone plate. Our study also emphasizes the importance of structure of the subchondral bone on the transport across osteochondral interface. Human samples that represent similar thickness and porosity of the subchondral plate/calcified cartilage showed very similar diffusion behavior in all time points (Figure 6.5A and Table 6.1). Enhanced porosity creates more access for the solutes to diffuse across the subchondral plate since the pores filled with soft tissue with high water content are more permeable than the mineralized regions of subchondral plate. A previous study on murine model of OA also suggested that the transport between cartilage and subchondral plate increases due to thinning of cartilage and subchondral plate [2], which is in agreement with our observations. It should be borne in mind that the inter-connectivity and tortuosity of the pores has not been investigated in this study, but could itself play an integral role in solutes distribution and partitioning. Since both young (equine) and old and perhaps slightly OA joints (human) were used in this study we can draw the conclusion that the interface of cartilage and subchondral bone plate is permeable to at least relatively small solutes (less than 2 kDa) in both healthy and slightly degenerated joints. To our best of knowledge, we were the first who investigated the transport of relatively larger solutes across osteochondral interface compared to other previous studies [13, 14] in both human and horse knees taking the morphology of the cartilage and bone into account.

Whereas the current study strived to be as thorough as possible, it is inevitably associated with some limitations. First, the calcified cartilage and subchondral plate could not be differentiated clearly from each other using micro-CT images, especially when the

contrast agent (iodixanol) diffused through it which limited the capability of studying the diffusion separately in these two zones. Second, although our study used largest solute among the similar studies and applied in large animal model and human, the diffusion of vital signaling macromolecules may be studied by labeling them with contrast agent. Furthermore, the effect of solute charge on diffusion in the subchondral plate/calcified cartilage could be investigated in future studies to enable studying charged signaling molecule transfer across the osteochondral interface.

The present study sheds light on the transport of a neutral solute across the interface of articular cartilage and subchondral plate. Our findings confirm the direct cross-talk between cartilage and subchondral bone/calcified cartilage in both human samples (slightly osteoarthritic) and equine samples (healthy) when applying a neutral contrast agent to nullify the mechano-electrical-affected diffusion in the articular cartilage. Besides, we highlighted that diffusion in the subchondral plate/calcified cartilage could be estimated when micro-architecture data concerning porosity and thickness of the subchondral plate/calcified cartilage and cartilage thickness are available.

6.5 Acknowledgements

This work was supported by a grant from Dutch Arthritis Foundation (LRP-22). The authors are grateful to Mr. Michael Afanasyev and Mr. Wim Verwaal for their assistance during high-resolution micro-CT scans.

6.6. REFERENCES

1. Weinans H., Siebelt M., Agricola R., Botter S.M., Piscaer T.M., Waarsing J.H., *Pathophysiology of peri-articular bone changes in osteoarthritis.* Bone, 2012. **51**(2): p. 190-6.
2. Pan J., Wang B., Li W., Zhou X., Scherr T., Yang Y., Price C., Wang L., *Elevated cross-talk between subchondral bone and cartilage in osteoarthritic joints.* Bone, 2012. **51**(2): p. 212-7.
3. Intema F., Hazewinkel H.A., Gouwens D., Bijlsma J.W., Weinans H., Lafeber F.P., Mastbergen S.C., *In early OA, thinning of the subchondral plate is directly related to cartilage damage: results from a canine ACLT-meniscectomy model.* Osteoarthritis Cartilage, 2010. **18**(5): p. 691-8.
4. Li B., Aspden R.M., *Mechanical and material properties of the subchondral bone plate from the femoral head of patients with osteoarthritis or osteoporosis.* Ann Rheum Dis, 1997. **56**(4): p. 247-54.
5. Botter S.M., van Osch G.J., Clockaerts S., Waarsing J.H., Weinans H., van Leeuwen J.P., *Osteoarthritis induction leads to early and temporal subchondral plate porosity in the tibial plateau of mice: an in vivo microfocal computed tomography study.* Arthritis Rheum, 2011. **63**(9): p. 2690-9.
6. Botter S.M., *Dynamic Subchondral Bone Changes in Murine Models of Osteoarthritis.* PhD thesis, 2010.
7. Sniekers Y.H., Intema F., Lafeber F.P., van Osch G.J., van Leeuwen J.P., Weinans H., Mastbergen S.C., *A role for subchondral bone changes in the process of osteoarthritis; a micro-CT study of two canine models.* BMC Musculoskelet Disord, 2008. **9**: p. 20.
8. Intema F., Sniekers Y.H., Weinans H., Vianen M.E., Yocum S.A., Zuurmond A.M., DeGroot J., Lafeber F.P., Mastbergen S.C., *Similarities and discrepancies in subchondral bone structure in two differently induced canine models of osteoarthritis.* J Bone Miner Res, 2010. **25**(7): p. 1650-7.
9. Westacott C., *Interactions between subchondral bone and cartilage in OA. Cells from osteoarthritic bone can alter cartilage metabolism.* J Musculoskelet Neuronal Interact, 2002. **2**(6): p. 507-9.
10. Radin E.L., Rose R.M., *Role of subchondral bone in the initiation and progression of cartilage damage.* Clin Orthop Relat Res, 1986(213): p. 34-40.
11. Pan J., Zhou X., Li W., Novotny J.E., Doty S.B., Wang L., *In Situ measurement of transport between subchondral bone and articular cartilage.* Journal of orthopaedic research : official publication of the Orthopaedic Research Society, 2009. **27**(10): p. 1347-1352.
12. Siebelt M., Waarsing J.H., Groen H.C., Muller C., Koelewijn S.J., de Blois E., Verhaar J.A., de Jong M., Weinans H., *Inhibited osteoclastic bone resorption through alendronate treatment in rats reduces severe osteoarthritis progression.* Bone, 2014. **66**: p. 163-70.
13. Arkill K.P., Winlove C.P., *Solute transport in the deep and calcified zones of articular cartilage.* Osteoarthritis Cartilage, 2008. **16**(6): p. 708-14.
14. Burstein D., Velyvis J., Scott K.T., Stock K.W., Kim Y.-J., Jaramillo D., Boutin R.D., Gray M.L., *Protocol issues for delayed Gd(DTPA)2--enhanced*

MRI (dGEMRIC) for clinical evaluation of articular cartilage. Magnetic Resonance in Medicine, 2001. **45**(1): p. 36-41.

15. Lyons T.J., McClure S.F., Stoddart R.W., McClure J., *The normal human chondro-osseous junctional region: evidence for contact of uncalcified cartilage with subchondral bone and marrow spaces.* BMC Musculoskelet Disord, 2006. **7**: p. 52.
16. Galbusera F., Brayda-Bruno M., Wilke H.-J., *Is post-contrast MRI a valuable method for the study of the nutrition of the intervertebral disc?* Journal of Biomechanics, 2014. **47**(12): p. 3028-3034.
17. Gullbrand S.E., Peterson J., Mastropolo R., Roberts T.T., Lawrence J.P., Glennon J.C., DiRisio D.J., Ledet E.H., *Low rate loading-induced convection enhances net transport into the intervertebral disc in vivo.* Spine J, 2015. **15**(5): p. 1028-33.
18. Gullbrand S.E., Peterson J., Ahlborn J., Mastropolo R., Fricker A., Roberts T.T., Abousayed M., Lawrence J.P., Glennon J.C., Ledet E.H., *ISSLS Prize Winner: Dynamic Loading-Induced Convective Transport Enhances Intervertebral Disc Nutrition.* Spine (Phila Pa 1976), 2015. **40**(15): p. 1158-64.
19. Rutges J.P.H.J., Jagt van der O.P., Oner F.C., Verbout A.J., Castelein R.J.M., Kummer J.A., Weinans H., Creemers L.B., Dhert W.J.A., *Micro-CT quantification of subchondral endplate changes in intervertebral disc degeneration.* Osteoarthritis and Cartilage, 2011. **19**(1): p. 89-95.

CHAPTER 7

NEUTRAL SOLUTE TRANSPORT ACROSS OSTEOCHONDRAL INTERFACE: A FINITE ELEMENT APPROACH*

* This chapter is submitted as a scientific paper:

Arbabi V., Pouran B., Weinans H., Zadpoor A.A. *Neutral solute transport across osteochondral interface: a finite element approach*. 2016 (under review).

ABSTRACT

Investigation of the solute transfer across articular cartilage and subchondral bone plate could nurture the understanding of the mechanisms of osteoarthritis (OA) progression. In the current study, we approached the transport of neutral solutes in human (slight OA) and equine (healthy) samples using both computed tomography and biphasic-solute finite element modeling. We developed a multi-zone biphasic-solute finite element model (FEM) accounting for the inhomogeneity of articular cartilage (superficial, middle and deep zones) and subchondral bone plate. Fitting the FEM model to the concentration-time curves of the cartilage and the equilibrium concentration of the subchondral plate/calcified cartilage enabled determination of the diffusion coefficients in the superficial, middle and deep zones of cartilage and subchondral plate. We found slightly higher diffusion coefficients for all zones in the human samples as compared to the equine samples. Generally the diffusion coefficient in the superficial zone of human samples was about 3-fold higher than the middle zone, the diffusion coefficient of the middle zone was 1.5-fold higher than that of the deep zone, and the diffusion coefficient of the deep zone was 1.5-fold higher than that of the subchondral plate/calcified cartilage. Those ratios for equine samples were 9, 2 and 1.5, respectively. Regardless of the species considered, there is a gradual decrease of the diffusion coefficient as one approaches the subchondral plate, whereas the rate of decrease is dependent on the type of species.

7.1. INTRODUCTION

Molecular exchange (diffusion) between articular cartilage and the underlying bone has been identified as one of the parameters that changes during osteoarthritis (OA) progression [1, 2]. The pathways for the molecular transport in diarthrodial joints span from direct cross-talk between articular cartilage and underlying subchondral bone plate to transport via synovial fluid [3, 4]. Few studies addressed the direct cross-talk between uncalcified cartilage and calcified cartilage [5] and between calcified cartilage and subchondral plate [3, 4], whereas vast majority of the studies dealing with molecular transport were mostly centered upon morphology-driven transport between intervertebral disk (IVD) and endplates [6, 7]. Two consecutive studies have shown the direct diffusion between calcified and non-calcified cartilage and subchondral plate in a murine model and have highlighted how remarkable reduction in subchondral plate and cartilage thickness post-OA enhanced the transport rate [3, 4]. Assessment of the Fickean molecular transport in OA and healthy joints of mice [3, 4] and uncalcified cartilage and calcified cartilage of horses [5] was achieved by fitting a simplified analytical formula to the fluorescent intensity versus time curves based on fluorescence loss induced by photobleaching (FLIP) technique and fluorescent intensity tracing technique to obtain the diffusion coefficient of sodium fluorescein (376 Da, charge=0). Molecular transport at osteochondral interface (OI) depends not only on the concentration and distribution of the exctracellular matrix (ECM) components but also on the morphological features, e.g. porosity and thickness of the calcified cartilage and subchondral plate, which determine the mass transfer resistance at the cartilage-bone interface [1, 3, 8, 9].

Previously, we developed biphasic-solute and multiphasic finite element models to study the diffusion of neutral and charged solutes across different zones of articular cartilage (chapters 3 and 9) [10, 11]. Those models allowed obtaining the diffusion coefficients and fixed charge density in various cartilage layers, i.e. superficial, middle and deep zones, and also shed light on the effect of inhomogeneity of articular cartilage across its thickness on the solute diffusion behavior. Besides, the application of the models capable of predicting the diffusive properties of cartilage in different zones, the models could potentially be extended to the cartilage-bone interface.

The current work, for the first time, introduces a combination of experimental set-up and computational models to enable studying the diffusion of neutral solutes across cartilage and osteochondral interface. The experimental setup includes monitoring the diffusion of a neutral solute from a finite bath inserted on the cartilage surface of cadaveric human and equine osteochondral plugs using serial micro-computed tomography (micro-CT) images. The computational models were established using a multi-zone biphasic-solute mixture approach. Determination of diffusion coefficients in various cartilage layers and subchondral bone was performed by simultaneously fitting the computational model to the experimental findings.

7.2. METHODOLOGY

7.2.1. EXPERIMENTS

The descriptive details of the experiments consisting of sample preparation, image acquisition, and image processing are presented elsewhere (chapter 6) [8]. Osteochondral plugs were obtained (diameter = 8.5 mm) from four cadaveric human (68-90 years old)

femoral condyles (one sample from each) and one equine femoral condyle (six samples) (Figure 7.1A). Upon harvest, the osteochondral plugs were wrapped with shrinking plastic sleeve to enable axial diffusion

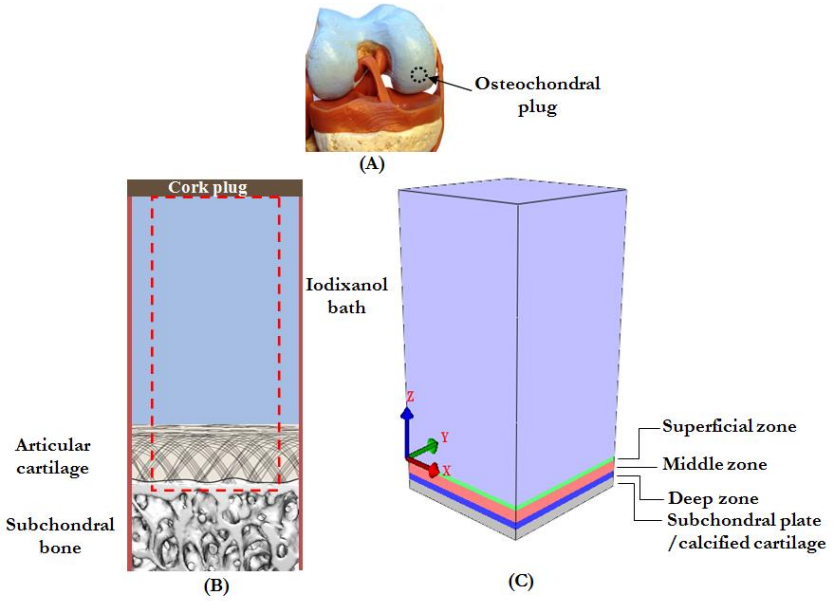

Figure 7.1. Schematics of A) femoral condyle and osteochondral sample location B) sample consisting of finite bath of iodixanol, articular cartilage and subchondral plate C) multi-zone biphasic-solute model**.**

of a neutral computed tomography (CT) contrast agent (iodixanol, 1551 Da, 290 *mOsm/kg* H_2o, charge=0, 420 mM). Finite volumes of the iodixanol solution was placed on the cartilage surface and its diffusion across the cartilage and subchondral bone was monitored up to 72 hours using micro-CT (*Qauntum FX, USA*) (Figure 7.1B).

The 3D reconstructed images (until 72 hours) were registered and after applying Gaussian filter (radius=2) 20 stacks of TIFF images

in the middle were selected. Average grey values within the cartilage and subchondral bone were converted to the actual iodixanol concentration using a linear calibration function. The morphological parameters, i.e. porosity and thickness of the subchondral plate/calcified cartilage, were calculated by locally thresholding the micro-CT image before injecting the contrast agent (Table 7.1).

Table 7.1. Morphological specifications i.e. of cartilage and subchondral plate/calcified cartilage in A) human samples and B) equine samples [8].

(A)

Sample	Cartilage thickness (mm)	Subchondral plate /calcified cartilage thickness (mm)	Subchondral plate /calcified cartilage porosity (%)
1	2.5	0.175	4.8
2	2.7	0.115	6.4
3	2.1	0.186	4.0
4	2.8	0.147	8.1

(B)

Sample	Cartilage thickness (mm)	Subchondral plate /calcified cartilage thickness (mm)	Subchondral plate /calcified cartilage porosity (%)
1	0.7	0.178	12.1
2	1.1	0.468	7.6
3	0.83	0.117	17.2
4	1.32	0.193	5.1
5	1.19	0.175	3.5
6	2.1	0.332	1.5

7.2.2. COMPUTATIONAL MODEL

Finite element models based on biphasic-solute mixture models can describe the transport of neutral solutes across biphasic tissues [12, 13]. Considering $\mathbf{T}$ as the Cauchy stress tensor for the mixture, $\mathbf{v}^s$ as the velocity of the solid matrix and $\mathbf{w}$ as the volume flux of the solvent (water) relative to the solid (tissue matrix), the conservation of linear momentum and mass for the mixture (tissue) can be described as:

$$div\,\mathbf{T} = 0 \tag{7.2}$$

$$div\left(\mathbf{v}^s + \mathbf{w}\right) = 0 \tag{7.3}$$

and the balance of mass for the solute can be given as:

$$\frac{1}{J}\frac{D^s(J\varphi^w\tilde{\kappa}\tilde{c})}{Dt} + \mathrm{div}\,\mathbf{j} = 0 \tag{7.4}$$

where $J = \det\mathbf{F}$, $\mathbf{F}$ is the deformation gradient of the solid matrix, D^s/Dt is the material time derivative in the spatial frame, $\mathbf{j}$ is the molar flux of solute relative to the solid, φ^w is volume fraction of the solvent, $\tilde{\kappa}$ is the effective solubility, c is the solute concentration and $(\tilde{c} = c/\tilde{\kappa})$ is the effective solute concentration, which is continuous across boundaries and contact surfaces [13, 14]. The relative molar solute flux, $\mathbf{j}$, is given as:

$$\mathbf{j} = \tilde{\kappa}d.\left(-(1-\frac{\varphi_r^s}{J})\mathrm{grad}\,\tilde{c} - \frac{\tilde{c}}{d_0}(\tilde{\mathbf{k}}.\mathrm{grad}\,p)\right) \tag{7.5}$$

while

$$\tilde{\mathbf{k}} = \left[\mathbf{k}^{-1} + \frac{R\theta}{\varphi^w} \frac{\tilde{\kappa}\tilde{c}}{d_0} \left(\mathbf{I} - \frac{\mathbf{d}}{d_0} \right) \right]^{-1} \tag{7.6}$$

where p is the fluid pressure, $\tilde{\mathbf{k}}$ is the hydraulic permeability tensor for the flow of the solution, i.e. solvent plus solute through the solid matrix, $\mathbf{k}$ is the hydraulic permeability tensor for the flow of pure solvent through the solid matrix, $\mathbf{d}$ is the diffusion coefficient tensor of the solute in the mixture, d_0 is the diffusion coefficient tensor in absence of the solid phase, R is the universal gas constant, θ is the absolute temperature, and φ_r^s is the volume fraction of the solid phase in the reference configuration [13, 15, 16].

Using the principle of virtual work, the above-mentioned equations could be solved simultaneously in an open-source finite element modeling platform FEBio 2.2.6 to describe the transport of a neutral solute through a mixture.

7.2.2.1. GEOMETRY

Osteochondral plugs contain two distinct phases namely uncalcified cartilage and subchondral plate/calcified cartilage. Previously, we have shown that a multi-zone biphasic-solute model could track the axial diffusion behavior of a neutral solute across articular cartilage (chapter 3) [10]. Therefore, we introduced a multi-zone model consisting of four different zones of superficial (20% of the cartilage thickness), middle (50% of the cartilage thickness), deep (30% of the cartilage thickness) [17] and subchondral plate/calcified cartilage (thickness obtained based on micro-CT [8]) to account for the inhomogeneity of osteochondral plugs (Figure 7.1C and Table 7.1). The overlaying iodixnol bath was 12 mm in height for all samples corresponding to the actual

experiments. We used an 8-node trilinear hexahedral element, which was refined in the vicinity of the interfaces. For each cartilage zone and subchondral plate/calcified cartilage, individual diffusion coefficients were calculated.

7.2.2.2. MECHANICAL AND PHYSICAL PROPERTIES

Cartilage and subchondral plate/calcified cartilage were modeled as neo-Hookean materials with effective solubility of 1 while the Young's modulus was chosen to be high enough to correspond to the realistic experimental deformations resulting from the osmotic pressure of the external bath. The diffusion coefficient tensor for bath, cartilage and bone was considered isotropic. The actual diffusion coefficient of iodixanol within the bath was 0.00025 $\mu m^2/s$ according to the previous studies [10, 18]. Four different values of water content for each cartilage zone as well as for subchondral plate/calcified cartilage were used: 0.8 for the superficial zone, 0.7 for the middle zone, 0.6 for the deep zone [17] and 0.2 for the subchondral plate/calcified cartilage [19] .

7.2.2.3. INITIAL AND BOUNDARY CONDITIONS

Actual experimental solute concentration in the bath (420 mM) was prescribed as the initial condition. Effective pressure ($p_{effective}$) is continuous across boundaries [13, 20] and is expressed as:

$$p_{effective} = p - R\theta c\phi, \tag{7.7}$$

where $R = 8.314\times10^{-6}$ mJ/nmol·K and ϕ is the osmotic coefficient that was set to 1. The ambient fluid pressure and absolute temperature were p =101 kPa and θ =298 K.

7.2.2.4. FITTING METHOD

To obtain the diffusion coefficients of different zones of uncalcified cartilage and subchondral plate/calcified cartilage regarded as two distinct phases, we fitted the computational data to the experimental concentration-time curves for the cartilage and to the equilibrium concentration point at 72 hours for subchondral plate/calcified cartilage. The latter is done since distinguishing the calcified cartilage from subchondral plate is infeasible using micro-CT (two mineralized materials) and that they are different materials in terms of diffusive properties [4]. Direct scanning of the parameter space was used to minimize the root mean square error (RMSE) values between computational and experimental concentration-time data (uncalcified cartilage) and between computational and experimental equilibrium concentration (subchondral plate/calcified cartilage) to obtain the diffusion coefficients of all uncalcifed cartilage zones as well as subchondral plate/calcified cartilage. This guarantees that all possible solutions can be found within the scanning resolution.

7.3. RESULTS

The near-equilibrium concentration (72 hours) in the cartilage and subchondral plate/calcified cartilage was 32.73±7.36 % (mean ± SD) and 5.16±1.84 % (mean ± SD) for the human samples and 41.4 ±7.05% (mean ± SD) and 8.08±4.50 % (mean ± SD) for the equine samples (Figure 7.2 and 7.3).

The computational model for the human and equine samples provided satisfactory fits over the experimental data (Figure 7.4 and 7.5). In general, our multi-zone biphasic model provided more robust fits in human samples as compared to equine samples

(Table 7.2A-B). The average diffusion coefficients for the superficial, middle, deep zones and subchondral plate/calcified cartilage of the human samples were 5.63±2.05, 2.07±0.78, 1.53±0.30 and 1.22±0.35 $\mu m^2/s$ (Table 7.3A). The average diffusion coefficients for the superficial, middle, deep zones and subchondral plate/calcified cartilage of the equine samples were 4.47±1.4, 0.60±0.34, 0.44±0.29 and 0.36±0.30 $\mu m^2/s$ (Table 7.3B). The ratio of the diffusion coefficients in human samples were as follows: superficial to middle ($D_{Superficial}/ D_{Middle}$): 2.73±0.54, middle to deep (D_{Middle}/ D_{Deep}): 1.35±0.47 and deep to subchondral plate/calcified cartilage (D_{Deep}/ D_{SPCC}):1.28±0.15 (Table 7.4A). The ratio of the diffusion coefficients in equine samples were as follows: superficial to middle ($D_{Superficial}/ D_{Middle}$): 8.70±2.42, middle to deep (D_{Middle}/ D_{Deep}):1.61±0.60 and deep to subchondral plate/calcified cartilage (D_{Deep}/ D_{SPCC}):1.50±0.33 (Table 7.4B).

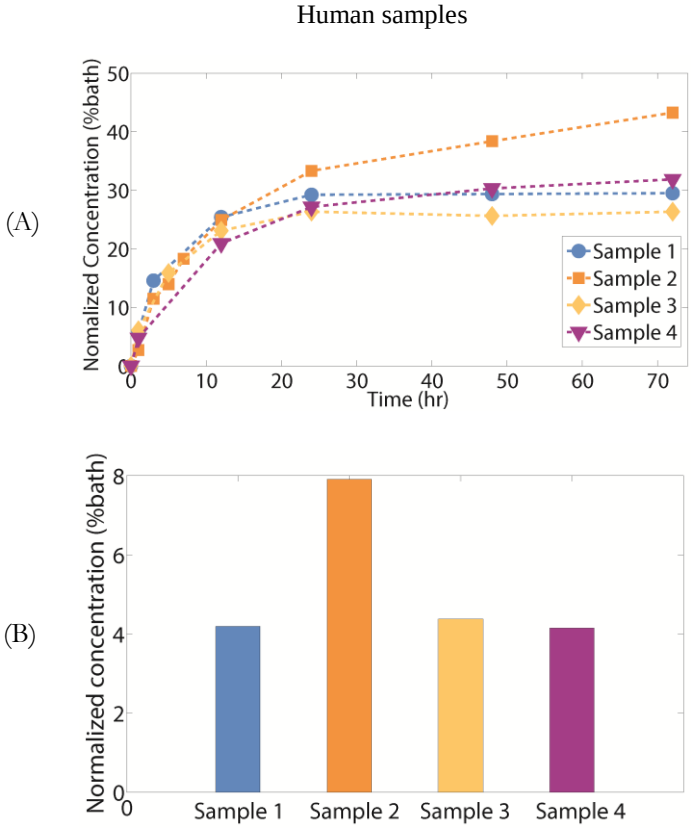

Figure 7.2. Plot of A) normalized concentration versus time of iodixanol in human cartilage and B) normalized equilibrium concentration in human subchondral plate/calcified cartilage.

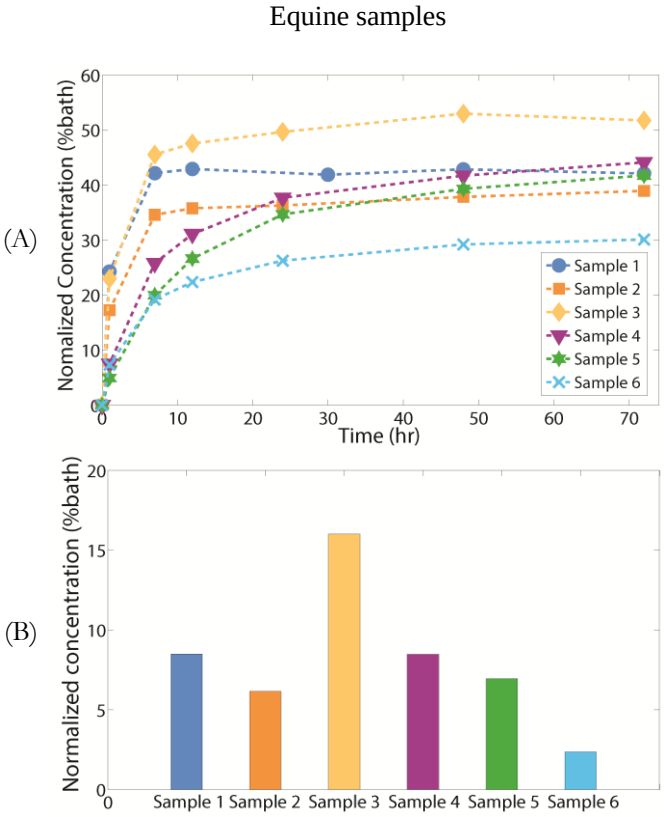

Figure 7.3. Plot of A) normalized concentration versus time of iodixanol in equine cartilage and B) normalized equilibrium concentration in equine subchondral plate/calcified cartilage.

Human samples

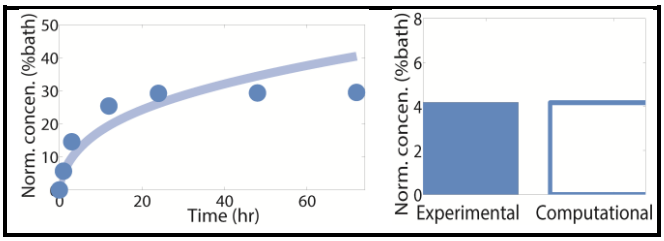

Sample 1

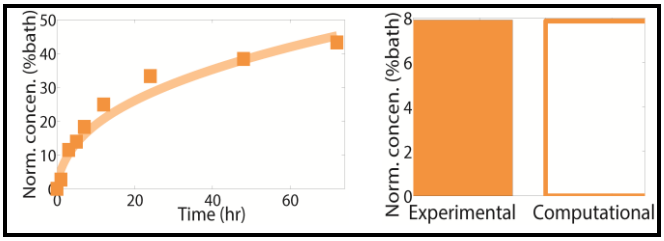

Sample 2

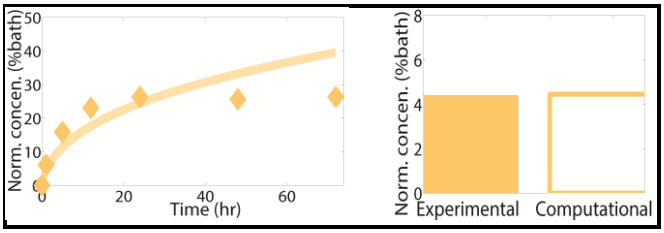

Sample 3

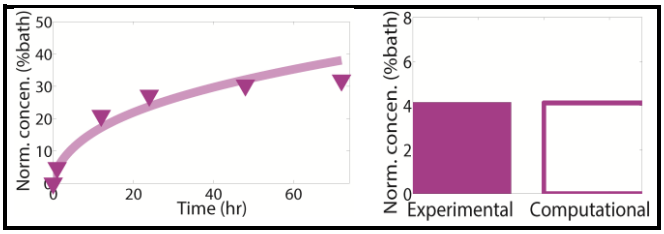

Sample 4

Figure 7.4. Experimental (symbols) and simulated (lines) normalized concentration versus time for human cartilage samples and normalized computational and experimental equilibrium concentration for human subchondral plate/calcified cartilage.

Equine samples

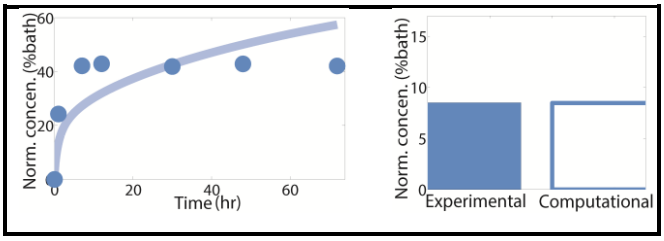

Sample 1

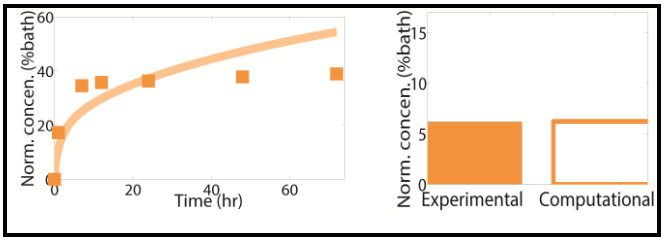

Sample 2

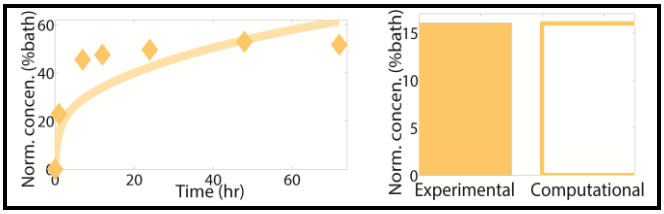

Sample 3

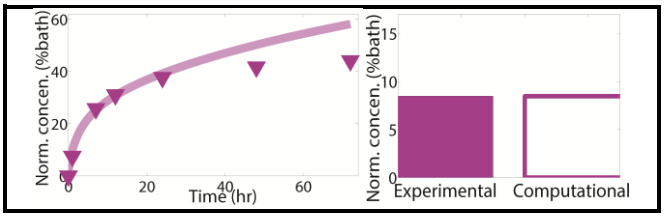

Sample 4

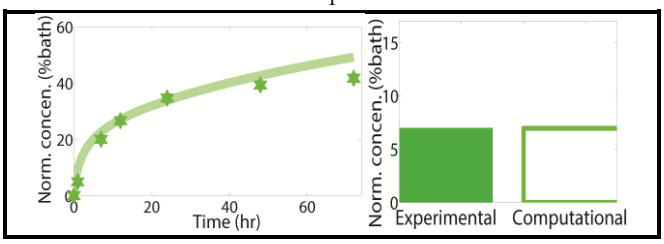

Sample 5

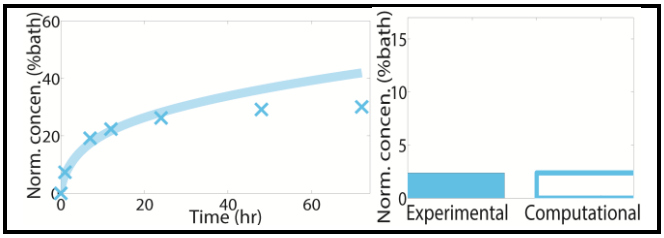

Sample 6

Figure 7.5. Experimental (symbols) and simulated (lines) normalized concentration versus time for equine cartilage samples and normalized computational and experimental equilibrium concentration for equine subchondral plate/calcified cartilage.

Table 7.2. A) RMSE and R^2 to compare the experimental and simulation solute concentration versus time in cartilage and RMSE to compare the experimental and simulation normalized equilibrium concentration in subchondral plate for A) human samples and B) equine samples.

(A)

		Human samples			
		Sample 1	Sample 2	Sample 3	Sample 4
Cartilage	R^2	0.86	0.98	0.85	0.95
	RMSE	0.0599	0.0281	0.0694	0.0377
Subchondral plate /calcified cartilage	RMSE	0.0002	0.0005	0.0007	0.0003

(B)

		Equine samples					
		Sample 1	Sample 2	Sample 3	Sample 4	Sample 5	Sample 6
Cartilage	R^2	0.73	0.80	0.83	0.96	0.97	0.95
	RMSE	0.1114	0.0906	0.1061	0.0680	0.0398	0.0574
Subchondral plate /calcified cartilage	RMSE	0.0003	0.0005	0.0004	0.0001	0.0003	0.0001

Table 7.3. Diffusion coefficients obtained from the multi-zone computational model for superficial, middle, deep and subchondral plate/calcified cartilage zones A) human samples B) equine samples.

	Diffusion coefficient ($\mu m^2/s$), human samples			
	Sample 1	Sample 2	Sample 3	Sample 4
$D_{Superficial}$	6.00	8.00	3.00	5.54
D_{Middle}	1.70	3.10	1.30	2.20
D_{Deep}	1.50	1.50	1.20	1.94
D_{SPCC}	1.20	1.00	0.95	1.72

	Diffusion coefficient ($\mu m^2/s$), equine samples					
	Sample 1	Sample 2	Sample 3	Sample 4	Sample 5	Sample 6
$D_{Superficial}$	4.35	4.25	4.80	3.40	3.00	7.00
D_{Middle}	0.4	0.50	0.44	0.60	0.40	1.30
D_{Deep}	0.18	0.43	0.18	0.55	0.35	0.95
D_{SPCC}	0.12	0.30	0.09	0.48	0.25	0.90

Table 7.4. The ratio of diffusion coefficients of superficial zone to middle zone $(D_{Superficial} / D_{Middle})$, middle zone to deep zone (D_{Middle} / D_{Deep}) and deep zone to subchondral plate/calcified cartilage (D_{Deep} / D_{SPCC}) for A) human samples and B) equine samples.

(A)	Human samples			
	Sample 1	Sample 2	Sample 3	Sample 4
$D_{Superficial}/D_{Middle}$	3.53	2.58	2.31	2.52
D_{Middle}/D_{Deep}	1.13	2.07	1.08	1.13
D_{Deep}/D_{SPCC}	1.25	1.50	1.27	1.13

(B)	Equine samples					
	Sample 1	Sample 2	Sample 3	Sample 4	Sample 5	Sample 6
$D_{Superficial}/D_{Middle}$	10.75	8.5	10.90	5.66	7.50	5.38
D_{Middle}/D_{Deep}	2.22	1.16	2.44	1.09	1.14	1.37
D_{Deep}/D_{SPCC}	1.50	1.43	2.00	1.14	1.40	1.05

7.4. Discussion

In the present study, we provided a quantitative approach to study neutral solute transport across cartilage and the subchondral bone plate based on a multi-zone biphasic-solute finite element model. We have previously shown the capability of the multi-zone biphasic-solute models in obtaining the diffusion coefficients in different equine cartilage zones when a finite bath of neutral solute is placed on the cartilage surface (chapter 3) [10]. In this study, we showed that for human samples (maximum thickness of 2.8 mm) and equine samples (maximum thickness of 2.1 mm) 72 hours of the diffusion experiments not only enabled determining the diffusion coefficient of the deep zone as well as that of the subchondral plate/calcified cartilage. The diffusion coefficients obtained in this study were the first reported for both human and equine osteochondral plugs using finite-bath multi-zone biphasic-solute models. Since the thickness of the cartilage used in the previous study was relatively high (~2.8 mm), the diffusion coefficient of the deep zone of cartilage could not be exclusively calculated using concentration-time curves (up to 48 hours). The rationale behind it is likely due to the insufficient time of the contrast to penetrate through the entire cartilage and bon layer (48 hours), which caused the diffusive resistance of the deep zone to overcome the required driving force.

In this study, diffusion coefficients found in different zones of uncalcified cartilage and subchondral plate/calcified cartilage in human samples were generally higher than those in equine samples (Table 7.3). However, the ratios of diffusion coefficients (D_{Middle}/ D_{Deep} and D_{Deep}/ D_{SPCC}) between human and equine samples were highly comparable (Table 7.4). The diffusion coefficients obtained for equine calcified cartilage/subchondral plate (femoral condyle) in the current study were in the same order of magnitude

compared to diffusion coefficient of equine calcified cartilage (metacarpophalangeal joint) in another study (using fluorescent trace distribution), although the molecular size of the molecule in our study (1550 Da) was four times larger (~ 400 Da) [5]. It should be noted that micro-CT experiments in our study did not allow differentiation between calcified cartilage and subchondral plate. Therefore, the values that we reported as the diffusion coefficients of the subchondral plate/calcified cartilage are in fact representative for the entire unit of calcified cartilage and subchondral bone plate. In spite of this mismatch, the values we obtained for the subchondral plate/calcified cartilage and the previously reported values fall within the same order of magnitude although the applied methods and the sample sources were different [4, 5]. The diffusion coefficient of the calcified cartilage is expected to be lower than that of subchondral plate in healthy joints since porosity of the calcified cartilage is lower (according to our high resolution micro-CT data (chapter 6) [8]) and therefore restricts the solute transport more considerably. However, upon transport across calcified cartilage, the thickness of the subchondral plate could also affect the transport due to mass transfer resistance imposed by the materials in the subchondral plate. In our previous study (chapter 3) [10] where equine cartilage (2.8 mm in thickness) was split into three distinct zones with their recommended water content similar to the current study we obtained extremely accurate fits (nine tests, average R^2=0.98) over the experimental data using multi-zone biphasic-solute model. In the current study, we observed a correlation between accuracy of the fit and cartilage thickness (Table 7.1 and 7.2). This indicates that thin samples may represent different zonal features i.e. water content and zonal percentages which contributed to larger errors associated with the computational fits (Table 7.2 and Figure 7.4 and 7.5). As a result, determination of exact properties of cartilage zones particularly for thin samples is recommended for future

diffusion-related works. Furthermore, we believe that accurate determination of diffusion coefficients of the cartilage zones requires knowledge of flux at the cartilage-subchondral bone interface as considered in this study. Therefore, failure in consideration of the flux boundary condition at the cartilage-subchondral plate/calcified cartilage might cause the obtained diffusion coefficients of cartilage to be error-prone. Although the loaded volume of the finite-bath was slightly less in the current study compared to the previous study (chapter 3) [10], the diffusion coefficients for the equine cartilage fell under a similar range as expected. The design of the current study implies that two different samples were used: human samples (slightly osteoarthritic) and equine samples (healthy), thereby the obtained diffusion coefficients for the healthy human samples may be slightly different, and perhaps higher than healthy human samples likely due to elevated permeability and disorientation and damage of collagen fibrils and proteoglycans. The solute used in this study although larger in size than in the previously used studies, still does not lie within the range of most signaling molecules, therefore, more research needs to emerge to account for the effect of size on the transport across articular cartilage and subchondral bone. The effect of solute's charge, particular positive, may be addressed in the future work to amplify agent delivery through the cartilage down to the subchondral plate.

In conclusion, the developed multi-zone biphasic-solute computational model enabled determining the diffusion coefficients of neutral solutes across cartilage and osteochondral interface. The findings of the current work deepen our understanding of how each layer within the cartilage and subchondral bone plate communicates when a neutral solute is administered on the articulating surface of cartilage.

7.5. REFERENCES

1. Botter S.M., van Osch G.J., Clockaerts S., Waarsing J.H., Weinans H., van Leeuwen J.P., *Osteoarthritis induction leads to early and temporal subchondral plate porosity in the tibial plateau of mice: an in vivo microfocal computed tomography study.* Arthritis Rheum, 2011. **63**(9): p. 2690-9.
2. Westacott C., *Interactions between subchondral bone and cartilage in OA. Cells from osteoarthritic bone can alter cartilage metabolism.* J Musculoskelet Neuronal Interact, 2002. **2**(6): p. 507-9.
3. Pan J., Wang B., Li W., Zhou X., Scherr T., Yang Y., Price C., Wang L., *Elevated cross-talk between subchondral bone and cartilage in osteoarthritic joints.* Bone, 2012. **51**(2): p. 212-7.
4. Pan J., Zhou X., Li W., Novotny J.E., Doty S.B., Wang L., *In Situ measurement of transport between subchondral bone and articular cartilage.* Journal of orthopaedic research : official publication of the Orthopaedic Research Society, 2009. **27**(10): p. 1347-1352.
5. Arkill K.P., Winlove C.P., *Solute transport in the deep and calcified zones of articular cartilage.* Osteoarthritis Cartilage, 2008. **16**(6): p. 708-14.
6. Galbusera F., Brayda-Bruno M., Wilke H.-J., *Is post-contrast MRI a valuable method for the study of the nutrition of the intervertebral disc?* Journal of Biomechanics, 2014. **47**(12): p. 3028-3034.
7. Sélard É., Shirazi-Adl A., Urban J.P.G., *Finite Element Study of Nutrient Diffusion in the Human Intervertebral Disc.* Spine, 2003. **28**(17): p. 1945-1953.
8. Pouran B., Arbabi, V., Weinans, H., Zadpoor, A.A, *Solute transport at the interface of cartilage and subchondral bone plate: effect of micro-architecture.* (under review), 2016.
9. Botter S.M., *Dynamic Subchondral Bone Changes in Murine Models of Osteoarthritis.* PhD thesis, 2010.
10. Arbabi V., Pouran B., Weinans H., Zadpoor A.A., *Transport of Neutral Solute Across Articular Cartilage: The Role of Zonal Diffusivities.* Journal of Biomechanical Engineering, 2015. **137**(7): p. 071001-071001.
11. Arbabi V., Pouran B., Weinans H., Zadpoor A.A., *Multiphasic modeling of charged solute transport across articular cartilage: Application of multi-zone finite-bath model.* Journal of Biomechanics, 2016.
12. Mauck R.L., Hung C.T., Ateshian G.A., *Modeling of Neutral Solute Transport in a Dynamically Loaded Porous Permeable Gel: Implications for Articular Cartilage Biosynthesis and Tissue Engineering.* Journal of biomechanical engineering, 2003. **125**(5): p. 602-614.
13. Ateshian G.A., Albro M.B., Maas S., Weiss J.A., *Finite element implementation of mechanochemical phenomena in neutral deformable porous media under finite deformation.* J Biomech Eng, 2011. **133**(8): p. 081005.
14. Ateshian G.A., *On the Theory of Reactive Mixtures for Modeling Biological Growth.* Biomechanics and modeling in mechanobiology, 2007. **6**(6): p. 10.1007/s10237-006-0070-x.

15. Ateshian G.A., Maas S., Weiss J.A., *Finite element algorithm for frictionless contact of porous permeable media under finite deformation and sliding.* J Biomech Eng, 2010. **132**(6): p. 061006.
16. Ateshian G., Weiss J., *Finite Element Modeling of Solutes in Hydrated Deformable Biological Tissues*, in *Computer Models in Biomechanics*, G.A. Holzapfel and E. Kuhl, Editors. 2013, Springer Netherlands. p. 231-249.
17. Sophia Fox A.J., Bedi A., Rodeo S.A., *The Basic Science of Articular Cartilage: Structure, Composition, and Function.* Sports Health, 2009. **1**(6): p. 461-468.
18. Nair N., Kim W.J., Braatz R.D., Strano M.S., *Dynamics of surfactant-suspended single-walled carbon nanotubes in a centrifugal field.* Langmuir, 2008. **24**(5): p. 1790-5.
19. Li B., Aspden R.M., *Mechanical and material properties of the subchondral bone plate from the femoral head of patients with osteoarthritis or osteoporosis.* Ann Rheum Dis, 1997. **56**(4): p. 247-54.
20. Ateshian G.A., Maas S., Weiss J.A., *Solute transport across a contact interface in deformable porous media.* Journal of Biomechanics, 2012. **45**(6): p. 1023-1027.

CHAPTER 8

APPLICATION OF MULTIPHYSICS MODELS TO EFFICIENT DESIGN OF EXPERIMENTS OF SOLUTE TRANSPORT ACROSS ARTICULAR CARTILAGE*

* This chapter is submitted as a scientific paper:

Pouran B., Arbabi V., Weinans H., Zadpoor A.A. *Application of multiphysics models to efficient design of experiments of solute transport across articular cartilage*. 2016 (under review).

ABSTRACT

Transport of solutes helps to regulate normal physiology and proper function of cartilage in diarthrodial joints. Multiple studies have shown the effects of characteristic parameters such as concentration of proteoglycans and collagens and the orientation of collagen fibrils on the diffusion process. However, not much quantitative information and accurate models are available to help understand how the characteristics of the fluid surrounding articular cartilage influence the diffusion process. In this study, we used a combination of micro-computed tomography experiments and biphasic-solute finite element models to study the effects of three parameters of the overlying bath on the diffusion of neutral solutes across cartilage zones. Those parameters include bath size, degree of stirring of the bath, and the size and concentration of the stagnant layer that forms at the interface of cartilage and bath. Parametric studies determined the minimum of the finite bath size for which the diffusion behavior reduces to that of an infinite bath. Stirring of the bath proved to remarkably influence neutral solute transport across cartilage zones. The well-stirred condition was achieved only when the ratio of the diffusivity of bath to that of cartilage was greater than ≈1000. While the thickness of the stagnant layer at the cartilage-bath interface did not significantly influence the diffusion behavior, increase in its concentration substantially elevated solute concentration in cartilage. Sufficient stirring attenuated the effects of the stagnant layer. Our findings could be used for efficient design of experimental protocols aimed at understanding the transport of molecules across articular cartilage.

8.1. INTRODUCTION

Synovial joints provide an excellent enclosed environment where exchange of macromolecules, small ions and solutes as well as oxygen between articular cartilage, synovium and subchondral bone can efficiently take place [1-3]. Delivery of therapeutic agents and solutes to articular cartilage and understanding of pathophysiology of the diseased synovial joints rely on various parameters including volume, viscosity and movement of the synovial fluid as well as the status of healthiness of articular cartilage [4-7]. Active mechanical loading of joints increases the transport of molecules by providing well-mixed synovial fluid and convection [8, 9]. Recently, efficient design of large cartilage constructs were accomplished by providing sufficient nutrient supply as well as enhancement of mechanical stirring in the medium [10, 11]. The micro-structure of articular cartilage including orientation and concentration of essential macromolecules namely collagen type II and proteoglycans across its thickness affects solute transport remarkably [7, 12-14]. Therefore, past experimental and computational efforts focusing on the diffusion across cartilage have acknowledged the inhomogeneity of cartilage and implemented it [12, 13]. However, the diffusion phenomena are not only linked with the conditions of articular cartilage but also with the characteristics of the overlying bath, which continuously supplies solutes to articular cartilage [15].

Several studies have tried to use well-stirred infinite baths of solutes for experiments aimed at understanding the diffusion behavior of cartilage [16, 17]. That is because application of the well-stirred finite bath boundary conditions simplifies the theoretical models that are needed for interpretation of the obtained data. However, creating infinite baths for the diffusion

experiments involving contrast enhanced micro-computed tomography (micro-CT) may require large volumes of contrast agent solution that the x-ray beam has to penetrate through. That adversely affects the accuracy of the micro-CT readings due to the beam hardening effect particularly when using concentrated contrast agent solutions. Therefore, the concept of finite baths of contrast agents have been recently introduced and computationally implemented to study the diffusion of neutral and charged solutes across articular cartilage [7, 12, 13]. The boundary between finite and infinite bath is, however, not clear and the errors introduced by assuming infinite bath conditions when the bath is finite have not been quantified before.

The assumption of a well-stirred bath is also difficult to realize in actual experiments, because that requires continuous stirring of the contrast agent solution inside the micro-CT chamber, which is not performed in the vast majority of the experiments performed to date. It is therefore important to understand how deviations from this assumption could influence interpretation of the experimental data. Finally, a stagnant layer forms at the interface of solid-liquid systems including the bath-cartilage interface in diffusion experiments. This stagnant layer has been studied analytically and is shown to change the diffusion characteristics [15, 18]. Nevertheless, most studies ignore the stagnant layer when interpreting the results of diffusion experiments.

In this study, we consider the three above-mentioned bath attributes, namely size of the bath, the stirring condition of the bath, and the proprieties of the stagnant layer, and quantify their effect on the computational results of models describing solute transport across articular cartilage. Towards that end, we use a combination of micro-CT experimental data and multi-zone computational biphasic-solute models. Our findings are expected to enhance the understanding of solute transport across cartilage

under various boundary conditions and provide a platform to more robustly design diffusion experiments.

8.2. METHODOLOGY

8.2.1. EXPERIMENTS

The experimental setup has been described in our previous study (chapter 5) [7]. Briefly, cylindrical osteochondral plugs (n=3, diameter=8.5 mm) were extracted from fresh femora's of 6-10 year-old horses post euthanasia. Finite volumes (650 μL) of a neutral contrast agent (iodixanol, MW=1560 g/mol, 420 mM) with osmolalities of 290 mOsm/kg water and 600 mOsm/kg water were injected on top of the cartilage surface, while iodixanol diffusion from lateral direction was restricted by wrapping the sample using heat-shrinking plastic sleeve. Temporal diffusion of iodixanol (up to 48 hours) was then monitored using a micro-CT machine (*Quantum FX, Perkin elmer, USA*, 40×40×40 μm^3 voxel size, scan time of 3 min, tube voltage of 90 kV and tube current of 180 μA) in a field of view consisting of bath, cartilage and subchondral bone. The grey values in the bath and cartilage were then converted to iodixanol concentration using a linear function presented previously [7, 13]. Post-injection of iodixanol on cartilage surface, thickness and concentration of stagnant layer forming at the cartilage-bath boundary as well as overlying homogeneous layer of the bath were measured (*imageJ v1.47*) and fed to the computational model (Figure 8.1A).

8.2.2. FINITE ELEMENT MODELING

Biphasic-solute models can accurately describe the transport of neutral solutes across articular cartilage [19] and can describe complex boundary conditions such as non-well stirred bath as well as solute transport across inhomogeneous tissues. The constitutive

equations of biphasic-solute model implemented in FEBio 2.4.1 have been presented extensively [19].

8.2.2.1. GEOMETRY AND BOUNDARY CONDITIONS

The entire height of the bath was 14 mm and the thickness of cartilage was 2.7 mm (Figure 8.1B) where the cartilage layer was, split into three different homogeneous zones i.e. superficial (20% of cartilage thickness), middle (50% of cartilage thickness) and deep (30% of cartilage thickness) [14] zones to account for the inhomogeneity of cartilage across its thickness [13]. We used a mesh consisting of eight-node trilinear hexahedral elements, that was further refined near the interfaces.

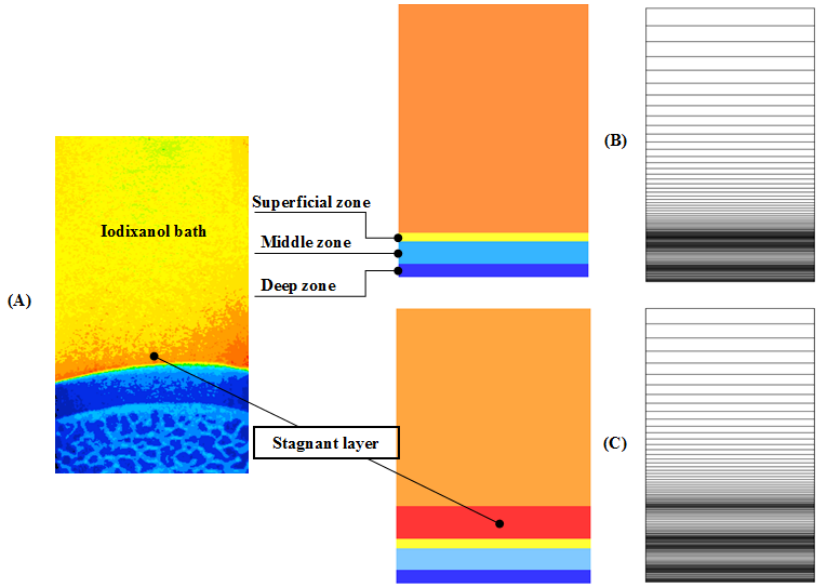

Figure 8.1. (A) Iodixanol finite bath including the stagnant layer, articular cartilage and subchondral bone are shown (B) Finite element model consisting of finite bath, superficial, middle and deep zones of articular cartilage (C) Finite element model including the stagnant layer.

We applied the no-flux boundary condition at the cartilage-bone interface and insulated the other faces of cartilage and bath to enable studying axial solute diffusion.

8.2.2.2. PHYSICAL AND MECHANICAL PROPERTIES

Both bath and cartilage were modeled as neo-Hookean materials with a Young's modulus of 10 MPa, hydraulic permeability of 10^{-3} mm^4/Ns and effective solute solubility of 1 according to our previous studies [12, 13]. The water content of each cartilage zone varied from 80% in the superficial zone and 70% in the middle zone to 60% in the deep zone [14]. The stagnant layer was tied to the overlying bath while it maintained contact with the underlying cartilage (Figure 8.1C). A prescribed displacement of 0.001 mm was used to ensure the stability of contact between boundaries.

8.2.2.3. PARAMETRIC STUDY

In our previous study, we fitted biphasic-solute model to experimental concentration versus time data to obtain the diffusivity of cartilage zones (chapter 3) [13]. Based on those results, we performed parametric studies to investigate the effects of bath size, bath stirring and stagnant layer on the diffusion behavior. To study the effect of bath size with identical solute concentrations on diffusion, different length ratios of bath to cartilage were used which spanned from 1 to 100 while cartilage thickness was maintained constant at 2.7 mm, reflecting the actual experiment design. Effect of bath stirring was investigated by step-wise increase of solute diffusivity in the bath relative to superficial zone of cartilage (diffusivity ratio varying from 10 to 10000) until fully well-stirred condition is satisfied. Increase in diffusivity ratio is equivalent to higher bath stirring while decrease in it could make the bath deviate from the conventional well-stirred assumption. To assess the effects of thickness and concentration of possible

stagnant layer formed at the cartilage-bath interface, computational models with different thicknesses and concentrations of the stagnant layer were built to perform a parametric study whose parameter ranges were based on the actual initial concentration and thickness of the stagnant layer observed during our experiments in six different conditions [7, 13].

8.3. RESULTS

8.3.1. EFFECT OF BATH SIZE (PARAMETER α)

Based on the previous studies (chapters 3 and 5) [7, 13] experimental concentration versus time for one sample is illustrated (Figure 8.2A) to provide a better understanding of the influence of bath size on diffusion behavior across articular cartilage. Concentrations versus time curves were plotted in different length ratios of bath to cartilage (α) ranging from 1 to 100, which covers a wide spectrum from a small finite bath to an infinite bath. Increase in bath size showed increase in the predicted concentrations up to 48 hours (Figure 8.2A). Ratios greater than 5.18 (previous experimental setup) resulted in root mean square error (RMSE) of 2e-6 and R^2 of 1 compared to length ratio of 10, yet, the solutions for length ratios above 10 converged to diffusion behavior corresponding to infinite baths (RMSE=2e-7 and R^2=1). RMSE values between solution at each length ratio and length ratio of 10 (infinite bath) indicate that length ratio of 5.18 (previous experimental setup) behaves the same as infinite bath (Table 8.1). To examine the effect of bath size on diffusion in different cartilage layers, we plotted the concentration versus time curves at a distance of 0.4 mm, 0.74 mm and 1.46 mm from the cartilage surface in an extended time period of 96 hours for length ratios 1 and 5.18 (equivalent to infinite bath). We observed lower concentration values in different cartilage zones corresponding to length ratio 1 compared to those corresponding to length ratio

5.18 at different time points including final time point (Figure 8.2B).

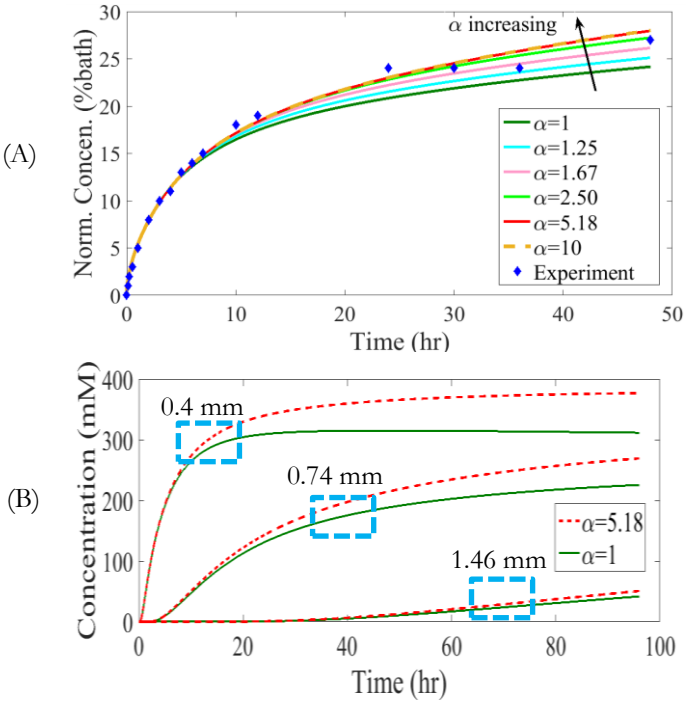

Figure 8.2. (A) Effect of length ratio of bath to cartilage (α) on concentration vs. time curves (B) Effect of length ratio of bath to cartilage (α) on zonal concentration vs. time curves at 0.4, 0.74 and 1.46 mm distance from the cartilage surface.

Table 8.1. RMSE to compare the concentration vs. time curves of different bath sizes with concentration vs. time curve of an infinite bath (α =10).

Length ratio of bath to cartilage (α)	RMSE
1.00	0.022192
1.25	0.011623
1.67	0.004247
2.50	0.000592
5.18	0.000002

8.3.2 Effect of stirring (parameter β)

A wide range of diffusivity ratios of bath to cartilage (β) from 10 to 10000 including the actual experimental setup $(\beta = 33.33)$ were used. RMSE and R^2 between concentration versus time curves of diffusivity ratio of 1000 and 10000 were 0.00018 and 1. Greater than 1000-fold diffusivity ratio resulted in fully stirred bath condition (Figure 8.3A) and the degree of stirring strongly influenced the concentration versus time curves (Table 8.2).

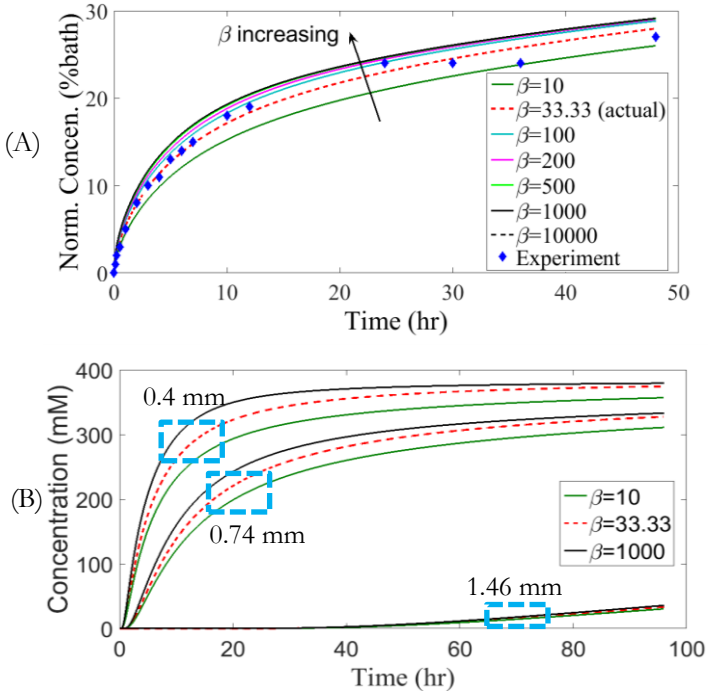

Figure 8.3. (A) Effect of bath stirring (β) on concentration vs. time curves. Note that the curves of β=1000 and β=10000 are almost overlapping (B) Effect of bath stirring (β) on zonal concentration vs. time curves at 0.4, 0.74 and 1.46 mm distance from the cartilage surface.

Concentration versus time curves for different cartilage layers at 0.4, 0.74 and 1.46 mm distance from cartilage surface explicitly demonstrate that more stirred bath generates higher concentration values in different time points across cartilage (Figure 8.3B).

Table 8.2. RMSE to compare the concentration vs. time of different degrees of stirring with curve-fitted concentration vs. time (actual bath diffusivity).

Stirring degree (β)	RMSE
10	0.0228
100	0.0078
200	0.0152
500	0.0229
1000	0.0265
10000	0.0304

8.3.3 EFFECT OF STAGNANT LAYER (PARAMETER γ)

The micro-CT observations on diffusion of iodixanol within the bath in six cases (chapter 3 and 5) [7, 13] showed that the thickness of stagnant layer varied from 1.6 to 2 mm and the concentration ratio of stagnant layer to overlying bath (γ) varied from 1.1 to 1.15 (iodixanol injection). To perform the parametric study, the maximum thickness of 2 mm and maximum concentration ratio of 1.15 were used and compared with the cases where stagnant layer was not considered (curve-fitting situation). Considering γ values of 1.5 and 2 completed the parametric study. As γ increased, the level of the concentration versus time curves increased (Figure 8.4A), while no considerable changes were observed when comparing curve fitted data without considering stagnant layer and the concentration versus time data with maximum realistic

concentration ratio of γ=1.15 and stagnant layer thickness of 2 mm (Table 8.3).

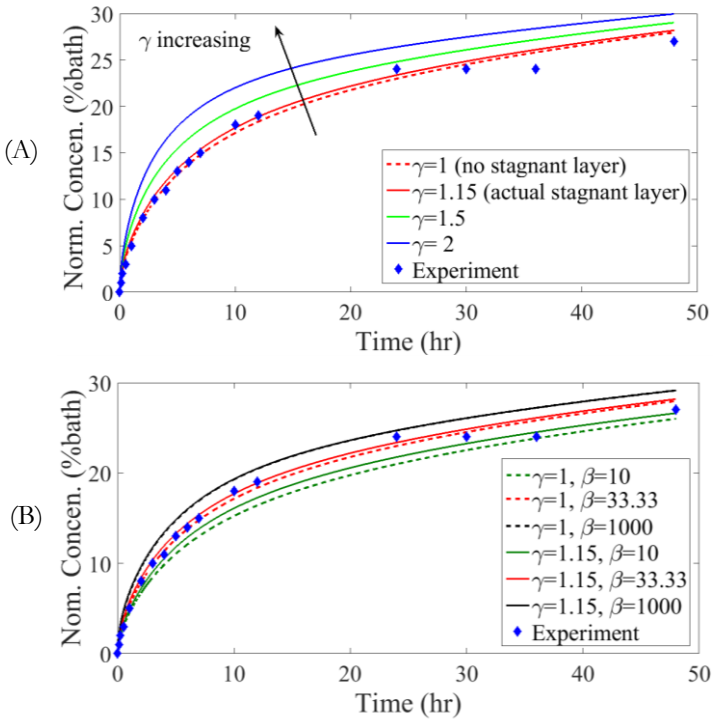

Figure 8.4. (A) Effect of concentration ratio of stagnant layer to overlying bath (γ) on concentration vs. time curves where γ=1.15 corresponds to maximum realistic concentration ratio of stagnant layer to overlying bath. (B) Effect of stirring (β) with or without stagnant layer on concentration vs. time curves.

Table 8.3. RMSE to compare the concentration vs. time of different concentration ratios of stagnant layer to overlying bath with the concentration vs. time of the case with no stagnant layer.

Concentration ratio of stagnant layer to overlying bath (γ)	RMSE
1.15	0.0018
1.50	0.0250
2.00	0.0300

Given the stagnant layer with a thickness of 2 mm and γ=1.15, stirring strongly affected its stability and diminished the effect of formation of the stagnant layer on the diffusion behavior (Figure 8.4B and Table 8.4). Changing the thickness of stagnant layer from 2 mm to 3 mm while keeping *a* and γ at 5.18 and 1.15 respectively did not affect the total concentration versus time curves (Figure 8.5A) nor the zonal ones (Figure 8.5B).

Table 8.4. RMSE to compare the concentration vs. time of different degrees of stirring (if γ=1.15) with the case with no stagnant layer.

Stirring effect on stagnant layer (β) (if γ=1.15)	RMSE
10	0.003818
33.33	0.001835
1000	0.000063

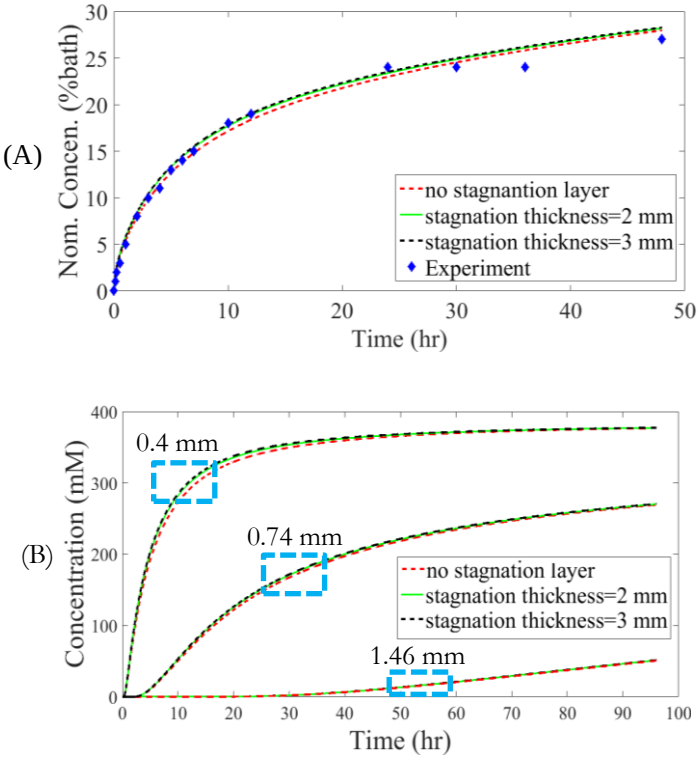

Figure 8.5. (A) Effect of stagnation thickness on concentration vs. time curves (if $\gamma = 1.15$) (B) Effect of stagnation thickness on zonal concentration vs. time curves (if $\gamma = 1.15$) at 0.4, 0.74 and 1.46 mm distance from the cartilage surface.

.

8.4. Discussion

The primary objective of this research was to develop a parametric computational study based on experimental micro-CT observations to investigate the effects of bath size, bath stirring and stagnant layer formation on the diffusion of neutral solutes across articular cartilage. Our results of bath size effect revealed that too low length ratio of bath to cartilage may lead to

insufficient penetration of solutes and thereby reduced equilibrium concentration. Furthermore, increase of bath size up to a convergence value seems to be necessary to ensure of sufficient supply of solute into the cartilage. Comparing the computational fit to the experimental concentration versus time curves (ratio of 5.18) with the curves corresponding to higher ratios showed that minimum approximate ratio of 5 can ensure of infinite diffusion behavior (Figure 8.2A and Table 8.1). This highlights the importance of considering the minimum solute required to reach equilibrium prior to designing the experiments. Appropriate selection of bath size, therefore, guarantees optimal required amount of solute as well as volume of the bath, which in case of micro-CT experiments can be of paramount significance chiefly due to possible effects of beam hardening [20] in large baths of contrast agent. The optimal ratio presented here may vary slightly depending on the concentration (compactness) of collagen and GAG, orientation of collagen fibrils and water content, which affect the solute partitioning [21].

The degree of stirring as well as formation of stagnant layer at bath-cartilage interface play roles in determining the maximum rate at which solute can be transported to the tissue, thereby became the second and third factors considered in this research.

In our study we investigated the stirring effect by changing the diffusivity ratio of bath to the curve fitted diffusivity of the cartilage superficial layer. Increasing the diffusivity of the bath relative to cartilage simulates different degrees of stirring without including the additional convection effects (vortex generation) commonly generated by mechanical stirrers. We observed that, as expected, stirring could substantially facilitate the transport of neutral solute across cartilage. Above 1000-factor higher diffusivity in the bath than in cartilage potentially makes the assumption of well-stirred condition legitimate (Figure 8.3A). The zonal influence

of stirring on diffusion decreased from the surface to the bottom of cartilage suggesting that solute transfer can be more effectively augmented in the superficial and middle zones (Figure 8.3B). Increasing the stirring lowers the mass transfer resistance in the bath, therefore allowing more solutes to penetrate into the superficial zone, although lower diffusivity of deeper layers dampens lowered mass transfer resistance in the bath side. Therefore, one may apply other approaches e.g. using positively charged solutes to target the deeper cartilage zones rather than inducing stirring mechanically, although surface of cartilage may be more easily accessible to the solutes post-stirring.

Based on the experimental observations, the typical concentration and thickness of stagnant layer on the cartilage-bath interface were obtained and applied to conduct parametric study. We showed that failure to consider the exact concentration of stagnant layer only causes small errors in tracking the concentration versus time curves as compared to the actual experimental situation (our experimental observations) (Figure 8.4A). However, care should be taken when the stagnant layer concentration lies highly above that of the overlying bath (Figure 8.4A), which might be the case in other experiments and may cause large deviations in e.g. estimation of equilibrium concentration. We also showed that when realistic concentration ratio of stagnant layer to the overlying bath is used, at high stirring rates, the role of the stagnant layer becomes minimal (Figure 8.4B). This can be explained in the way that high stirring power more easily dissipates the formed boundary layer at the cartilage-bath interface and therefore homogenizes the bath and minimizes the effect of stagnant layer. Finally, our findings support that the thickness of the stagnant layer has little effect on the concentration versus time curves with lowest effect on the equilibrium concentration (Figure 8.5). This infers that formation of stagnant layer as long as it does not cause large concentration

gradients within the bath, does not affect the diffusion attributes of neutral solutes although this may be different for charged solutes [12] due to their repulsive-driven diffusion that may even facilitate the transport into cartilage. Surface chemistry of articular cartilage, as the substrate changes the solute-substrate interactions which affects the rate of solute adsorption and possibly the stability and formation of stagnant layers [22]. Moreover, the size of the solutes and the viscosity of the solution influence the diffusivity within the bath that can affect the size of unstirred layer at the interfaces [18].

This study is associated with some limitations with respect to experiments and computations. The presented study strived to provide a realistic approach on diffusion problems. However, minor assumptions such as considering uniform stagnant layer in the biphasic-solute model were made. The findings of the study may be extended in the future works to investigating the effects of bath size, stirring and stagnant layer formation on charged solutes.

8.5. CONCLUSIONS

The presented study provided an opportunity to study the effects of bath size, degree of bath stirring and stagnant layer on the diffusion of a neutral solute with the aid of multi-zone finite element modeling. Degree of stirring and size of the bath as well as concentration of the stagnant layer relative to overlying bath concentration were identified as the dominant factors affecting neutral solute transport across articular cartilage. The findings of this study may be used in robust design of diffusion experiments particularly when cartilage as the tissue type is used.

8.6. REFERENCES

1. Wang Y., Wei L., Zeng L., He D., Wei X., *Nutrition and degeneration of articular cartilage.* Knee Surg Sports Traumatol Arthrosc, 2013. **21**(8): p. 1751-62.
2. Maroudas A., *Distribution and diffusion of solutes in articular cartilage.* Biophys J, 1970. **10**(5): p. 365-79.
3. Zhang L., Gardiner B.S., Smith D.W., Pivonka P., Grodzinsky A., *The effect of cyclic deformation and solute binding on solute transport in cartilage.* Arch Biochem Biophys, 2007. **457**(1): p. 47-56.
4. Bajpayee A.G., Quadir M.A., Hammond P.T., Grodzinsky A.J., *Charge based intra-cartilage delivery of single dose dexamethasone using Avidin nano-carriers suppresses cytokine-induced catabolism long term.* Osteoarthritis Cartilage, 2016. **24**(1): p. 71-81.
5. Abazari A., Thompson R.B., Elliott J.A., McGann L.E., *Transport phenomena in articular cartilage cryopreservation as predicted by the modified triphasic model and the effect of natural inhomogeneities.* Biophys J, 2012. **102**(6): p. 1284-93.
6. Wang P., Li Y., Hu X.C., Cai X.L., Hou L.P., Wang Y.F., Hu J.H., Li Q.W., Suo L.J., Fan Z.G., Zhang B., *Cryoprotective effects of low-density lipoproteins, trehalose and soybean lecithin on murine spermatogonial stem cells - CORRIGENDUM.* Zygote, 2013: p. 1.
7. Pouran B., Arbabi V., Zadpoor A.A., Weinans H., *Isolated effects of external bath osmolality, solute concentration, and electrical charge on solute transport across articular cartilage.* (Under review), 2016.
8. Garcia A.M., Frank E.H., Grimshaw P.E., Grodzinsky A.J., *Contributions of Fluid Convection and Electrical Migration to Transport in Cartilage: Relevance to Loading.* Archives of Biochemistry and Biophysics, 1996. **333**(2): p. 317-325.
9. Entezari V., Bansal P.N., Stewart R.C., Lakin B.A., Grinstaff M.W., Snyder B.D., *Effect of mechanical convection on the partitioning of an anionic iodinated contrast agent in intact patellar cartilage.* J Orthop Res, 2014. **32**(10): p. 1333-40.
10. Cigan A.D., Nims R.J., Albro M.B., Vunjak-Novakovic G., Hung C.T., Ateshian G.A., *Nutrient channels and stirring enhanced the composition and stiffness of large cartilage constructs.* J Biomech, 2014. **47**(16): p. 3847-54.
11. Nims R.J., Cigan A.D., Albro M.B., Vunjak-Novakovic G., Hung C.T., Ateshian G.A., *Matrix Production in Large Engineered Cartilage Constructs Is Enhanced by Nutrient Channels and Excess Media Supply.* Tissue Eng Part C Methods, 2015. **21**(7): p. 747-57.
12. Arbabi V., Pouran B., Weinans H., Zadpoor A.A., *Multiphasic modeling of charged solute transport across articular cartilage: application of finite-bath model.* Journal of Biomechanics, 2016.
13. Arbabi V., Pouran B., Weinans H., Zadpoor A.A., *Transport of Neutral Solute Across Articular Cartilage: The Role of Zonal Diffusivities.* Journal of Biomechanical Engineering, 2015. **137**(7): p. 071001-071001.

14. Sophia Fox A.J., Bedi A., Rodeo S.A., *The Basic Science of Articular Cartilage: Structure, Composition, and Function.* Sports Health, 2009. **1**(6): p. 461-468.
15. Torzilli P.A., Askari E., Jenkins J.T., *Water Content and Solute Diffusion Properties in Articular Cartilage*, in *Biomechanics of Diarthrodial Joints*, A. Ratcliffe, S.-Y. Woo, and V. Mow, Editors. 1990, Springer New York. p. 363-390.
16. Tuomo S.S., Harri T.K., Jukka S.J., Thomas M.Q., Miika T.N., Juha T., *Diffusion and near-equilibrium distribution of MRI and CT contrast agents in articular cartilage.* Physics in Medicine and Biology, 2009. **54**(22): p. 6823.
17. Kokkonen H.T., Jurvelin J.S., Tiitu V., Toyras J., *Detection of mechanical injury of articular cartilage using contrast enhanced computed tomography.* Osteoarthritis Cartilage, 2011. **19**(3): p. 295-301.
18. Pohl P., Saparov S.M., Antonenko Y.N., *The size of the unstirred layer as a function of the solute diffusion coefficient.* Biophys J, 1998. **75**(3): p. 1403-9.
19. Mauck R.L., Hung C.T., Ateshian G.A., *Modeling of Neutral Solute Transport in a Dynamically Loaded Porous Permeable Gel: Implications for Articular Cartilage Biosynthesis and Tissue Engineering.* Journal of biomechanical engineering, 2003. **125**(5): p. 602-614.
20. Meganck J.A., Kozloff K.M., Thornton M.M., Broski S.M., Goldstein S.A., *Beam hardening artifacts in micro-computed tomography scanning can be reduced by X-ray beam filtration and the resulting images can be used to accurately measure BMD.* Bone, 2009. **45**(6): p. 1104-16.
21. Nimer E., Schneiderman R., Maroudas A., *Diffusion and partition of solutes in cartilage under static load.* Biophys Chem, 2003. **106**(2): p. 125-46.
22. Decker S.G., Moeini M., Chin H.C., Rosenzweig D.H., Quinn T.M., *Adsorption and distribution of fluorescent solutes near the articular surface of mechanically injured cartilage.* Biophys J, 2013. **105**(10): p. 2427-36.

CHAPTER 9

MULTIPHASIC MODELING OF CHARGED SOLUTE TRANSPORT ACROSS ARTICULAR CARTILAGE: APPLICATION OF MULTI-ZONE FINITE-BATH MODEL*

* This chapter is published as a scientific paper:

Arbabi V., Pouran B.,Weinans H., Zadpoor A.A. *Multiphasic modeling of charged solute transport across articular cartilage: application of finite-bath model.* Journal of Biomechanics, 0021-9290, 2016.

ABSTRACT

Charged and uncharged solutes penetrate through cartilage to maintain the metabolic function of chondrocytes and to possibly restore or further breakdown the cartilage tissue in different stages of osteoarthritis. In this study the transport of charged solutes across the various zones of cartilage was quantified, taken into account the physicochemical interactions between the solute and the cartilage constituents. A multiphasic finite-bath finite element (FE) model was developed to simulate equine cartilage diffusion experiments that used a negatively charged contrast agent (ioxaglate) in combination with serial micro-computed tomography (micro-CT) to measure the diffusion. By comparing the FE model with the experimental data both the diffusion coefficient of ioxaglate and the fixed charge density (FCD) were obtained. In the multiphasic model, cartilage was divided into multiple (three) zones to help understand how diffusion coefficient and FCD vary across cartilage thickness. The direct effects of charged solute-FCD interaction on diffusion were investigated by comparing the diffusion coefficients derived from the multiphasic and biphasic-solute models. We found a relationship between the FCD obtained by the multiphasic model and ioxaglate partitioning obtained from micro-CT experiments. Using our multi-zone multiphasic model, diffusion coefficient of the superficial zone was up to ten-fold higher than that of the middle zone, while the FCD of the middle zone was up to almost two-fold higher than that of the superficial zone. In conclusion, the developed finite-bath multiphasic model provides us with a non-destructive method by which we could obtain both diffusion coefficient and FCD of different cartilage zones. The outcomes of the current work will also help understand how charge of the bath affects the diffusion of a charged molecule and also predict the diffusion behavior of a charged solute across articular cartilage.

9.1. INTRODUCTION

Extracellular matrix of articular cartilage (AC) is a heterogeneous material that mainly consists of collagen fibrils, self-assembled aggrecan molecules that contain negatively charged glycosaminoglycans chains (GAGs), mobile counter-ions, and interstitial water [1, 2]. Understanding the interactions of external diffusing solutes with the cartilage matrix particularly charged solutes can help us better understand the role of GAG loss, damaged collagen (type II) fiber organization, and alterations of water content as hallmarks of osteoarthritis (OA) [3]. Two distinct mechanisms contribute to the diffusion of solutes in cartilage: I) steric hindrance imparted by GAG chains and collagen fibers and II) electrostatic interactions between FCD of GAG chains and solute's charge [1, 4]. Numerous studies have been investigating the transport of neutral and charged solutes such as drug carriers, computed tomography (CT) and magnetic resonance imaging (MRI) contrast agents across normal and osteoarthritic articular cartilage [5-13]. However, the vast majority of previous works have applied Fickean models to obtain the diffusion coefficient of cartilage. As described before [14], the use of purely Fickian models might result in inaccurate diffusion coefficients. In a recent study, we introduced a biphasic-solute finite-bath finite element model to establish a platform by which the diffusion coefficients of neutral solutes in different cartilage zones could be accurately determined (chapter 3) [14]. The finite-bath model enables us to I) minimize the effect of beam-hardening artifacts while employing micro-computed tomography technique (micro-CT) to study the diffusion of CT contrast agents [15, 16] II) minimize the required volume of bath solution III) maximize the spatial resolution of CT/MRI [17, 18], and IV) more realistically mimic the physiology of the diarthrodial joints given the fact that the volume of synovial fluid within the joints is finite.

Different methods were proposed to obtain the FCD of cartilage such as delayed gadolinium-enhanced MRI (dGEMRIC), nuclear magnetic resonance (NMR), indentation, conductivity and dimethylmethylene blue (DMMB) binding assay (destructive) [19-25], although many of them are based on the ideal Donnan theory that might cause inaccuracies when calculating FCD. Recently, a more advanced approach using combination of dGEMRIC and Monte Carlo simulations was developed to more precisely take the electrostatic interactions into account [26]. Moreover, accurate FCD calculation using known GAG content by DMMB binding assay requires accounting for ratio of Keratin sulfate (KS) to Chondroitin sulfate (CS) in the tissue [25]. Recently, multiphasic computational models in Abaqus using subroutines have emerged to study swelling behavior of healthy and OA cartilage [27-29]. Other related work applied user-developed codes based on multiphasic models to calculate diffusion coefficient and fixed charge density across cartilage [30].

We aim to introduce a multiphasic finite element model based on finite-bath model to account for the electrostatic interaction between a charged solute and the constituents of articular cartilage particularly FCD of GAGs. We fit the computational data to the contrast-enhanced micro-CT data to obtain the FCD and diffusion coefficients simultaneously in different zones within articular cartilage. The outcome of this work enables determination of FCD and diffusion coefficients non-destructive. Our findings based on the multiphasic multi-zone model will be compared with those obtained using biphasic-solute model to thoroughly investigate the effects of solute's charge and FCD i.e. electrostatic interactions on the molecular diffusion in cartilage.

9.2. METHODOLOGY
9.2.1. EXPERIMENTS

The design of experiments was described thoroughly in our previous works [14, 31]. A brief description of the experimental steps is provided in this study. Ioxaglate solutions (1268.9 g/mol, charge=-1, 420 mM, 600 mOsm/kg H_2O, *GE Healthcare, The Netherlands*) were prepared. Osteochondral plugs (n=3, cartilage thickness= 2.8 mm, and diameter= 8.5 mm) were extracted out of two fresh equine femora using a custom-made drill bit. The schematic of the sample comprising of cartilage, subchondral bone, cork plug, contrast agent solution, wrapping sleeve is illustrated (Figure 9.1A).

We used a micro-CT scanner (*Quantum FX, Perkin Elmer, USA*) to monitor the transport of ioxaglate across cartilage (ambient temperature ≈ 25 ℃). The samples were placed on a holder during scans to minimize possible movement artifacts. The volume of ioxaglate bath was 650 µL (equal to 14 mm bath height) and it was injected on the articular surface of the cartilage specimens. We acquired images at 17 time points within 48 hours using the following scan parameters: 180 µA tube current, 90 kV tube voltage, 2 min scan time, 40×40×40 μm^3 voxel size, and 3600 projections.

The 3D reconstructed images were converted to 2D slices (TIFF format) using in-built software of the micro-CT machine (Analyze 11.0). We used *imageJ v 1.47* to select the mid sagittal slice and create regions of interest (ROI) containing the cartilage according to the previous study (chapters 3 and 5) [14, 31]. The average grey values of cartilage at different time points were then calculated and converted to ioxaglate concentration.

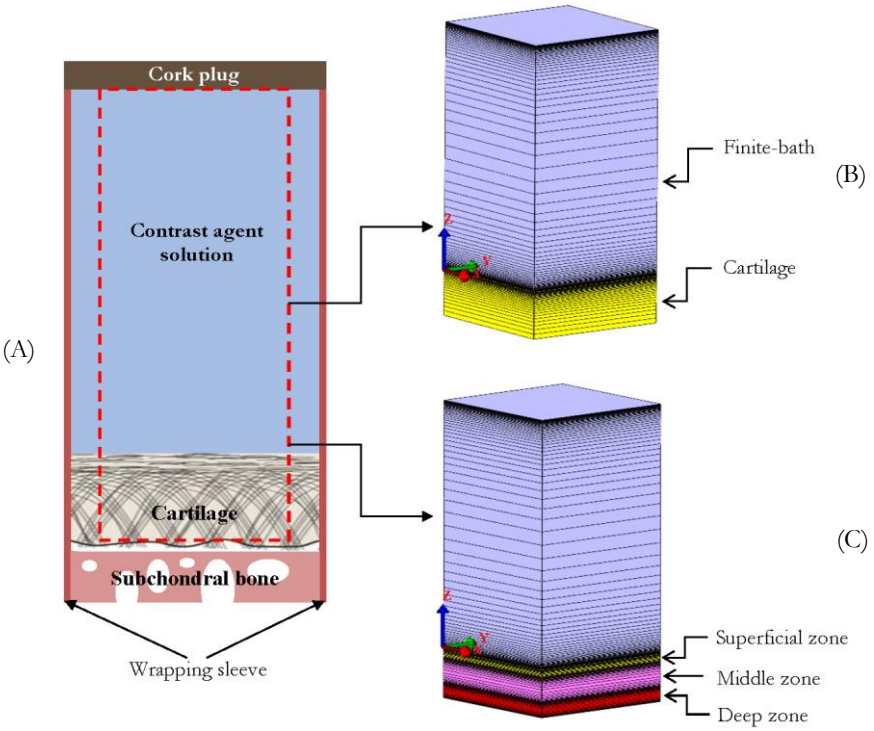

Figure 9.1. Schematic of experimental setup (A), the single-zone (B) and multi-zone models (C). Single-zone model consists of a finite-bath and a uniform cartilage and multi-zone model consists of a finite-bath and a cartilage with superficial, middle and deep zones. Mesh is finer near the interfaces.

9.2.2. COMPUTATIONAL MODEL

Diffusion of charge molecules across cartilage could be described computationally using multiphasic finite element models [32-36]. The formulas used below are adopted from the previous work of Gerard Ateshian [34].

Conservation of momentum for the mixture in the absence of external body forces and in the quasi-static condition is given as:

$$\mathrm{div}\,\mathbf{T}=0 \tag{9.1}$$

where $\mathbf{T}$ is the Cauchy stress for the mixture. Conservation of mass for the mixture and for the solute when solid volume fraction is negligible compared to the solute and solvent content can be given as:

$$\mathrm{div}\,(\mathbf{v}^s + \mathbf{w}) = 0 \tag{9.2}$$

$$\frac{1}{J}\frac{D^s}{Dt}(J\varphi^w\tilde{\kappa}^\alpha\tilde{c}^\alpha) + \mathrm{div}\mathbf{j}^\alpha = 0 \tag{9.3}$$

where $\mathbf{v}^s$ is the solid velocity and $\mathbf{w}$ is the volume flux of solvent relative to the solid. $J = \det \boldsymbol{F}$, $\boldsymbol{F}$ is the deformation gradient of the solid matrix, $D^s(\cdot)/Dt$ is the material time derivative in spatial frame following the solid, $\mathbf{j}^\alpha$ is the molar flux of the solute α relative to the solid and φ^w the volume fraction of the solvent. The effective solute concentration ($\tilde{c}^\alpha$) is given by:

$$\tilde{c}^\alpha = c^\alpha / \tilde{\kappa}^\alpha \tag{9.4}$$

where c^α is molar concentration of solute α and $\tilde{\kappa}^\alpha$ is the partition coefficient of solute α relative to an ideal solution:

$$\tilde{\kappa}^\alpha = \frac{\kappa^\alpha}{\gamma^\alpha}\exp\left(-\frac{z^\alpha F_c \psi}{R\theta}\right) \tag{9.5}$$

where κ^α is the solubility of solute α in the mixture, γ^α is the activity coefficient of solute α, z^α is the charge number of solute α, F_c is Faraday's constant, ψ is electric potential, R is universal gas constant and θ is absolute temperature.

The volume flux of solvent relative to the solid, $\mathbf{w}$, and the relative molar flux of solute α, $\mathbf{j}^{\alpha}$, are expressed as:

$$\mathbf{w} = -\tilde{\mathbf{k}}.\left(\operatorname{grad}\tilde{p} + R\theta \sum_{\beta} \frac{\tilde{\kappa}^{\beta}}{d_0^{\beta}} \mathbf{d}^{\beta}.\operatorname{grad}\tilde{c}^{\beta} \right) \tag{9.6}$$

$$\mathbf{j}^{\alpha} = \tilde{\kappa}^{\alpha}\mathbf{d}^{\alpha}.\left(-\varphi^{w}\operatorname{grad}\tilde{c}^{\alpha} + \frac{\tilde{c}^{\alpha}}{d_0^{\alpha}}\mathbf{w} \right) \tag{9.7}$$

where

$$\tilde{\mathbf{k}} = \left[\mathbf{k}^{-1} + \frac{R\theta}{\varphi^{w}} \sum_{\alpha} \frac{\tilde{\kappa}^{\alpha}\tilde{c}^{\alpha}}{d_0^{\alpha}} \left(\mathbf{I} - \frac{\mathbf{d}^{\alpha}}{d_0^{\alpha}} \right) \right]^{-1} \tag{9.8}$$

where $\tilde{p}$ is the effective fluid pressure which is the mechanical contribution of the total mechanochemical pressure (p) and $R\theta\Phi\sum_{\alpha} c^{\alpha}$ is the osmotic contribution of p:

$$\tilde{p} = p - R\theta\Phi\sum_{\alpha} c^{\alpha} \tag{9.9}$$

where $\mathbf{d}^{\alpha}$ is the diffusivity tensor of solute α in the mixture (solid + fluid), d_0^{α} is the isotropic diffusivity of solute in free solution (fluid), $\tilde{\mathbf{k}}$ is the hydraulic permeability tensor of the porous solid to the interstitial fluid (solvent + solutes), $\mathbf{k}$ is the hydraulic permeability tensor of the porous solid to the interstitial solvent and Φ is the osmotic coefficient.

Electroneutrality requires the following relationship to hold:

$$\sum_{\alpha} z^{\alpha}c^{\alpha} = 0 \tag{9.10}$$

Multiplying equation 9.3 by z^{α} and using electroneutrality constraint yields:

$$\operatorname{div}\sum_{\alpha} z^{\alpha}\mathbf{j}^{\alpha} = 0 \tag{9.11}$$

In cartilage due to presence of fixed charges of proteoglycans, fixed charge density $c^{F} \equiv z^{s}c^{s}$ is defined. Conservation of fixed charge in the solid matrix can be expressed as:

$$c^{F} = \frac{1-\varphi_{r}^{s}}{J-\varphi_{r}^{s}} c_{r}^{F} \tag{9.12}$$

where c_{r}^{F} is the fixed charge density in the reference configuration. In the presence of fixed charge density, the electroneutrality can be expressed as follows:

$$c^{F} + \sum_{\alpha} z^{\alpha}c^{\alpha} = 0 \tag{9.13}$$

Finite element method was used to discretize and solve the aforementioned equations simultaneously.

9.2.2.1. GEOMETRY

We assumed the diffusion to take place only from the cartilage surface in the axial direction (chapter 3) [14]. Similar to our previous study, we used both single-zone and multi-zone models to investigate the axial diffusion from the finite-bath through cartilage (chapter 3) [14]. Single-zone model assumes that cartilage is homogeneous across its thickness. Therefore, only one diffusion coefficient and fixed charge density can be defined (Figure 9.1B). The multi-zone model (Figure 9.1C) assumes that cartilage properties remain constant within individual zones but different in each zone. Those differences may originate from inhomogeneous

distribution of glycosaminoglycans, orientation of collagen (type II) fibers, and water content. The first zone in this model represents the superficial zone (20% of cartilage thickness), while the second (50% of cartilage thickness) and third zones (30% of cartilage thickness) represent middle and deep zones [37]. Both single- and multi-zone models used eight-node trilinear hexahedral elements for mesh generation, which was refined near the boundaries (Figure 9.1B and C).

9.2.2.2. MECHANICAL AND PHYSICAL PROPERTIES OF CARTILAGE AND BATH

We modeled the cartilage as a neo-Hookean material with a Young's modulus of 10 MPa, Poisson's ratio of 0, hydraulic permeability of 10^{-3} mm^4/Ns, and effective solute solubility of 1 (chapter 3) [14]. We examined the effect of hydraulic permeability and Poisson's ratio on the concentration-time curves and found negligible impact when they were changed within their expected ranges. The Young's modulus was chosen high enough to resist the osmotic pressure which in agreement with the experiments, large deformations could be prevented. We used a viscosity-dependent relationship to estimate the diffusion coefficient of ioxaglate in the bath considering actual diffusion coefficient of iodixanol [38]. Cartilage water content was assumed to be 0.8 throughout the cartilage thickness in the single-zone model [14, 31, 39, 40]. In the multi-zone model, however, it was assumed to gradually decrease from 0.8 in the superficial zone to 0.7 in the middle zone and finally to 0.6 in the deep zone [37, 41, 42]. We considered a wide range of possible FCD (0-350 mEq/l) across cartilage [11, 43, 44].

9.2.2.3. INITIAL AND BOUNDARY CONDITIONS

The following steps were prescribed to define FCD, initial, and boundary conditions:

Step 1, Steady-state: we used the same effective fluid pressures and concentrations inside and outside cartilage while rising FCD to the desired value. This allowed equilibrium free swelling of the cartilage and bath.

Step 2, Transient: to set the concentration in the bath, we linearly increased the solute concentrations and effective fluid pressures at the bath boundaries to the desired level. The diffusion coefficient of the solute in the bath was chosen to be high enough to maintain the bath well-stirred to enable assigning a single concentration throughout the bath. Time at which the solute was added and diffusion coefficient of the solute in the bath were considered as two factors with which we minimized solute diffusion in the cartilage. This would help to converge the problem.

Step 3, Transient: we removed the prescribed solute concentrations and effective fluid pressures at the bath boundary and reverted the diffusion coefficient of the solute in the bath to its actual value.

There is one more level of complexity that needs to be addressed: In the step 3, once we remove all the boundary conditions for the solute concentrations, there will no longer be any electrical grounding of the mixture. This means that the electric potential can float and the analysis will either converge very slowly or fail to converge. To resolve this problem, we needed to add two other monovalent counter-ions to the bath and tissue. Since the concentration of monovalent counter-ions does not interfere with the diffusion of other solutes, we set their concentrations to some arbitrary values (e.g. 1 mM) both as initial conditions and as

boundary conditions at the bath boundary. The precise value of the monovalent concentrations does not matter as long as it does not significantly affect the osmotic pressure of the analysis. To maintain realistic deformation one needs to choose sufficiently high Young's modulus to overcome the effect of generated osmotic pressure in the bath. Ambient fluid pressure and temperature were considered $p = 101\ \text{kPa}$ and $\theta = 298\ \text{K}$, respectively.

9.2.2.4. FITTING METHOD

We developed a MATLAB (2013b, TU Delft, Delft, The Netherlands) code to automatically perform simulations in FEBio in wide range of FCDs and diffusion coefficients for all cartilage zones, to plot the concentration-time curves and find the minimum root mean square error (RMSE) between experimental and computational values of concentration at all time points.

9.3. RESULTS

9.3.1. EXPERIMENTS

Diffusion rate was highest in the early time points followed by a gradual decrease until the near-equilibrium ioxaglate concentration (Figure 9.2A). The near-equilibrium ioxaglate concentration for these samples was reached after 24 hours and was 23.31±4.66 % of the initial average bath concentration (Figure 9.2A).

9.3.2. COMPUTATIONAL MODEL

9.3.2.1. SINGLE-ZONE MODEL

To account for the effects of charged solute in the bath and FCD of cartilage and their interactions we have compared the results obtained by biphasic-solute (solid/fluid) and multiphasic model (solid/fluid/charge). We obtained the diffusion coefficients using

both a biphasic-solute model and a multiphasic model while also calculating the FCDs in the latter case (Figure 9.2A and 9.3A).

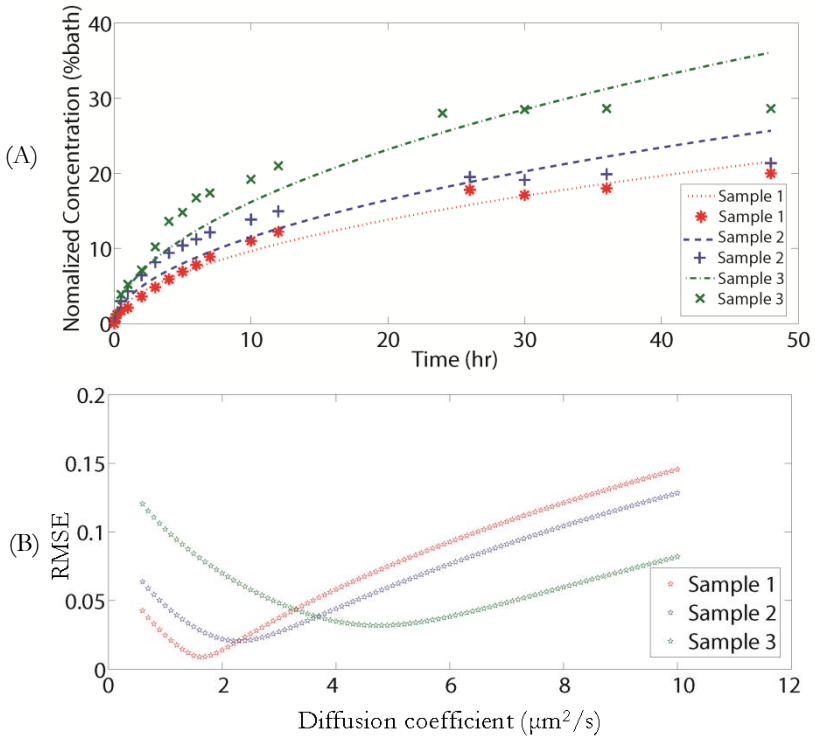

Figure 9.2. Plots of normalized ioxaglate concentration (% initial bath concentration) measured from the micro-CT data versus time (experiment: symbol, FE model: dotted line) (A) and root mean square error (RMSE) versus diffusion coefficient (B) in samples 1-3 using single-zone biphasic-solute model.

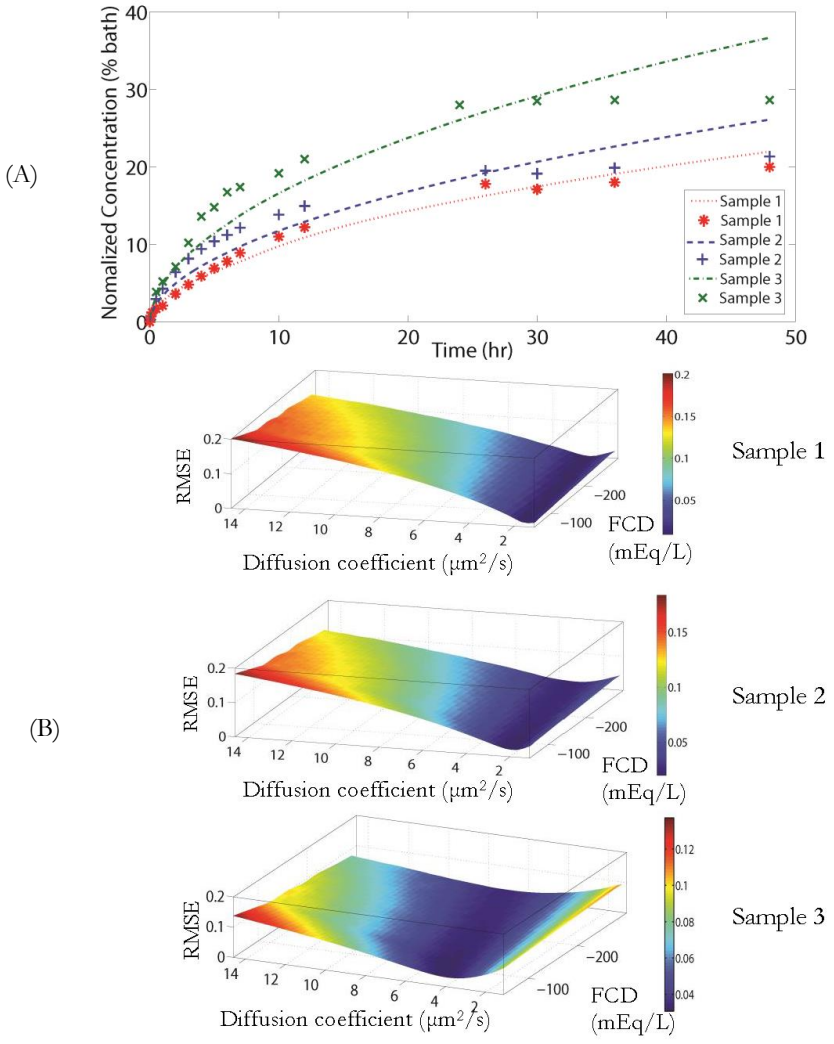

Figure 9.3. Plots of normalized ioxaglate concentration based on the initial bath concentration versus time (experiment: symbol, FE model: dotted line) (A) and root mean square error (RMSE) versus diffusion coefficient and FCD (B) in samples 1-3 using single-zone multiphasic model.

RMSE was used to ensure the models fit to the experimental data (Figure 9.2B and 9.3B). The entire solution process is provided as a flowchart (Figure 9.4). The diffusion coefficients and R^2 obtained for both biphasic-solute and multiphasic models were quite similar while the results of multi-phasic model were slightly more accurate than those of biphasic-solute model (Table 9.1A).

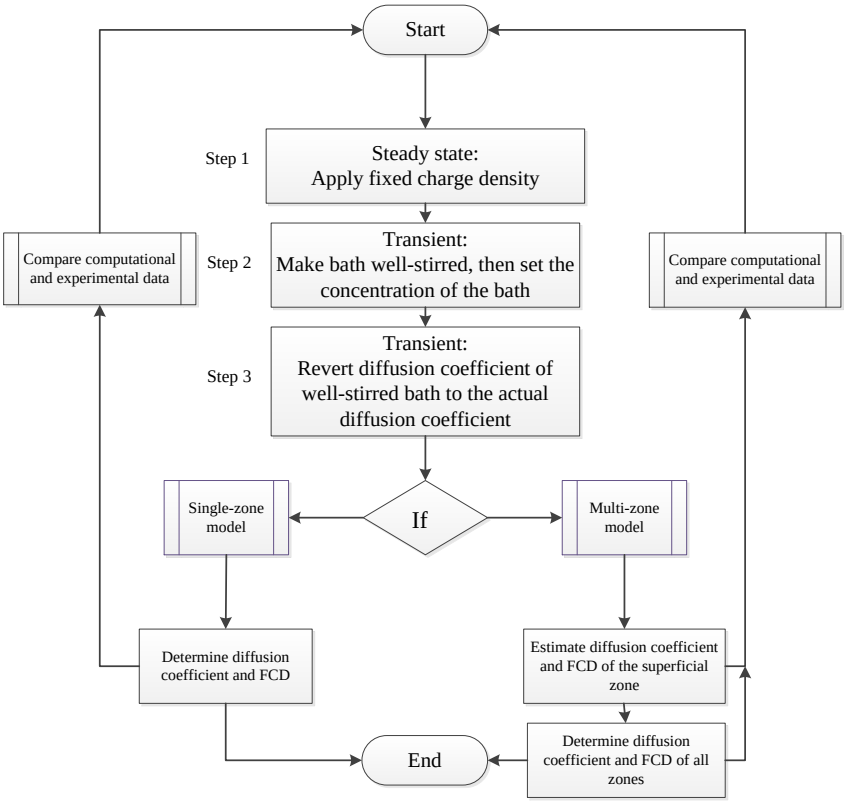

Figure 9.4. Matlab-FEBio interface to solve the multiphasic finite element model of a finite-bath.

Table 9.1. Root mean square error (RMSE) and R^2 for single-zone biphasic-solute and multiphasic models (A). Diffusion coefficients for single-zone biphasic-solute and multiphasic models and FCD for single-zone multiphasic model are presented (B).

(A)

	Fitting data	Biphasic-solute model	Multiphasic model
Sample 1	R^2	0.98	0.98
	RMSE	0.0091	0.0089
Sample 2	R^2	0.94	0.95
	RMSE	0.0207	0.0203
Sample 3	R^2	0.92	0.93
	RMSE	0.032	0.0308

(B)

	Fitting data	Diffusion coefficient ($\mu m^2/s$)	Fixed charged density (mEq/L)
Sample 1	Biphasic solute model	1.6	-
	Multiphasic model	1.6	-125
Sample 2	Biphasic solute model	2.3	-
	Multiphasic model	2.1	-65
Sample 3	Biphasic solute model	4.7	-
	Multiphasic model	4.6	-80

9.3.2.2. MULTI-ZONE MODEL

The multi-zone biphasic model was capable of capturing the trends of experimental data for all samples (Figure 9.5).

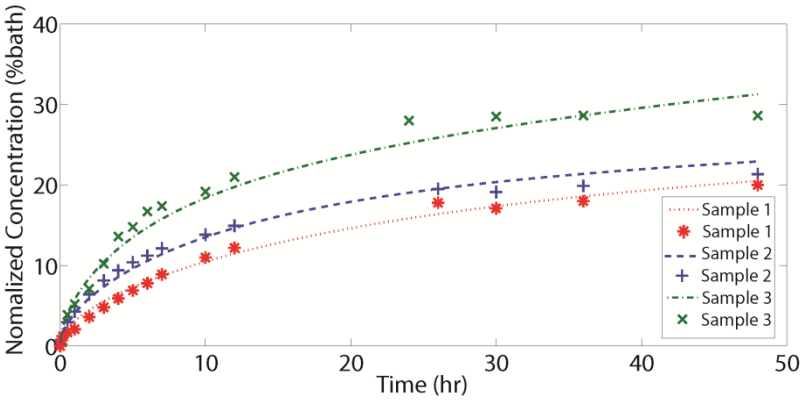

Figure 9.5. Plots of normalized ioxaglate concentration based on the initial bath concentration versus time using multi-zone biphasic-solute model (experiment: symbol, FE model: dotted line).

The optimization algorithm of the multiphasic model requires to consider several parameters i.e. diffusion coefficients and FCDs of the superficial, middle and deep zones which makes the entire process computationally expensive. Therefore, we first estimated the diffusion coefficient and FCD of the superficial zone by minimizing RMSE (Figure 9.6A). This was done in such a way that changing diffusion coefficient and FCD of the middle and deep zones did not affect the curve trend before ~3 h (Figure 9.6A). Using the estimated diffusion coefficient and FCD in the superficial zone, we continued the simulation until we reached the minimum RMSE to obtain the diffusion coefficients and FCDs for the cartilage zones (Figure 9.6B). RMSE and R^2 for both biphasic-solute and multiphasic models confirmed robust results (Table 9.2A). Larger differences between the diffusion coefficients obtained from biphasic-solute and multiphasic models were observed in the middle zone than in the superficial zone (Table 9.2B).

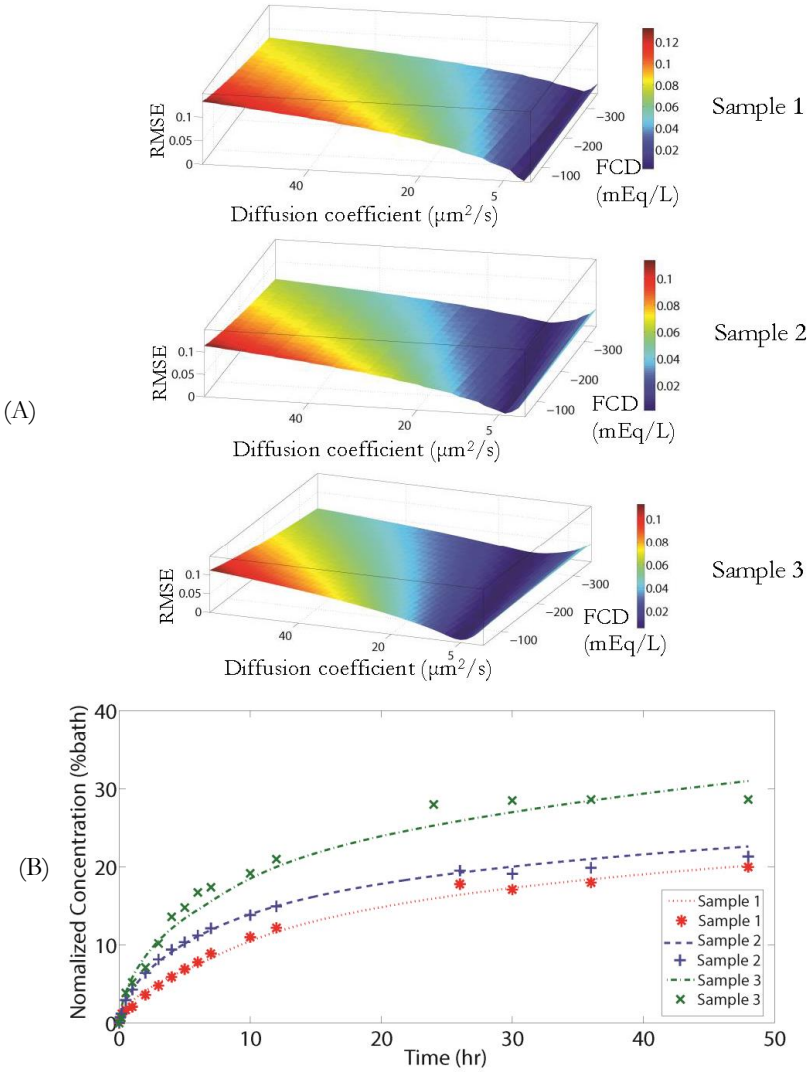

Figure 9.6. Plot of root mean square error (RMSE) against the diffusion coefficient and FCD until ~3 hrs (A) and curve-fitting using multi-zone multiphasic model (experiment: symbol, FE model: dotted line) (B).

Table 9.2. Root mean square error (RMSE) and R^2 for multi-zone biphasic-solute and multiphasic models (A). Diffusion coefficients for multi-zone biphasic-solute and multiphasic models for each zone and FCD of each zone for multi-zone multiphasic model are presented (B).

(A)

	Fitting data	Biphasic solute model	Multiphasic model
Sample 1	R^2	0.99	0.99
	RMSE	0.0064	0.0049
Sample 2	R^2	0.99	1
	RMSE	0.0079	0.0021
Sample 3	R^2	0.98	0.98
	RMSE	0.0150	0.0140

(B)

Condition		Diffusion coefficient (μm²/s)			Fixed charged density (mEq/L)		
		$D_{Superficial}$	D_{Middle}	D_{Deep}	$FCD_{Superficial}$	FCD_{Middle}	FCD_{Deep}
Sample 1	Biphasic-solute model	1.9	0.15	*Insensitive**	-	-	-
	Multiphasic model	1.75	0.22	*Insensitive*	-130	-250	*Insensitive*
Sample 2	Biphasic-solute model	3.4	0.15	*Insensitive*	-	-	-
	Multiphasic model	4.1	0.4	*Insensitive*	-115	-210	*Insensitive*
Sample 3	Biphasic-solute model	7.1	0.95	*Insensitive*	-	-	-
	Multiphasic model	7.1	1.1	*Insensitive*	-80	-160	*Insensitive*

* The average concentration values were not sensitive enough to the diffusion coefficient and fixed charged density of the deep cartilage zone to enable us determine the diffusion coefficient and fixed charged density of the deep cartilage zone.

The ratios of the diffusion coefficient in the superficial to that of the middle zone were more consistent using multiphasic model i.e. 8.25±1.89 as compared to those obtained using the biphasic-solute model, i.e. 14.39± 7.90 (Table 9.3). Furthermore, the ratio of FCDs of the middle zone to the FCDs of the superficial zone was 1.9±0.09 (Table 9.3).

Table 9.3. The ratio of diffusion coefficient of superficial zone to middle zone (DSuperficial/DMiddle) and the ratio of FCD of middle zone to the superficial zone (FCDMiddle/FCDSuperficial).

		$D_{Superficial}/D_{Middle}$	$FCD_{Middle}/FCD_{Superficial}$
Sample 1	Biphasic-solute model	12.7	-
	Multiphasic model	8	1.9
Sample 2	Biphasic-solute model	23	-
	Multiphasic model	10.25	1.82
Sample 3	Biphasic-solute model	7.47	-
	Multiphasic model	6.5	2

Equilibrium partitioning of ioxaglate clearly illustrated the FCD difference between three samples (Figure 9.7A). There was an inverse relationship between the concentration of ioxaglate and FCD in the superficial zone and in the middle zone (Figure 9.7B).

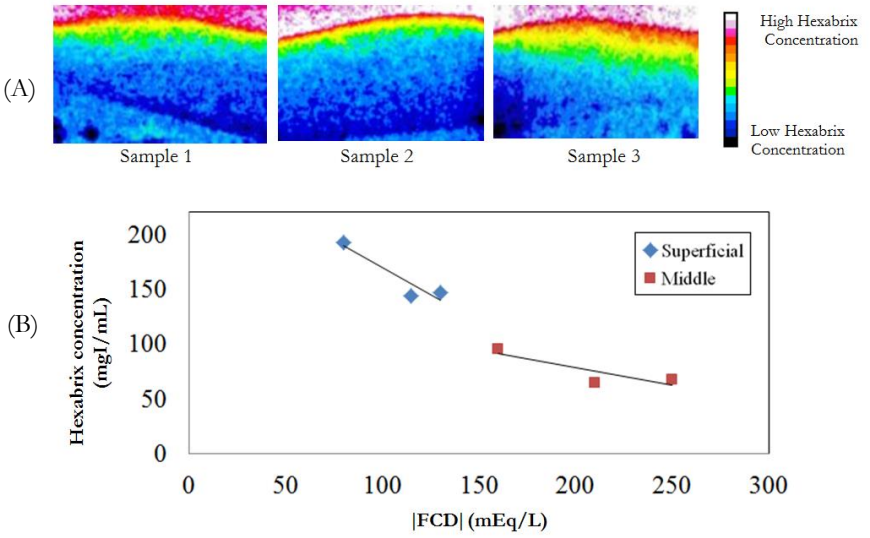

Figure 9.7. Near-equilibrium partitioning of ioxaglate in samples 1-3 where the color bar represents the ioxaglate partitioning across cartilage samples (A) and strong relationship between near-equilibrium ioxaglate concentration in the superficial and middle zones and FCD calculated using multi-zone multiphasic model.

9.3.2.3. PARAMETRIC STUDY

We investigated the direct effects of FCD on the concentration-time curve by comparing the outputs of the multiphasic model that did or did not consider FCD, i.e. FCD=0 (Figure 9.8A-C). In all samples, concentration-time curves obtained from the multiphasic model that considered FCD were below those obtained from the multiphasic model that did not consider FCD. We investigated the direct effect of bath ionic strength on the concentration-time curve by comparing concentration-time curves obtained from the biphasic-solute model and multiphasic model that did not consider FCD (Figure 9.8A-C). The curves obtained using the biphasic-solute model were below those obtained from multiphasic model that did not consider FCD. The synergistic effect of bath ionic strength and FCD in cartilage can be observed by comparing the

concentration-time curves of the biphasic-solute model with that of the multiphasic model that considered FCD (Figure 9.8A-C).

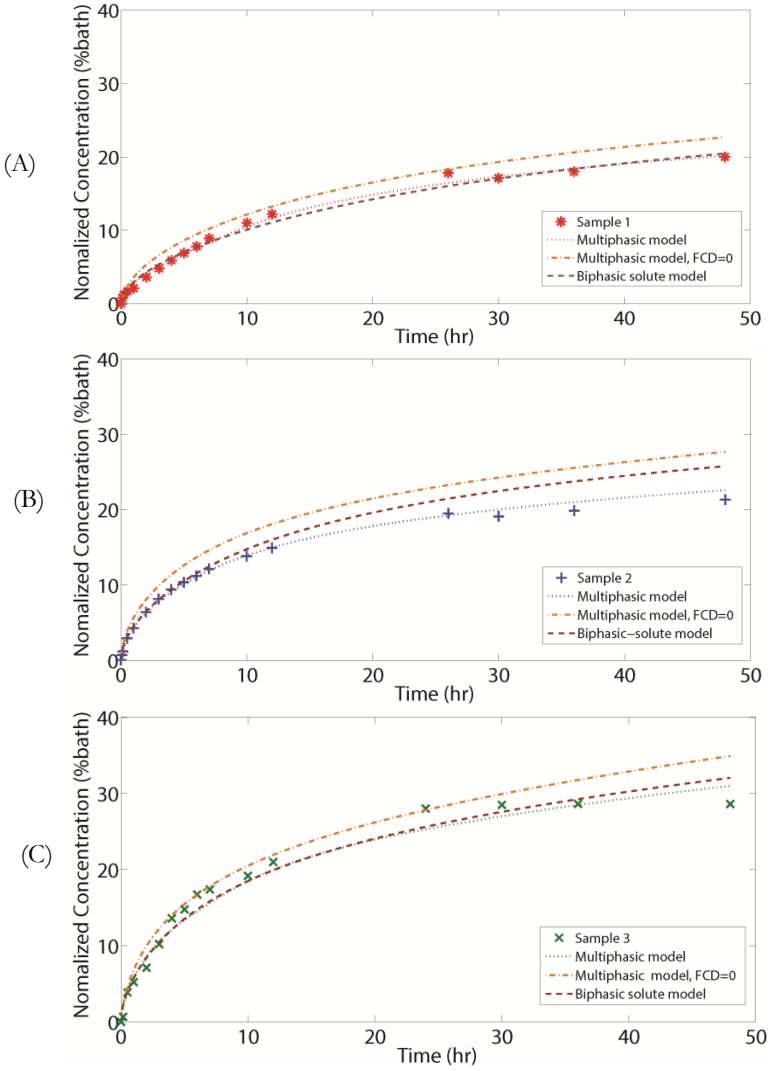

Figure 9.8. Comparing fit obtained using multi-zone multiphasic model, multi-zone multiphasic model without considering FCD (FCD=0) and multi-zone biphasic-solute model for samples 1-3 to elucidate the effects of FCD and bath ionic strength (experiment: symbol, FE model: dotted line).

9.4. Discussion

Both single-zone biphasic-solute and multiphasic models could capture the experimental curves (Figure 9.2A and 9.3A; Table 9.1A). However, curve trends could not be fully predicted by both single-zone models (Figure 9.2A and 9.3A). The multi-zone biphasic and multiphasic models produced excellent fit over the experimental curves (Figure 9.5 and 9.6B; Table 9.2A). The rationale behind can be sought through variation in cartilage properties such as water content, FCD and orientation of collagen fibers across its thickness [14, 31].

In the single-zone model, quite similar diffusion coefficients between biphasic and multiphasic models were observed (Table 9.1B). Multi-zone model resulted in more distinct diffusion coefficients between biphasic-solute and multiphasic models in the middle zone (Table 9.2B). Small differences between the diffusion coefficients of the superficial zone calculated with biphasic-solute and multiphasic models may be due to the fact that movement of negatively charged solutes from the bath to the cartilage (self-repulsion) counterbalances the repulsion force between the negatively charged solute and negative fixed charges of cartilage in this zone. Nevertheless, in the biphasic-solute model, likely due to neglecting the interaction between charged bath and fixed charges in the middle zone, the difference between the diffusion coefficients of multiphasic and biphasic-solute model are more pronounced. These messages imply that efficient delivery of charged therapeutics relies on both sufficient charge density as well as taking the role of higher FCD in the middle and deep zones into account e.g. intra-articular injection systems. This corroborates the strategy that was previously suggested to enhance penetration depth and retention of pharmaceutics by using a positively charged carrier (Avidin) across cartilage [12, 13]. Although determination of diffusion coefficient and FCD in the deep zone for these

samples (Figure 9.7A) is infeasible due to little diffusion in this zone, previous data shows that the FCD of the deep zone of equine cartilage remains similar to that of the middle zone [44]. Consistent diffusion coefficient ratios ($D_{Superficial}/D_{Middle}$) may be linked to the more realistic diffusion coefficients predicted by the multiphasic model as compared to the biphasic-solute model. Our findings show that the ratio of FCD of the middle to that of the superficial zone was found to be almost 1.9 (Table 9.3). This is consistent with the reported ratio of FCD (correlated with GAG) in the middle zone to that of the superficial zone [44]. Partition of a negatively charged solute such as ioxaglate is inversely related to FCD [8]. ioxaglate partitioning in sample 3 implicitly indicates that FCD in this sample should be lower than the other two samples (Figure 9.7A). This is in agreement with FCD values reported (Table 9.2B). Due to proximity of equilibrium partitioning of ioxaglate in samples 1 and 2 it is difficult to draw a conclusion in terms of their FCDs (Figure 9.7A and Table 9.2B), yet, a linear relationship between ioxaglate equilibrium concentration and FCD (Figure 9.7B) exists in the superficial and middle zones of all samples.

According to Figure 9.8A-C, diffusion curve of biphasic-solute model always stayed below the diffusion curve of the multiphasic model that did not consider FCD. This comparison shows that the diffusion of negatively charged solutes can be amplified via downward repulsion forces within the overlaying baths that direct the solutes toward bath-cartilage interface. Comparing the diffusion curves between the multiphasic models that did and did not consider FCD suggests that FCD can significantly hinder the penetration of negatively charged ioxaglate through cartilage. These conclusions might help design efficient OA treatment strategies by considering e.g. therapeutics' charge and injection volume as well as GAG content of cartilage. In addition, our

findings might open windows toward better understanding of OA (e.g. GAG loss) through interactions between charged solute and cartilage matrix.

The multi-zone multiphasic model could very well capture the diffusion of a relatively small charged molecule through articular cartilage. However, steric hindrance due to uneven distribution of collagen fibers and their interaction especially with larger solutes such as therapeutically relevant solutes cannot be yet described using the existing model and therefore requires further research. In order to determine the diffusion coefficient and FCD of deep zone of cartilage using the developed multiphasic model we offer some solutions: thinner samples, prolonged experimental time as well as using positively charged solute in the bath such as CA^{4+} [16]. Moreover, diffusion is an anisotropic tensor. Performing experiments involving radial diffusion might therefore add further information in terms of spatial distribution of cartilage components. The solution containing ioxaglate used in our experiment was a hyper-osmolal solution (600 mOsm/kg H_2O) and its effect was not assessed in the current work, however, this will be addressed in our future studies.

In summary, multiphasic model enabled obtaining both FCD and diffusion coefficients in the different zones of equine cartilage in a finite-bath model of diffusion in a non-destructive way while considering the negative charges imparted by both keratin sulfate and chondroitin sulfate. The equilibrium partitioning of ioxaglate was shown to correlate with the FCD obtained using our multiphasic model. The findings of this work suggest that diffusion coefficient of the superficial zone can be up to 10 times higher than that of the middle zone and that FCD can be up to two times higher in the middle zone as compared to the superficial zone.

9.5. ACKNOWLEDGEMENT

We would like to kindly express our acknowledgements for all the scientific supports of Professor Gerard Ateshian (Columbia University). This work was supported by a grant from Dutch Arthritis Foundation (13-3-406).

9.6. REFERENCES

1. Tavakoli Nia H., Han L., Soltani Bozchalooi I., Roughley P., Youcef-Toumi K., Grodzinsky A.J., Ortiz C., *Aggrecan Nanoscale Solid–Fluid Interactions Are a Primary Determinant of Cartilage Dynamic Mechanical Properties.* ACS Nano, 2015. **9**(3): p. 2614-2625.
2. Nia Hadi T., Han L., Li Y., Ortiz C., Grodzinsky A., *Poroelasticity of Cartilage at the Nanoscale.* Biophysical Journal, 2011. **101**(9): p. 2304-2313.
3. Weinans H., Siebelt M., Agricola R., Botter S.M., Piscaer T.M., Waarsing J.H., *Pathophysiology of peri-articular bone changes in osteoarthritis.* Bone, 2012. **51**(2): p. 190-6.
4. Kulmala K.A., Karjalainen H.M., Kokkonen H.T., Tiitu V., Kovanen V., Lammi M.J., Jurvelin J.S., Korhonen R.K., Toyras J., *Diffusion of ionic and non-ionic contrast agents in articular cartilage with increased cross-linking--contribution of steric and electrostatic effects.* Med Eng Phys, 2013. **35**(10): p. 1415-20.
5. Kokkonen H.T., Jurvelin J.S., Tiitu V., Toyras J., *Detection of mechanical injury of articular cartilage using contrast enhanced computed tomography.* Osteoarthritis Cartilage, 2011. **19**(3): p. 295-301.
6. Kokkonen H.T., Mäkelä J., Kulmala K.A.M., Rieppo L., Jurvelin J.S., Tiitu V., Karjalainen H.M., Korhonen R.K., Kovanen V., Töyräs J., *Computed tomography detects changes in contrast agent diffusion after collagen cross-linking typical to natural aging of articular cartilage.* Osteoarthritis and Cartilage, 2011. **19**(10): p. 1190-1198.
7. Ding C., Cicuttini F., Jones G., *How important is MRI for detecting early osteoarthritis?* Nat Clin Pract Rheum, 2008. **4**(1): p. 4-5.
8. Kulmala K.A.M., Korhonen R.K., Julkunen P., Jurvelin J.S., Quinn T.M., Kröger H., Töyräs J., *Diffusion coefficients of articular cartilage for different CT and MRI contrast agents.* Medical Engineering & Physics, 2010. **32**(8): p. 878-882.
9. Bajpayee A.G., Quadir M.A., Hammond P.T., Grodzinsky A.J., *Charge based intra-cartilage delivery of single dose dexamethasone using Avidin nano-carriers suppresses cytokine-induced catabolism long term.* Osteoarthritis and Cartilage.
10. Abazari A., Thompson R.B., Elliott J.A., McGann L.E., *Transport phenomena in articular cartilage cryopreservation as predicted by the modified triphasic model and the effect of natural inhomogeneities.* Biophys J, 2012. **102**(6): p. 1284-93.
11. Abazari A., Elliott J.A.W., McGann L.E., Thompson R.B., *MR spectroscopy measurement of the diffusion of dimethyl sulfoxide in articular cartilage and comparison to theoretical predictions.* Osteoarthritis and Cartilage, 2012. **20**(9): p. 1004-1010.
12. Bajpayee A.G., Wong C.R., Bawendi M.G., Frank E.H., Grodzinsky A.J., *Avidin as a model for charge driven transport into cartilage and drug delivery for treating early stage post-traumatic osteoarthritis.* Biomaterials, 2014. **35**(1): p. 538-549.

13. Bajpayee A.G., Scheu M., Grodzinsky A.J., Porter R.M., *Electrostatic interactions enable rapid penetration, enhanced uptake and retention of intra-articular injected avidin in rat knee joints.* Journal of Orthopaedic Research, 2014. **32**(8): p. 1044-1051.
14. Arbabi V., Pouran B., Weinans H., Zadpoor A.A., *Transport of Neutral Solute Across Articular Cartilage: The Role of Zonal Diffusivities.* Journal of Biomechanical Engineering, 2015. **137**(7): p. 071001-071001.
15. Meganck J.A., Kozloff K.M., Thornton M.M., Broski S.M., Goldstein S.A., *Beam hardening artifacts in micro-computed tomography scanning can be reduced by X-ray beam filtration and the resulting images can be used to accurately measure BMD.* Bone, 2009. **45**(6): p. 1104-16.
16. Bansal P.N., Stewart R.C., Entezari V., Snyder B.D., Grinstaff M.W., *Contrast agent electrostatic attraction rather than repulsion to glycosaminoglycans affords a greater contrast uptake ratio and improved quantitative CT imaging in cartilage.* Osteoarthritis Cartilage, 2011. **19**(8): p. 970-6.
17. Aula A.S., Jurvelin J.S., Töyräs J., *Simultaneous computed tomography of articular cartilage and subchondral bone.* Osteoarthritis and Cartilage, 2009. **17**(12): p. 1583-1588.
18. Tuomo S. Silvast J.S.J., Virpi Tiitu, Thomas M. Quinn and Juha Töyräs, *Bath Concentration of Anionic Contrast Agents Does Not Affect Their Diffusion and Distribution in Articular cartilage In Vitro.* Cartilage, 2013. **4**(1): p. 42-51.
19. Le N.-A.T., Fleming B.C., *Measuring fixed charge density of goat articular cartilage using indentation methods and biochemical analysis.* Journal of Biomechanics, 2008. **41**(3): p. 715-720.
20. Shapiro E.M., Borthakur A., Gougoutas A., Reddy R., *23Na MRI accurately measures fixed charge density in articular cartilage.* Magn Reson Med, 2002. **47**(2): p. 284-91.
21. Bashir A., Gray M.L., Hartke J., Burstein D., *Nondestructive imaging of human cartilage glycosaminoglycan concentration by MRI.* Magn Reson Med, 1999. **41**(5): p. 857-65.
22. Lu X.L., Sun D.N., Guo X.E., Chen F., Lai W.M., Mow V., *Indentation Determined Mechanoelectrochemical Properties and Fixed Charge Density of Articular Cartilage.* Annals of Biomedical Engineering, 2004. **32**(3): p. 370-379.
23. Lesperance L.M., Gray M.L., Burstein D., *Determination of fixed charge density in cartilage using nuclear magnetic resonance.* Journal of Orthopaedic Research, 1992. **10**(1): p. 1-13.
24. Dai H., Potter K., McFarland E.W., *Determination of Ion Activity Coefficients and Fixed Charge Density in Cartilage with 23Na Magnetic Resonance Microscopy.* Journal of Chemical & Engineering Data, 1996. **41**(5): p. 970-976.
25. Jackson A.R., Yuan T.Y., Huang C.Y., Gu W.Y., *A conductivity approach to measuring fixed charge density in intervertebral disc tissue.* Ann Biomed Eng, 2009. **37**(12): p. 2566-73.

26. Algotsson J., Forsman J., Topgaard D., Soderman O., *Electrostatic interactions are important for the distribution of Gd(DTPA) in articular cartilage.* Magn Reson Med, 2015.
27. Manzano S., Doblare M., Doweidar M.H., *Parameter-dependent behavior of articular cartilage: 3D mechano-electrochemical computational model.* Comput Methods Programs Biomed, 2015. **122**(3): p. 491-502.
28. Manzano S., Gaffney E.A., Doblare M., Hamdy Doweidar M., *Cartilage dysfunction in ALS patients as side effect of motion loss: 3D mechano-electrochemical computational model.* Biomed Res Int, 2014. **2014**: p. 179070.
29. Manzano S., Manzano R., Doblare M., Doweidar M.H., *Altered swelling and ion fluxes in articular cartilage as a biomarker in osteoarthritis and joint immobilization: a computational analysis.* J R Soc Interface, 2015. **12**(102): p. 20141090.
30. Huttunen J.M.J., Kokkonen H.T., Jurvelin J.S., Töyräs J., Kaipio J.P., *Estimation of fixed charge density and diffusivity profiles in cartilage using contrast enhanced computer tomography.* International Journal for Numerical Methods in Engineering, 2014. **98**(5): p. 371-390.
31. Pouran B., Arbabi V., Villamar J.A., Baka N., Zadpoor A.A., Weinans H., *Isolated effects of external bath osmolality, solute concentration, and electrical charge on solute transport across articular cartilage.* Journal of Biomechanical Engineering (Under review), 2015.
32. Gu W.Y., Lai W.M., Mow V.C., *A mixture theory for charged-hydrated soft tissues containing multi-electrolytes: passive transport and swelling behaviors.* J Biomech Eng, 1998. **120**(2): p. 169-80.
33. Ateshian G., Weiss J., *Finite Element Modeling of Solutes in Hydrated Deformable Biological Tissues*, in *Computer Models in Biomechanics*, G.A. Holzapfel and E. Kuhl, Editors. 2013, Springer Netherlands. p. 231-249.
34. Ateshian G.A., Maas S., Weiss J.A., *Multiphasic Finite Element Framework for Modeling Hydrated Mixtures With Multiple Neutral and Charged Solutes.* Journal of Biomechanical Engineering, 2013. **135**(11): p. 111001-111001.
35. Sun D.N., Gu W.Y., Guo X.E., Lai W.M., Mow V.C., *A mixed finite element formulation of triphasic mechano-electrochemical theory for charged, hydrated biological soft tissues.* International Journal for Numerical Methods in Engineering, 1999. **45**(10): p. 1375-1402.
36. Lai W.M., Hou J.S., Mow V.C., *A triphasic theory for the swelling and deformation behaviors of articular cartilage.* J Biomech Eng, 1991. **113**(3): p. 245-58.
37. Sophia Fox A.J., Bedi A., Rodeo S.A., *The Basic Science of Articular Cartilage: Structure, Composition, and Function.* Sports Health, 2009. **1**(6): p. 461-468.
38. Brillo J., Pommrich A.I., Meyer A., *Relation between self-diffusion and viscosity in dense liquids: new experimental results from electrostatic levitation.* Phys Rev Lett, 2011. **107**(16): p. 165902.

39. Ateshian G.A., Albro M.B., Maas S., Weiss J.A., *Finite element implementation of mechanochemical phenomena in neutral deformable porous media under finite deformation.* J Biomech Eng, 2011. **133**(8): p. 081005.
40. Ateshian G.A., Maas S., Weiss J.A., *Solute transport across a contact interface in deformable porous media.* Journal of Biomechanics, 2012. **45**(6): p. 1023-1027.
41. Leddy H.A., Guilak F., *Site-Specific Molecular Diffusion in Articular Cartilage Measured using Fluorescence Recovery after Photobleaching.* Annals of Biomedical Engineering, 2003. **31**(7): p. 753-760.
42. Salo E.N., Nissi M.J., Kulmala K.A.M., Tiitu V., Töyräs J., Nieminen M.T., *Diffusion of Gd-DTPA2− into articular cartilage.* Osteoarthritis and Cartilage, 2012. **20**(2): p. 117-126.
43. Wheaton A.J., Casey F.L., Gougoutas A.J., Dodge G.R., Borthakur A., Lonner J.H., Schumacher H.R., Reddy R., *Correlation of T1rho with fixed charge density in cartilage.* J Magn Reson Imaging, 2004. **20**(3): p. 519-25.
44. Malda J., Benders K.E., Klein T.J., de Grauw J.C., Kik M.J., Hutmacher D.W., Saris D.B., van Weeren P.R., Dhert W.J., *Comparative study of depth-dependent characteristics of equine and human osteochondral tissue from the medial and lateral femoral condyles.* Osteoarthritis Cartilage, 2012. **20**(10): p. 1147-51.

CHAPTER 10

MULTIPHYSICS COMPUTATIONAL MODELING IN CARTILAGE BIOMECHANICS: ESTIMATION OF MECHANICAL AND PHYSICAL PROPERTIES*

*Arbabi V., Pouran B., Weinans H., Zadpoor A.A. *Multiphysics computational modeling in cartilage biomechanics: Estimation of mechanical and physical properties. (a review: in progress)*

ABSTRACT

Multiphysics computational modeling of soft hydrated tissues has become a popular trend toward more realistic prediction of mechanical and physical properties of tissues. As the mainstay of multiphysics modeling, finite element models (FEM) have pursued user-friendly approaches by which accurate estimation of crucial parameters of articular cartilage was achieved. Those advanced strategies enabled the implementation of properties that have persistently been challenging. To date, determination of diffusivity and fixed charge density of articular cartilage in different zones using FE-models proved to be feasible. Since recently, FE-models could not only quantify mechanical loading and solute diffusion experiments but also coupling them with advanced techniques such as artificial neural networks boosted their efficacy. The advantage of coupling artificial neural network (post-training) with FE-models is that it could lift the need for FE-modeling. The aim of this chapter is to review critically the lately established efficient FE-models describing indentation and diffusion tests and essential underlying material models as well as to open up key opportunities to apply FE-models in a more smooth, practical and effortless way.

10.1. INTRODUCTION

Computational models have been used extensively to describe behavior of biological materials and tissues under complicated geometries and boundary conditions [1-9]. Selection of appropriate implemented material models in finite element analysis assists substantially in accurate identification of the behavior of biological materials and tissues such as articular cartilage [1, 2, 8, 10]. The major components of articular cartilage are collagens, proteoglycans (PGs) and water where their concentrations change across their thicknesses which provide the articular cartilage its excellent mechanical properties [11-13]. Given the extracellular matrix (ECM) of cartilage comprising two distinct phases of interstitial fluid and the solid matrix, the tissue can be perceived as a biphasic material. However, the fixed charges of PGs render the cartilage a negatively charged hydrated tissue, which the negative charge is counterbalanced by the action of mobile ions permeating through water influx. Therefore, articular cartilage is truly a structured multiphasic material as it contains neutral and charged solutes floating within the interstitial fluid as well as essential macromolecules of PGs and collagens (Figure 10.1). The negative fixed charge density (FCD) in ECM causes the tissue to swell due to osmotic gradient between inside and outside the ECM attracting water from the synovial fluid [14-18]. The swelling pressure not only protects the cartilage from compressive loads but also produces constant stretch on collagen fibrils (pre-stress), giving the tissue its elastic stiffness. Another interesting hypothesis concerning the collagen stretching has been regarding its potential key role in preserving them from excessive enzymatic cleavage [19, 20].

In osteoarthritis (OA), cartilage experiences aggravation of its physical and mechanical properties due to loss of proteoglycans and disruption of collagen fibrils [21-23]. Advanced computational

models are demanding to provide possibility of detecting slight (early OA) and large (advanced OA) alterations in cartilage properties.

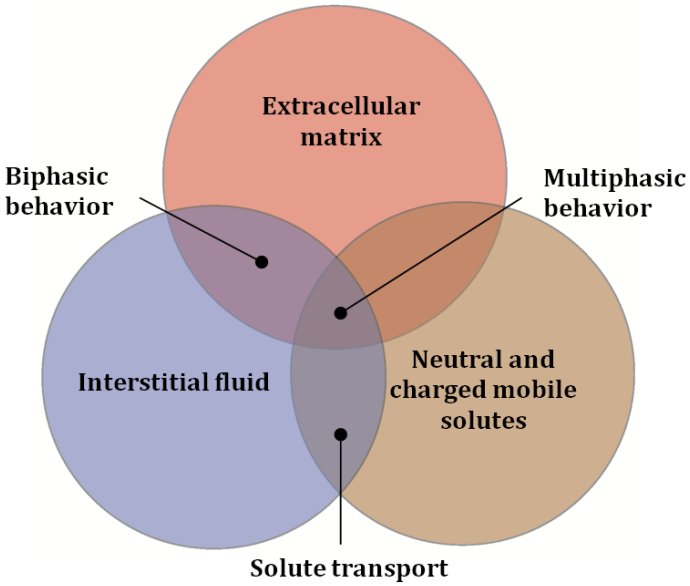

Figure 10.1. Schematic of the multiphasic principle: The interactions between solid matrix of extracellular matrix, interstitial fluid conveying mobile neutral and charged solutes throughout extracellular matrix swell the cartilage.

Several fundamental material models have been adopted to simulate the mechanical behavior of articular cartilage namely elastic, hyperelastic, viscoelastic, poroelastic (biphasic), poroviscoelastic and fiber-reinforced hyper-poroviscoleastic [2, 24-27]. To investigate the neutral solute transport across articular cartilage biphasic-solute models needed to be developed and implemented [3, 28, 29]. However, description of solute transport when the solute of interest is charged requires adopting multiphasic models that account for continuous interactions between the solute and FCD of articular cartilage [30, 31].

Cartilage properties such as Young's modulus, Poisson's ratio and permeability can be obtained using experimental techniques among which confined and unconfined tests as well as indentation (nano and micro) are the most widely used [26, 32, 33]. Indentation stands out from the other techniques in the sense that it can be performed to determine local mechanical and physical properties of articular cartilage, is minimally invasive, maintains physiologic properties of sample. Furthermore indentation tests can even be performed in-vivo [34, 35]. Indentation experiments can be performed in creep mode or in stress-relaxation mode, where in creep mode force is applied and displacement of indenter is recorded, whereas in stress-relaxation mode displacement is applied and reaction force between indenter and cartilage surface is recorded [34]. Diffusive properties of cartilage namely diffusivity can be characterized by tracking temporal solute diffusion using advanced imaging modalities e.g. computed tomography (CT), nuclear magnetic resonance (MRI) and fluorescent-based methods [36-40]. To characterize physical and mechanical properties of cartilage FE-models need to provide the best obtainable fit to the experimental curves [36, 41].

Applications of FE-models may be restricted to the labs where highly sophisticated computational expertise is available. An invaluable opportunity can be therefore conceived if assisting tools eliminate the need for computational expertise. Artificial neutral networks (ANNs) are powerful tools for non-linear mapping from input data space (e.g. FE-output) to target data space (e.g. FE-input: mechanical and physical properties) [41-44]. Recent findings (Chapter 2 and 4) confirmed that using trained ANNs accompanied by finite element data enabled the mechanical and physical properties to be determined without any need for computational expertise [41, 45].

In this overview we aim to not only provide the latest implemented models and computational approaches, which enable characterizing the mechanical and physical features of articular cartilage using the output of indentation and diffusion tests, but also suggest future perspectives to even enhance the model efficiency to possibly detect the earliest possible changes of the cartilage in OA. The main items of this chapter fall into three categories. The first category discusses the available computational tools based on indentation data to determine cartilage mechanical and physical properties. In the second category, finite element models to quantify the experimental diffusion data will be discussed and critically reviewed. Finally, the capabilities and advantages of ANN-assisted determination of mechanical and physical properties of cartilage will be discussed thoroughly and future remarks for efficient modeling of diffusion and indentation and their combination will be provided.

10.2. MULTIPHYSICS COMPUTATIONAL MODELING OF INDENTATION

The level of accuracy in predicting mechanical and physical properties of articular cartilage post-indentation tests depends remarkably on the solution methods of governing equations that are used for curve fitting. To this end, analytical and computational methods have been proposed [10, 27, 46, 47]. The application of analytical methods could not be extended further than elastic, hyperelastic and viscoelastic theories [47, 48]. The only analytical method to obtain properties of poroelastic materials was limited to viscoelastic assumption in creep mode where Poisson's ratio equals 0.5 (Table 10.1)[47]. Since viscoelastic models are not fully able to capture intrinsic biphasic behavior of articular cartilage, developing models based on biphasic theories seems inevitable. Previous study (chapter 2) showed that using poroelastic models for spherical indentation enables determination of Young's modulus,

permeability and Poisson's ratio simultaneously [41]. Spherical indentation likely raises an advantage, that is, estimation of local cartilage properties can be accomplished since fluid flow is gradually and continuously initiated and propagated which firmly reflects the biphasic behavior of cartilage more accurately (Figure 10.2).

Table 10.1. Availability of analytical solutions for creep and stress-relaxation modes of indentation test when using different material models of articular cartilage and common geometries of indentation tip.

Analytical solution	Indentation mode	Indenter shape		
		Cylindrical	Conical	Spherical
Linear elasticity	Creep	✓	✓	✓
	Stress-relaxation	✓	✓	✓
Hyperelasticity	Creep	✓	✓	✓
	Stress-relaxation	✓	✓	✓
Viscoelasticity	Creep	✓	N/A*	✓
	Stress-relaxation	✓	✓	✓
Poroelasticity	Creep	N/A	N/A	N/A
	Stress-relaxation	N/A	N/A	N/A

* Not available

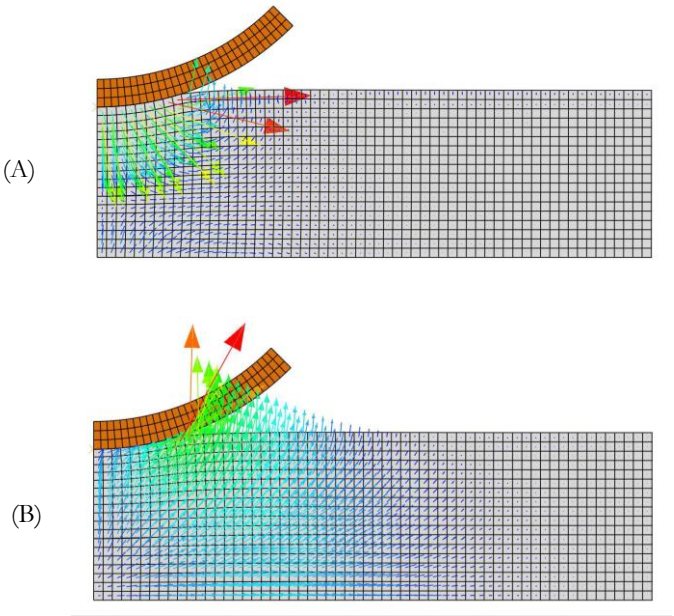

Figure 10.2. Schematic of axisymmetric model used for indentation of articular cartilage (sample thickness 3 mm, Young's modulus 0.54 MPa, Permeability 4×10^{-3} mm4/N.s and Poisson's ratio 0.08) as a poroelastic material in stress relaxation mode (spherical indenter with radius of 5 mm was moved linearly for 2 seconds with a total of 0.3 mm displacement) (A) fluid velocity vectors at 2 s and (B) after some time-lapse (1000 s) of indenting articular cartilage.

In addition, based on a model presented in the previous research (chapter 2) [41], parametric study with FEM on Young's modulus, permeability and Poisson's ratio of poroelastic spherical indentation in stress relaxation mode revealed that each parameter could affect the reaction force between indenter and cartilage surface (Figure 10.3). Since the effect of each parameter on reaction force is tangible, the biphasic model has a potential to precisely estimate the cartilage properties after fitting it to the entire force-time data.

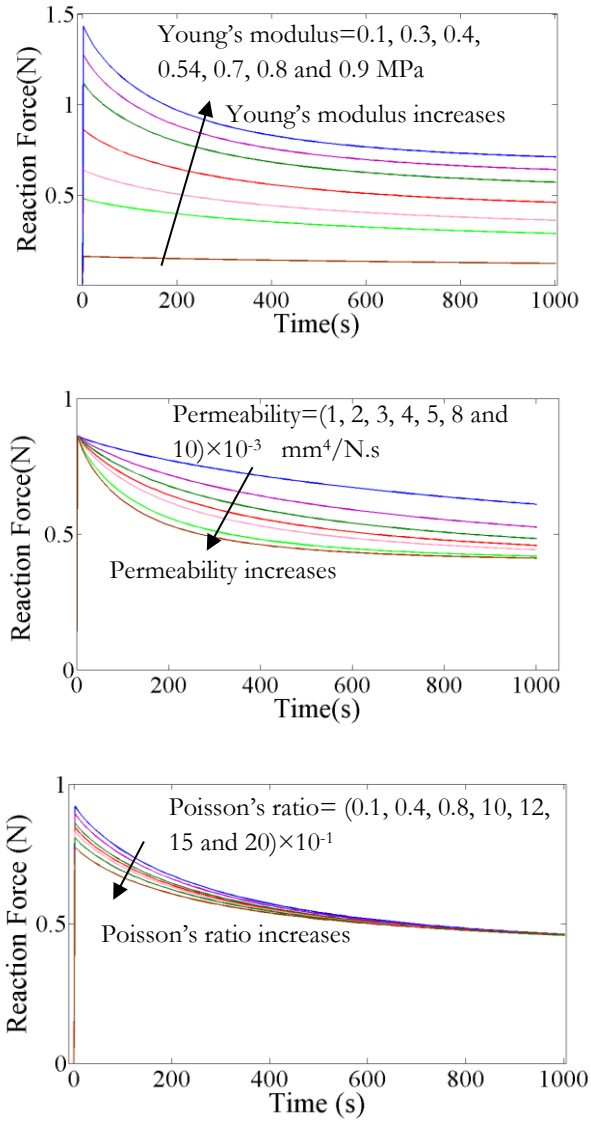

Figure 10.3. Parametric finite element study on (A) Young's modulus, (B) permeability and (C) Poisson's ratio of the indentation test (sample thickness=3 mm, Young's modulus 0.54 MPa, Permeability 4×10^{-3} $mm^4/N.s$ and Poisson's ratio 0.08, spherical indenter with radius of 5 mm was moved linearly for 2 seconds with a total of 0.3 mm displacement). The model's sensitivity to these three essential parameters indicates its appropriateness for cartilage modeling.

Moreover, material models such as fiber-reinforced poroelastic and nonlinear fiber-reinforced poro-hyperviscoelastic have been implemented based on poroelastic models [1, 2]. These models, however, can be used for specialized purposes for example, when effect of fibers on the mechanical response of cartilage needs to be investigated. In spherical indentation of poroelastic-based materials contact detection between the indenter and cartilage surface remains a challenge that has been addressed using user subroutines associated with Abaqus [33, 41], although in FEBio software (nonlinear finite element analysis in biomechanics and biophysics) it has been internally incorporated [49]. To account for effects of FCD and mobile ions in ECM of cartilage, multiphasic models can provide a more realistic approach for cartilage characterization [30, 50]. Applying multiphasic indentation opens a window to obtain FCD [51]. Previous studies determined FCD of cartilage by adopting indentation although the indentation data was analyzed based on biphasic theory [52, 53]. Finite difference was employed to discretize governing equations to determine FCD [51, 54]. Nevertheless, application of finite difference may be limited to simplified problems e.g. small deformations; therefore, FE-modeling of multiphasic indentation can be preferred. Finite element modeling of multiphasic phenomena has previously been implemented and verified [30, 31]. Cartilage swelling is naturally observed in multiphasic models, therefore, to preserve the contact between indenter and cartilage surface, depending on the type of indentation test i.e. creep or stress relaxation, one needs to assign a small load or displacement. To apply FCD in cartilage, algorithms have recently been proposed consisting (chapter 9) of two steps of computationally efficient steady state step where FCD is raised to a desired value and transient step where the solution is initiated and completed [30, 41]. Since cartilage is a heterogeneous material denoting that the concentrations of its components vary from surface to deep zone e.g. water content varies from 0.8 at the

surface to 0.6 at the deep zone [11], multiphasic indentation can be performed utilizing multi-zone cartilage approach to enhance the precision.

Poroelastic-based modeling of cartilage indentation in dynamic mode in broad spectrum of indentation frequencies enables obtaining dynamic Young's modulus and permeability of fibrillar and non-fibrillar cartilage network [55]. Multiphasic models can be applied to dynamic indentation, which can result in more reliable estimations of Young's modulus and permeability across the cartilage zones.

10.3. MULTIPHYSICS COMPUTATIONAL MODELING OF SOLUTE TRANSFER

To study the diffusive properties of articular cartilage, various experimental setups based on CT, MRI and fluorescent solute tracing have been proposed [39, 50, 56-59]. Quantification of diffusive properties requires analytical and computational models [36, 40, 60]. Analytical models can only be applied to relatively scarce cases of diffusion i.e. Fickean diffusion with simplified boundary conditions and geometries [61, 62]. Different numerical schemes have been proposed to model the diffusion process in porous media [36, 50, 60, 63-65]. Recent advances in finite element modeling of solute transport in soft hydrated tissues confirmed its capability and robustness when used for complicated boundary conditions and geometries [3, 4, 29-31, 36, 50, 66]. Biphasic-solute based finite element models incorporate essential equations to describe transport of neutral solutes across articular cartilage and cartilaginous tissues [3, 29]. Besides, the advent of multiphasic models facilitated studying charged solute transport across soft deformable tissues [5, 6, 30, 50, 67]. Implementation of neutral solute transport across different geometries and in the presence of infinite and finite sources of solute in contact with articular

cartilage has been successfully conducted, which allowed obtaining diffusivity [3, 29, 36]. Multi-zone models were shown to accurately track the diffusion behavior of neutral solutes across articular cartilage (chapters 3, 5 and 9) when intrinsic inhomogeneity of the tissue is considered, which allows determination of diffusivity in different zones of cartilage [36, 40, 50]. Similar to implementation of multiphasic indentation mentioned earlier, two steps including steady state and transient were applied to build potent multiphasic models in FEBio (chapter 9). Multiphasic models supplied with multi-zone approach were recently developed (chapter 9) which in addition to diffusivity allowed obtaining the FCD of cartilage layers [68]. Multiphasic and biphasic-solute indentation of articular cartilage can be performed in diffusion setups to determine dynamic diffusivity of charged solutes and FCD as well as dynamic diffusivity of neutral solutes, respectively.

10.4. Multiphysics computational modeling coupled with Artificial Neural Networks

Artificial neural networks (ANNs) were applied in biomechanical engineering applications particularly in studying bone remodeling [42, 69, 70] and estimating diffusive and mechanical properties of articular cartilage [41, 45]. ANNs are powerful nonlinear mapping tools that bridge two spaces of data [41, 45, 70]. Optimization algorithms are demanding in every finite element modeling application to derive mechanical and physical properties of tissues. This implies that computational expertise is mandatory which hinders its widespread use and also potential clinical applications. Additionally FEM along with optimization algorithms should be repeated for every individual experiment, which is a cumbersome and time-consuming process. It is therefore wise to perceive a package, which clears the need for computational expertise and is particularly beneficial for the non-FEM specialists working in the labs and clinics (chapters 2 and 4). ANNs receive simulated data

from FEM as input to become trained and return biomaterial/tissue properties. One obstacle against wide application of ANN is that small amount of noise associated with experimental data can easily impair the functionality of ANN [41, 69]. To overcome this, ANNs were trained with different noise levels to mimic existing experimental noise [41, 69, 71-73]. After inserting the experimental data into each ANN trained with a distinct level of noise, a solution can be obtained, however, the correct solution between different noise levels is not generally known. Traditionally, one may run multiple FEM models to identify the correct level of noise linking to the solution of the problem. To overcome this baffling problem, a complementary ANN (forward-ANN) was suggested to associate the first ANN (inverse-ANN) (chapter 4)[45]. Inverse-ANN receives the material properties and returns simulated data. Since training of ANN requires performing FEM simulation over a wide interval of material properties, identification of effective parameters is important (chapter 4). To extract material properties using the above algorithm, one needs to directly use the proposed flowchart (Figure 10.4) (chapter 4) [45].

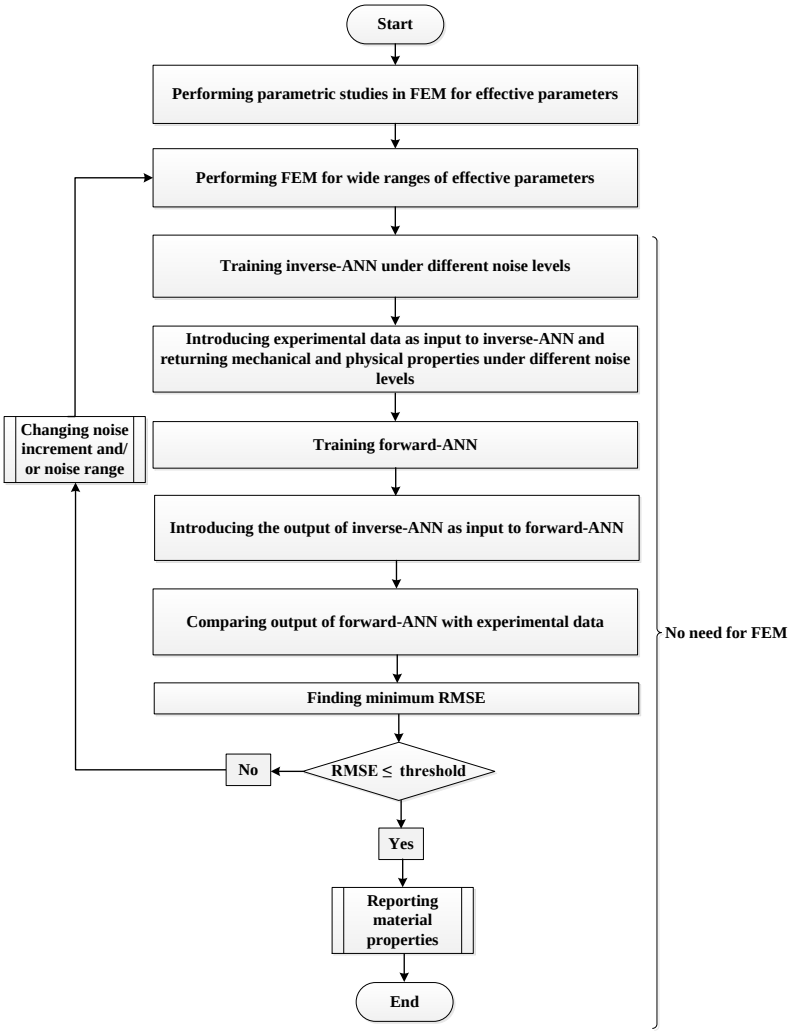

Figure 10.4. Flowchart of the proposed inverse-forward ANNs for determination of the mechanical and physical properties of materials.

10.5. REMARKS AND SUGGESTIONS

Recently, finite element models have been shown to be the most robust computational tools in modeling multiphysics phenomena in cartilage across different scales [31, 36, 41, 50, 74]. Those models advanced such that essential cartilage parameters i.e. fixed charge density, diffusivity of charged and uncharged solutes could be successfully implemented [30, 31, 36, 50]. Besides, potentials of the combination of these advanced finite element models with artificial neural networks have received attention since they can be readily used [41, 45]. In the light of the above-mentioned advantages of FEM models we will review and discuss material models with gradual increase in complexity order with respect to the underlying multiphysics model.

10.5.1. BIPHASIC MATERIAL MODEL

Biphasic material model has been widely used to describe the behavior of articular cartilage since it can satisfy the essential minimum conditions of cartilage from a component (interstitial fluid and solid matrix) point of view [33, 52, 55, 75]. The model has been applied in different studies including determination of dynamic modulus using dynamic indentation and determination of fixed charge density using indentation [55, 74]. In line with those researches, the parametric study in continuum scale and using indentation shown earlier in chapter 2 confirmed that biphasic model is a proper principle material model for articular cartilage. In the past research, OA detection could be possible using elastic model at nano-scale but not in micro-scale [76], however, biphasic models may be preferred to elastic models such that its application can be suggested for OA detection at micro-scale. One benefit of poroelastic models belonging to the primary family of biphasic models is the relatively low number of material parameters involved helping application of ANN to be more straightforward.

Training ANNs using wide ranges of mechanical and physical properties for different indenter tip geometries, size and indentation protocols may be suggested to provide a package, which can be customized in existing indentation machines and even in-vivo arthroscopic indentation machines.

10.5.2. BIPHASIC-SOLUTE MODEL

Biphasic-solute models concern the combination of a biphasic material model and the transferring neutral solute that disperses across the tissue [3, 29, 36]. Multi-zone models associated with biphasic-solute model enable accurate estimation of diffusivity in cartilage zones (chapter 3) [36]. Combination of multi-zone biphasic-solute models with biphasic-solute indentation is suggested prior to obtaining dynamic properties of different cartilage layers e.g. dynamic diffusivity. Dynamic indentation in normal physiologic conditions boasts an advantage in the sense that it can more realistically identify persistently slight changes in cartilage properties as these may occur in the course of osteoarthritis. Therefore, a thorough study on cartilage specimens with various levels of cartilage degeneration could be performed in a hope to efficaciously address long-lasting problem of identifying the first signs of osteoarthritis and its consequences for the physical/mechanical behavior. A platform can be established by coupling ANN with multi-zone biphasic-solute model to reduce the reliance on finite element models and to characterize articular cartilage flawlessly. Osteoarthritis progression is closely associated with GAG loss, which indicates less friction (steric-hindrance) between the diffusing neutral solute and the ECM of cartilage. Subsequently, application of biphasic-solute models can be proposed to capture alterations in solute diffusivity after the first signs of GAG loss or during progression of the early phase of osteoarthritis.

10.5.3. MULTIPHASIC MODEL

Multiphasic models since their introduction revolutionized the studies in the realm of solute transport particularly transport of charged solutes [30]. Using these models one investigates the interactions between charged diffusing solute and fixed charges of PGs since they can be implemented using recently developed algorithm [30, 50]. Multiphasic models have been shown to be capable of obtaining fixed charge density and diffusivity in cartilage zones (chapter 9) [50]. However, studying dynamic diffusion of charged solutes requires taking both multiphasic indentation and multiphasic diffusion into account, which raises difficulty confronting the solution due to multitude of parameters. This issue can be tackled by a dual step strategy: first, determining the fixed charge density in cartilage zones using a single diffusion experiment employing charged solutes and second, inserting the obtained fixed charge density in the multiphasic indentation model to obtain other properties of articular cartilage. Application of combined multi-zone multiphasic indentation and ANN although useful, may encounter computational problems due to large number of required simulations leading to excessive time needed for convergence.

10.6. CONCLUSIONS

Multiphysics models with their recent advancements not only provide an easy-to-use application but can also be applied in different areas of cartilage research including studying deterioration of cartilage quality as this might relate to etiology of osteoarthritis. Combining multiphysics models and artificial neural networks enables their application to be accessible without any need for computational expertise.

10.7. REFERENCES

1. Gupta S., Lin J., Ashby P., Pruitt L., *A fiber reinforced poroelastic model of nanoindentation of porcine costal cartilage: A combined experimental and finite element approach.* Journal of the Mechanical Behavior of Biomedical Materials, 2009. **2**(4): p. 326-338.
2. Seifzadeh A., Wang J., Oguamanam D.C., Papini M., *A nonlinear biphasic fiber-reinforced porohyperviscoelastic model of articular cartilage incorporating fiber reorientation and dispersion.* J Biomech Eng, 2011. **133**(8): p. 081004.
3. Ateshian G., Weiss J., *Finite Element Modeling of Solutes in Hydrated Deformable Biological Tissues*, in *Computer Models in Biomechanics*, G.A. Holzapfel and E. Kuhl, Editors. 2013, Springer Netherlands. p. 231-249.
4. Ateshian G.A., Albro M.B., Maas S., Weiss J.A., *Finite element implementation of mechanochemical phenomena in neutral deformable porous media under finite deformation.* J Biomech Eng, 2011. **133**(8): p. 081005.
5. Manzano S., Manzano R., Doblare M., Doweidar M.H., *Altered swelling and ion fluxes in articular cartilage as a biomarker in osteoarthritis and joint immobilization: a computational analysis.* J R Soc Interface, 2015. **12**(102): p. 20141090.
6. Manzano S., Doblare M., Doweidar M.H., *Parameter-dependent behavior of articular cartilage: 3D mechano-electrochemical computational model.* Comput Methods Programs Biomed, 2015. **122**(3): p. 491-502.
7. Gu W.Y., Lai W.M., Mow V.C., *A triphasic analysis of negative osmotic flows through charged hydrated soft tissues.* J Biomech, 1997. **30**(1): p. 71-8.
8. Pierce D.M., Ricken T., Holzapfel G.A., *A hyperelastic biphasic fibre-reinforced model of articular cartilage considering distributed collagen fibre orientations: continuum basis, computational aspects and applications.* Comput Methods Biomech Biomed Engin, 2013. **16**(12): p. 1344-61.
9. Pierce D.M., Trobin W., Trattnig S., Bischof H., Holzapfel G.A., *A phenomenological approach toward patient-specific computational modeling of articular cartilage including collagen fiber tracking.* J Biomech Eng, 2009. **131**(9): p. 091006.
10. Taffetani M., Griebel M., Gastaldi D., Klisch S.M., Vena P., *Poroviscoelastic finite element model including continuous fiber distribution for the simulation of nanoindentation tests on articular cartilage.* Journal of the Mechanical Behavior of Biomedical Materials, 2013(0).
11. Sophia Fox A.J., Bedi A., Rodeo S.A., *The Basic Science of Articular Cartilage: Structure, Composition, and Function.* Sports Health, 2009. **1**(6): p. 461-468.
12. Leddy H.A., Guilak F., *Site-Specific Molecular Diffusion in Articular Cartilage Measured using Fluorescence Recovery after Photobleaching.* Annals of Biomedical Engineering, 2003. **31**(7): p. 753-760.
13. Leddy H.A., Guilak F., *Site-specific effects of compression on macromolecular diffusion in articular cartilage.* Biophys J, 2008. **95**(10): p. 4890-5.

14. Gu W.Y., Yao H., *Effects of hydration and fixed charge density on fluid transport in charged hydrated soft tissues.* Ann Biomed Eng, 2003. **31**(10): p. 1162-70.
15. Maroudas A., *Distribution and Diffusion of Solutes in Articular Cartilage.* Biophysical Journal, 1970. **10**(5): p. 365-379.
16. Maroudas A., *Biophysical chemistry of cartilaginous tissues with special reference to solute and fluid transport.* Biorheology, 1975. **12**(3-4): p. 233-48.
17. Venn M., Maroudas A., *Chemical composition and swelling of normal and osteoarthrotic femoral head cartilage. I. Chemical composition.* Ann Rheum Dis, 1977. **36**(2): p. 121-9.
18. *weinans.*
19. Hosseini S.M., Wu Y., Ito K., Donkelaar C.C., *The importance of superficial collagen fibrils for the function of articular cartilage.* Biomechanics and Modeling in Mechanobiology, 2013. **13**(1): p. 41-51.
20. Heck T.A., Wilson W., Foolen J., Cilingir A.C., Ito K., van Donkelaar C.C., *A tissue adaptation model based on strain-dependent collagen degradation and contact-guided cell traction.* J Biomech, 2015. **48**(5): p. 823-31.
21. Alexopoulos L.G., Williams G.M., Upton M.L., Setton L.A., Guilak F., *Osteoarthritic changes in the biphasic mechanical properties of the chondrocyte pericellular matrix in articular cartilage.* Journal of Biomechanics, 2005. **38**(3): p. 509-517.
22. Hendren L., Beeson P., *A review of the differences between normal and osteoarthritis articular cartilage in human knee and ankle joints.* The Foot, 2009. **19**(3): p. 171-176.
23. Siebelt M., Waarsing J.H., Kops N., Piscaer T.M., Verhaar J.A., Oei E.H., Weinans H., *Quantifying osteoarthritic cartilage changes accurately using in vivo microCT arthrography in three etiologically distinct rat models.* J Orthop Res, 2011. **29**(11): p. 1788-94.
24. Wilson W., van Donkelaar C.C., van Rietbergen B., Huiskes R., *A fibril-reinforced poroviscoelastic swelling model for articular cartilage.* Journal of Biomechanics, 2005. **38**(6): p. 1195-1204.
25. Suh J.K., Bai S., *Finite element formulation of biphasic poroviscoelastic model for articular cartilage.* J Biomech Eng, 1998. **120**(2): p. 195-201.
26. Mow V.C., Kuei S.C., Lai W.M., Armstrong C.G., *Biphasic Creep and Stress Relaxation of Articular Cartilage in Compression: Theory and Experiments.* Journal of Biomechanical Engineering, 1980. **102**(1): p. 73-84.
27. Bo Qiang M., IEEE, James Greenleaf, Fellow, IEEE, Michelle Oyen,, Zhang a.X., *Estimating Material Elasticity by Spherical Indentation Load-Relaxation Tests on Viscoelastic Samples of Finite Thickness.* 2011.
28. Mauck R.L., Hung C.T., Ateshian G.A., *Modeling of Neutral Solute Transport in a Dynamically Loaded Porous Permeable Gel: Implications for Articular Cartilage Biosynthesis and Tissue Engineering.* Journal of biomechanical engineering, 2003. **125**(5): p. 602-614.
29. Ateshian G.A., Maas S., Weiss J.A., *Solute transport across a contact interface in deformable porous media.* Journal of Biomechanics, 2012. **45**(6): p. 1023-1027.

30. Ateshian G.A., Maas S., Weiss J.A., *Multiphasic Finite Element Framework for Modeling Hydrated Mixtures With Multiple Neutral and Charged Solutes.* Journal of Biomechanical Engineering, 2013. **135**(11): p. 111001-111001.
31. Ateshian G.A., Nims R.J., Maas S., Weiss J.A., *Computational modeling of chemical reactions and interstitial growth and remodeling involving charged solutes and solid-bound molecules.* Biomech Model Mechanobiol, 2014.
32. Boschetti F., Pennati G., Gervaso F., Peretti G.M., Dubini G., *Biomechanical properties of human articular cartilage under compressive loads.* Biorheology, 2004. **41**(3-4): p. 159-66.
33. Pawaskar S.S., Fisher J., Jin Z., *Robust and general method for determining surface fluid flow boundary conditions in articular cartilage contact mechanics modeling.* J Biomech Eng, 2010. **132**(3): p. 031001.
34. Oyen M.L., *Nanoindentation of Biological and Biomimetic Materials.* Experimental Techniques, 2013. **37**(1): p. 73-87.
35. Lu X.L., Mow V.C., *Biomechanics of articular cartilage and determination of material properties.* Med Sci Sports Exerc, 2008. **40**(2): p. 193-9.
36. Arbabi V., Pouran B., Weinans H., Zadpoor A.A., *Transport of Neutral Solute Across Articular Cartilage: The Role of Zonal Diffusivities.* Journal of Biomechanical Engineering, 2015. **137**(7): p. 071001-071001.
37. Hontoir F., Clegg P., Nisolle J.-F., Tew S., Vandeweerd J.-M., *Magnetic resonance compositional imaging of articular cartilage: what can we expect in veterinary medicine?* The Veterinary Journal, (0).
38. Decker S.G., Moeini M., Chin H.C., Rosenzweig D.H., Quinn T.M., *Adsorption and distribution of fluorescent solutes near the articular surface of mechanically injured cartilage.* Biophys J, 2013. **105**(10): p. 2427-36.
39. Salo E.N., Nissi M.J., Kulmala K.A.M., Tiitu V., Töyräs J., Nieminen M.T., *Diffusion of Gd-DTPA2− into articular cartilage.* Osteoarthritis and Cartilage, 2012. **20**(2): p. 117-126.
40. Pouran B., Arbabi V., Zadpoor A.A., Weinans H., *Isolated effects of external bath osmolality, solute concentration, and electrical charge on solute transport across articular cartilage.* (under review), 2016.
41. Arbabi V., Pouran B., Campoli G., Weinans H., Zadpoor A.A., *Determination of the mechanical and physical properties of cartilage by coupling poroelastic-based finite element models of indentation with artificial neural networks.* Journal of Biomechanics, 2016. **49**(5): p. 631-637.
42. Zadpoor A.A., Campoli G., Weinans H., *Neural network prediction of load from the morphology of trabecular bone.* Applied Mathematical Modelling, 2012. **37**(7): p. 5260-5276.
43. Darling E.M., Guilak F., *A neural network model for cell classification based on single-cell biomechanical properties.* Tissue Eng Part A, 2008. **14**(9): p. 1507-15.
44. Ardestani M.M., Chen Z., Wang L., Lian Q., Liu Y., He J., Li D., Jin Z., *A neural network approach for determining gait modifications to reduce the contact force in knee joint implant.* Medical Engineering & Physics, 2014. **36**(10): p. 1253-1265.

45. Arbabi V., Pouran B., Weinans H., Zadpoor A.A., *Combined inverse-forward artificial neural networks for fast and accurate estimation of the diffusion coefficients of cartilage based on multiphysics models.* (under review), 2016.
46. Oyen M.L., *Analytical techniques for indentation of viscoelastic materials.* Philosophical Magazine, 2006. **86**(33-35): p. 5625-5641.
47. Oyen M.L., *Poroelastic nanoindentation responses of hydrated bone.* Journal of Materials Research, 2011. **23**(05): p. 1307-1314.
48. Rauker J., Moshtagh P.R., Weinans H., Zadpoor A.A., *Analytical Relationships for Nanoindentation-Based Estimation of Mechanical Properties of Biomaterials.* Journal of Mechanics in Medicine and Biology, 2014. **14**(03): p. 1430004.
49. Meng Q., Jin Z., Fisher J., Wilcox R., *Comparison between FEBio and Abaqus for biphasic contact problems.* Proc Inst Mech Eng H, 2013. **227**(9): p. 1009-19.
50. Arbabi V., Pouran B., Weinans H., Zadpoor A.A., *Multiphasic modeling of charged solute transport across articular cartilage: Application of multi-zone finite-bath model.* Journal of Biomechanics, 2016.
51. Lu X.L., Wan L.Q., Guo X.E., Mow V.C., *A linearized formulation of triphasic mixture theory for articular cartilage, and its application to indentation analysis.* J Biomech, 2010. **43**(4): p. 673-9.
52. Le N.-A.T., Fleming B.C., *Measuring fixed charge density of goat articular cartilage using indentation methods and biochemical analysis.* Journal of Biomechanics, 2008. **41**(3): p. 715-720.
53. Lu X.L., Sun D.N., Guo X.E., Chen F., Lai W.M., Mow V., *Indentation Determined Mechanoelectrochemical Properties and Fixed Charge Density of Articular Cartilage.* Annals of Biomedical Engineering, 2004. **32**(3): p. 370-379.
54. Abellan M.A., Zahouani H., Bergheau J.M., *Contribution to the determination of in vivo mechanical characteristics of human skin by indentation test.* Comput Math Methods Med, 2013. **2013**: p. 814025.
55. Nia Hadi T., Han L., Li Y., Ortiz C., Grodzinsky A., *Poroelasticity of Cartilage at the Nanoscale.* Biophysical Journal, 2011. **101**(9): p. 2304-2313.
56. Pouran B., Arbabi V., Weinans H., Zadpoor A.A., *Solute transport at the interface of cartilage and subchondral bone plate: effect of micro-architecture.* (under review), 2016.
57. Abazari A., Elliott J.A.W., McGann L.E., Thompson R.B., *MR spectroscopy measurement of the diffusion of dimethyl sulfoxide in articular cartilage and comparison to theoretical predictions.* Osteoarthritis and Cartilage, 2012. **20**(9): p. 1004-1010.
58. Silvast T.S., Jurvelin J.S., Lammi M.J., Töyräs J., *pQCT study on diffusion and equilibrium distribution of iodinated anionic contrast agent in human articular cartilage – associations to matrix composition and integrity.* Osteoarthritis and Cartilage, 2009. **17**(1): p. 26-32.
59. Decker Sarah G.A., Moeini M., Chin Hooi C., Rosenzweig Derek H., Quinn Thomas M., *Adsorption and Distribution of Fluorescent Solutes near*

the Articular Surface of Mechanically Injured Cartilage. Biophysical Journal, 2013. **105**(10): p. 2427-2436.
60. Kokkonen H.T., Jurvelin J.S., Tiitu V., Toyras J., *Detection of mechanical injury of articular cartilage using contrast enhanced computed tomography.* Osteoarthritis Cartilage, 2011. **19**(3): p. 295-301.
61. Crank J., *The mathematics of diffusion.* Clarendon Press:, Oxford, Eng:, 1979.
62. Torzilli P.A., Adams T.C., Mis R.J., *Transient solute diffusion in articular cartilage.* Journal of Biomechanics, 1987. **20**(2): p. 203-214.
63. Huttunen J.M.J., Kokkonen H.T., Jurvelin J.S., Töyräs J., Kaipio J.P., *Estimation of fixed charge density and diffusivity profiles in cartilage using contrast enhanced computer tomography.* International Journal for Numerical Methods in Engineering, 2014. **98**(5): p. 371-390.
64. Kulmala K.A., Karjalainen H.M., Kokkonen H.T., Tiitu V., Kovanen V., Lammi M.J., Jurvelin J.S., Korhonen R.K., Toyras J., *Diffusion of ionic and non-ionic contrast agents in articular cartilage with increased cross-linking--contribution of steric and electrostatic effects.* Med Eng Phys, 2013. **35**(10): p. 1415-20.
65. Tuomo S.S., Harri T.K., Jukka S.J., Thomas M.Q., Miika T.N., Juha T., *Diffusion and near-equilibrium distribution of MRI and CT contrast agents in articular cartilage.* Physics in Medicine and Biology, 2009. **54**(22): p. 6823.
66. Ateshian G.A., Maas S., Weiss J.A., *Finite element algorithm for frictionless contact of porous permeable media under finite deformation and sliding.* J Biomech Eng, 2010. **132**(6): p. 061006.
67. Manzano S., Gaffney E.A., Doblare M., Hamdy Doweidar M., *Cartilage dysfunction in ALS patients as side effect of motion loss: 3D mechano-electrochemical computational model.* Biomed Res Int, 2014. **2014**: p. 179070.
68. Arbabi V., B. Pouran, H. Weinans and A. A. Zadpoor, *Multiphasic modeling of charged solute transport across articular cartilage: application of finite-bath model.* Journal of Biomechanics (under review), 2015.
69. Campoli G., Weinans H., Zadpoor A.A., *Computational load estimation of the femur.* J Mech Behav Biomed Mater, 2012. **10**: p. 108-19.
70. Hambli R., Katerchi H., Benhamou C.L., *Multiscale methodology for bone remodelling simulation using coupled finite element and neural network computation.* Biomech Model Mechanobiol, 2011. **10**(1): p. 133-45.
71. Yulei Jiang R.M.Z., Lorenzo L. Pesce, and Karen Drukker, *A Study of the Effect of Noise Injection on the Training of Artificial Neural Networks.* Proceedings of International Joint Conference on Neural Networks, Atlanta, Georgia, USA, 2009.
72. Zur R.M., Jiang Y., Pesce L.L., Drukker K., *Noise injection for training artificial neural networks: A comparison with weight decay and early stopping.* Medical Physics, 2009. **36**(10): p. 4810-4818.
73. Zur R.M., Jiang Y., Pesce L.L., Drukker K., *Noise injection for training artificial neural networks: a comparison with weight decay and early stopping.* Med Phys, 2009. **36**(10): p. 4810-8.
74. Tavakoli Nia H., Han L., Soltani Bozchalooi I., Roughley P., Youcef-Toumi K., Grodzinsky A.J., Ortiz C., *Aggrecan Nanoscale Solid–Fluid*

Interactions Are a Primary Determinant of Cartilage Dynamic Mechanical Properties. ACS Nano, 2015. **9**(3): p. 2614-2625.

75. Yousefi T., Golikand A.N., Mashhadizadeh M.H., *Synthesis and characterization of cerium oxide nano-particles in chloride bath: Effect of the H2O2 concentration and bath temperature on morphology*. Materials Science in Semiconductor Processing, 2013. **16**(6): p. 1943-1948.

76. Stolz M., Gottardi R., Raiteri R., Miot S., Martin I., Imer R., Staufer U., Raducanu A., Duggelin M., Baschong W., Daniels A.U., Friederich N.F., Aszodi A., Aebi U., *Early detection of aging cartilage and osteoarthritis in mice and patient samples using atomic force microscopy*. Nature Nanonotechnology, 2009. **4**(3): p. 186-192.

Chapter 11

Concluding remarks & summary

11.1. CONCLUSIONS

Multi-physics finite element models were developed in this thesis to estimate the mechanical and physical properties of articular cartilage. Experimental data were also presented to support the development of multi-physics finite element models and to enable estimation of the mechanical and physical properties of cartilage through fitting the developed multi-physics models to the experimental data. Overall, it was generally that our understanding of the mechanical and physical phenomena governing the function of articular cartilage could be significantly improved using multi-physics models. Multi-physics models and the associated experimental data were particularly helpful for accurate quantification of the contribution of various factors such as the mechanical properties, diffusion coefficient, fixed charge density, and morphology of the cartilage to the response of cartilage to mechanical and/or osmotic loading. Quantifying the contribution of different factors is instrumental in evaluating their relative importance and optimizing experimental protocols and the structure of the computational or analytical models that are used for interpretation of the obtained experimental data. The detailed conclusions drawn from the different chapters of the thesis are presented below.

Chapter 2: Cartilage is a biphasic material. That necessitates application of advanced finite element models for describing its indentation behavior that, in turn, allows for obtaining physical and mechanical properties of cartilage. An Abaqus user subroutine was developed to detect the contact between a spherical indenter and cartilage surface. Wide range of physical and mechanical properties, i.e. Young's modulus, Poisson's ratio, permeability and friction coefficient of cartilage surface was used to run the developed model prior to constructing an artificial neutral network (ANN). The ANN received the simulated force-time data as input

and mechanical and returned the physical properties of cartilage as output. We identified that noise had a considerable effect on the performance of the trained ANN to determine mechanical and physical properties of cartilage. Therefore, the ANN was trained with noisy input data (random noise) to make it robust against possible external uncertainties. In conclusion, trained ANN with noisy data enabled robust estimation of cartilage properties without any need for computational expertise.

Chapter 3: A set of experiments based on micro-computed tomography was designed to monitor the diffusion of neutral solute from a finite bath through articular cartilage. A biphasic-solute model was developed and verified with analytical solution to study the transport of neutral solute across cartilage. For an inhomogeneous tissue such as cartilage, our biphasic-solute model based on single zone proved incapable of tracking the diffusion behavior of neutral solute. Therefore, a biphasic-solute model based on a multi-zone approach, i.e. superficial, middle and deep cartilage zones, was developed which was successful in capturing the diffusion behavior of neutral solutes. It was the first model by which diffusivity of equine cartilage in different zones could be obtained and the model revealed that the diffusivity of superficial zone is one order of magnitude higher than that of the middle zone.

Chapter 4: Quantification of experimental observations where computational expertise is scarce is sometimes considered as a major bottleneck. The goal of this chapter was to present a novel algorithm that allows eliminating the need for computational expertise to obtain the diffusivity of a neutral solute in different cartilage zones based on experimental setup and biphasic-solute model introduced in chapter 3. This was carried out by coupling two artificial neural networks (ANN), i.e. inverse and forward ANNs. The inverse ANN was trained using biphasic-solute finite

element model (concentration versus time curves contaminated with different levels of noise) considering the wide range of diffusivities of various cartilage layers. The forward ANN was trained using diffusivities of cartilage layers as input and simulated concentration versus time curves as output. The inverse ANN mitigates the effect of noise associated with experimental data and the forward ANN eliminates the need to create a new computational model for every new experiment. Working together, these ANNs enable experimental labs to determine the diffusivity of cartilage without any need for computational expertise (after training both ANNs). The diffusivities obtained using the inverse-forward ANNs were similar to those obtained using optimization algorithm indicating the robustness of the proposed approach.

Chapter 5: Contrast enhanced micro-computed tomography experiments were used to monitor the diffusion of neutral and negatively charged solutes with similar molecular weight across articular cartilage. To isolate the effects of osmolality, concentration and charge on diffusion, different bath conditions were prepared. Our results suggested that osmolality and concentration had no significant effect on diffusion behavior in different cartilage zones. However, the effect of charge dominated the other effects in all cartilage zones and the flux of negatively charged solute obtained from a multi-zone biphasic-solute was significantly lower than that of neutral solute.

Chapter 6: Serial monitoring of diffusion using contrast enhanced micro-computed tomography technique was used to investigate the transport of neutral solute across osteochondral interface. Our findings not only confirmed the diffusion of neutral solute across osteochondral interface of equine and human samples, but also showed that the diffusion of molecules at the boundary of cartilage and subchondral bone is linked with morphological features of articular cartilage and subchondral bone plate.

Chapter 7: Using experimental setup of chapter 6, the diffusivity of different cartilage zones and subchondral bone plate were obtained using a multi-zone biphasic-solute model. This was done by fitting the computational model to the concentration versus time curves of cartilage and to final concentration value of subchondral bone plate. Regardless of the species, a gradual decrease in diffusivity from cartilage zones to subchondral bone plate was observed.

Chapter 8: The effects of size and stirring of the bath containing neutral solute as well as thickness and concentration of stagnant layer at bath-cartilage interface on diffusion across cartilage were investigated using parametric biphasic-solute computational studies and experimental data. Our findings suggested that an optimal bath size can be designed prior to experiments. Stirring of the bath could substantially affect the diffusion behavior in cartilage. Unlike concentration of the stagnant layer, its thickness did not significantly affect the diffusion in cartilage.

Chapter 9: Transport of a negatively charged solute was monitored using serial contrast enhanced micro-computed tomography (chapter 5). A novel multiphasic finite element model based on the properties of different cartilage zones was developed. Using the proposed model, one can obtain diffusivities and fixed charge density of different cartilage zones simultaneously.

Chapter 10: Application of multiphysics computational modeling to obtain mechanical and physical properties of cartilage was reviewed and suggestions were made to elucidate further application of those models in future research.

The thesis presented finite element approaches to address challenging multiphysics problems in cartilage mechanics. Combination of artificial neural networks and finite element models showed to be capable of creating user-friendly packages,

which will potentially meet the clinical applications. Extension of the presented biphasic and multiphasic models is recommended for complicated cartilage modeling phenomena to quantify dynamic diffusion and indentation phenomena with highest possible accuracy.

11.2. SUMMARY

Recent advances in the realm of computational modeling of complex multiphysics phenomena in articular cartilage enabled efficient and precise determination of articular cartilage properties. However, still accurate quantification of complicated indentation and diffusion processes tying closely with the inhomogeneity of articular cartilage remains challenging. In the present thesis accurate approaches are proposed to capture the mechanical and physical behavior of articular cartilage as faithfully as possible. Finite element models (FE-models) capable of detecting contact between indenter and cartilage surface are developed and applied to spherical indentation process. To predict mechanical and physical properties of cartilage artificial neural networks (ANN) were used and to guarantee the efficacy of the generated ANN they were trained using simulated noisy force-time data. The combination of FE-model and ANN trained with noisy data allowed obtaining cartilage properties robustly. FE-models taking the inhomogeneity of articular cartilage into account were developed and validated and applied to capture neutral (biphasic-solute model) and charged (multiphasic model) solute transfer across articular cartilage in a finite bath experimental setup. Those models could capture the behavior of solute diffusion across cartilage and provide diffusivities and fixed charge densities (FCD) of different cartilage zones. An algorithm consisting of inverse and forward ANNs was developed to obtain the diffusivities of cartilage layers which eliminates the need for computational expertise. The final goal of this algorithm is to introduce a methodology by which properties of cartilage can be determined without any need for computational expertise, which provides a promising opportunity to meet the needs for clinics when it comes to assess the healthiness of articular cartilage during osteoarthritis progression. Effects of bath osmolarity, concentration and charge

of solute were investigated using a combination of micro-CT experiments and FE-models. The results suggested that solute charge unlike the osmoalrity and solute concentration had a profound effect on solute diffusion. Porosity and thickness of subchondral plate were identified as two primary factors affecting the diffusion of neutral solutes across subchondral plate. Using a developed multi-zone biphasic-solute model allowed obtaining the diffusivities of cartilage layers as well as subchondral plate. Using a multi-zone biphasic-solute model, we found that overlying bath size, bath stirring and thickness of the formed stagnant layer can substantially influence the diffusion across cartilage. This provides an opportunity to optimally design diffusion experiments.

11.3. SAMENVATTING

In dit proefschrift is gebruik gemaakt van computermodellen waarmee de vervorming en vloeistofstroming in kraakbeen wordt gesimuleerd. Deze eindige elementen computermodellen worden vervolgens gerelateerd aan experimentele gegevens, zodat fysische eigenschappen zoals elasticiteit en permeabiliteit nauwkeurig kunnen worden bepaald. Omdat veel fysische parameters voor het kraakbeen en de experimentele setting niet exact bekend zijn, moeten we aannamen doen om de werkelijkheid in de computer modellen zo goed mogelijk weer te geven. In feite gebruiken we het model op zodanige wijze dat we beter inzicht verkrijgen in het experiment en tegelijkertijd de fysische eigenschappen toch nog goed kunnen benaderen.

Voor het simuleren van indentatie proeven op kraakbeen is er zo goed mogelijk rekening gehouden met de mechanische interactie tussen indentor en kraakbeen, waarbij contactcondities zoals wrijving een essentiële rol spelen. Om de elasticiteits- en stromingseigenschappen snel en nauwkeurig te kunnen voorspellen, is er gebruik gemaakt van artificiële neurale netwerken die het 'overall' gedrag van het kraakbeen weergeven. Zo'n neuraal netwerk dient 'getraind' te worden om de oplossingen in de modellen goed weer te geven. Het blijkt dat een zekere mate van ruis in de data, de oplossingen van het neurale netwerk om de kraakbeeneigenschappen te voorspellen, sterk verbeterd.

Vervolgens zijn ook de inhomogeniteiten van het kraakbeen in de modellen verwerkt en zijn diffusie experimenten gesimuleerd. Hierbij zijn moleculen met verschillend molecuulgewicht en lading gebruikt. Deze zogenaamde multi-fase modellen van moleculair transport door het kraakbeen, konden de bijpassende experimenten zeer goed beschrijven. Wederom zijn neurale netwerken ingezet om ook deze meer complexe diffusie weer te

geven. Het voordeel van de neurale netwerken is dat de eigenschappen van het kraakbeen hiermee bepaald kunnen worden zonder kennis te hebben van complexe eindige elementen modelvorming. Wellicht een handige manier om het e.e.a. in te zetten voor klinische toepassingen waarbij de fysische eigenschappen van kraakbeen bepaald dienen te worden als criterium voor de mate van kraakbeenkwaliteit of ernst van artrose.

Vervolgens is met de modellen onderzocht wat het effect van de osmolariteit is op de diffusie-eigenschappen. Aangezien osmolariteit zorgt voor uitzetting van het weefsel, zou dit een effect kunnen hebben. Dit bleek nauwelijks het geval, echter vooral de lading van de moleculen was van doorslaggevend belang voor de diffusie-eigenschappen. Daarnaast werden porositeit en dikte van het kraakbeen gevonden als belangrijke parameters voor diffusie.

Tenslotte is in detail onderzocht wat het effect is op diffusie van de wijze waarop de vloeistof met de diffunderende moleculen is aangebracht. Het volume van de vloeistof, de wijze waarop deze geroerd wordt en de mate van een stilstaande vloeistoflaag tegen het kraakbeen, heeft een substantiële invloed op de uitkomsten van de diffusie-experimenten. De eindige elementen modellen kunnen aldus bijdragen aan het uitvoeren van verbeterde diffusie-experimenten, waaruit de fysische eigenschappen van kraakbeen gemakkelijker en nauwkeuriger te bepalen zijn.

APPENDIX

EXPERIMENTAL AND FINITE ELEMENT PROTOCOL TO INVESTIGATE TRANSPORT OF NEUTRAL AND CHARGED SOLUTES ACROSS ARTICULAR CARTILAGE*

* This appendix is submitted as a scientific video journal (Invited):

Arbabi V., Pouran B., Zadpoor A.A., Weinans H. *Experimental and finite element protocol to investigate transport of charged and neutral solutes across articular cartilage.* Journal of Visualized Experiments, 2016 (under review).

ABSTRACT

Osteoarthritis (OA) is a debilitating disease that is associated with degeneration of articular cartilage and subchondral bone. Degeneration of articular cartilage impairs its load-bearing function substantially as it experiences tremendous chemical degradation, i.e. proteoglycan loss and collagen fibril disruption. One promising way to investigate chemical damage mechanisms during OA is to expose the cartilage specimens to an external solute and monitor the diffusion of the molecules. The degree of cartilage damage (i.e. concentration and configuration of essential macromolecules) is associated with collisional energy loss of external solutes while moving across articular cartilage creates different diffusion characteristics compared to healthy cartilage. In this study, we introduce a protocol which consists of several steps and is based on previously developed experimental micro-computed tomography (chapter 5) and finite element modeling (chapters 3 and 9). The transport of charged and uncharged iodinated molecules is first recorded using micro-computed tomography, which is followed by applying biphasic-solute and multiphasic finite element models to obtain diffusion coefficients and fixed charge densities across cartilage zones.

INTRODUCTION

Molecular transport plays a vital role in the homeostasis of articulating joints, delivery of therapeutics to articular cartilage and contrast-enhanced cartilage imaging [1-3]. Factors such as cartilage integration and intactness, solute charge and size as well as osmolarity and concentration of bath in contact with cartilage may influence the transport rate [4-6]. The transport of solutes -either neutral or charged can be different between articular cartilage zones, because each zone consists of different concentrations and orientations of major extracellular matrix molecules, namely proteoglycans (PGs) and collagen type II [1, 7]. More importantly, the transport of charged solutes can be highly dependent on the concentration of proteoglycans comprising negative fixed charges within the extracellular matrix which increases across articular cartilage [8, 9]. Those parameters particularly fixed charge density (FCD), orientation of collagen fibrils and water content variation across cartilage may undergo alterations as osteoarthritis (OA) progresses, thereby signifying the importance of studying diffusion across cartilage.

In the current study, a protocol based on previously established experimental and computational studies (chapters 3, 5 and 9) [4, 9, 10] is proposed to accurately investigate diffusion under various boundary conditions using neutral and charged solutes in a finite-bath model of diffusion. The proposed methods are composed of micro-computed tomography imaging (micro-CT) of a system including cartilage and a finite-bath supported by advanced biphasic-solute and multiphasic finite element models. These models enable obtaining the diffusion coefficients of neutral and charged molecules as well as FCDs across various zones of articular cartilage. Using these models, one can gain better understanding of the behavior of the diffusing neutral and charged molecules that could be used to investigate the interactions

between cartilage and overlaying finite-bath.

PROTOCOL

Note: The protocol presented here is adopted from the experimental and computational procedures of ongoing and recent research papers (chapters 3, 5 and 9) [4, 9, 10]. The protocol is illustrated in Figure 1.
The cadaveric materials were collected with permission from veterinary faculty of Utrecht University.

1. SAMPLE AND BATH PREPARATION

1.1. Drill out cylindrical osteochondral plugs (diameter of 8.5 mm) from cadaveric equine femoral condyles using custom-made drill bit (Figure 1) while spraying cool phosphate buffer serum (PBS) to prevent overheating and subsequent cartilage damage.

1.2. Heat-shrink the osteochondral plugs with a plastic shrinking sleeve to minimize the lateral diffusion of the overlaying bath. The osteochondral plug with cartilage at the top was mounted initially inside the plastic shrinking sleeve followed by blowing hot air to it. Wet cotton pieces were added on the surface of cartilage to prevent heat-related damage.

1.3. Prepare finite-baths of charged (650 μL, 420 mM, ioxaglate, molecular weight (MW) = 1269 Da, charge=-1) and neutral (650 μL, 420 mM, iodixanol, MW= 1550 Da) solutes separately.

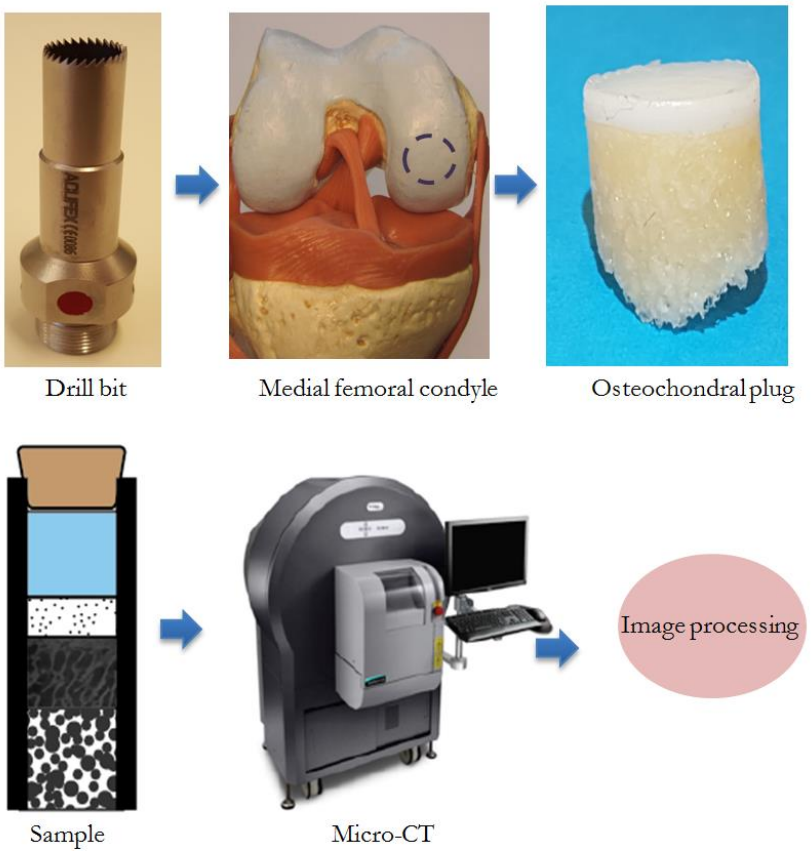

Figure 1. A) Sample extraction procedure using a custom-made drill bit, B) Micro-CT imaging procedure to monitor diffusion process.

1.4. Load the prepared finite-baths on the surface of cartilage using a syringe and place a cork plug on the wrapped sample to prevent evaporation during experiments at room temperature (Figure 2A). To study the neutral solute transport place the iodixanol bath and to study the negatively charged solute transport place ioxaglate bath onto the cartilage surface.

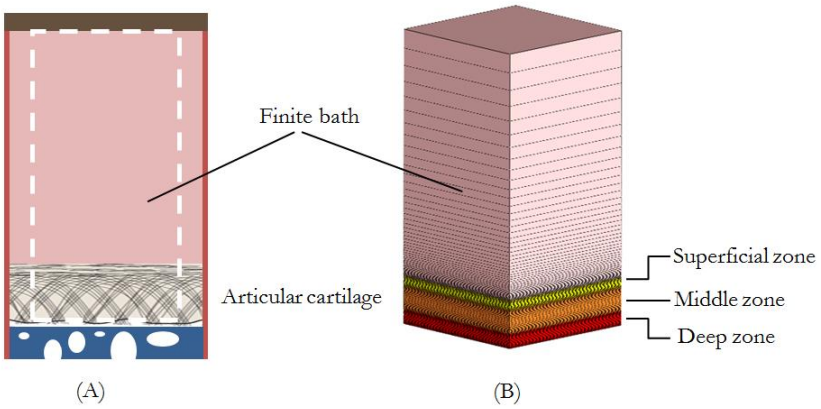

Figure 2. A) Schematic of experimental sample design B) multi-zone computational model consisting of the finite bath, superficial, middle and deep zones of cartilage and associated mesh.

2. IMAGING AND IMAGE PROCESSING

2.1. Place the wrapped samples on a custom-made holder attached to the motorized stage of a micro-CT. The sample was placed so that cartilage surface covered with contrast agent solution was facing upward.

2.2. Scan using the micro-CT (voxel size of 40×40×40 μm^3, scan time of 3 minutes, tube voltage of 90 kV and tube current of 180 μA) a field of view consisting of cartilage, subchondral plate, and finite-bath in several time points until equilibrium state (48 hours) is reached (Figure 2A). The equilibrium state can be determined when concentration values do not change over time.

2.3. Register the 3D images in different time points based on the initial image to facilitate positioning of the region of interest (ROI) using manufacturer's software (e.g., Analyze).

2.4. Convert the 3D reconstructed micro-CT images into 2D tagged image file format (TIFF) stack before processing them using manufacturer's software.

2.5. Globally segment (ImageJ>Adjust>Threshold) the cartilage from the subchondral bone and overlying bath in imageJ software.

2.6. Obtain the average grey value of cartilage at different time points (ImageJ>Analyze>Measure) using the generated cartilage mask in the previous step.

2.7. Use a linear calibration curve to convert the average grey values to the actual concentration of solutes (based on the initial bath concentration). Our previous data support the fact that grey values maintain a linear relationship with the concentration of contrast agents.

2.8. Plot the solute concentrations versus experimental time points.

3. COMPUTATIONAL MODELING

3.1. The diffusion in this problem is assumed to take place in 1D (along z-axis) which complies with the experimental boundary condition. Therefore, the geometry could be arbitrarily created. Build finite-bath based cartilage multi-zone models: 1) cartilage consisting of superficial zone (20% of the total cartilage thickness), middle zone (50% of the total cartilage thickness) and deep zone (30% of the total cartilage thickness) [11] 2) finite-bath in FEBio[12, 13] (Figure 2B).

3.2. Assign the mechanical and physical properties of different zones of cartilage and bath in FEBio. Young's modulus (10 MPa)

was assumed to be high enough to resist the osmotic pressure exerted by the overlying bath and therefore protect the cartilage from excessive deformations. Hydraulic permeability of 10^{-3} mm^4/Ns and Poisson's ratio of 0 were used. Actual solute diffusivity of the bath was used in the simulations [9, 10].

3.3. Generate mesh (8-node trilinear hexahedral elements) and refine it near the boundaries (Figure 2B)[9, 10].

3.4. Biphasic-solute model

3.4.1. Apply initial solute concentration in the bath and effective pressure corresponding to it. Look at the description of effective pressure in [10, 14].

3.4.2. Run the model in transient mode to obtain solute concentration versus time curves according to the prescribed diffusion coefficients in different cartilage zones.

3.5. Multiphasic model

Note: The electric fluctuation between bath and tissue can be circumvented by adding two monovalent counter-ions to both bath and tissue.

3.5.1. For steady-state models: use the same effective fluid pressures and concentrations in cartilage and overlying bath while increasing FCD to its desired value.

3.5.2. For transient models: create a well-stirred finite-bath by keeping the diffusion coefficient in the bath sufficiently high. Inject the solute from the bath-air interface into the bath to reach its desired concentration value.

3.5.3. Transient: remove the prescribed solute concentration boundary condition in the previous step and revert the diffusion coefficient of the finite-bath to its actual diffusion coefficient.

3.5.4. Run the model to obtain solute concentration-time curves based on applied FCDs and diffusion coefficients in different cartilage zones.

3.6. FEBio-MATLAB interface

3.6.1. Develop a MATLAB code to automatically perform simulation in FEBio and plot concentration-time curves (FEBio-MATLAB interface)[9, 10].

3.6.2. Change diffusion coefficients and FCDs in cartilage zones using FEBio-MATLAB interface. Run models in FEBio and extract solute concentration-time curves [9, 10].

3.6.3. Compare the obtained solute concentration-time curves with the experimental data and obtain sets of diffusion coefficients and FCDs in different cartilage zones based on minimum root mean square error (RMSE)[9, 10].

REPRESENTATIVE RESULTS

The representative results provided here are adopted from previous and ongoing research papers (chapters 3, 5 and 9) [4, 9, 10].

In OA, articular cartilage undergoes significant changes most importantly GAG loss and collagen fibril damage [15-17]. Those changes may affect the diffusive behavior of solutes through articular cartilage [18, 19]. We studied axial diffusion of two iodinated contrast agents, i.e. iodixanol (charge=0) and ioxaglate

(charge=-1), in cadaveric equine osteochondral plugs using micro-computed tomography. To quantify the diffusion process of a neutral solute (iodixanol), a biphasic-solute model and a charged solute (ioxaglate) multiphasic model were developed in FEBio that considered the zonal structure of cartilage. The biphasic-solute and multiphasic models could predict the diffusion of iodixanol and ioxaglate across articular cartilage (Figure 3). These models enabled obtaining diffusion coefficient of iodixanol (biphasic-solute) and diffusion coefficient as well as FCD (ioxaglate) in different cartilage zones (chapters 3 and 9)[9, 10].

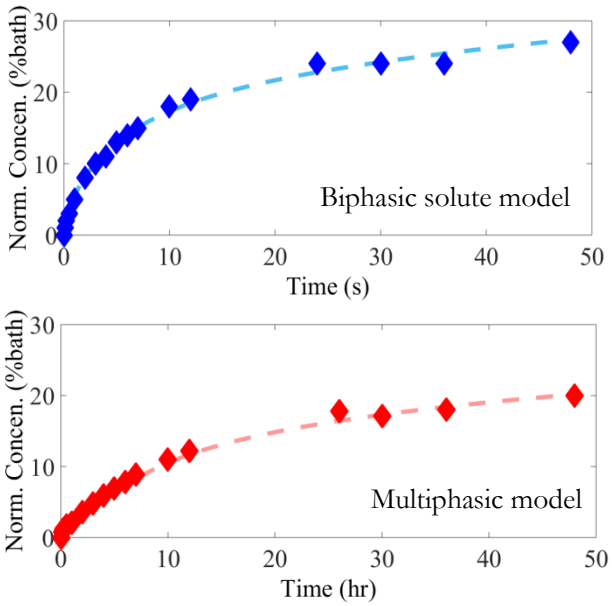

Figure 3: Multi-zone biphasic-solute and multiphasic models fits (dashed) versus experimental data (symbol) [9, 10].

DISCUSSION

We presented an experimental protocol combined with a finite element modeling procedure to study the diffusion of neutral and

charged solutes across articular cartilage. According to our recent studies (chapters 3 and 9), the proposed models could accurately describe the transport of both neutral (biphasic-solute) and negatively charged (multiphasic) solutes across different zones of articular cartilage [9, 10]. It is widely believed that articular cartilage becomes functionally limited through loss of its vital components such as negatively charged GAG macromolecules as well as collagen fibrils during OA progression [19, 20]. Using the technique proposed in this study, one can potentially examine the healthiness of articular cartilage. The transport of neutral solute may be augmented in OA primarily because of lower interactions between the solute as well as GAGs and collagens. On the other hand, the transport of negatively charged solutes could help acquire information with respect to the concentration of fixed charges of proteoglycans, thereby giving some indication of the level of OA progression.

The biphasic-solute and multiphasic models that were developed based on the emergence of finite-bath concept according to the previous studies could serve as platforms by which accurate estimation of zonal properties of articular cartilage could be provided. Limitations associated with large baths of contrast agents namely possible beam-hardening artifacts and assigning a single diffusion coefficient to articular cartilage [7, 18, 21-24] drove the motivation to develop the current study. In the future OA research, our developed models might potentially find applications for early OA diagnosis.

There are some critical steps required both in experiments and computational simulations. To preserve cartilage integrity during experiments, one would require adding sufficient amounts of protease inhibitors to prevent subsequent enzymatic activities. In case of using one sample for more than one experiment, wash-out time for the penetrated solutes after equilibration was

approximately 48 hours. The wash-out efficiency needs to be checked using micro-CT. When using our set up employing equine cartilage, the minimum volume of the overlying bath equivalent to an infinite bath was calculated to be five times higher than cartilage volume. Moreover, to perform finite element modeling of diffusion, it is critical to apply actual bath diffusivity since deviation from that could affect the outcomes.

In the underlying finite element models solute size effect was not implemented and therefore could not be studied. Our proposed finite-bath model offers some advantages such as capability to better understanding diffusion process in the articulating joints as well as significant reduction of beam hardening artefacts. Our proposed technique combining experiments and computational models enables scrutinizing the diffusion attributes of cartilage when positively charged contrast agents are applied. In case of diffusion experiments employing finite baths in the future, actual diffusion coefficient of bath needs to be available which may be missing for some solutions. This would require either obtaining the diffusion coefficient of bath experimentally or readily using literature values.

In conclusion, we proposed a general protocol consisting of experiments and computations to investigate the transport of charged and uncharged solutes across articular cartilage. Using the protocol, one can successfully obtain diffusion coefficients and fixed charged densities in different cartilage layers.

ACKNOWLEDGMENTS

This work was supported by a grant from Dutch Arthritis Foundation (13-3-406).

REFERENCES

1. Arkill K.P., Winlove C.P., *Solute transport in the deep and calcified zones of articular cartilage.* Osteoarthritis Cartilage, 2008. **16**(6): p. 708-14.
2. Chin H.C., Moeini M., Quinn T.M., *Solute transport across the articular surface of injured cartilage.* Arch Biochem Biophys, 2013. **535**(2): p. 241-7.
3. Leddy H.A., Guilak F., *Site-specific effects of compression on macromolecular diffusion in articular cartilage.* Biophys J, 2008. **95**(10): p. 4890-5.
4. Pouran B., Arbabi V., Zadpoor A.A., Weinans H., *Isolated effects of external bath osmolality, solute concentration, and electrical charge on solute transport across articular cartilage.* (under review), 2016.
5. Leddy H.A., Guilak F., *Site-Specific Molecular Diffusion in Articular Cartilage Measured using Fluorescence Recovery after Photobleaching.* Annals of Biomedical Engineering, 2003. **31**(7): p. 753-760.
6. Gu W.Y., Yao H., *Effects of hydration and fixed charge density on fluid transport in charged hydrated soft tissues.* Ann Biomed Eng, 2003. **31**(10): p. 1162-70.
7. Kulmala K.A.M., Korhonen R.K., Julkunen P., Jurvelin J.S., Quinn T.M., Kröger H., Töyräs J., *Diffusion coefficients of articular cartilage for different CT and MRI contrast agents.* Medical Engineering & Physics, 2010. **32**(8): p. 878-882.
8. Arbabi V., Pouran B., Weinans H., Zadpoor A.A., *Multiphasic modeling of charged solute transport across articular cartilage: application of finite-bath model.* Journal of Biomechanics, 2016.
9. Arbabi V., Pouran B., Weinans H., Zadpoor A.A., *Transport of Neutral Solute Across Articular Cartilage: The Role of Zonal Diffusivities.* Journal of Biomechanical Engineering, 2015. **137**(7): p. 071001-071001.
10. Arbabi V., Pouran B., Weinans H., Zadpoor A.A., *Multiphasic modeling of charged solute transport across articular cartilage: Application of multi-zone finite-bath model.* J Biomech, 2016. **49**(9): p. 1510-7.
11. Sophia Fox A.J., Bedi A., Rodeo S.A., *The Basic Science of Articular Cartilage: Structure, Composition, and Function.* Sports Health, 2009. **1**(6): p. 461-468.
12. Ateshian G., Weiss J., *Finite Element Modeling of Solutes in Hydrated Deformable Biological Tissues*, in *Computer Models in Biomechanics*, G.A. Holzapfel and E. Kuhl, Editors. 2013, Springer Netherlands. p. 231-249.
13. Ateshian G.A., Maas S., Weiss J.A., *Multiphasic Finite Element Framework for Modeling Hydrated Mixtures With Multiple Neutral and Charged Solutes.* Journal of Biomechanical Engineering, 2013. **135**(11): p. 111001-111001.
14. Arbabi V., Pouran B., Weinans H., Zadpoor A.A., *Transport of neutral solute across articular cartilage and subchondral plate.* 22nd Congress of the European Society of Biomechanics, Lyon, France, 2016.
15. Hosseini S.M., Wu Y., Ito K., Donkelaar C.C., *The importance of superficial collagen fibrils for the function of articular cartilage.* Biomechanics and Modeling in Mechanobiology, 2013. **13**(1): p. 41-51.

16. Alexopoulos L.G., Williams G.M., Upton M.L., Setton L.A., Guilak F., *Osteoarthritic changes in the biphasic mechanical properties of the chondrocyte pericellular matrix in articular cartilage.* Journal of Biomechanics, 2005. **38**(3): p. 509-517.
17. Felson D.T., Lawrence R.C., Dieppe P.A., Hirsch R., Helmick C.G., Jordan J.M., Kington R.S., Lane N.E., Nevitt M.C., Zhang Y., Sowers M., McAlindon T., Spector T.D., Poole A.R., Yanovski S.Z., Ateshian G., Sharma L., Buckwalter J.A., Brandt K.D., Fries J.F., *Osteoarthritis: new insights. Part 1: the disease and its risk factors.* Ann Intern Med, 2000. **133**(8): p. 635-46.
18. Kokkonen H.T., Jurvelin J.S., Tiitu V., Toyras J., *Detection of mechanical injury of articular cartilage using contrast enhanced computed tomography.* Osteoarthritis Cartilage, 2011. **19**(3): p. 295-301.
19. Raya J.G., Melkus G., Adam-Neumair S., Dietrich O., Mutzel E., Reiser M.F., Putz R., Kirsch T., Jakob P.M., Glaser C., *Diffusion-tensor imaging of human articular cartilage specimens with early signs of cartilage damage.* Radiology, 2013. **266**(3): p. 831-41.
20. Tavakoli Nia H., Han L., Soltani Bozchalooi I., Roughley P., Youcef-Toumi K., Grodzinsky A.J., Ortiz C., *Aggrecan Nanoscale Solid–Fluid Interactions Are a Primary Determinant of Cartilage Dynamic Mechanical Properties.* ACS Nano, 2015. **9**(3): p. 2614-2625.
21. Kokkonen H.T., Mäkelä J., Kulmala K.A.M., Rieppo L., Jurvelin J.S., Tiitu V., Karjalainen H.M., Korhonen R.K., Kovanen V., Töyräs J., *Computed tomography detects changes in contrast agent diffusion after collagen cross-linking typical to natural aging of articular cartilage.* Osteoarthritis and Cartilage, 2011. **19**(10): p. 1190-1198.
22. Decker Sarah G.A., Moeini M., Chin Hooi C., Rosenzweig Derek H., Quinn Thomas M., *Adsorption and Distribution of Fluorescent Solutes near the Articular Surface of Mechanically Injured Cartilage.* Biophysical Journal, 2013. **105**(10): p. 2427-2436.
23. Tuomo S. Silvast J.S.J., Virpi Tiitu, Thomas M. Quinn and Juha Töyräs, *Bath Concentration of Anionic Contrast Agents Does Not Affect Their Diffusion and Distribution in Articular cartilage In Vitro.* Cartilage, 2013. **4**(1): p. 42-51.
24. Silvast T.S., Jurvelin J.S., Lammi M.J., Töyräs J., *pQCT study on diffusion and equilibrium distribution of iodinated anionic contrast agent in human articular cartilage – associations to matrix composition and integrity.* Osteoarthritis and Cartilage, 2009. **17**(1): p. 26-32.

LIST OF PUBLICATIONS

PEER REVIEWED / SUBMITTED / TO BE SUBMITTED JOURNAL PUBLICATIONS:

1. **Arbabi V**., Pouran B., Weinans H., Zadpoor A.A., *Transport of Neutral Solute Across Articular Cartilage: The Role of Zonal Diffusivities.* Journal of Biomechanical Engineering, 2015. **137**(7): p. 071001-071001.

2. **Arbabi V**., Pouran B., Campoli G., Weinans H., Zadpoor A.A., *Determination of the mechanical and physical properties of cartilage by coupling poroelastic-based finite element models of indentation with artificial neural networks.* Journal of Biomechanics, 2016. **49**(5): p. 631-637.

3. **Arbabi V**., Pouran B., Weinans H., Zadpoor A.A., *Multiphasic modeling of charged solute transport across articular cartilage: Application of multi-zone finite-bath model.* Journal of Biomechanics, 2016. **49**(9): p. 1510-7.

4. Moshtagh P.R., Pouran B., van Tiel J., Rauker J., Zuiddam M.R., **Arbabi V**., Korthagen N.M., Weinans H., Zadpoor A.A., *Micro- and nano-mechanics of osteoarthritic cartilage: The effects of tonicity and disease severity.* Journal of the Mechanical Behavior of Biomedical Materials, 2016. **59**: p. 561-571.

5. **Arbabi V**., Pouran B., Weinans H., Zadpoor A.A., *Neutral solute transport across osteochondral interface: a finite element approach,* 2016. (under review)

6. **Arbabi V**., Pouran B., Weinans H., Zadpoor A.A., *Combined inverse-forward artificial neural networks for fast and*

accurate estimation of the diffusion coefficients of cartilage based on multiphysics models. Journal of Biomechanics, 2016. (in press)

7. **Arbabi V**., Pouran B., Zadpoor A.A., Weinans H., *Experimental and finite element protocol to investigate transport of charged and neutral solutes across articular cartilage*. Journal of Visualized Experiments, 2016. 49: p.631–637.

8. **Arbabi V**., Pouran B., Weinans H., Zadpoor A.A., *Multiphysics computational modeling in cartilage biomechanics: estimation of mechanical and physical properties*. (in progress)

9. Pouran B., **Arbabi V**., Zadpoor A.A., Weinans H., *Solute transport at the inter-face of cartilage and sub-chondral bone plate: effect of micro-architecture.*, 2016. (under review)

10. Pouran B., **Arbabi V**., Zadpoor A.A., Weinans H., *Isolated effects of external bath osmolality, solute concentration, and electrical charge on solute transport across articular cartilage*, 2016. (under review)

11. Pouran B., **Arbabi V**., Weinans H., Zadpoor A.A., *Application of multiphysics models to efficient design of experiments of solute transport across articular cartilage*, 2016. (under review)

12. Pouran B., **Arbabi V**., Weinans H., Zadpoor A.A., *Solute transport at the interface of cartilage and subchondral bone plate: effect of micro-architecture*, 2016. (under review)

BOOK CHAPTER:

13. **Arbabi V**., Pouran B., Weinans H., Zadpoor A.A. *Computational models of diffusion in cartilage*. Academic press, Elsevier, 2016. (Invited: in progress)

CONFERENCE PAPERS:

14. **Arbabi V.**, Campoli G., Weinans H., Zadpoor A.A., *Nanoindentation-based estimation of cartilage properties using artificial neural networks trained with finite element data.* Simulia BENELUX Regional User Meetings, Hoeven, The Netherlands (invited speaker), 2013.

15. **Arbabi V.**, Campoli G., Weinans H., Zadpoor A.A., *Estimation of cartilage properties using indentation tests, finite element models, and artificial neural networks.* 11th World Congress on Computational Mechanics & 5th European Conference on Computational Mechanics, Barcelona, Spain, 2014.

16. **Arbabi V.**, Pouran B., Weinans H., Zadpoor A.A., *Coupled finite element model-artificial neural networks can predict mechanical properties of articular cartilage.* Orthopaedic Research Society Annual Meeting, Las Vegas, Nevada, 2015.

17. Pouran B., **Arbabi V.**, Villamar J., Zadpoor A.A., Weinans H. *Contrast agent's transport across healthy articular cartilage under various bath conditions.* Orthopaedic Research Society Annual Meeting, Las Vegas, Nevada, 2015.

18. **Arbabi V.**, Pouran B., Weinans H., Zadpoor A.A., *Multiphasic finite element models enable determining fixed charge density and the diffusion coefficient of charged solutes in articular cartilage.* Orthopaedic Research Society Annual Meeting, Orlando, Florida, 2016.

19. Pouran B., **Arbabi V**., Zadpoor A.A., Weinans H., *Micro-features affect the transport of solutes at the interface of cartilage and subchondral plate.* Orthopaedic Research Society 2016 Annual Meeting, Orlando, Florida, 2016.

20. Pouran B., **Arbabi V**., Zadpoor A.A., Weinans H., *Micro-architecture affects the transport of solutes at the interface of cartilage and bone.* Osteoarthritis and Cartilage, 2016.

21. **Arbabi V**., Pouran B., Weinans H., Zadpoor A.A., *Transport of neutral solute across articular cartilage and subchondral plate.* 22nd Congress of the European Society of Biomechanics, Lyon, France, 2016.

22. Pouran B., **Arbabi V**., Zadpoor A.A., Weinans H., *Eeffects of bath attributes on the transport of solute across articular cartilage* 22nd Congress of the European Society of Biomechanics, Lyon, France, 2016.

23. **Arbabi V**., Pouran B., Weinans H., Zadpoor A.A., *Combined artificial neural networks for robust estimation of the diffusion coefficients across cartilage* 22nd Congress of the European Society of Biomechanics, Lyon, France, 2016.

24. Pouran B., **Arbabi V**., Zadpoor A.A., Weinans H., *Mechanical condition of articular cartilage regulates ezymatic activity* International Workshop on Osteoarthritis Imaging (IWOAI), Oulo, Finland, 2016.

25. **Arbabi V**., Pouran B., Weinans H., Zadpoor A.A., *Application of a biphasic-solute model in predicting diffusive properties of osteochondral interface.* International Workshop on Osteoarthritis Imaging (IWOAI), Oulo, Finland, 2016.

ACKNOWLEDGEMENTS

The overall success of a PhD researcher depends on factors such as his knowledge, skills, required resources, trainings, contributions and motivation. Motivation is like an internal force that makes a person moving toward a goal. Professor Harrie Weinans thanks for your support, patience, motivation and scientific inspirations. I have been enjoying your interesting point of views and fruitful conversations. Dr. Amir A. Zadpoor thanks for your sincere guidance and continuous scientific support during my PhD journey. I really appreciate that.

It is my pleasure to thank Professor Gerard Ateshian (Columbia University) for his scientific support. Dear Gerard, I have to say without your support, finishing my thesis with such an extensive amount of developed computational models would not be possible.

I would like to thank Prof. Gerhard Holzapfel, Prof. Victor Barocas, Prof. Keita Ito, Prof. Miika Nieminen, Prof. Simo Saarakkala and Dr. Mikko Nissi for their scientific advice and the time that I have discussed with them about my research.

Behdad Pouran and I were working on the experimental and computational aspects of solute diffusion across articular cartilage. We spent considerable amount of time together on discussion over our theses even in the weekends. I would like to thank you because of the amazing contribution we have had during the last three years.

I would like to extend a special word of thanks to Dr. Seyed Yousef Ahmadi form University of Bijand.

Thanks to Dr. Jie Zhou for his kind advices. I also would like to acknowledge Ms. Mascha Toppenberg in graduate school of 3mE.

I would like to thank the secretarial team of Biomechanical Engineering Department: Anouk, Diones, Sabrina, Nancy, Hanneke, Carla and also specially, department managers Dineke and Merijam for their support.

A special thanks to my friend Reza Hedayati for his time for cover designing of my thesis.

I would like to thank my friends: Hasan, Gianni, Mohamad, Shahram, Reza, Nazli, Sander, Zahra, Sina, Amin, Mehdi, Nader, Parisa, Abbas, Mina, Axel, Bram, Ewout, Martijn, Edo, Helene, Budi, Steven, Bart and Alistair.

Moving toward the more personal acknowledgments, I would love to express my special thanks to my wife and my family: My parents, my father and mother in-law, Safura, Saeed, Sara, Mohamad Javad, Mehdi, Bahar, Bita, Amir Mahdi, Masoud, Forough and Saman. Thanks for your kind words during this journey.

Finally, I would like to thank my wife Firoozeh. A special thanks for your never-ending support, encouragement, quiet patience and unwavering love. Thanks for the motivation that was like a gift from you.

ABOUT THE AUTHOR

Vahid Arbabi was born on April 29, 1980 in Zabol, Iran. He graduated from department of mechanical engineering of Yazd University, Yazd, Iran. In his master thesis he developed a new analytical method for determining dynamic yield stress of ductile porous materials. He was interested to work in an academic position, therefore, after his graduation he continued as an instructor and lecturer.

In May 2012, he joined department of biomechanical engineering at Delft University of Technology as a PhD researcher under supervision of Professor Harrie Weinans and Dr. Amir A. Zadpoor. Since he was interested in computational mechanics, during his research he focused on the articular cartilage characterizations considering estimation of its mechanical and physical properties using advanced computational models. He had two major goals during his research: first to develop advanced and simple yet accurate models to extract cartilage properties and second to develop algorithms based on trained artificial neural networks to obtain cartilage properties without any need for computational expertise.

In December 2015, since the completion of his PhD materials was performed on-time, he started his appointment as a post-doctoral researcher in the department of orthopedics at University Medical Center Utrecht. His post-doctoral topic revolved around microscopic evaluation of damage in articular cartilage which gave him the opportunity to develop advanced visualization skills at the molecular level such as focused ion-beam scanning electron microscopy, Raman spectroscopy and polarized light microscopy. He aims to continue his research on experimental and computational mechanochemistry of soft tissues.

This thesis includes part of the peer reviewed journal papers that Vahid Arbabi contributed to publish during his PhD.

NOTES

ISBN/EAN: 978-94-6186-713-1

TU Delft Delft University of Technology

Knowledge of mechanical and physical properties of articular cartilage is crucial in proper understanding of osteoarthritis progression and etiology. Advanced computational models associated with algorithms were developed and applied to spherical indentation tests and diffusion tests based on micro-computed tomography to determine Young's modulus, Poisson's ratio, permeability, solute diffusivity and fixed charge density of articular cartilage. As computational expertise among clinicians and experimentalists does not always exist, a novel intelligent system based on combined artificial neural networks-finite element models was proposed to eliminate experimental noise and computational expertise. This algorithm proved to be efficacious when applied to problems of solute transport across articular cartilage and indentation of poroelastic materials e.g. articular cartilage.